



This work is licensed under a [Creative Commons Attribution-NonCommercial-ShareAlike 4.0 International License](https://creativecommons.org/licenses/by-nc-sa/4.0/).

How to cite this thesis / dissertation (APA referencing method):

Surname, Initial(s). (Date). *Title of doctoral thesis* (Doctoral thesis). Retrieved from [http://scholar.ufs.ac.za/rest of thesis URL on KovsieScholar](http://scholar.ufs.ac.za/rest_of_thesis_URL_on_KovsieScholar)

Surname, Initial(s). (Date). *Title of master's dissertation* (Master's dissertation). Retrieved from [http://scholar.ufs.ac.za/rest of thesis URL on KovsieScholar](http://scholar.ufs.ac.za/rest_of_thesis_URL_on_KovsieScholar)

Geostatistical surface modelling of radionuclide distribution patterns over gold tailings: The New Machavie TSF case study

Luan Nel

2014121319

Dissertation submitted in fulfilment of the requirements for the degree *Magister Scientiae* in Geology at the University of the Free State, Bloemfontein Campus

Project Supervisor: Dr R.N. Hansen and Mr R. Rentel

April 2018



UFS·UV

UNIVERSITY OF THE FREE STATE
UNIVERSITEIT VAN DIE VRYSTAAT
YUNIVESITHI YA FREISTATA

DISCLAIMER

I declare that the dissertation hereby submitted by me for the degree *Magister Scientiae* in Geology at the University of the Free State is my own independent work and has not been previously submitted by me to another University/Faculty. I further cede copyright of the dissertation in favour of the University of the Free State.

Signature: Luann Vel

Date: April 2018

Place: UFS, Bloemfontein, South Africa.

PROJECT ABSTRACT

Motivated by an identified need for research specifically focused on providing industry with a better understanding of tailings impoundments, the project aimed to deliver a geostatistical 3D surface model of a typical tailings storage facility, which upon completion, would be capable of identifying radionuclide distribution patterns, for either prospecting or environmental assessment purposes. In an attempt to keep project expenses at a minimum, the 3D surface model was created using alternative methods of data acquisition, working in conjunction with a capable geostatistical-interpolator, as an alternative approach to more traditional geochemical sampling and laboratory analyses. Since the combination of portable X-ray fluorescence (PXRF) spectroscopy, natural gamma-ray spectrometry and Ordinary Prediction-based Kriging has not been tested for uranium exploration or environmental assessment over tailings impoundments before, the project, being the first of its kind, aimed to validate the viability of the approach.

Evidenced by the successful identification of both radionuclide anomalies (potassium, thorium and uranium), as well as their respective migration pathways, results were found to validate the approach as a respectable alternative to conventional methods. Given the anionic and oxidative nature of the TSF in question, both analytical techniques identified changes in elevation, as being the dominant mechanism governing the distribution of mobilised radionuclides over the New Machavie TSF. While literature proposed the accumulation of radionuclides (K, Th and U) to the centre of the impoundments, results seemed to indicate the exact opposite, as radionuclides were found to migrate away from the top of the impoundments, before accumulating on the lower side slopes, following the natural flow direction of the TSF. With results stating the presence of uranium migration, geochemical indices were incorporated to quantify the extent of the migration. Despite literatures doubtfulness with regards to how radioactive disequilibrium would influence the results, both indices proved to be quite effective in verifying the radionuclide anomalies.

Keywords: 3D surface model, Alternative approach, Migration, Radionuclides, Tailings Storage Facility

PROJEK UITTREKSEL

Gemotiveerd deur 'n geïdentifiseerde aanvraag na navorsing, spesifiek gefokus op die bevordering van kennis met betrekking tot slikdamme, was die doel van die projek om 'n geostatistiese 3D-oppervlakmodel van 'n tipiese slikdamkompleks te ontwerp. Na voltooiing van die vereistes sal die model in staat wees om radionuklied verspreidingspatrone te identifiseer vir beide uraanprospektering- en omgewingsevaluering doeleindes. In 'n poging om projekuitgawes tot 'n minimum te beperk, was die 3D-oppervlakmodel geskep deur gebruik te maak van alternatiewe metodes van dataverkryging, in samewerking met 'n bekwame geostatistiese interpoleerder, as 'n alternatiewe benadering tot tradisionele geochemiese steekproefneming en laboratoriumontledings. Aangesien die kombinasie van draagbare-XRF, natuurlike gamma-straal spektrometrie en voorspellings-gebaseerde Kriging nog nie getoets is vir uraanprospektering of omgewingsevaluering oor slikdamme nie, was die projek daarop gemik om die lewensvatbaarheid van die benadering te bekragtig.

Gebaseer op die sukses behaal met die identifikasie van beide radionuklied-anomalieë, asook hul onderskeie migrasiepatrone, is daar bevind dat die benadering wel kan dien as 'n alternatief tot meer konvensionele metodes. Gegewe die anioniese en oksidatiewe aard van die betrokke slikdamkompleks, het beide analitiese tegnieke verandering in elewasie uitgewys as die dominante meganisme verantwoordelik vir die verspreiding van gemobiliseerde radionukliede. Waar literatuur die akkumulاسie van radionukliede na die middel van 'n slikdam voorgestel het, het die resultate presies die teenoorgestelde gestaaf, nadat radionukliede gevind is om weg te beweeg van die bopunt van slikdamme, voordat hul aan die onderkant van die slikdamhelling akkumuleer, na aanleiding van die natuurlike vloerigting van die slikdamkompleks. Met die identifikasie van uraanmigrasie, is daar gebruik gemaak van geochemiese indekse om die omvang van die migrasie te probeer kwantifiseer. Ten spyte van literatuur se twyfelagtigheid, met betrekking tot hoe radioaktiewe onewewigtigheid, die resultate van die geochemiese indekse sou beïnvloed, was daar gevind dat albei indekse effektief die radionuklied-anomalieë kon verifieer.

Sleutelwoorde: 3D-oppervlakmodel, Alternatiewe benadering, Migrasie, Radionukliede, Slikdamkompleks

ACKNOWLEDGEMENTS

The author would like to express his gratitude to the individuals listed below for their continual support, assistance and input throughout the duration of the project. The author also owes a debt of gratitude to the organisations listed below for their technical support, access and digital software packages.

- ✚ Dr. Robert Hansen (Project Supervisor)
- ✚ Mr. Raimund Rentel (Project Co-supervisor)
- ✚ Dr. Frederick Roelofse (Head of Department: Geology)
- ✚ Mr. Piet van Deventer (Assisting supervisor)
- ✚ Mr. Jaco Koch (Assisting supervisor)
- ✚ Mrs. Megan Purchase (XRF Analysis)
- ✚ Mr. Dirk Pretorius (SMC-Synergy group)
- ✚ Eleazer Mining Company (Owners of the New Machavie TSF)
- ✚ African Mineral Standards “AMIS” (PXRF reference material provider)
- ✚ Stellenbosch University’s Centre for Geographical Analysis (DSM image provider)



TABLE OF CONTENT

DISCLAIMER	I
PROJECT ABSTRACT	II
PROJEK UITTREKSEL	III
ACKNOWLEDGEMENTS	IV
TABLE OF CONTENT	V
LIST OF FIGURES.....	X
LIST OF TABLES	XIV
LIST OF EQUATIONS	XV
LIST OF ACRONYMS AND ABBREVIATIONS	XVI
CHAPTER 1: INTRODUCTION.....	1
1.1 Background.....	1
1.2 Problem Statement	4
1.3 Hypothesis	5
1.4 Motivation.....	5
1.5 Aim and Objectives.....	6
1.5.1 Project Aim	6
1.5.2 Project Objectives.....	7
1.5.2.1 Objective 1	7
1.5.2.2 Objective 2	8
1.5.2.3 Objective 3	8

CHAPTER 2: LITERATURE REVIEW	9
2.1 Radiometric theory and Disequilibrium.....	9
2.1.1 Alpha decay (α -decay)	9
2.1.2 Beta decay (β -decay).....	10
2.1.3 Electron capture.....	10
2.1.4 Gamma radiation	11
2.1.5 The various radioactive series of naturally occurring radionuclides	11
2.1.5.1 The Uranium series	11
2.1.5.2 The Thorium series	14
2.1.5.3 The Actinium series.....	14
2.1.5.4 The Potassium series.....	14
2.2 Geochemical behaviour of radionuclides	16
2.3 Characteristics of gold tailings	19
2.3.1 Composition, geochemistry and AMD	19
2.3.2 The internal structure of a gold tailings impoundment	23
2.3.2.1 Oxidation zone	23
2.3.2.1.1 Cemented layers and hardpans.....	24
2.3.2.2 Oxidation front.....	25
2.3.2.3 Reduction zone	26
2.3.2.4 Saturated zone.....	27
CHAPTER 3: STUDY AREA.....	28
3.1 Locality and site history	28
3.1.1 Site Description.....	28
3.1.2 Site History	29
3.2 Topography and drainage	31
3.2.1 Topography	31
3.2.2 Drainage.....	35

3.3 Geological Setting	36
3.3.1 Introduction	36
3.3.2 The Transvaal Supergroup	37
3.3.3 The Black Reef Formation	38
3.3.3.1 Distribution and Structure of the Black Reef Formation	38
3.3.3.2 Composition of the Black Reef Formation	40
3.3.3.3 Origin of the gold and radionuclides in the Black Reef Formation	41
3.3.4 The Malmani Subgroup.....	43
3.3.4.1 The Oaktree Formation	43
3.3.4.2 The Monte Christo Formation	44
3.4 Pedology.....	46
 CHAPTER 4: MATERIALS AND METHODS.....	 49
4.1 Materials	49
4.2 Analytical methods	49
4.3 Project methodology	51
4.3.1 Site selection and sample grid establishment.....	51
4.3.2 Geochemical sampling and sample preparation.....	54
4.3.3 Analytical methods.....	55
4.3.3.1 Radiometric survey.....	55
4.3.3.2 Field Portable-XRF analysis	56
4.3.4 Geostatistical data processing	57
4.3.4.1 Data normalisation	57
4.3.4.2 Correlation and regression comparisons	57
4.3.4.3 Uranium Migration Index (UMI).....	58
4.3.4.4 Radionuclide Ratio Maps.....	59
4.3.4.5 Radiation Exposure Rate and Equivalent Radiation Dose Rate.....	59

4.3.5	3D Geostatistical surface modelling	60
4.3.5.1	Elevation survey	60
4.3.5.2	Ordinary Prediction-based Kriging	60
CHAPTER 5: GEOSTATISTICAL DATA PROCESSING.....		62
5.1	Introduction	62
5.2	Chapter objectives and motivations	63
5.3	Results and discussion	63
5.3.1	Data normalisation	63
5.3.2	Correlation and regression comparisons.....	67
5.4	Chapter conclusion	73
CHAPTER 6: SPATIAL DISTRIBUTION PATTERNS OF RADIONUCLIDES		74
6.1	Introduction	74
6.2	Chapter objectives and motivation	75
6.3	Results and discussion	75
6.3.1	Spatial distribution patterns of radionuclides	75
6.3.2	Spatial distribution patterns of uranium over the tailings impoundments	77
6.3.3	Spatial distribution patterns of uranium over the surrounding area of influence	83
6.3.4	Spatial distribution patterns of thorium over the New Machavie TSF	86
6.4	Chapter conclusion	91
CHAPTER 7: URANIUM MIGRATION AND ANOMALY VERIFICATION.....		94
7.1	Introduction	94
7.2	Chapter objectives and motivation	96
7.3	Results and discussion	96
7.3.1	Uranium Migration Index	96
7.3.2	Radionuclide Ratio Maps	104

7.3.3 Radiation Exposure Rate (RER) and Equivalent Radiation Dose Rate (ERDR).....	109
7.4 Chapter conclusion	113
CHAPTER 8: FINAL CONCLUSION AND RECOMMENDATIONS	115
8.1 Conclusion	115
8.2 Recommendations.....	116
8.2.1 Resource evaluation purposes.....	116
8.2.2 Environmental assessment purposes	116
REFERENCES.....	122
APPENDICES.....	132
Appendix A: Geostatistical data processing	132
Appendix B: Spatial distribution patterns of radionuclides	136
Appendix C: Uranium migration and anomaly verification.....	143

LIST OF FIGURES

Figure 1: Locality map of the New Machavie Tailings Storage Facility, showing the opencast mining activity and respective tailings impoundments	30
Figure 2: Digital Elevation Model of the New Machavie Tailings Storage Facility and surrounding area of influence	32
Figure 3: Digital Elevation Model of Tailings dam No.1	33
Figure 4: Digital Elevation Model of Tailings dam No.2 to No.5	34
Figure 5: A simplified geological map of the Transvaal Supergroup, highlighting the spatial extent of the Black Reef Formation and overlying Transvaal Supergroup strata (modified after Fuchs <i>et al.</i> , 2016).....	39
Figure 6: Surface geology of the New Machavie Tailings Storage Facility	45
Figure 7: Surface pedology of the New Machavie Tailings Storage Facility	48
Figure 8: Surface geochemical sampling grid: Highlighting the extent and density of the sampling procedure.....	53
Figure 9: Data normalisation: PXRF derived uranium concentrations (ppm), plotted against the expected normal distribution of the dataset	65
Figure 10: Data normalisation: PXRF derived thorium concentrations (ppm), plotted against the expected normal distribution of the dataset	65
Figure 11: Data normalisation: Equivalent uranium concentrations (ppm), plotted against the expected normal distribution of the dataset	66
Figure 12: Data normalisation: Data normalisation: Equivalent thorium concentrations (ppm), plotted against the expected normal distribution of the dataset	66
Figure 13: Statistical comparison of recorded uranium concentrations, as measured by the portable-XRF and natural gamma-ray spectrometry respectively	70
Figure 14: Statistical comparison of recorded thorium concentrations, as measured by the portable-XRF and natural gamma-ray spectrometry respectively	70

Figure 15: Statistical comparison of recorded uranium concentrations, as measured by laboratory based XRF and natural gamma-ray spectrometry respectively	71
Figure 16: Statistical comparison of recorded thorium concentrations, as measured by laboratory based XRF and natural gamma-ray spectrometry respectively	71
Figure 17: Statistical comparison of recorded uranium concentrations, as measured by laboratory based XRF and the portable-XRF respectively	72
Figure 18: Statistical comparison of recorded thorium concentrations, as measured by laboratory based XRF and the portable-XRF respectively	72
Figure 19: 3D surface model illustrating the spatial distribution of equivalent uranium concentrations, as measured by the natural gamma-ray spectrometer.....	78
Figure 20: 3D surface model illustrating the spatial distribution of measured uranium concentrations, as derived from the portable-XRF.....	79
Figure 21: 3D surface model illustrating the spatial distribution of equivalent thorium concentrations, as measured by the natural gamma-ray spectrometer.....	89
Figure 22: 3D surface model illustrating the spatial distribution of measured thorium concentrations, as derived from the portable-XRF.....	90
Figure 23: 3D surface model illustrating the spatial distribution of calculated “original” uranium concentrations, prior to the formation of the oxidising environment seen today.....	101
Figure 24: 3D surface model of quantified uranium migration values, illustrating the migration of uranium away from the impoundments, following the natural flow direction of the TSF	102
Figure 25: 3D surface model illustrating the rate of uranium migration, either into (+ values) or away from (- values) a specific location.....	103
Figure 26: 3D surface model illustrating eU/eTh ratios: Verifying uranium anomalies relative to thorium concentrations.....	107
Figure 27: 3D surface model illustrating eU/K% ratios: Verifying uranium anomalies relative to potassium concentrations.....	108
Figure 28: 3D surface model illustrating the rate of uranium exposure over the New Machavie TSF	111

Figure 29: 3D surface model illustrating the equivalent dose of radiation a person would be exposed to over the New Machavie TSF	112
Figure 30: 3D surface model illustrating the methodology of Chakraborty <i>et al.</i> (2017), using measured copper concentration as an example	118
Figure 31: 3D surface model illustrating the probability distribution of measured copper concentrations, exceeding the NEMWA threshold level of 16ppm	119
Figure 32: 3D surface model illustrating the methodology of Chakraborty <i>et al.</i> (2017), using measured arsenic concentration as an example	120
Figure 33: 3D surface model illustrating the probability distribution of measured copper concentrations, exceeding the NEMWA threshold level of 16ppm	121
Figure 34: Statistical comparison between recorded uranium and thorium concentrations, as measured by natural gamma-ray spectrometry	133
Figure 35: Statistical comparison between recorded uranium and thorium concentrations, as measured by portable-XRF spectroscopy	133
Figure 36: Ordinary prediction-based Kriging interpolation of equivalent uranium concentrations, projected over contemporary high resolution imagery.....	137
Figure 37: Ordinary prediction-based Kriging interpolation of measured uranium concentrations, projected over contemporary high resolution imagery.....	138
Figure 38: Ordinary prediction-based Kriging interpolation of equivalent thorium concentrations, projected over contemporary high resolution imagery.....	139
Figure 39: Ordinary prediction-based Kriging interpolation of measured thorium concentrations, projected over contemporary high resolution imagery.....	140
Figure 40: Ordinary prediction-based Kriging interpolation of measured potassium concentrations (%), projected over contemporary high resolution imagery	141
Figure 41: Ordinary prediction-based Kriging interpolation of calculated “original” uranium concentrations, projected over contemporary high resolution imagery.....	144
Figure 42: Ordinary prediction-based Kriging interpolation of quantified uranium migration values, projected over contemporary high resolution imagery	145

Figure 43: Ordinary prediction-based Kriging interpolation of uranium migration rate values, projected over contemporary high resolution imagery	146
Figure 44: Ordinary prediction-based Kriging interpolation of eU/eTh ratios, projected over contemporary high resolution imagery	147
Figure 45: Ordinary prediction-based Kriging interpolation of eU/K% ratios, projected over contemporary high resolution imagery	148
Figure 46: Ordinary prediction-based Kriging interpolation of eTh/K% ratios, projected over contemporary high resolution imagery	149
Figure 47: Ordinary prediction-based Kriging interpolation of Radiation Exposure Rate values, projected over contemporary high resolution imagery	150
Figure 48: Ordinary prediction-based Kriging interpolation of Equivalent Radiation Dose Rate values, projected over contemporary high resolution imagery	151

LIST OF TABLES

Table 1: ^{238}U decay series (Directional arrows indicate α - decay between isotopes, while vertically stacked isotopes undergo β^- - decay)	13
Table 2: ^{232}Th decay series (Directional arrows indicate α - decay between isotopes, while vertically stacked isotopes undergo β^- - decay)	15
Table 3: ^{235}U (Actinium) decay series (Directional arrows indicate α - decay between isotopes, while vertically stacked isotopes undergo β^- - decay)	15
Table 4: Generalised stratigraphic column of the Ventersdorp Supergroup, showing the Loraine Formation, which outcrops in close proximity to the New Machvie TSF	36
Table 5: Generalised stratigraphic column of the Black Reef Formation, underlying the New Machvie TSF	38
Table 6: Generalised stratigraphic column of the Malmani Subgroup, underlying the New Machvie TSF	43
Table 7: A summary of the two types of material sampled from the New Machvie TSF	49
Table 8: A summary of the various analytical techniques and geochemical indices, used throughout the duration of the project	50
Table 9: Pearson Correlation Matrix showing the linear elemental relationships found between the respective measured concentrations	67
Table 10: Table illustrating the raw radionuclide concentrations of the selected samples, used to evaluate the statistical relationship between the measured concentrations of each analytical techniques respectively.	134
Table 11: Variogram parameters used to create the optimal Ordinary Prediction-based Kriging interpolation model for each individual dataset	135
Table 12: Pearson Correlation Matrix, showing the linear relationship found between respective datasets.	142

LIST OF EQUATIONS

Equation 1: $\text{FeS}_2 + 7/2\text{O}_2 + \text{H}_2\text{O} \rightarrow \text{Fe}^{2+} + 2\text{SO}_4^{2-} + 2\text{H}^+$	21
Equation 2: $\text{Fe}^{2+} + 1/4\text{O}_2 + \text{H}^+ \rightarrow \text{Fe}^{3+} + 1/2\text{H}_2\text{O}$	21
Equation 3: $\text{Fe}^{3+} + 3\text{H}_2\text{O} \rightarrow \text{Fe}(\text{OH})_3 + 3\text{H}^+$	21
Equation 4: $\text{FeS}_2 + 14 \text{Fe}^{3+} + 8\text{H}_2\text{O} \rightarrow 15\text{Fe}^{2+} + 2\text{SO}_4^{2-} + 16\text{H}^+$	21
Equation 5: $\text{FeS}_2 + 15/4\text{O}_2 + 7/2\text{H}_2\text{O} \rightarrow \text{Fe}(\text{OH})_3 + 2\text{SO}_4^{2-} + 16\text{H}^+$	22
Equation 6: $\text{UO}_{2(\text{s})} + 4\text{H}^+ \rightarrow 2\text{H}_2\text{O} + \text{U}^{4+}$	22
Equation 7: $\text{UO}_2^{2+} + \text{SO}_4^{2-} \rightarrow \text{UO}_2\text{SO}_4$	22
Equation 8: $U_o = eTh \times (\text{unit } eU / eTh)$	58
Equation 9: $U_m = U_p - U_o$	58
Equation 10: $U_{m\%} = (U_m / U_p) \times 100$	58
Equation 11: eU/eTh	59
Equation 12: $eU/K\%$	59
Equation 13: $eTh/K\%$	59
Equation 14: $\text{RER } (\mu\text{R/h}) = 1.505 * K (\%) + 0.653 * eU (\text{ppm}) + 0.287 * eTh (\text{ppm})$	59
Equation 15: $\text{ERDR } (\text{mSv/y}) = 0.0833 * \text{RER } (\mu\text{R/h})$	59

LIST OF ACRONYMS AND ABBREVIATIONS

2D	Two Dimensional (2D map visualisation)
3D	Three Dimensional (3D map visualisation)
Ac	Actinium
AMD	Acid Mine Drainage
AMIS	African Mineral Standards
ARD	Acid Rock Drainage
BGO	Bismuth Germanium Oxide crystal natural gamma-ray spectrometer
Bi	Bismuth
DEM	Digital Elevation Model
DSM	Digital Surface Model
ERDR	Equivalent Radiation Dose Rate
eTh	Equivalent Thorium (as measured (in ppm) by the radiometric survey)
eU	Equivalent Uranium (as measured (in ppm) by the radiometric survey)
g/ton	Grams per ton
GIS	Geographic Information System
GPS	Global Positioning System
IAEA	International Atomic Energy Agency
K%	Potassium percentage (as measured by the radiometric survey)
Ma	Million years
Mt.	Million tons
ORP	Oxidation-Reduction Potential
oz.	Ounce

Pb	Lead
ppm	Parts per Million
PTE	Potentially Toxic Element
PXRF	Field Portable X-ray Fluorescence
Ra	Radon
RER	Radiation Exposure Rate (in $\mu\text{R/h}$)
RMSE	Root-Mean-Square Error (Standardized)
T1	Refers to Tailings dam No.1 (Yellowish coloured tailings)
T2	Refers to Tailings dam No.2 (Sand tailings)
T3	Refers to Tailings dam No.3 (Dark greyish coloured tailings)
T4	Refers to Tailings dam No.4 (Partly reclaimed tailings)
T5	Refers to Tailings dam No.5 (Pinkish calcine tailings)
Th	Thorium
TIN	Triangulated Irregular Network
Tl	Thallium
TSF	Tailings Storage Facility
U	Uranium
U_m	Uranium migration value
$U_{m\%}$	Uranium migration rate
UMI	Uranium Migration Index
U_o	Original uranium concentration
wt. %	Weight percentage
XRF	X-ray Fluorescence

CHAPTER 1: INTRODUCTION

1.1 Background

Referring to English proverbs, one in particular, perfectly explains the face of the South African tailings sector at this very moment. The proverb: “*one man’s trash is another man’s treasure*”, or in the case of the South African tailings sector “*one man’s tailings is another man’s gold*”, comes to mind, when referring to the changing face of tailings retreatment and rehabilitation in South Africa (Wilkins, 2013 and Mintails, 2012). Some may call it the “*modern day gold rush*”, while others say it might even hold the answer to successful mine closure, the fact of the matter is; with the South African gold industry steadily declining, the next logical step is to move to mine closure, while still turning a profit (Wilkins, 2013 and Mintails, 2012).

Following the discovery of vast gold reserves in 1886, gold mining, both in the past as well as the present, has played a central role in South Africa’s economic, political and social-economic development (Adler *et al.*, 2007). Over the past few years various factors, including the high cost of deep level mining, low recoveries, fractious labour, as well as what some industry insiders view as an unsympathetic government, have led to mining houses exploring alternative avenues, in order to maintain margins and unlock new sources of profit (Wilkins, 2013 and Mintails, 2012).

Covering an area of more than 400 km² in the goldfields of the Witwatersrand Basin alone (Tutu *et al.*, 2009), the reprocessing of low grade legacy tailings, for the extraction of both gold and uranium resources, has become an attractive proposition for several mining companies (Wilkins, 2013). With South African tailings material typically containing about 0.3 g/ton of residual gold (Mintails, 2012), the extraction of low grade resources from tailings material, has long been researched by metallurgists (Bosch, 1990). Bosch (1990) added that the residue contained in legacy tailings of old, consist essentially of three products, namely (i) separated sand, (ii) slime, and (iii) material from the all-sliming processes. As a result gold content, although dependant on a number of factors, ranged between 0.3 - 1.5 g/ton for sand dams, while slime dams produced between 0.05 - 0.5 g/ton (Bosch, 1990). Today’s tailings on the other hand constitutes to virtually all the residue sent from gold extraction plants, resulting in a more homogeneous particle size distribution, while gold content is believed to range between 0.1 g/ton and 0.5 g/ton (Bosch, 1990). Due to a combination of recent developments in technology, lower overheads and a current gold price of around \$1346.70/oz. (London Metal Exchange on 18 April 2018), these low grade resources have now become profitable to mine, resulting in what people call “*the modern day gold rush*” (Mintails, 2012 and Bosch, 1990).

Several years after the discovery of gold in 1886, Dr A. W. Rogers noted that the gold ores mined from the goldfields of the Witwatersrand Basin contained radioactive substances (Whiteside, 1970). It was not until 1945 that Professor George W. Bain recognised that the Witwatersrand conglomerates proved to be a source of low grade uranium (Whiteside, 1970). Although recovered as a by-product of gold mining (Tutu *et al.*, 2009 and Whiteside, 1970), late Professor Charles Davidson described the Witwatersrand Basin as “*one of the largest low grade uranium fields in the world*”. Unfortunately, uranium production is dependent on the price of gold, which means, despite having “*one of the largest low grade uranium fields in the world*” these reserves only becomes economically viable, when mined concurrently with South Africa’s vast gold reserves (Whiteside, 1970). The main driver behind uranium mining in South Africa came in the form of U.S initiated governmental programs such as the Manhattan Project, during the mid-1940s, which set out to secure strategically important uranium resources, for the development of nuclear bombs (Winde, 2006). From the early 1950s onward, the uranium-bearing gold reefs of the West-Rand and Far West-Rand were used for large-scale uranium production, to such an extent, that at one stage, nine out of the twenty-two gold mines within these goldfields produced uranium in seven metallurgical recovery plants (Winde, 2006). As a result one of the world’s largest continuous producers of uranium oxide at the time, the Nuclear Fuels Corporation of South Africa (NUFCOR), was established in the area (Winde, 2006).

Since the decline in uranium production in the late 1980’s, uranium has largely been discarded onto gold tailings impoundments (Tutu *et al.*, 2009). During mining and mineral extraction, the rock mass is extensively fragmented, resulting in a dramatic increase in surface area, volume and consequently the rate of acid production, which in turn contributes to environmental implications (McCarthy, 2011). Despite South African uranium grades being classified as “*of very low grade*” by world standards, Whiteside (1970) stated that the material in old slime dams would one day become economically viable to rework, as the material has already been mined, crushed and is easily available (Whiteside, 1970). Due to the current demand for cleaner, alternative sources of energy, a series of exploration projects, as well as a number of uranium mines have been established in the Witwatersrand Basin (Tutu *et al.*, 2009). Although the price of uranium is considered to be low at present, it is believed that the price would be driven up, in a sustainable manner, by the international demand for power station fuel, as well as the construction of several proposed extraction plants on the West Rand (Wilkins, 2013). Since focus of recovery from tailings have shifted from the East to the West Rand, investments in new gold and uranium extraction plants, have become more feasible (Wilkins, 2013).

From an environmental perspective, the deposition of gold mine residue, along the goldfields of the Witwatersrand Basin has left South Africa with a legacy, which has not only been an eyesore but also a source of irritation and contamination (Bosch, 1990). Minerals in South Africa

are highly diversified, plentiful and profitable (Adler *et al.*, 2007). As a result government has granted certain privileges, to enable the industry to maximize profits, sometimes at the expense of the environment (Adler *et al.*, 2007). Fortunately times have changed, with South Africa recently incorporating objectives of sustainability and social justice into its constitution (Adler *et al.*, 2007). However, the resulting environmental implications associated with mining are often numerous and may exist for prolonged time periods, usually depending on the degree of severity. One such potential impact is the contamination of the surrounding environment in terms of water, air and soil quality. This is crucial for South Africa, especially when taking the magnitude of the South African mining sector into account. It is therefore essential that guidelines are established for the prevention of contamination, by first identifying the potential sources of contamination, and secondly, understanding the mechanisms behind these sources, before rehabilitation or mitigation specification criteria is established (Van Deventer and Slabbert, 2011).

Demers *et al.* (2008) on the other hand stated that the management of acid generating tailings is regarded as one of the main concerns within the mining industry. Not too long ago, a global approach, called “*Integrated Tailings Management*”, was proposed by Bois *et al.* (2005) and Bussière *et al.* (2002). The approach set out to encourage industry to maximize the re-use of acid-generating tailings, by reducing the volume of tailings stored in Tailings Storage Facilities (TSF), by means of desulphurization through flotation and the re-mining of ore containing material. Not only has the changing face of the tailings sector influence the way industries view ore containing legacy tailings, but also the way it should be rehabilitated. New developments, which permits better management in both reprocessing and rehabilitation strategies, includes the classification of mine residue by cycloning, as well as the use of thickened cyclone underflow for underground backfilling purposes (Wilkins, 2013 and Bosch, 1990). By using cyclones, mines are presented with the opportunity to manage three important tailings criteria, namely footprint, tonnage and rehabilitation, as cycloning permits the separation of coarse and fine material (Wilkins, 2013 and Bosch, 1990). As the quantity of commodities recovered from reclaimed tailings, amount to only fractions per ton of treated material, a need has arisen for bigger tailings impoundments, as well as the implementation of integrated design and operational methodologies, in order to make rehabilitation and the assessment of TSF's easier (Wilkins, 2013 and Bosch, 1990).

As with any proposed project of this scale, information pertaining to tailings impoundments is required in order to conduct a feasibility study (Bosch, 1990). Taking this information into consideration, while referring back to the changing face of the tailings sector, the idea of combining both reclamation and rehabilitation feasibility studies into one, came to mind. According to Koch (2014) and Bosch (1990), both studies require similar methodologies (bulk

sampling, laboratory analyses, and data interpretation), which could become expensive, time consuming and labour intensive, in order to gather enough information to justify each project. In the spirit of exploring alternative avenues, the project proposed an alternative approach to conventional feasibility studies, whether used for exploration or environmental assessment purposes. The project proposed a combination of two alternative methods of data acquisition, working in collaboration with a geostatistical-interpolator, capable of generating data points at unsampled locations, before projecting the interpolated data over a digital elevation model of the study area, to ease interpretation. The combination of techniques according to literature should provide the user with a highly effective alternative to traditional geochemical sampling and laboratory based chemical analyses, as measurements are taken *in situ*, while results are produced and mapped from a single computer, in the matter of days (Chakraborty *et al.*, 2017).

1.2 Problem Statement

The current predicament in which the South African gold industry finds itself, has led to the exploration of alternative avenues, in order to maintain margins and unlock new sources of profit (Wilkins, 2013 and Mintails, 2012). Not only has the changing face of the South African tailings sector shifted its focus, as well as its resources toward the lucrative potential hidden inside legacy tailings, but also to the way these legacy tailings are viewed from an environmental perspective (Wilkins, 2013 and Mintails, 2012). For many years the metaphorical “*thorn in the side*” of both respective fields has been the cost and time constraints associated with traditional laboratory based chemical analyses (Chakraborty *et al.*, 2017), as it not only affects project feasibility studies in the case of exploration projects (Koch, 2014), but also constrains spatial variability in the case of environmental assessment studies. In both cases, the deficiencies that exist within literature could also be ascribed, albeit in an indirect manner, to the limitations associated with traditional laboratory based chemical analyses, as authors from both respective fields supported the need for future research to focus on providing the industry with a better understanding of tailings impoundments in general.

With no shortage in the availability of acid mine drainage related articles (Hansen, 2015), several authors stated the need for studies specifically focused on the use of geochemical and geostatistical modelling techniques (Hansen, 2015; Koch, 2014; Tutu *et al.*, 2009 and Goovaerts, 1999), in order to answer the knowledge deficiency mentioned above. Hansen (2015) further mentioned that not one peer reviewed study could be sourced, with regards to geochemical models of Witwatersrand tailings impoundments. Although natural scientists are showing a growing interest in the use of geostatistics, the same could be said of geostatistical analysis, as its use is limited to the creation of colourful probability maps, while the practical use of geostatistics for decision making purposes, receives little attention (Goovaerts, 1999). Despite offering formidable advantages over traditional laboratory based chemical analyses

(Chakraborty *et al.*, 2017), the same could once again be said of portable X-ray fluorescence spectroscopy (PXRF), as only a few studies have incorporated PXRF spectroscopy as an alternative to traditional chemical analyses. It is this resistance to change, that underscores the need for studies specifically focused on providing industry with a better understanding of tailings impoundments (Hansen, 2015), through the use of “*alternative*” and in most cases already available tools and methods.

1.3 Hypothesis

Based on the success achieved using these “*alternative methods*” individually, as stated in literature (Chakraborty *et al.*, 2017; Koch, 2014; Assran *et al.*, 2012 and Goovaerts, 1999), the author hypothesised that the combination of these alternative methods, would prove highly effective in the identification of radionuclide accumulation hotspots, as it provides the user with a cheaper, faster and less labour intensive alternative to conventional geochemical sampling and analytical analyses.

1.4 Motivation

As previously mentioned a global approach, called “*Integrated Tailings Management*”, was proposed by Bois *et al.* (2005) and Bussière *et al.* (2002), which set out to encourage industry to maximize the re-use of acid-generating tailings material. Taking into consideration the popularity of mining companies reclaiming ore from legacy tailings and how it has changed the way industry view legacy tailings in general, it is without doubt that industry has indeed taken notice of the proposition. It is with this same enthusiasm towards change, that alternative methods of not only data acquisition, but also data interpretation, should be explored.

Classified as a previously abandoned gold mining complex, New Machavie houses five heavily eroded tailings impoundments, containing valuable mineral resources, while contributing to the environmental contamination of even more valuable natural resources. Even though the tailings impoundments still contain low grade gold and uranium ore (derived from the Black Reef Formation), the amount of available material would not be sufficient to support full scale reclamation activities, unless supplemented by conventional opencast- or underground mining operations (Koch, 2014). New Machavie therefore provides the ideal setting to conduct studies aimed at providing industry with relevant information regarding tailings impoundments and the manner in which they are assessed. This information would then have the potential to not only benefit reclamation operations, but also the assessment of environmental implications for rehabilitation purposes.

Although the price of uranium is considered to be low at present (\$20.50 per pound U_3O_8 (Tradetech on 13 April 2018)), a series of exploration projects, as well as a number of uranium

mines have been established in the Witwatersrand Basin (Tutu *et al.*, 2009). Project feasibility studies, used for exploration projects generally make use of geochemical soil sampling techniques and expensive laboratory analyses (Bosch, 1990), to identify areas of interest, before drilling commences. These analyses and techniques tend to be time consuming, labour intensive and expensive, resulting in a high initial costs to company. The project therefore aimed at validating the viability of using a combination of natural gamma-ray spectrometry and PXRF spectroscopy to acquire a wider range of radiometric data, compared to the more traditional approach, before interpreting the data by means of a geostatistical-interpolator, in the form of Ordinary Prediction-based Kriging. This alternative approach, based on literature (Chakraborty *et al.*, 2017 and Koch, 2014), is hypothesised to provide a much cheaper, faster and less labour intensive alternative to conventional geochemical sampling and analytical analyses. By projecting the acquired data over a three dimensional, digital elevation model of the New Machavie TSF, the model would provide the ideal platform for users to access and interpret relevant data, while also being able to visually represent their findings.

When viewed from an environmental perspective, the potential usefulness of the model might even exceed that of its initial purpose, as it provides the ideal platform for the investigation of the mechanics at work within a tailings impoundment. By interpolating the datasets, using a geostatistical-interpolator, capable of generating data points at unsampled locations (Chakraborty *et al.*, 2017 and Goovaerts, 1999), the model gains the ability to identify both radionuclide concentration levels, their respective distribution patterns, as well as the potential radioactivity of the TSF; both knowledge deficiencies pointed out by Tutu *et al.* (2009) and Tutu *et al.* (2003) respectively. When combined with the rapid assessment capabilities of PXRF spectroscopy on the other hand, which has the potential to analyse more than a dozen elements in a matter of seconds (Chakraborty *et al.*, 2017), the model gains the ability to assess metal trace element (including gold) distribution patterns over the tailings impoundment itself, as well as too the surrounding area of influence. In conclusion, the combination of the two alternative methods of data acquisition, working in conjunction with a capable geostatistical-interpolator, would provide a highly effective alternative, for the identification of radionuclide anomalies, whether used for exploration or environmental assessment purposes.

1.5 Aim and Objectives

1.5.1 Project Aim

Upon completion of the project's desktop study, it was duly noted that a need existed within literature, for future studies to focus on providing industry with a better understanding of the mechanics behind tailings impoundments. With some authors recommending the use of geochemical modelling (Hansen, 2015 and Tutu *et al.*, 2009), while others recommended a

geostatistical approach (Chakraborty *et al.*, 2017; Koch, 2014 and IAEA, 2003), it quickly became clear that the real problem did not necessarily lie in the analytical approach, but rather in the availability of relevant data. In most cases the unavailability of relevant data, whether used for exploration or environmental assessment purposes, could be ascribed to traditional laboratory based chemical analyses being too costly and time consuming (Chakraborty *et al.*, 2017). With this in mind, the decision was made to create a geostatistical surface model, where data was gathered using alternative analytical techniques (natural gamma-ray spectrometry and PXRF spectroscopy), capable of obtaining a much wider range of data, at a much lower cost to company.

The project therefore aimed to deliver a geostatistical 3D surface model of the New Machavie TSF, which upon completion could be used to assist in the identification of radionuclide distribution patterns, for either prospecting (exploratory drilling) or the assessment of the tailings impoundments for environmental purposes. Despite PXRF spectroscopy having the ability to analyse more than a dozen elements in a matter of seconds (Chakraborty *et al.*, 2017), for the purpose of this project, attention was focused on using the PXRF as an alternative approach, for rapid identification of radionuclide anomalies over a TSF. Since the combination of PXRF spectroscopy, natural gamma-ray spectrometry and Ordinary Prediction-based Kriging has not been tested for uranium exploration or environmental assessment over tailings impoundments before, the project aimed to validate the viability of the approach, as an alternative to more traditional geochemical sampling and laboratory based analyses.

1.5.2 Project Objectives

Given the multi-disciplinary nature of the model, for the purpose of the project, attention was focused on identifying radionuclide distribution patterns, over the tailings impoundments itself, as well as to the surrounding area of influence. In doing so, the model would have the ability to identify radionuclide concentration levels at any given location, while at the same time allowing the user to identify areas of radionuclide accumulation, as well as the migration paths leading to the anomaly itself. Upon completion, the geostatistical 3D model could be used to assist in the identification of areas of interest for either prospecting or the assessment of the tailings impoundments for environmental purposes. In order to create a model of this magnitude, the following objectives needed to be completed:

1.5.2.1 Objective 1

“Quantify the natural surface gamma radiation, as well as element concentration levels of selected radionuclides, using both radiometric spectrometry and portable X-ray fluorescence spectroscopy”.

In accordance to Chakraborty *et al.* (2017), the accuracy, immediacy and inexpensiveness of portable X-ray fluorescence spectroscopy, offers more advantages over traditional laboratory based chemical analyses. Since the study was in need of an alternative analytical technique, which would serve as the ground truthing method to the radiometric survey, PXRF spectroscopy was chosen, as it also provided an alternative approach to identifying uranium anomalies, *in situ* and in the field. Therefore, as a subordinate of the current objective, the best suited analytical technique, for quick and cost effective uranium prospecting or environmental assessment, over tailings impoundments, was identified.

1.5.2.2 Objective 2

“After creating the geostatistical 3D surface model, identify the spatial distribution patterns of selected radionuclides over the New Machavie TSF”.

According to literature, both radiometric spectrometry (IAEA, 2003), as well as PXRF spectroscopy (Chakraborty *et al.*, 2017), coupled with the spatial visualisation of geostatistical-interpolations, provides a straightforward approach to identifying and interpreting radionuclide distribution patterns. Since the combination of PXRF spectroscopy, natural gamma-ray spectrometry and Ordinary Prediction-based Kriging has not been tested for uranium exploration or environmental assessment over tailings impoundments before, the project aimed to validate the viability of the approach, as an alternative to traditional laboratory based chemical analyses.

1.5.2.3 Objective 3

“By making use of geochemical indices, generally reserved for uranium exploration within a geological unit, quantify the extent of the uranium migration and verify the previously identified uranium anomalies.”

Stated by several authors, the Uranium Migration Index (UMI) is considered to be a valuable variable in the assessment of uranium migration (Assran *et al.*, 2012 and Abu-Deif *et al.*, 2001), whether used for exploration or environmental assessment purposes (Koch, 2014). Further aiding in the identification of uranium anomalies, Ratio Maps not only provides a better indication of preferential accumulation (IAEA, 2003), but also assists in uranium exploration by identifying and confirming uranium-enriched areas (Assran *et al.*, 2012). As a subordinate of the current objective, the radioactivity of the New Machavie TSF was assessed using both Radiation Exposure Rate (RER) and Equivalent Radiation Dose Rate (ERDR) calculations, as the lack of radioactivity measurements were identified as a deficiency in literature by Tutu *et al.* (2009).

CHAPTER 2: LITERATURE REVIEW

2.1 Radiometric theory and Disequilibrium

In 1789, German chemist Martin Klaproth discovered uranium by chance, while conducting research on the mineral pitchblende (UO_2 , with variable proportions of U_3O_8) (Mahed, 2009 and IAEA, 2003). Characterized as a heavy, ductile metal with slight paramagnetic qualities, this silverish-white coloured metal holds the position of the last naturally occurring element on the periodic table. In 1896, Henry Becquerel identified uranium as the first element that possessed radioactive qualities, which as a naturally occurring element contributes to low levels of natural background radiation in the environment (Gavrilescu *et al.*, 2009 and IAEA, 2003). Uranium can be found in all rock types, usually varying in concentration between small to trace amounts. It is widely dispersed in the earth's crust and can also be found in the overlaying soils, generally as the result of enriched-bedrock erosion and element recycling (Gavrilescu *et al.*, 2009). Literature states that lower concentrations of uranium are generally found in basic rock types, when directly compared to that of acidic rock types, but that average radioactivity measurements in soils were found to be similar to that of the bedrock from which it was derived (Gavrilescu *et al.*, 2009). As a result uranium is be considered to be more abundant than gold, silver, mercury and even cadmium, while being more or less as common as arsenic, cobalt, tin and lead (Gavrilescu *et al.*, 2009).

According to Gavrilescu *et al.* (2009), Mahed (2009) and the IAEA (2003), natural uranium consists of three isotopes, namely ^{238}U , ^{235}U and ^{234}U , all of which are radioactive. Uranium-238, which forms part of the uranium decay series, together with ^{234}U , is considered to be the most abundant isotope (99.27%), whereas ^{235}U from the actinium decay series holds the position of the second most abundant isotope (0.72%) of the three (Gavrilescu *et al.*, 2009 and Mahed, 2009). When isotopes have too much energy, they are regarded as unstable and will disintegrate into more stable isotopes through the process of nuclear radiation, which usually takes place in the form of particle or energy discharge (Aswathanarayana, 1985). Aswathanarayana (1985) further stated that radioactive decay generally occurs as a result of one of the following processes:

2.1.1 Alpha decay (α -decay)

In order for thorium and uranium isotopes to reach stability, these radionuclides need to reduce both their mass and charge (Larkin, 2013), by radioactively decaying to one of the more stable isotopes of lead. With the most efficient way being the emission of several α -particles (helium nuclei), both proton and neutron numbers are reduced by a value of two, while mass is reduced by a value of four (Larkin, 2013 and IAEA, 2003). The process of α -particle transformation itself

is quite complex and cannot be explained by classical physics (Martin, 2006 (cited by Larkin, 2013)). Because an α -particle does not possess over the necessary energy required to penetrate the large potential energy barrier of the parent nucleus, the α -particle instead rely on attacking the barrier by bouncing back and forth within the nucleus (Larkin, 2013).

The back and forth movement in conjunction with the de Broglie wavelength, eventually leads to the α -particle "*tunnelling through*" the barrier (Larkin, 2013). The probability of emission therefore increases with an increase in α -particle energy. The process is further aided by the interaction of higher energy α -particles, with the thinner parts of the barrier, thereby further increasing the probability of "*tunnelling through*", while lower energy α -particles are left to interact with the thicker parts of the potential barrier (Larkin, 2013).

2.1.2 Beta decay (β -decay)

Beta decay can be divided into Beta minus (β^-) and Beta plus (β^+) decay respectively (IAEA, 2003). With reference to β^- -decay, a neutron within the parent nucleus spontaneously decays into a proton, β^- -decay particle and an anti-neutrino (Larkin, 2013 and IAEA, 2003). In contrast, β^+ -decay refers to the spontaneous decay of a proton within the parent nucleus, into a neutron, β^+ -decay particle and an electron neutrino respectively (Larkin, 2013). Although energetically impossible in the case of a free proton, the possibility does however arise in the case of an unstable nucleus, as the extra energy needed for the reaction is supplied.

2.1.3 Electron capture

Electron capture refers to the capture of a K or L-shell electron, by a proton (forming a neutron and an electron neutrino) within the nucleus (Larkin, 2013 and IAEA, 2003). Despite K-shell electrons being the closest to the nucleus to begin with, hence most captures being identified as K-capture, it is however possible for L-shell electrons to be captured, when positioned in close proximity to the nucleus in question (Larkin, 2013). The process occurs as a result of the wave motion of the orbital electrons, which positions the electrons in such close proximity to the unstable nucleus, that the process results in a decrease in the number of protons within the nucleus itself (Larkin, 2013). As a result, both the atomic number and chemical properties are changed, while the atomic mass remains the same (Larkin, 2013).

The process however continues as the vacancy, left during the capture of an electron from the innermost orbital, is immediately filled by electrons originating from the outer, higher energy orbitals (Larkin, 2013). The movement of an electron from a higher energy orbital to a lower energy orbital in turn produces characteristic X-rays, generally associated with the daughter nucleus itself. During instances where these X-rays do not escape from the atom, but rather

interact with the electrons of the outer electron shell, an electron is driven out from the electron shell to produce what is known as an “*auger electron*” (Larkin, 2013).

2.1.4 Gamma radiation

Similar to the emission of characteristic X-rays during the process of electron capture, the emission of gamma-ray photons are associated with both alpha (α) and beta (β) decay. Ascribed to the daughter nucleus being in an excited state, which compromises the manner in which the protons and neutrons are stacked within the shells of the nucleus itself, excess energy is emitted in the form of electromagnetic radiation, during the rearrangement of nuclear components to its lowest energy state (Larkin, 2013).

2.1.5 The various radioactive series of naturally occurring radionuclides

While there are many elements that have radioactive isotopes, only four naturally occurring elements, namely Actinium (Ac), Thorium (Th), Uranium (U), and Potassium (K) holds enough energy to have their own respective radioactive series (IAEA, 2003 and Aswathanarayana, 1985). With these decay schemes being the principal decay chains used to measure radioactivity during radiometric surveys (Larkin, 2013), attention was given to each decay chain respectively.

2.1.5.1 The Uranium series

The uranium series (see Table 1), with a half-life of 4.46×10^9 years, starts with ^{238}U and follows a long series, consisting of thirteen different radionuclides, before reaching a stable state in the form of ^{206}Pb (Gavrilescu *et al.*, 2009). As previously mentioned, during the radioactive decay of radionuclides, alpha and/or beta radiation is emitted, with some radionuclides also emitting gamma radiation in the process. If the daughter isotopes remain in place until the radionuclides have reached a stable state, the decay chain is believed to be in radioactive equilibrium (IAEA, 2003). However, in the natural environment, radioactive disequilibrium occurs as a result of disturbances, including physical and/or chemical processes, which promote the loss or gain of a certain decay product from the system (Tutu *et al.*, 2009 and IAEA, 2003). These processes include, but are not limited to weathering, erosion, sedimentation, precipitation, dissolution, crystallisation and the selective leaching of isotopes from the system (Koch, 2014 and Tutu *et al.*, 2009).

While radioactive disequilibrium might be a rarity in both the thorium and potassium decay series, the same cannot be said of the uranium series, as disequilibrium is quite common and could occur at several points along the decay series (IAEA, 2003). Ascribed to its gamma emitters being positioned in the lower margin of the decay series, ^{238}U could be selectively

leached relative to ^{234}U , while ^{234}U could be selectively leached relative to ^{238}U . Thorium-230 and ^{226}Ra on the other hand could be selectively removed from the decay chain, while ^{222}Rn (radon gas), due to its mobility, could escape from soils and rocks into the atmosphere (IAEA, 2003). As equilibrium depends on the half-lives of its radioisotopes, it may take days, weeks and even millions of years before equilibrium is restored (IAEA, 2003).

According to literature, disequilibrium in the uranium decay series has been identified as a serious source of error, with regards to radiometric surveys and the interpretation of the derived datasets (IAEA, 2003). It is therefore of the utmost importance, that equilibrium is not assumed, especially when working on disturbed areas, where clear signs of weathering and/or oxidation are visible (Koch, 2014). The source of errors arises from uranium concentrations being estimated “*indirectly*” off its progeny isotopes (Tutu *et al.*, 2003), generally based on measurement taken from ^{214}Pb and ^{214}Bi isotope abundances (IAEA, 2003; Aswathanarayana, 1985 and Richards, 1981). Because estimates are based on the assumption of equilibrium conditions, estimates of uranium and thorium concentrations are usually reported as “*equivalent*” uranium (eU) and thorium (eTh) respectively. Literature does however provide an answer to the problem, by accounting for disequilibrium and correcting the radiometric data, using results derived from Inductively Coupled Plasma Mass Spectrometry (ICP-MS) analysis (Koch, 2014; Aswathanarayana, 1985 and Richards, 1981).

Table 1: ^{238}U decay series (Directional arrows indicate α - decay between isotopes, while vertically stacked isotopes undergo β^- - decay)

Uranium Series		Atomic Mass																
		238	236	234	232	230	228	226	224	222	220	218	216	214	212	210	208	206
Atomic Number	92	U		U														
	91			Pa														
	90			Th		Th												
	89																	
	88							Ra										
	87																	
	86								Rn									
	85																	
	84										At							
	83										Po							
	82												Po					
	81												Bi					
80												Pb						
														Po				
														Bi				
														Pb				
														Tl				
																Pb		
																Tl		
																	Hg	

2.1.5.2 The Thorium series

The thorium decay series (see Table 2), with a half-life of 1.39×10^{10} years (IAEA, 2003), involves the decay of ^{232}Th to the stable state of the ^{208}Pb isotope. Similar to the uranium series, gamma emitters in the form of ^{228}Ac , ^{224}Ra , ^{212}Pb , ^{212}Bi and ^{208}Tl , could be used to calculate thorium content “indirectly” from its progeny isotopes, present within a sample. Radioactive disequilibrium in the thorium and potassium series however, has been found to be somewhat of a rarity (Koch, 2014 and IAEA, 2003). This is due to the gamma-emitting daughter isotopes being positioned quite close to the parent isotope, resulting in a lower susceptibility to being selectively leached (Aswathanarayana, 1985 and Richards, 1981). Tutu *et al.* (2009) adds that thorium and its progeny isotopes also tend to be less mobile, when directly compared to uranium and its respective progeny isotopes. Koch (2014) on the other hand stated that thorium showed signs of stability under oxidising conditions, thereby providing an explanation to the rarity of radioactive disequilibrium in the thorium decay series.

2.1.5.3 The Actinium series

The actinium series (see Table 3), with a half-life of 7.13×10^8 years (Koch, 2014), involves the decay of ^{235}U , before finally reaching a stable state in the form of ^{207}Pb (Gavrilescu, *et al.*, 2009; Aswathanarayana, 1985 and Richards, 1981).

2.1.5.4 The Potassium series

The potassium decay series, with a half-life of 1.251×10^9 years (Koch, 2014), involves the decay of ^{40}K directly to ^{40}Ar , through the process of electron capture (IAEA, 2003). Potassium-40 is one of only a hand full of isotopes that undergoes all three types of β -decay, which results in not only the production of gamma radiation, but also ^{40}Ca (Aswathanarayana, 1985 and Richards, 1981).

Table 2: ^{232}Th decay series (Directional arrows indicate α - decay between isotopes, while vertically stacked isotopes undergo β^- - decay)

Thorium Series		Atomic Mass												
		232	230	228	226	224	222	220	218	216	214	212	210	208
Atomic Number	90	Th		Th										
	89			Ac										
	88			Ra		Ra								
	87													
	86						Rn							
	85													
	84								Po			Po		
	83											Bi		
	82											Pb		Pb
	81												Tl	Tl

Table 3: ^{235}U (Actinium) decay series (Directional arrows indicate α - decay between isotopes, while vertically stacked isotopes undergo β^- - decay)

Actinium Series		Atomic Mass														
		235	233	231	229	227	225	223	221	219	217	215	213	211	209	207
Atomic Number	92	U														
	91			Pa												
	90			Th												
	89				Th											
	88				Ac											
	87						Ra									
	86						Fr									
	85								Rn							
	84								At			At				
	83										Po		Po			
	82										Bi		Bi			
	81												Pb		Pb	

2.2 Geochemical behaviour of radionuclides

When referring to environmental contamination, not all contaminants can be considered pollutants, but all pollutants can be classified as contaminants (Chapman *et al.*, 2003 (cited by Chapman, 2007)). Throughout the years, many expressions have been given to an element, which although present in minor concentrations (<1000 mg/kg) has the ability to impact the biological system either adversely or favourably (Robinson *et al.*, 2005). Herselman *et al.* (2005) for example, prefers to use the expression “*potentially toxic element*” (PTE’s), when referring to elements with the potential to contribute towards environmental contamination, whereas Hooda (2010a) prefers to use the expression “*heavy metals*”. The most recent preferred expression however is “*metal trace elements*”, as defined by Alloway (2012). Based on the information mentioned above, contamination can therefore be defined as the presence or input of a substance into an environment where it is not typically found (Chapman, 2007); generally to such an extent that it exceeds natural background concentrations.

As stated by Kabata-Pendias and Mukherjee (2007) the behaviour and availability of metal trace elements (which includes radionuclides) in soils, are controlled by the different sorption phases of the soil and the movement of the metal trace elements between these phases. Metal trace elements are generally present in both the soil solution and solid phases, but could also be found as different chemical species within the soil itself (Kabata-Pendias and Mukherjee, 2007 and Rösner *et al.*, 2001). With regards to the soil solution, the available metal trace elements are either derived from the easily soluble phase, comprising of free ions, organic and inorganic complexes, or the exchangeable sorption phase, which comprises of adsorbed exchangeable ions and compounds found in the diffuse double layer, surrounding the soil particle (Alloway, 2013; Hooda, 2010b and Rösner *et al.*, 2001). On the other hand, available metal trace elements present within the solid sorption phases, are usually derived from elements bound to organic matter, iron- and manganese oxides, or the residual fraction, which is the least mobile and thus not involved in chemical reactions of the soil. In contrast, the easily soluble and exchangeable fractions are considered to be the most mobile and therefore used to determine the bioavailability of the metal trace element in question (Kabata-Pendias, 1994 (cited by Rösner and van Schalkwyk, 2000)).

While the mobility of other metal trace elements might be governed by sorption phases, weathering of underlying geology is regarded as the primary factor controlling the mobility of radionuclides in overlying soils (Kabata-Pendias, 2011). Working in conjunction with the weathering, Pulford (2010), as well as Vandenhove *et al.* (2007) identified secondary controlling factors, which included the adsorption of radionuclides by both clay minerals and Al, Fe or Mn oxides, as well as the precipitation of radionuclides in the form of organic complexes, that governs the mobility of radionuclides in the soils. Kabata-Pendias (2011) on the other hand

identified both soil organic material and soil pH as the secondary controlling factors, stating that these two factors tend to regulate the distribution of radionuclides within soils, while being facilitated by either complexation (with anions, under oxidising conditions) or precipitation (with organic material, under reducing conditions), depending on the pH conditions of the soil in question. In order to fully understand the geochemical behaviour of radionuclides, each radionuclide needs to be investigated individually. For the purpose of this study however, attention was focused on the geochemical behaviour of uranium and thorium exclusively.

With regards to the geochemical behaviour of uranium and thorium respectively, the reduced (U^{4+} / Th^{4+}) and oxidized states (U^{6+} / Th^{6+}) are considered to be the most important valence states in any geological environment (Pulford, 2010; Gavrilesco *et al.*, 2009 and Vandenhove *et al.*, 2009). In both cases, these radionuclides are found either being sorbed (to both soil particles and pore water), complexed, precipitated or in reduced forms, all of which influences the mobility of the radionuclides differently (Gavrilescu *et al.*, 2009). Taking into consideration that uranium is generally in an oxidized form when present in soil, whereas it is present as a uranyl hydroxyl carbonate complex (UO_2CO_3 or $(UO_2)_2CO_3(OH)_3^-$) in water, the mobility of the uranium in soils or its vertical transport to groundwater (leaching) is dependent on the properties of the soil (Gavrilescu *et al.*, 2009). These include, but are not limited to redox potential, pH, soil porosity, material particle size, the concentration of complexing anions and sorption properties, as well as the amount of water available. The retention of uranium in soils on the other hand is mainly due to ion exchange, adsorption, chemisorption or a combination of mechanisms (Gavrilescu *et al.*, 2009). It can therefore be assumed that any alteration to the sorption mechanism, by any soil property, would alter the mobility of the radionuclide in the soil.

Similar to most metal trace elements, the mobility of uranium, in the natural environment, is largely governed by the presence of both complexation and redox reactions (Gavrilescu *et al.*, 2009). Even though uranium can exist in various valence states (U^{3+} , U^{4+} , U^{5+} or U^{6+}), only U^{4+} and U^{6+} are stable in aqueous media. Uranium in soils can also be transformed by means of abiotic and biological processes in the form of oxidation-reduction reactions, where soluble U^{6+} is converted to insoluble U^{4+} (Gavrilescu *et al.*, 2009). When in solution, uranium exist predominantly as UO_2^{2+} or soluble carbonate complexes, for example $(UO_2)_2CO_3(OH)_3^-$ and $UO_2(CO_3)_2^{2-}$. In acid solutions, UO_2^{2+} is the predominant form, with hexavalent uranium compounds believed to be the most soluble of them all (Gavrilescu *et al.*, 2009).

The speciation of uranium is considered to be pH and redox dependent, which results in different species being found at different pH ranges and environmental conditions (Pulford, 2010 and Vandenhove *et al.*, 2009). Between a pH of 4.0 and 7.5, the pH of most soils, U^{6+} exist primarily in a hydrolysed form, thereby stating that it is more active than U^{4+} , with a range of speciation possibilities (Gavrilescu *et al.*, 2009). Under oxidizing to mildly reducing conditions,

uranium, for example uranyl, will exist in the 6+ state. As a result, UO_2^{2+} will be the dominant U^{6+} species where the pH drops below 5.0 (Pulford, 2010 and Vandenhove *et al.*, 2009). U^{4+} on the other hand is stable under reducing conditions, generally occurring in the insoluble form of uranium dioxide (UO_2), which is believed to be relatively immobile. Under these type of conditions however, it is possible for dissolved U^{3+} to oxidize to U^{4+} , while micro-particles that are transported through porous media can be oxidized to U^{6+} , if transported to an oxidising environment (Koch, 2014; Pulford, 2010; Gavrilescu *et al.*, 2009 and Vandenhove *et al.*, 2009).

Another factor that contributes to the mobility of uranium in an aqueous medium is its solubility (Gavrilescu *et al.*, 2009). The solubility of uranium is greatly affected by factors such as redox potential, pH, ligand type and content, and lastly the presence of adsorbing minerals such as iron oxides, clays, phosphate minerals and organic matter (Pulford, 2010 and Vandenhove *et al.*, 2009). A good example of the statement mentioned above, is the presence of carbonates, which generally increases the mobility of uranium, through the formation of a negatively charged uranium complex, which cannot be adsorbed to iron oxides or clay minerals. In contrast, uranyl (UO_2^{2+}), which is believed to be very soluble in water, thus increasing its mobility, can be adsorbed to either iron oxides, clay particles, organic matter or phosphate minerals, which dramatically decreases its mobility (Pulford, 2010 and Vandenhove *et al.*, 2009).

Thorium on the other hand, as mentioned above, has a similar valence state as uranium, but only exists under environmental conditions as Th^{4+} (Vandenhove *et al.*, 2009). Literature states that organic matter, as well as iron and manganese oxides tend to be the main adsorption particulates of thorium (Vandenhove *et al.*, 2009 and US EPA, 1999). Even though the solubility of thorium is significantly lower than that of uranium, thorium is still soluble under a wide range of pH conditions, as a direct result of its Th^{4+} valence state (Alloway, 2012). Thorium has the ability to form a variety of hydroxyl species above a pH of 3.0, despite the Th^{4+} cation being resistant to hydrolysis (Vandenhove *et al.*, 2009 and US EPA, 1999). As a result most of the thorium species available under environmental conditions are considered to be insoluble and resistant to weathering (Koch, 2014 and Vandenhove *et al.*, 2009).

2.3 Characteristics of gold tailings

2.3.1 Composition, geochemistry and AMD

In Chapter 1, gold mining and its importance to the economic, political and social-economic development of South African were emphasised (Adler *et al.*, 2007). In accordance to Tutu *et al.* (2003) an unfortunate environmental consequences of this mining activity has been the release and distribution of metal trace elements into the surrounding area of influence, as a direct result of Acid Mine Drainage (AMD) arising from the oxidizing pyrite within the tailings impoundments. Yibas *et al.* (2010) on the other hand states that the unsaturated zone of a tailings impoundment is responsible for environmental contamination, as it is the zone where oxidation processes are most active. Yibas *et al.* (2010) further stated that the oxidation processes within tailings impoundments are governed by interplay between many factors, including geochemical and mineralogical composition, oxygen and water availability, catalysing bacteria and finally the weathering of oxidation products. It is therefore important to include criteria such as mineralogy, geochemistry, grain size, permeability, water and oxygen content and lastly the age of the tailings dam, when addressing tailings characteristics and oxidation (Yibas *et al.*, 2010).

Literature states that the mineralogical composition of Witwatersrand gold tailings are dominated by quartz (70 to 90%) and phyllosilicates (10 to 30%), as a direct result of it being derived from quartzite- or quartz-rich conglomerate ore (Koch, 2014; Yibas *et al.*, 2010; Bezuidenhout and Rousseau, 2005; Aucamp and van Schalkwyk, 2003 and Tutu *et al.*, 2003). In addition Koch (2014) and Yibas *et al.* (2010) both stated that quartz, mica and chlorite are the major minerals present in tailings material, while pyrophyllite and traces of K-feldspar, as well as other primary minerals, including pyrite (0.5 to 3 wt.%) and in some cases radionuclides, occur in minor amounts. Whenever uranium does occur in tailings material, its generally in the form of either uraninite (UO_2) or brannerite (UTi_2O_6), as these forms are normally associated with gold-bearing ores of the Witwatersrand Basin (Tutu *et al.*, 2003). With limited information available on the mineralogical composition of gold tailings, especially those derived from the Transvaal Supergroup's Black Reef Formation (as is the case of New Machavie), it could be assumed that the general composition would be similar to that of Witwatersrand gold tailings, as the Black Reef Formation consist of both a quartzite- and quartz-rich conglomerate unit. This assumption was later confirmed by the findings of Aucamp and van Schalkwyk (2003), which correlated well with that mentioned above, after identifying the major minerals within New Machavie tailings material as quartz, dolomite ($\text{CaMg}(\text{CO}_3)_2$), mica, chlorite, jarosite ($\text{KFe}^{3+}_3(\text{OH})_6(\text{SO}_4)_2$) and gypsum ($\text{CaSO}_4 \cdot 2\text{H}_2\text{O}$). Detailed mineralogical descriptions of both the Black Reef Formation, as well as the Witwatersrand auriferous ore are available from Rösner *et al.* (2001), Coetzee (1996) and Frankel (1940).

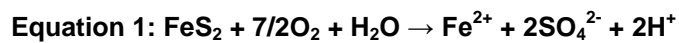
With reference to the geochemical nature of Witwatersrand gold tailings impoundments, Yibas *et al.* (2010) describe them as being dominated by pyrite. The statement becomes apparent when taking into consideration the effect the oxidation has on, not only the mineralogy of the tailings material, but also element distribution within the tailings itself. Yibas *et al.* (2010) further stated that in the top part of the oxidation zone, pyrite concentrations tend to decrease with depth, as jarosite makes its concomitant appearance, due to ferric iron precipitation. Quartz concentrations on the other hand tend to increase as one moves downward through a tailings profile, while pyrophyllite ($\text{Al}_2\text{Si}_4\text{O}_{10}(\text{OH})_2$) and mica, decrease with depth (Yibas *et al.*, 2010). Both Koch (2014) and Yibas *et al.* (2010) further stated that the concentration of pyrite and jarosite are in agreement with the progress of oxidation, with regards to depth, as jarosite concentrations decrease with depth, while pyrite concentrations tend to increase below the oxidation front. These statements are further supported by the findings of Bezuidenhout and Rousseau (2005), who while conducting research on the hydraulic properties of tailings dams, found that the pH tends to increase with depth, as a result of the limited penetration depth of oxygen, which in turn causes a decrease in pyrite oxidation. In order to fully understand the mechanics at work, with regards to the oxidizing environment and how it controls element distribution patterns within gold tailings impoundments, attention needed to be focused on the chemical reactions at work, in this case the reactions contributing to the formation of acid mine drainage.

According to Akcil and Koldas (2006), AMD is recognised as one of the more serious environmental problems, associated with the mining industry. During mining and mineral extraction, the rock mass is extensively fragmented, resulting in a dramatic increase in surface area, volume and consequently the rate of acid production (McCarthy, 2011). If the host rock contains large amounts of neutralizing material, the acid is usually neutralized and AMD does not become a serious problem (Bezuidenhout and Rousseau, 2005). Unfortunately, this is not the case for South African gold tailings, as the insufficient buffer capacity of the tailings material is overwhelmed by sufficient sulphide content, resulting in large quantities of metal enriched acidic water to leach into the surrounding area of influence (Hansen, 2015; McCarthy, 2011 and Yibas *et al.*, 2010). As the pH significantly decreases ($\text{pH} < 4$), the acidic water causes an increase in the solubility of uranium and other metal trace elements associated with the ore deposit, which not only renders the water toxic, but can have serious human health, as well as ecological implications.

Acid Mine Drainage is produced when sulphide-bearing material is exposed to oxygen, water and sulphide-oxidizing microorganisms (Akcil and Koldas, 2006). The production of AMD is associated, but not exclusive to iron sulphide-aggregated rocks. Acid mine drainage in its natural form is referred to as Acid Rock Drainage (ARD), which has the potential to emanate

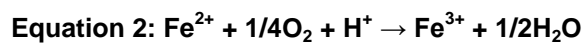
from mine waste rock piles and tailings material, as well as mine structures (Akcil and Koldas, 2006). In other words AMD is primarily regarded a function of the mineralogy of the local rock material, in the presence of available water (or a humid atmosphere) and an oxidant, generally in the form of oxygen (Akcil and Koldas, 2006). The associated metal contamination on the other hand, depends on various factors including the type and amount of oxidized sulphide-minerals, as well as the type of gangue minerals present in the host rock. Initially described by Garrels and Thompson (1960) and later improved by several authors, including Singer and Stumm, 1970 (cited by Chandra *et al.*, 2010), the oxidation of pyrite (FeS_2) and its subsequent acidity can be explained by means of the following reactions:

The chain of reactions starts off with the oxidation of the sulphide mineral, represented by pyrite (FeS_2) in the following reactions, into sulphate, hydrogen and dissolved iron ions.

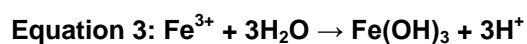


With reference to Equation 1, the residual sulphide minerals present in the tailings material becomes unstable when exposed to atmospheric oxygen and therefore undergoes oxidation (Tutu *et al.*, 2003). The result is the generation of acidity, an increase in total dissolved solids (TDS) and the release of metalloids and metal trace elements into the environment. If not neutralised, the solution pH will decrease significantly (Akcil and Koldas, 2006).

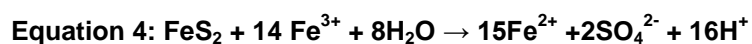
Equation 2 illustrates a sufficiently oxidized environment. The presence of sufficient oxygen concentrations, a lowered solution pH and the presence of bacterial activity, results in the oxidation of ferrous iron to ferric iron (Akcil and Koldas, 2006).



With reference to Equation 3, an environment is illustrated where the solution pH has been lowered to a pH of between 2.3 and 3.5. At such low pH values, ferric iron tends to precipitate as ferrihydrite and jarosite, leaving little ferric iron in the solution (Akcil and Koldas, 2006). This leads to a further decrease in the solution pH as acidity is generated by the reaction (Akcil and Koldas, 2006). This statement correlates well with that of Hansen (2015), who stated that ferric iron becomes soluble at a pH value below three and will continue to precipitate according to Equation 3, until sufficient acidity is produced by Equation 1.



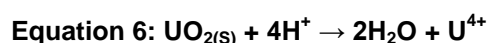
Referring to Equation 4, any residual ferric iron (Fe^{3+}) left over from Equation 2, which did not precipitate in accordance with Equation 3, can be used to further oxidize any additional pyrite (Akcil and Koldas, 2006).



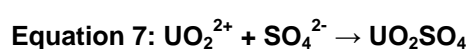
Equation 5 illustrates a combination of Equation 1 to Equation 3 and represents an acid generating reaction, where the pH is significantly lowered, which in turn results in an increase in the mobility and toxicity of the metal trace elements present (Tutu *et al.*, 2003).



As mentioned by Hallbauer, 1986 (cited by Hansen, 2015), as soon as the tailings solution becomes acidic, silicate minerals and pyrite grains tend to dissolve, releasing the metal trace elements previously stored in the mineral structure. With reference to uranium, during the weathering of uraninite and bannerite, a series of secondary minerals, which include U^{6+} -oxyhydroxides, silicates and sulphates are precipitated and later constituted as source phases for uranium mobilisation (Tutu *et al.*, 2003). Because uranium is seen as a proxy for transuranic actinides, these elements are generally present as either dissolved species (UO_2^{2+}), adsorbed onto mineral surfaces (coatings of tailings material) or precipitated in a similar manner as mentioned above (Tutu *et al.*, 2003). With Robb and Meyer, 1995 (cited by Hansen, 2015) stating that uranium reacts in the solution to produce soluble uranium under acidic conditions (see Equation 6), while Tutu *et al.* (2003) indicated that uranium occurs predominantly as uranyl-sulphate complexes under similar conditions (see Equation 7), the decision was made to include reactions stating both their findings.



Identified as a mineral weathering reaction, present in both the tailings material, as well as the soil system surrounding the tailings impoundment (Hansen, 2014), Equation 6 visually illustrates the statement of Robb and Meyer, 1995 (cited by Hansen, 2015), where uraninite, under acidic conditions, reacts within the solution to produce soluble uranium.



Equation 7 on the other hand, visually illustrates the dominant mechanism responsible for the mobilisation and chemical speciation of uranium (under oxidising conditions), where uranyl- and sulphate ions reacts within the solution, to form a uranium-sulphate complex (Vandenhove *et al.*, 2009).

2.3.2 The internal structure of a gold tailings impoundment

Upon investigation of the internal structure of gold tailings impoundments in general, it became apparent that gold tailings of the Witwatersrand Basin could be divided into distinct zones, based solely on their geochemical characteristics. Hansen (2015) stated that literature (Nengovhela *et al.*, 2007 and Dold and Fontboté, 2002) tend to agree with this statement, as both the mentioned authors, as well as Yibas *et al.* (2010) and Bezuidenhout and Rousseau (2005) identified three distinct zones, while conducting research on the internal structure of gold tailings. Identified as the Oxidation zone, the Oxidation front and the Reduction zone, also known as the Un-oxidized zone respectively, these distinct zones tend to differ in terms of geochemical composition, redox potential; oxygen concentration and moisture content (Yibas *et al.*, 2010). While conducting research on the Oxidation-Reduction Potential (ORP) of a gold tailings derived from the Black Reef Formation, Koch (2014) included a fourth distinct zone to his profile, namely the Saturated zone, after ORP profiles indicated a sharp decrease in the lowest part of the Reduction zone. The geochemical characteristics of each distinct zone will now be discussed in more detail:

2.3.2.1 Oxidation zone

The first distinctive zone, known as the Oxidation zone occurs from the surface of the tailings impoundment, inwards to the Oxidation front, which forms the boundary between the oxidized- and the un-oxidised sulphides (Hansen, 2015). Generally yellow to orange-brown in colour, the oxidation zone is characterized by the depletion of pyrite relative to other minerals such as chlorite, sulpho-salts (gypsum and jarosite) and secondary iron oxy-hydroxides, in the form of sulphide oxidation products (Hansen, 2015). This statement correlates well with that of Koch (2014) and Yibas *et al.* (2010) who both characterised the Oxidation zone as being depleted of elements such as iron (Fe), aluminium (Al), magnesium (Mg) and calcium (Ca), relative to the Oxidation front, as a direct result of leaching. Yibas *et al.* (2010) further stated that the depletion of these elements is suggestive of pore water carrying soluble secondary minerals into the Oxidation front, during migration. The concentration of metal trace elements (Co, Cr, Cu, Ni, Pb and Zn) on the other hand, depends mainly on the relative concentration of sulphide minerals, from which these elements are primarily leached (Yibas *et al.*, 2010).

The Oxidation zone is further characterised by a low pH tailings solution, high concentrations of dissolved solids, as well as the mobilisation and leaching of metal trace elements (Hansen, 2015 and Koch, 2014). Stated by the reaction illustrated in Equation 1, Yibas *et al.* (2010) further states that the pH of the tailings solution provided a good indication of the abundance of sulphide minerals and the presence or absence of acid neutralizing minerals in the tailings material. Fuelled by a high oxidation-reduction potential and the penetration of oxygen readily

into the Oxidation zone, the Oxidation zone could be characterised as being in the late stages of oxidation, evidenced by mineral paragenesis indicating the consumption of sulphide minerals with the concomitant precipitation of jarosite (Yibas *et al.*, 2010).

With reference to the radionuclides present in the Oxidation zone, limited information was found with regards to element concentrations, mobilisation or uranium speciation, relative to each individual zone; a deficiency in literature also highlighted by Koch (2014). According to Vandenhove *et al.* (2009) the dominant mechanism responsible for the mobilisation and chemical speciation of uranium under oxidizing conditions, is the complexation of the uranyl ion (UO_2^{2+}) to form uranium-sulphates, in the form of UO_2SO_4 and $\text{UO}_2(\text{SO}_4)^{2-}$ (see Equation 7). These uranium-sulphates, as stated by both Alloway (2012) and Pulford (2010), are considered to be mobile and will therefore leach in a similar manner as the metals mentioned above. Using down-hole natural gamma spectrometry, Koch (2014) found that measurements indicated lower uranium content within the Oxidation zone, compared to that of the zones below it. Thorium on the other hand did not show any significant signs of being leached from the Oxidation zone, thereby showing attributes of stability under oxidizing conditions (Koch, 2014).

2.3.2.1.1 Cemented layers and hardpans

Commonly associated with desert environments and agricultural practices, used to describe a cemented layer, which act as a barrier to root growth in soils, the term “hardpan” is also used in mining environments to describe zones of secondary mineral phase accumulation within tailing impoundments (Lottermoser and Ashley, 2006). Defined as surface and/or subsurface secondary mineral accumulations, that binds the exposed tailing material into an extensive or discontinuous cemented sheet (Lottermoser and Ashley, 2006), these hardpans are believed to form as a result of changes in pH-Eh conditions, while also acting as hydraulic permeability and diffusion barriers within the impoundment (DeSisto, 2008). As these Fe-rich, trace element-bearing hardpans have been reported to develop anywhere between the surface and the reduction zone (Graupner *et al.*, 2007), the formation of these cemented layers therefore hold significant environmental and economic implications (Blowes *et al.*, 1991).

Despite discrepancies still existing within literature with regards to the formation of hardpans and cemented layers in general (DeSisto, 2008), literature does however agree that it involves several processes, which include the dissolution of primary minerals and the precipitation of secondary mineral phases (gypsum, goethite and jarosite) through mechanisms such as wetting and drying cycles (Graupner *et al.*, 2007 and McGregor and Blowes, 2002). With regards to sulphide-bearing tailing impoundments, as found at the New Machavie TSF, dry climatic conditions favour evaporation above precipitation and therefore contribute to the formation of an oxidizing environment (Aucamp and van Schalkwyk, 2003). The formation of Fe-rich hardpans

are initiated by the release of ferrous iron (Fe^{2+}) from sulphide particles during active oxidation, onto which the oxidation of ferrous iron (Fe^{2+}) and the hydrolysis of ferric iron (Fe^{3+}) follows, before cemented layers are formed through the binding of tailing particles with precipitated hydrous ferric oxides (Graupner *et al.*, 2007 and Lottermoser and Ashley, 2006). The type of cement on the other hand is dependent on factors such as pH-Eh conditions, the concentration and availability of elements, mineralogical differences between adjacent particles and the saturation level of the impoundment in question, as a single hardpan unit could consist of multiple cemented layers (Graupner *et al.*, 2007 and Lottermoser and Ashley, 2006).

According to Lottermoser and Ashley (2006) cemented Fe-rich hardpans typically consist of thin layers (0.2 – 2mm thick) comprised of strongly hydrous ferric oxide cemented tailings, interlayered with material usually containing lesser amounts of hydrous ferric oxides. In contrast to tailing material, these cemented-hardpans typically contain significantly higher amounts of trace elements, in particular elevated thorium and uranium content (DeSisto, 2008 and Lottermoser and Ashley, 2006). The elevated concentrations could be ascribed to the trace elements being selectively captured, possibly through coprecipitation into sulphates and/or adsorption onto secondary mineral phases (jarosite) and hydrous ferric oxides (Lottermoser and Ashley, 2006). It should however be noted that the capture of these elements are not permanent and that seasonal wetting, drying and drainage from the tailings impoundment could lead to the release of sorbed elements from mineral surfaces, as well as the dissolution of precipitated metal sulphate salts (Lottermoser and Ashley, 2006).

2.3.2.2 Oxidation front

Located directly beneath the Oxidation zone, the Oxidation front forms the boundary between the oxidized- and the un-oxidised sulphides (Hansen, 2015). While similar in colour, compared to the Oxidation zone, the Oxidation front is characterised by active sulphide oxidation and the enrichment of metals relative to pyrite (Hansen, 2015 and Koch, 2014). Although an increase in metal concentrations are generally associated with the Oxidation front, the distribution of metals between the upper zones are governed by the interplay between factors such as the position of hard pans, upward capillary and osmotic actions, variations in permeability and lastly geochemical variations in the tailings material (Yibas *et al.*, 2010). Jurjovec *et al.* (2002) added that the mobility of metals are further governed by pH plateaus, as Co, Ni and Zn becomes mobile when the solution pH dips below 5.7, whereas Al, Cd, Cr, Pb and vanadium (V) remains immobile until the solution pH decreases to below 4.0. The statement correlated well with that of Smith and Huyck (1999), who pointed out that metal solubility, is generally inversely proportional to the solution pH, thereby confirming the increase in mobility.

With regard to the solution pH of the Oxidation front, Hansen (2015) stated that the solution remained acidic due to pore water filtering through the Oxidation zone, as well as the ongoing oxidation of pyrite, which generates acidity in accordance with Equation 1. Hansen (2015) further stated that the solution pH tend to increase slightly as one move to the base of the Oxidation front, ascribing the phenomena to a decrease in the rate of pyrite oxidation, rather than the presence of any buffering capacity. A similar pattern is seen when referring to the oxidation-reduction profile of the Oxidation front, as Koch (2014) identified a sharp increase in the ORP, followed by a sudden decrease. Koch (2014) stated that the sharp increase in ORP is attributable to the active oxidation of pyrite in the top portion of the Oxidation front, while the sudden decrease in the lower portion of the profile could be ascribed to the relative depletion of oxygen and less reactive elements starting to fulfil the role of the oxidant.

Referring to the presence of radionuclides in the Oxidation front, no definitive features were identified by Koch (2014), other than a slight increase in the uranium content with depth, while thorium concentrations decreased overall. According to Koch (2014) the decrease in the Oxidation fronts thorium concentrations, should be ascribed to depositional concentrations, rather than secondary alterations. Koch (2014) further stated that uranium showed a stronger correlation to the ORP compared to thorium, as uranium concentrations tend to increase with a corresponding decrease in ORP.

2.3.2.3 Reduction zone

Positioned directly beneath the Oxidation front, the Reduction zone, also known as the Un-oxidised zone, is characterised by a rapid colour transition from the iron-stained Oxidation front, to various shades of grey, depending on the moisture content (Yibas *et al.*, 2010 and Bezuidenhout and Rousseau, 2005). The rapid transition as stated by Bezuidenhout and Rousseau (2005) marks the position of transition from oxic to anoxic conditions, as redox conditions were found to be a function of ferrous (Fe^{2+}) and ferric iron (Fe^{3+}) conditions. Literature states that diffusion is considered to be the dominant transport mechanism of oxygen through tailings material, rather than as a dissolved infiltration fluid (Bezuidenhout and Rousseau, 2005 and Richie, 1994 (cited by Hansen, 2015)). Richie, 1994 (cited by Hansen, 2015) further stated that as a result of transport limitations, it could be expected that oxygen concentrations would decrease with an increase in depth. The statement was later confirmed by Bezuidenhout and Rousseau (2005), while conducting research on the rate and depth of weathering in gold tailings.

Koch (2014) added that the depleted oxygen associated with the Reduction zone, is attributable to the utilization of most of the available oxygen, by the active oxidation of pyrite in the Oxidation front, as well as the limited penetration-depth of oxygen, as described by Bezuidenhout and

Rousseau (2005) and Richie, 1994 (cited by Hansen, 2015). As a result, reactions within the Reduction zone tend to make use of other oxidising agents, for example Fe^{3+} , as illustrated by Equation 4 (Koch, 2014). Oxidation-reduction profiles of the Reduction zone indicated a fairly low, but still positive oxidation potential (Koch, 2014). This statement correlates well with that of Hansen (2015), who indicated a decrease in sulphate concentrations and an increase in pyrite concentrations, ascribing the modelling results to a slower average pyrite oxidation rate.

Referring to the presence of radionuclides, both Yibas *et al.* (2010) and Bezuidenhout and Rousseau (2005) indicated little to no mobilisation of metals in the Reduction zone, providing evidence in the form of pyrite precipitating within the cracks below the Oxidation front. This statement correlated well with that of both Hansen (2015) and Koch (2014), who both indicated a slight increase in the uranium content, while Hansen (2015) indicated elevated concentrations of Al, Fe, Mn and Ni. Koch (2014) further stated that the elevated uranium concentrations could be ascribed to uranium being in the U^{4+} valence state, leaving it relatively immobile, except through colloidal movement. Thorium content on the other hand was found to decrease for unknown reasons.

2.3.2.4 Saturated zone

Forming the bottom part of the Reduction zone, literature characterises the Saturated zone as being permanently saturated with water, while containing no oxygen to act as an oxidizing agent (Koch, 2014). As a result it has a negative ORP and therefore function as a reducing environment (Koch, 2014). During active deposition the top of the Saturated zone forms a pool of water on the surface of the tailings impoundment, generally surrounded by what is known as the “Beach”. When active deposition stops and no more water is added to the system, except for precipitation, the Saturated zone tends to shrink, thereby increasing the depth to which the unsaturated zone extends (Koch, 2014).

With regards to the availability of radionuclides in the Saturated zone, both uranium and thorium would most likely be in their reduced forms of U^{4+} and Th^{4+} , which is considered to be insoluble and could only be transported within fluids as colloidal particles (Koch, 2014). The Saturated zone would therefore immobilise any radionuclides and prevent the transportation of these radionuclides away from the tailings impoundment. Using down-hole natural gamma spectrometry, Koch (2014) recorded elevated concentrations of both uranium and thorium in the Saturated zone of an abandoned gold tailings impoundment. Speculating while making the statement, Koch (2014) ascribed the accumulation of mobilised uranium and thorium in the Saturated zone, to the elements being in their reduced forms, which according to Koch (2014) immobilised them, but stated that further investigations into the accumulation is needed.

CHAPTER 3: STUDY AREA

3.1 Locality and site history

3.1.1 Site Description

Situated upon the north-western edge of the Witwatersrand Basin (Antrobus *et al.*, 1986), the New Machavie TSF, forms part of the KOSH mining region and is located approximately 22 km east of Potchefstroom and 24 km north of Stilfontein (Koch, 2014), between the latitudes of S 26.660, S 26.680 and longitudes of E 26.860, E 26.880. Known for having the best Black Reef development in the area (De Bever, 1997), the New Machavie TSF is currently being re-mined, under the ownership of the Eleazer Mining Company (in conjunction with Kuma Community Projects), who acquired the mining rights to extract the leftover resources contained within the previously derelict TSF (see Figure 1). The TSF is situated adjacent to the Kromdraaispruit, which forms part of the C24A quaternary drainage system and comprises of an area dominated by agricultural activities (dry-land, irrigation and livestock farming), as well as the occasional gold mine (Botha, 2015 and Koch, 2014).

Although situated close to the border between the Moist Highveld and Dry Highveld grassland climatic regions of South Africa, the New Machavie TSF seemed to retain the characteristics of the latter (Botha, 2015 and Koch, 2014). Despite site-specific climatic data being unavailable, climatic data courtesy of the South African Weather Service, as published by both Botha (2015) and Koch (2014) provided a clear indication of what could be expected. The climatic data defined the area as having a highly fluctuating wind direction, while annual precipitation was identified as ranging between 580 and 625 mm/a (Botha, 2015 and Koch, 2014). Koch (2014) further indicated a general wind direction of North to North-East, stating that wind speeds rarely exceed 8.7m.s^{-1} . These values correlated well with that of Kruger (2004), who also noticed the fluctuating wind directions, confirming the general wind direction as North to North-East. With regards to annual precipitation, Kruger (2004) indicated an annual precipitation of roughly 450 to 700 mm/a, adding that the maximum precipitation is generally recorded in the months of December and January.

Mucina and Rutherford (2006) on the other hand characterized the region as having a high annual evaporation rate (1500 to 1700 mm/a), as evaporation values, sometimes as high as 2407 mm/a, have been recorded in the past. The statement is shared by Funke, 1990 (cited by Tutu *et al.*, 2009) and provided an explanation to the presence of white to yellowish-coloured salt precipitates, regularly observed over the surface of the transported tailings material. Also noticed by Aucamp and van Schalkwyk (2003), these salt-precipitates, form as the result of the upward capillary movement of salt-rich solutions within the tailings material (Lloyd, 1997 (cited

by Aucamp and van Schalkwyk, 2003)). During times of water deficit, the salt-rich solutions evaporate, resulting in the precipitation of salts, which are usually very soluble and rich in metal trace elements (Spotts *et al.*, 1997 (cited by Aucamp and van Schalkwyk, 2003)).

3.1.2 Site History

Not a lot is known about the history of the New Machavie gold mine, other than it was intermittently operational between the year 1888 and 1943 (Aucamp, 2000 and De Bever, 1997). Although several mining companies operated the New Machavie mine throughout the years, mining of the Black Reef Formation, commenced in 1904, under the ownership of the New Machavie Mining Co. Ltd (De Bever, 1997). Literature states that the New Machavie mine stoped the lode along strike, for more than a kilometre, finally reaching a maximum vertical depth of 150 meters (De Bever, 1997). These records corresponded well with that of King *et al.* (2007) who stated that the mine exploited roughly 1400 meters of quartzite and conglomerate unit, at a maximum depth of 130 meters. By the end of the 1940's, approximately 5200 kg of gold was recovered from more than 1 Mt of Black Reef Formation ore (Antrobus *et al.*, 1986). In turn, this resulted in the creation of five distinct tailings impoundments (Aucamp and van Schalkwyk, 2003), each derived from one of three distinct channels mined.

Aucamp and van Schalkwyk (2003) reported that after the mine closed in 1945, the five tailings dams (identified as T1 to T5 in Figure 1), containing roughly 2.5 Mt of material were left behind without any stabilization or protection and have been contributing to environmental contamination ever since (see Figure 1). Records state that the mine was scheduled to reopen in 2003, but was delayed due to problems acquiring surface mining rights (Koch, 2014 and King *et al.*, 2007). As a result of its abandonment, wind and water erosion have prevailed, dispersing tailings material down slope and covering an area of more than 1.2 km² with sheetwash and aeolian tailings material (Aucamp and van Schalkwyk, 2003). Up until recently, the New Machavie TSF fell under the ownership of the Tlokwe Municipality and has become the topic of several studies (Botha, 2015; Koch, 2014; Larkin, 2013; Winde and Sandham, 2004; Aucamp and van Schalkwyk, 2003 and Aucamp, 2000). After acquiring the necessary documentation, the mine is currently being re-mined under the ownership of the Eleazer Mining Company, who is exploiting the Black Reef Formation by means of opencast surface mining.

Location of the New Machavie TSF

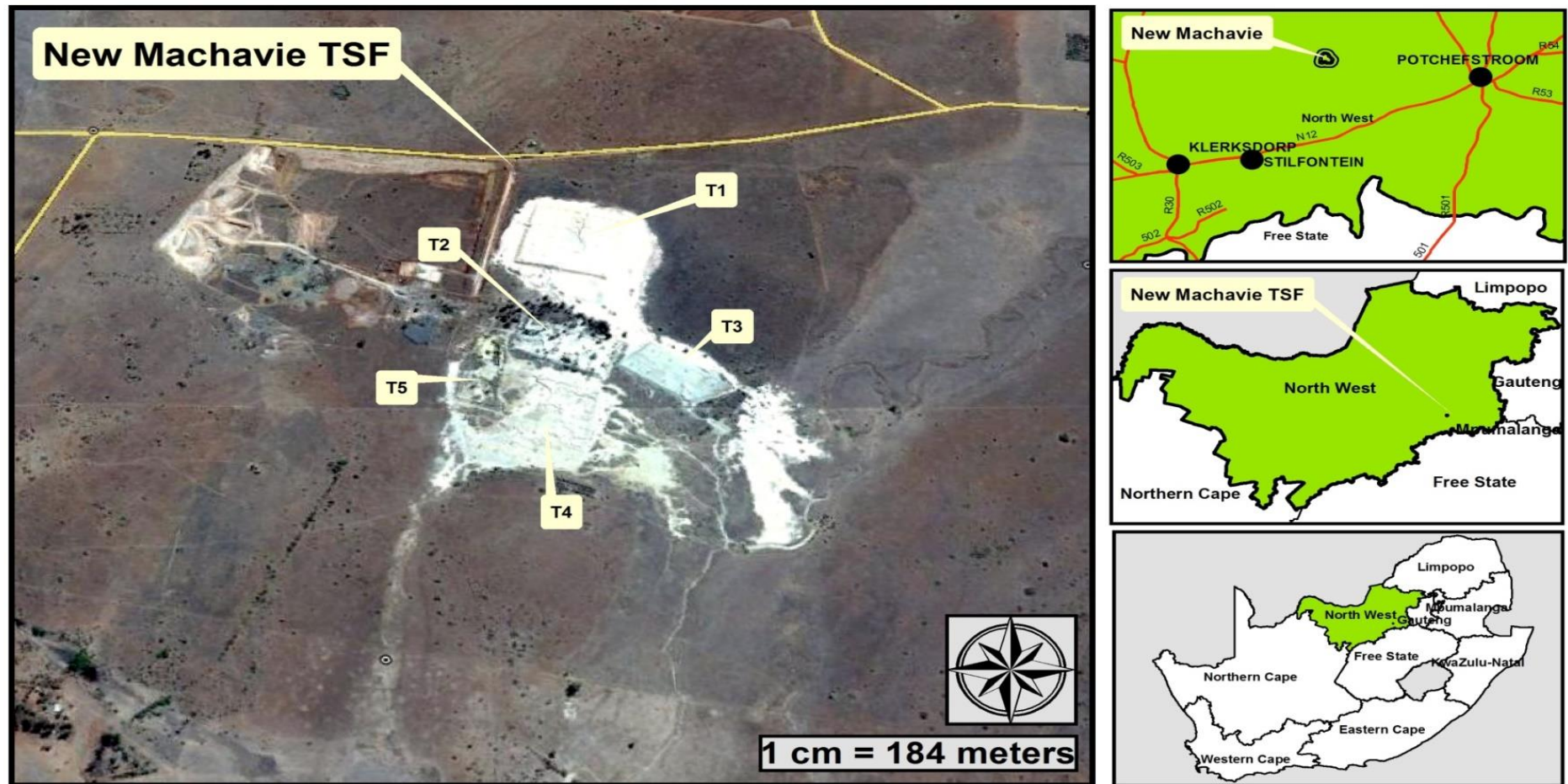


Figure 1: Locality map of the New Machavie Tailings Storage Facility, showing the opencast mining activity and respective tailings impoundments

3.2 Topography and drainage

3.2.1 Topography

Using Digital Surface Model (DSM) images of the New Machavie TSF (2626DB), courtesy of Stellenbosch University's Centre for Geographical Analysis and the SMC-Synergy group, a Digital Elevation Model (DEM) of the New Machavie TSF was created. The model indicated an average elevation of 1383.0 meters above sea level, while showing a gradual decrease in elevation as one move from the north-western mining boundary to the south-east (see Figure 2). The highest section within the study area was identified as a rocky ridge, located to the immediate west of the mining boundary, with an elevation exceeding 1400.0 meters above sea level. The lowest section on the other hand, with an elevation of 1373.0 meters above sea level, was identified as the Kromdraaispruit, which also forms the south-eastern mining boundary (see Figure 2). Despite being derived from a DEM, these values were found to correspond well with those mentioned in literature, even though most authors made use of alternative and in most cases more traditional methods, to determine the topography (Koch, 2014; Larkin, 2013 and Aucamp, 2000).

With reference to the model, the study area is located within a broad, flat valley that cuts through surrounding plains and allows for surface water to drain into the Kromdraaispruit tributary (Pretorius and Dennis, 2007 (cited by Botha, 2015) and Antrobus *et al.*, 1986), following the natural flow direction of the TSF (Koch, 2014). The model also identified two rocky hills, situated to the immediate east and south of the tailings impoundments respectively, which further alters the drainage dynamics of the TSF. As previously mentioned, the New Machavie TSF comprised of five heavily eroded tailings dams, situated to the immediate west of the Kromdraaispruit floodplain (Aucamp and van Schalkwyk, 2003). The model indicated that Tailings dam No.1 rises to a maximum elevation of 1395.0 meters above sea level, resulting in a maximum height of 15 meters over its south-western section (see Figure 3). While elevation was found to decrease in a northern direction over Tailings dam No.1, the erosion trench recorded a minimum elevation of 1382.0 meters above sea level, thereby stating the severity of the erosion.

Tailings dam No.2 to No.5 on the other hand recorded a maximum elevation of 1392.0, 1389.0, 1383.0 and 1385.0 respectively (see Figure 4). With the exception of Tailings dam No.2, which showed an inward decrease in elevation, the majority of the tailings impoundments showed a decrease in elevation towards their respective south-eastern slopes. The model further indicated erosion trenches to follow the natural flow direction of the TSF, thereby contributing to the creation of concentrated surface flow paths (Aucamp, 2000), generally in the direction of the Kromdraaispruit floodplain.

Digital Elevation Model of New Machavie

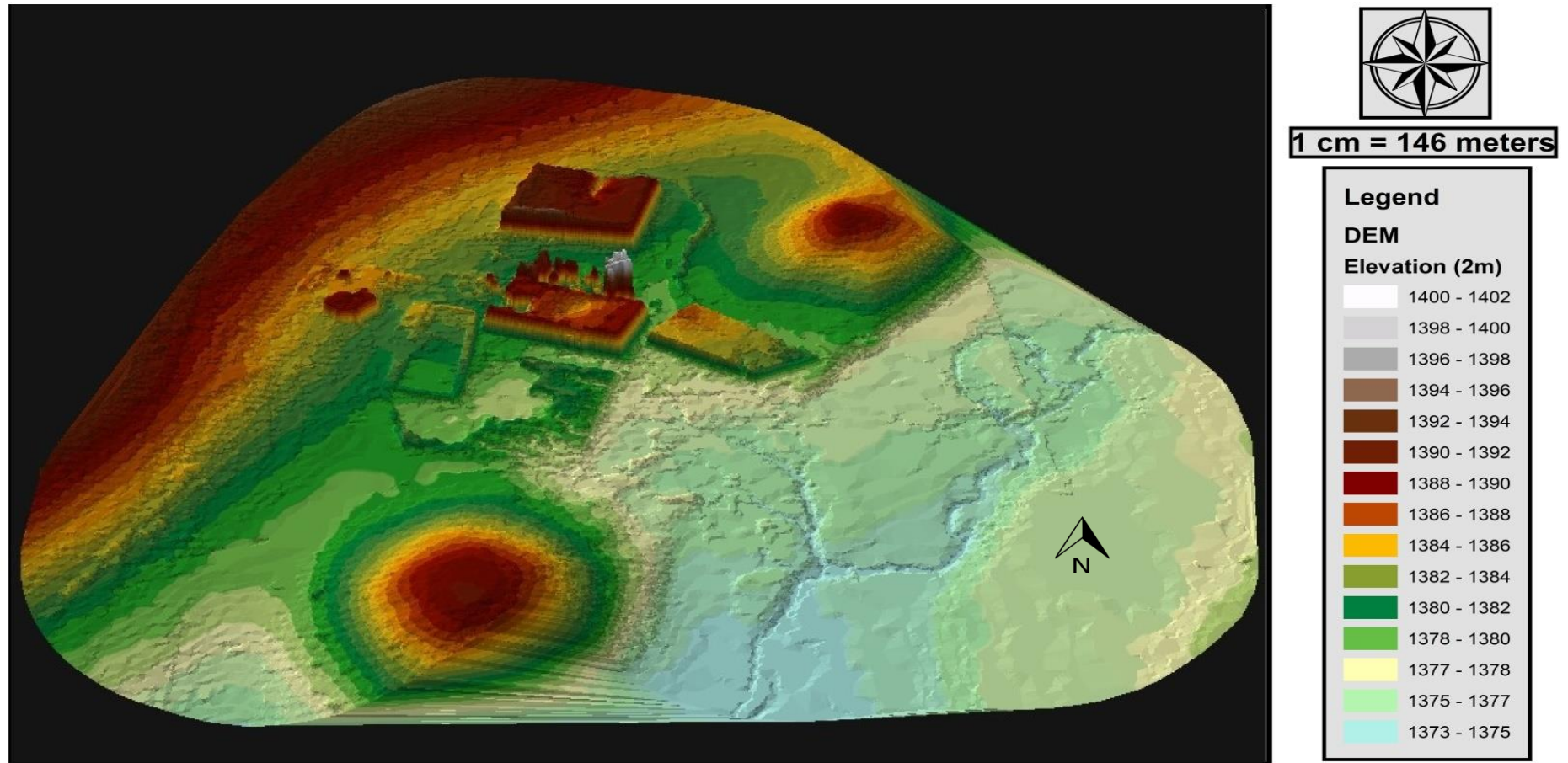


Figure 2: Digital Elevation Model of the New Machavie Tailings Storage Facility and surrounding area of influence

Digital Elevation Model of Tailing Dam No.1

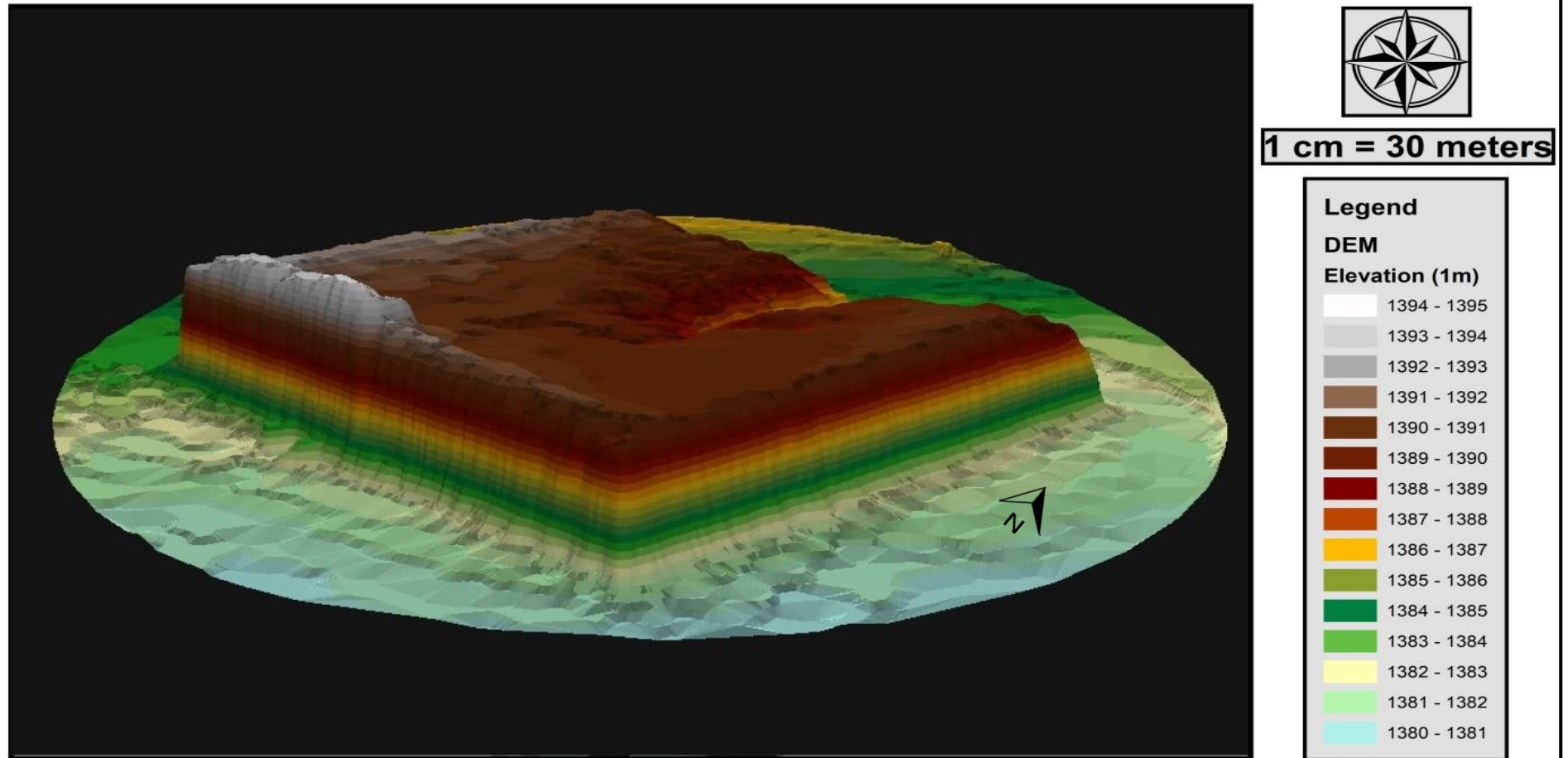


Figure 3: Digital Elevation Model of Tailings dam No.1

Digital Elevation Model of Tailing Dam T2 - T5

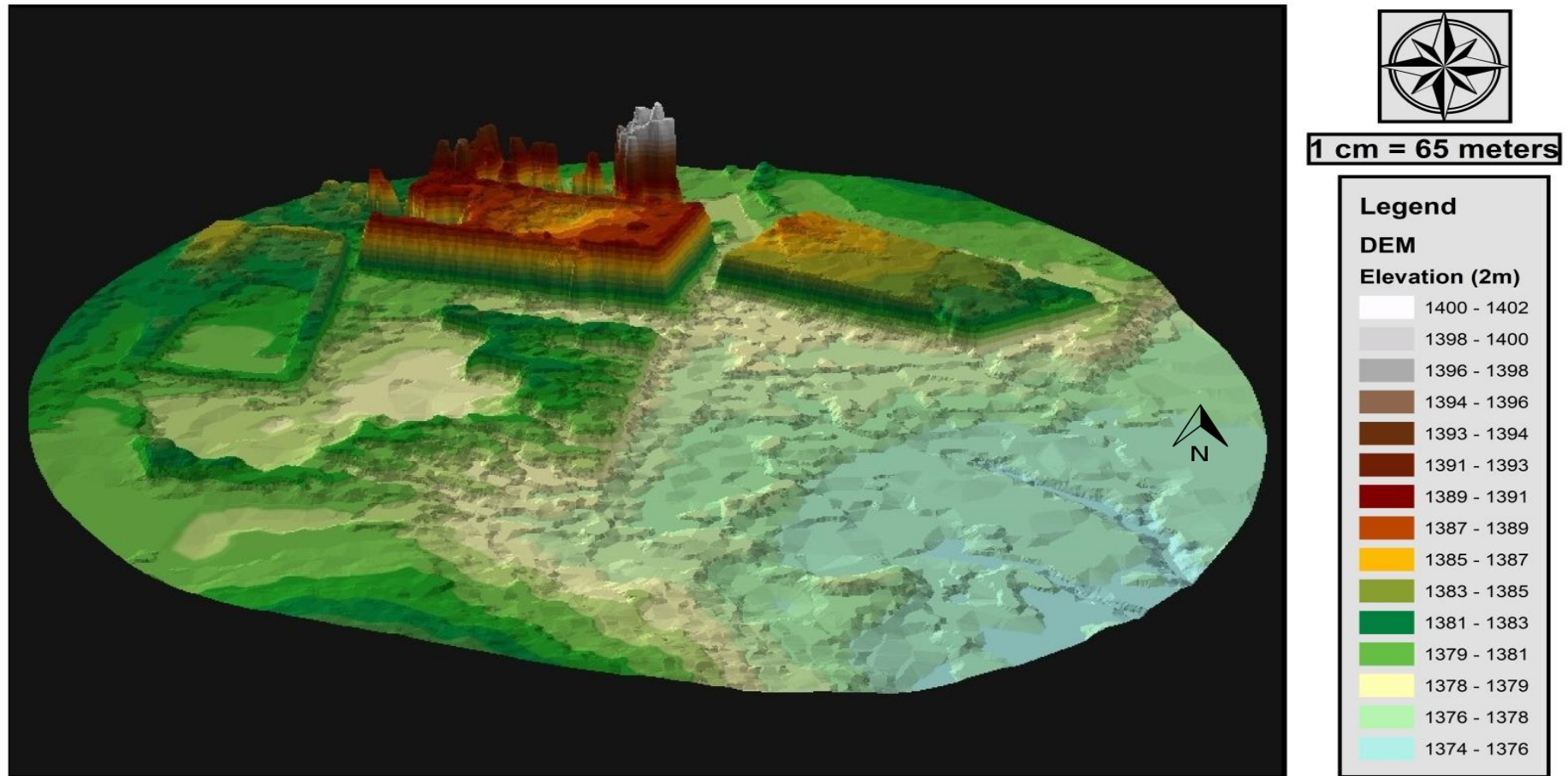


Figure 4: Digital Elevation Model of Tailings dam No.2 to No.5

3.2.2 Drainage

As discussed, the New Machavie TSF is situated within a broad, flat valley, located to the immediate west of the Kromdraaispruit tributary, which forms part of the C24A quaternary drainage system (Botha, 2015). First identified by means of visual observation and later verified by literature (Aucamp, 2000), sheet-wash, predominantly in a south to south-easterly direction, was identified as the dominant drainage mechanism present at the site. Responsible for not only the formation of a floodplain, covered with eroded tailings material, but also for the creation of several dongas, that showed signs of concentrated surface flow (Aucamp, 2000), the presence of sheet-wash poses a noteworthy threat. With airborne gamma-ray spectroscopy analyses of the Witwatersrand Basin, pointing to streams as the preferred pathway for radioactive contaminant transport, the presence of these concentrated surface flow paths might lead to far greater environmental implications than first anticipated (Winde and Sandham, 2004 and Coetzee, 1995).

Other factors that might affect the drainage dynamics of the site are the presence of seepage flow within the tailings itself, as well as subsurface seepage flow patterns into the adjacent streams (see Figure 2). Even though the investigation of subsurface seepage flow patterns falls outside the general scope of the project, it still plays a significant role in the migration of dissolved elements. The term “*seepage*”, used to describe the water that drains from the tailings impoundment, could be ascribed to a difference in hydraulic gradient, between the phreatic surface (developed water table) inside the tailings impoundment and the natural groundwater level of the surrounding area (Winde and Sandham, 2004). In turn, the resulting hydraulic gradient forces the water from the non-capillary tailings pores, towards underlying aquifers and adjacent streams within the vicinity (Winde and Sandham, 2004). Literature states that seepage from decommissioned South African gold tailings impoundments could be regarded as “*insignificant*”, since all the applied water eventually evaporates, due to the negative annual water balance found in these semi-arid areas (Funke, 1990 (as cited in Tutu et al., 2009)). Although true, the statement only applies to the uppermost layers of the tailings impoundment, as pore water content tend to increase with depth (Winde and Sandham, 2004).

Koch (2014), as well as Winde and Sandham (2004) stated that the amount of water lost through seepage, is counterbalanced by means of infiltrating rainwater during storm events. This in turn results in a dynamic equilibrium between infiltration gains and seepage losses. Since infiltration through fine-grained material tends to be a rather slow process, the dynamic equilibrium fall behind rainfall variations, which allows for pore water to be retained during dry seasons (Winde and Sandham, 2004). With a permanent supply of seepage water, tailings impoundments have the tendency to raise adjacent alluvial groundwater tables to such an extent that low laying parts of the floodplain, as well as the toe paddocks are seasonally

submerged with groundwater (Winde and Sandham, 2004). In order to avoid increases in pore water levels, older gold tailings impoundments were preferably constructed upon well-drained dolomitic soils, as is the case of the New Machavie TSF. This method allowed for faster construction, as geotechnical stability increases with a decrease in water content (Robertson, 2008 (cited by Koch, 2014)). Unfortunately, this method of deposition has the tendency to increase the likelihood of environmental contamination, as subsurface contamination plumes are in direct contact with groundwater reservoirs (Winde and Sandham, 2004).

3.3 Geological Setting

3.3.1 Introduction

Situated upon the north-western edge of the Witwatersrand Basin (Antrobus *et al.*, 1986), the general geology of the New Machavie TSF comprises of sedimentary rocks of the Transvaal Supergroup, while Loraine Formation andesitic lavas from the Ventersdorp Supergroup outcrops to the north-west of the mining boundary (see Table 4). Belonging to the Klipriviersberg Group of the Ventersdorp Supergroup, the Loraine Formation's composition is dominated by aphyric micro-crystalline to medium-grained andesitic lavas (Antrobus *et al.*, 1986), while holding a stratigraphic thickness of roughly 217 meters in the West Rand area (Van der Westhuizen and De Bruijn, 2006). Defined by the presence of olive-green amygdaloids, as well as marker horizons in the form of alteration zones (Van der Westhuizen and De Bruijn, 2006), the Loraine Formation will not be discussed in more detail, as it is irrelevant to the context of the study.

Table 4: Generalised stratigraphic column of the Ventersdorp Supergroup, showing the Loraine Formation, which outcrops in close proximity to the New Machavie TSF

Supergroup	Group	Subgroup	Formation
Ventersdorp Supergroup (± 2700 Ma)	Klipriviersberg Group (2699 ± 50 Ma)		Edenvale Formation
			Loraine Formation
			Jeannette Formation
			Orkney Formation
			Alberton Formation
		East Driefontein Subgroup	Westonaria Formation
			Venterspost Formation

Represented by the Chuniespoort Group, which subdivides further into the Malmani Subgroup, the New Machavie TSF is underlain by both, the Oaktree and Monte Christo Formations, as well as the Black Reef Formation (see Figure 6), which forms the basal unit of both the Malmani Subgroup, as well as the Transvaal Supergroup (Aucamp and van Schalkwyk, 2003 and De Bever, 1997). While the only visible outcrops in the C24A drainage basin were identified as andesitic lavas of the Loraine Formation, quartzite from the Black Reef Formation and dolomite from the Oaktree Formation respectively (Botha, 2015), it is the Black Reef Formation which is of most importance (see Table 5). Each individual geological unit will now be discussed in more detail.

3.3.2 The Transvaal Supergroup

Identified as an erosional-tectonic remnant, the Transvaal Supergroup covers an area of more than 250 000 km², while outcrop-limits extend over the Northern Cape, North West, Free State and Limpopo provinces respectively (De Bever, 1997). In accordance to Button, 1986 (cited by De Bever, 1997) the southern sequence of the Transvaal Supergroup was deposited unconformably upon Archaean basement granites, while lapping across Witwatersrand strata and younger Ventersdorp volcanics. The statement correlated well with that of Papenfus, 1964 (cited by De Bever, 1997), who stated that within the Witwatersrand Basin, the Transvaal Supergroup tend to overlie Ventersdorp Supergroup rocks over the largest part of the basin.

Characterised by its sedimentary lithology, the primary composition of the Transvaal Supergroup could be described as having a small-pebbled conglomerate and gritstone basal unit, overlain by siliceous orthoquartzites, which are interbedded by overlying carbonaceous shales and in the case of the Malmani Subgroup, overlain by Fe and Mn rich dolomites (King, *et al.*, 2007). Forming the basal unit of both the Malmani Subgroup and Transvaal Supergroup, the Black Reef Formation is characterised by its dark coloured, gold bearing quartzite and conglomerate units (Eriksson *et al.*, 2006 and Whiteside, 1970). The Malmani Subgroup on the other hand could be further divided into five subdivisions, based on its chert content, stromatolite morphology, intercalated shales and erosional surfaces (Anhaeusser *et al.*, 2006). As a result the subgroup is further divided into the Oaktree, Monte Christo, Lyttelton, Eccles and Frisco Formations, of which only the Oaktree and Monte Christo Formations are of importance for the purpose of this study (Anhaeusser *et al.*, 2006).

3.3.3 The Black Reef Formation

3.3.3.1 Distribution and Structure of the Black Reef Formation

Literature states that within the North West province, outcrop-limits of the Black Reef Formation follows the southern boundary of the Transvaal Basin westwards past Ventersdorp (see Figure 5), turning directly north, west of Lichtenburg, before crossing the border into Botswana, in the vicinity of Lobatse (De Bever, 1997). Twenty five kilometres east of Ventersdorp, a second exposure diverges, trending south-westward in the direction of Klerksdorp, before disappearing under younger Karoo Supergroup strata (De Bever, 1997). Although extensively prospected for auriferous Black Reef Formation strata, the only area to be successfully exploited, albeit in a minor way, is the south-westward trending second exposure, located in the Klerksdorp - Ventersdorp - Potchefstroom area (De Bever, 1997).

With regards to the structure of the Black Reef Formation, in the North West province, the second exposure follows the general strike of the underlying geology, trending north-east to south-west, while dipping between three and twenty degrees, in a south-eastward direction (De Bever, 1997). According to literature the structural boundaries are defined by a series of north-east trending grabens and horsts, with the tendency to be downthrown in a south-easterly direction (De Bever, 1997). As a result, the thickness of the Transvaal Supergroup rocks, especially the dolomites of the Malmani Subgroup, tends to increase in the direction of the Vredefort Dome (De Bever, 1997 and Coetzee, 1996).

Table 5: Generalised stratigraphic column of the Black Reef Formation, underlying the New Machavie TSF

Supergroup	Group	Subgroup	Formation
Transvaal Supergroup (± 2650 Ma)	Chuniespoort Group (± 2642 Ma)		Black Reef Formation (± 2642 Ma)

Literature further states that no faulting of Witwatersrand age is known with certainty, as most of the faulting were associated with lavas from the post-Kliprivierberg Group and of pre-Transvaal age (Antrobus *et al.*, 1986). The statement correlated well with that of Els *et al.* (1995), who stated that limited faulting and folding structures were noted in the Black Reef Formation, even when compared to areas where major structural disturbances were noted in the underlying geology. The information mentioned above corresponded well with that of the New Machavie TSF, as the Black Reef Formation in the study area was also found to strike north-east to south-west, while dipping at between eight and ten degrees in a south-easterly direction (see Figure 6). Two dykes were noted crossing the area, while Antrobus *et al.* (1986) identified a number of oblique faults in the area surrounding the New Machavie TSF.

Spatial Distribution of the Black Reef Formation

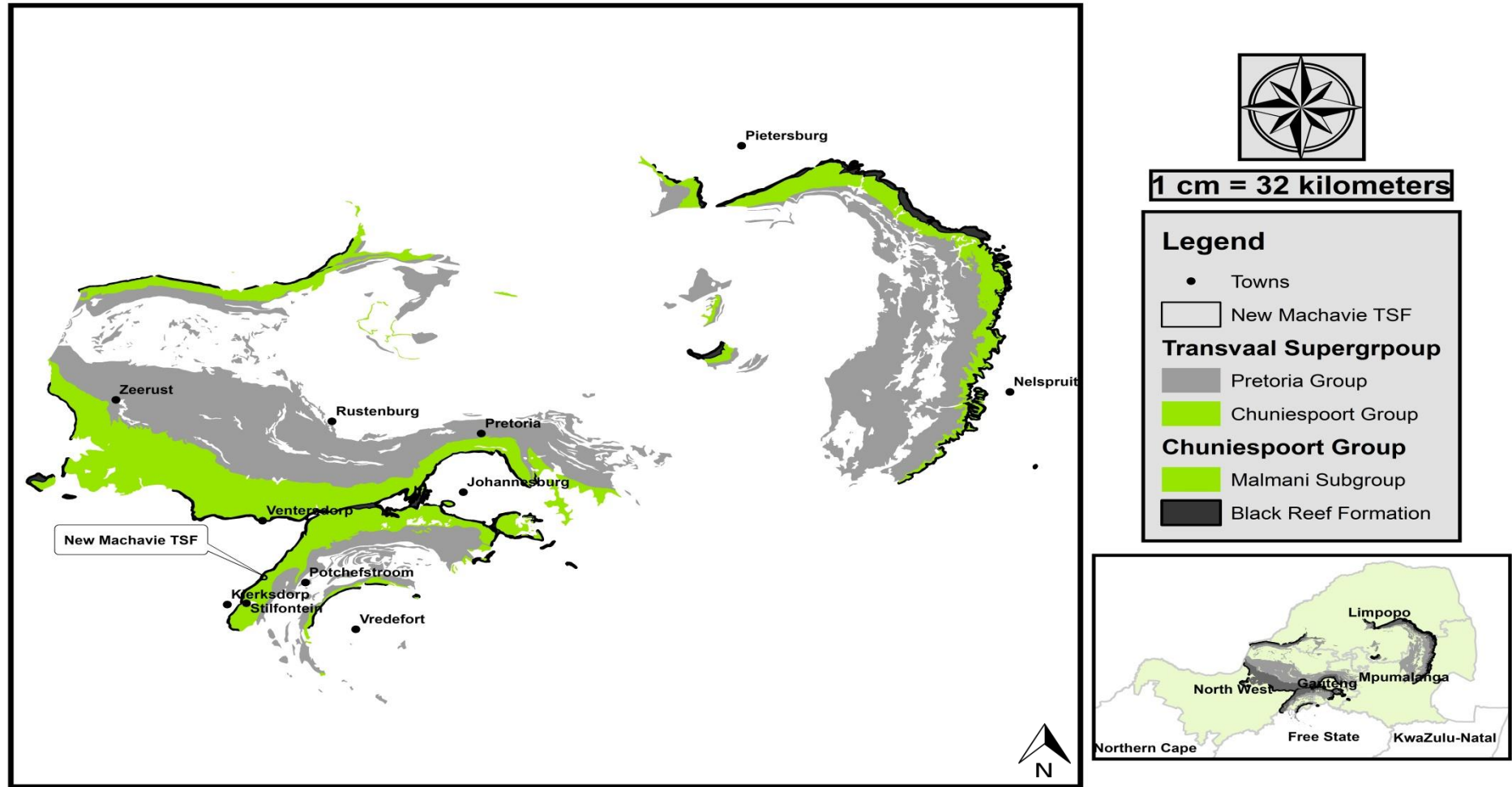


Figure 5: A simplified geological map of the Transvaal Supergroup, highlighting the spatial extent of the Black Reef Formation and overlying Transvaal Supergroup strata (modified after Fuchs *et al.*, 2016)

3.3.3.2 Composition of the Black Reef Formation

Having similar lithological characteristic to the underlying Witwatersrand placers deposits, the basal conglomeratic unit of the Black Reef Formation, is believed to contain the youngest gold bearing placer deposits in South Africa (Els *et al.*, 1995). Stated by various authors, the name “*Black Reef*” does not necessarily refer to the geographic location of the Black Reef Formation, but rather to a mining term, early miners used to describe the dark coloured, auriferous basal conglomerates and overlying quartzite’s of the Black Reef Formation (SACS, 1980 (cited by De Bever, 1997); Whiteside, 1970 and Liebenberg, 1955 (cited by De Bever, 1997)). Ascribed to the presence of abundant chlorite and disseminated carbon, originating from the interbedded carbonaceous shales, the presence of disseminated carbon not only contributed to the dark colour of the Black Reef Formation (Liebenberg, 1955 (cited by De Bever, 1997)), but also to poor gold recoveries, as the carbon tend to reabsorb the gold during processing (Body, 1988 (cited by De Bever, 1997)).

As previously mentioned the Black Reef Formation was deposited upon a major angular unconformity, consisting of Archaean basement granites and Ventersdorp lavas (King, *et al.*, 2007 and Eriksson *et al.*, 2006). Literature tend to characterise the basal conglomerate unit as being “*not uniformly continues*”, as pebbles tend to be poorly-sorted, while varying widely in shape, size and mineral composition (King, *et al.*, 2007 and Antrobus *et al.*, 1986). Where present, the basal unit is characterised by its alluvial gravel composition, consisting of interbedded massive conglomerates and medium scale, cross-bedded, planar quartzite (Els *et al.*, 1995). Although the dominant clast lithology was identified as varying amounts of quarts, quartzite tends to be more common in the northern outcrops, while chalcedony and chert dominates the southern and central outcrops respectively (Els *et al.*, 1995).

While literature mentioned that clast composition appeared to be random, Eriksson *et al.* (2006) stated that quartz arenites prevailed in the lower conglomerate unit, while an overall ascending trend of coarsening grain-size distribution was noted in the successions of overlaying quartzite. Ascribing the highly variable pebble roundness to a number of localised sources, Els *et al.* (1995) stated that clast sizes tend to be larger where the Black Reef Formation diverges into the east-west and south-west trending branches, although no orderly lateral size variations were noted. In the case of the New Machavie TSF, three north-east to south-west trending channels, consisting of basal conglomerates of up to 6.5 meters in thickness, were mined for its auriferous Black Reef (De Bever, 1997). Literature states that high gold grades were in most cases associated with the clast-supported conglomerates, especially in areas where buckshot pyrite prevailed (Body, 1988). Consisting predominantly of vein-quarts, large clasts found within the basal conglomerate unit, also contained minor amounts of chert, quartzite, shale and agates, as

well as andesitic lavas. Their shapes were identified as angular to sub-angular, while the majority of clasts ranged from 15 - 20 centimetres in size (Antrobus *et al.*, 1986).

The upper quartzite unit could be defined as a thin yet extensive sheet of quartzite (Eriksson *et al.*, 2006), with an average thickness of roughly 25 meters, while its characteristic dark-grey colour is ascribed to the chloritic and carbonaceous nature of the Black Reef Formation quartzite's (Antrobus *et al.*, 1986). Antrobus *et al.* (1986) further stated that the upper quartzite unit could be further divided, as the basal conglomerates are overlain by a zone of argillaceous quartzite's and barren shales, varying in thickness, before being overlain by a 50 centimetre thick, well mineralised conglomerate, containing high gold values. Overlying the well mineralised conglomerate unit, is the 20 meter thick zone of dark-grey quartzite's and interbedded carbonaceous shales (Body, 1988 and Antrobus *et al.*, 1986), as previously stated by Eriksson *et al.* (2006) and evidenced by descriptions of the New Machavie upper quartzite unit.

In the absence of the basal conglomeratic unit, the upper quartzite unit tends to extend to the base of the footwall, except where proto-basinal facies are present (De Bever, 1997). Literature states that grain-size distribution (Eriksson *et al.*, 2006), as well as textural maturity (Van den Berg, 1994) increases upwards, as cross-bedded, medium grained and moderately matured quartz-arenites, found at the base of the unit, changes to very mature quartzite's near the top of the succession (Coetzee, 1995 and Brink, 1979 (cited by Aucamp, 2000)). Literature further states that oscillation ripples are in some cases present near the upper contact of the quartzite unit, while one of five variably positioned, laminated mudstones are interbedded into the siliceous unit, making up roughly two-thirds of the entire unit's thickness (Els *et al.*, 1995).

3.3.3.3 Origin of the gold and radionuclides in the Black Reef Formation

Despite being a rather controversial subject, not a lot is known, albeit with great certainty, with regards to the origin of the Black Reef Formation's gold content (Whiteside, 1970). As small amounts of gold is present throughout the entire Black Reef Formation, advocates of the hydrothermal enrichment theory had to concede that the gold is of placer origin, despite the gold associated with highly pyritic areas, being regarded as typically of hydrothermal enrichment (Frankel, 1940). Adding fuel to the fire, higher grades were in most cases associated with areas where the Black Reef Formation rested upon Witwatersrand Supergroup strata, as was the case at the New Machavie TFS, except higher grades were associated with depressions in the Ventersdorp floor, rather than Witwatersrand strata (De Bever, 1997 and Frankel, 1940). The statement correlated well with that of Whiteside (1970) who described the gold content of the Black Reef Formation as being "*erratic*", but found higher grades to be associated with areas where the Black Reef Formation was deposited directly on top of the Witwatersrand conglomerates.

In 1940, Frankel (1940) published his theory to the origin of the Black Reef Formation's gold content, stating that the majority of the gold was of placer origin, while being derived from the Witwatersrand Supergroup. Frankel (1940) further stated that the gold had however undergone solution, some transportation, as well as re-precipitation in a similar manner to that of the underlying Witwatersrand Supergroup. Describing the Black Reef Formation as having a “*sympathetic relationship*” between the gold and radionuclides, Aswathanarayana (1986) stated that the event that enriched the Black Reef Formation with gold also mobilised the uranium, thereby enriching the Black Reef Formation with radionuclides (Koch, 2014). Evidenced by the deposition of Black Reef conglomerates in linear channels, which cuts into the less resistant sediments, in close proximity to underlying outcrops of the Main, Bird and Kimberley Reefs, the phenomenon strongly suggests the source of gold to be attributable to the underlying Witwatersrand Supergroup (Tucker *et al.*, 2016).

Similar to the Ventersdorp Contact Reef, a clear spatial association exist between the gold-rich Black Reef Formation and the underlying Witwatersrand conglomerates (Tucker *et al.*, 2016). However, while conducting microprobe analyses on pyrite grains derived from the Black Reef Formation, Fuchs *et al.* (2016) revealed that the trace element signatures from the Black Reef pyrite, differs from that of the underlying Witwatersrand reefs. The research suggests that while the depositional environment of the Black Reef Formation was similar to that of the Witwatersrand clastic sediments, the large volumes of native gold, uranium and pyrobitumen, were the result of hydrothermal alteration, by means of circulating aqueous and hydrocarbon fluids (Fuchs *et al.*, 2016 and Tucker *et al.*, 2016). Fuchs *et al.* (2016) further stated that despite the presence of pyrite not being ascribed to the reworking of the underlying Witwatersrand strata, close spatial associations strongly suggests that the gold and uranium were hydrothermally recycled from the underlying Witwatersrand reefs. It could therefore be concluded that the Witwatersrand reefs acted as a proto-ore to the Black Reef Formation, while hydrothermal activities later remobilised the gold and uranium, thereby changing the character and appearance of the Black Reef Formation to that what is seen today (Fuchs *et al.*, 2016 and Tucker *et al.*, 2016).

With regards to the New Machavie TSF, gold recovery was always poor, as the disseminated carbon, marcasite and pyrrhotite present in the reef, tend to reabsorb the gold during processing, while the marcasite and pyrrhotite oxidised rapidly, to form cyanides in the form of thiosulfate and sulphite (Body, 1988). Between 1888 and 1943, the New Machavie mine stoped the lode along the north-east to south-westerly trending strike, for more than a kilometre, while reaching a maximum vertical depth of 150 meters (De Bever, 1997). Although records are incomplete, the highly pyritic ore reached values of 50 to 60 g/ton (Au), with 55 to 60% of the gold occurring free, while the remaining 40 to 45% were either locked up in associated pyrite or

silver content (Frankel, 1940). Frankel (1940) further stated that although a fair amount of gold was found to replace the pyrite, a modest percentage was closely associated with the sphalerite, which acted as an important precipitant. By the end of the 1940's, approximately 5200 kg of gold were recovered from more than 1 Mt of ore (Antrobus *et al.*, 1986), resulting in the creation of five distinct tailings impoundments (Aucamp and van Schalkwyk, 2003), each derived from one of the three channels mined from the associated Black Reef Formation.

3.3.4 The Malmani Subgroup

Table 6: Generalised stratigraphic column of the Malmani Subgroup, underlying the New Machavie TSF

Supergroup	Group	Subgroup	Formation
Transvaal Supergroup (± 2650 Ma)	Chuniespoort Group (± 2642 Ma)	Malmani Subgroup	Frisco Formation
			Eccles Formation
			Lyttelton Formation
			Monte Christo Formation
			Oaktree Formation

3.3.4.1 The Oaktree Formation

Identified among the oldest known carbonate deposits, the dolomites of the Malmani Subgroup are believed to be the result of marine transgression, which not only ended the fluvial conditions, but also contributed to clear water conditions, amenable to the precipitation of chemical sediments (Van den Berg, 1994). Overlying the Black Reef Formation, the Oaktree Formation is characterised by its predominant composition of finely-bedded to massive dark dolomites, with carbonaceous shales and quartzite being abundant near the base of the formation, while stromatolites and chert are rarely present (De Bever, 1997). Evidenced by the presence of dolomite grains in the upper quartzite unit of the Black Reef Formation, it could be assumed that a soft contact exist between the Black Reef Formation and overlying Malmani Subgroup (De Bever, 1997). Further evidenced by the presence of quartzite and mudstone beds, above the stratigraphic boundary of the Black Reef Formation, the evidence not only indicates a conformable transition, but also suggests a gradual decrease in clastic sedimentation (De Bever, 1997). The transitional relationship between the two geological units also provides an explanation to why geologist finds it difficult to define the Black Reef Formation stratigraphically, when demarcating the top of the formation (De Bever, 1997).

Although predominantly characterised as a chert-poor, iron and manganese-rich dolomite (King, *et al.*, 2007), Eriksson and Truswell, 1979 (cited by Aucamp, 2000) stated that the Oaktree Formation could be further divided into six individual stratigraphic units, which includes zones of thin shale units, domical stromatolites, as well as convoluted chert markers. Identified as having an average thickness of roughly 330 meters in the West Rand area, dolines and palaeo-sinkholes seems to be absent in the Oaktree Formation, however erosion-slump structures have been noted by several authors (Van Deventer and Slabbert, 2011 and Pretorius and Dennis, 2007 (cited by Botha, 2015)). Some authors also mention the presence of *in situ* developed dolomites (King, *et al.*, 2007 and Obbes, 2000), which correlated well with the presence of dolomite grains in the upper quartzite unit of the Black Reef Formation, and the assumed soft contact between the geological units.

3.3.4.2 The Monte Christo Formation

Characterised by its light coloured chert-rich, recrystallized dolomite, containing basal-oolitic dolomite bands, as well as stromatolites, the Monte Christo Formation overlies the Oaktree Formation (see Table 6) and holds an average thickness of 740 meters in the West Rand area (Brink, 1979 (cited by Aucamp, 2000)). Outcrops of the Monte Christo Formation tend to be dominated by massively weathered chert-rich bands, as well as the occasional erosion-slump structure (King, *et al.*, 2007 and Pretorius and Dennis, 2007 (cited by Botha, 2015)). In addition, Van Deventer and Slabbert (2011) pointed out that the Monte Christo Formation contains less iron and manganese-oxides, compared to the underlying Oaktree Formation. According to Coetzee (1996) the Monte Christo dolomites appeared to be extensively fractured, when viewed under a microscope, as a multitude of finely-veined criss-crosses tend to divide the rock into seemingly undisturbed sections. Evidenced by dolomite grains of varying grain-sizes, while comprising of a mosaic of irregular and inter-locking granular texture, the phenomenon undoubtedly represents the recrystallization of the originally fine-grained micritic carbonate precipitates (Coetzee, 1996).

New Machavie Geology

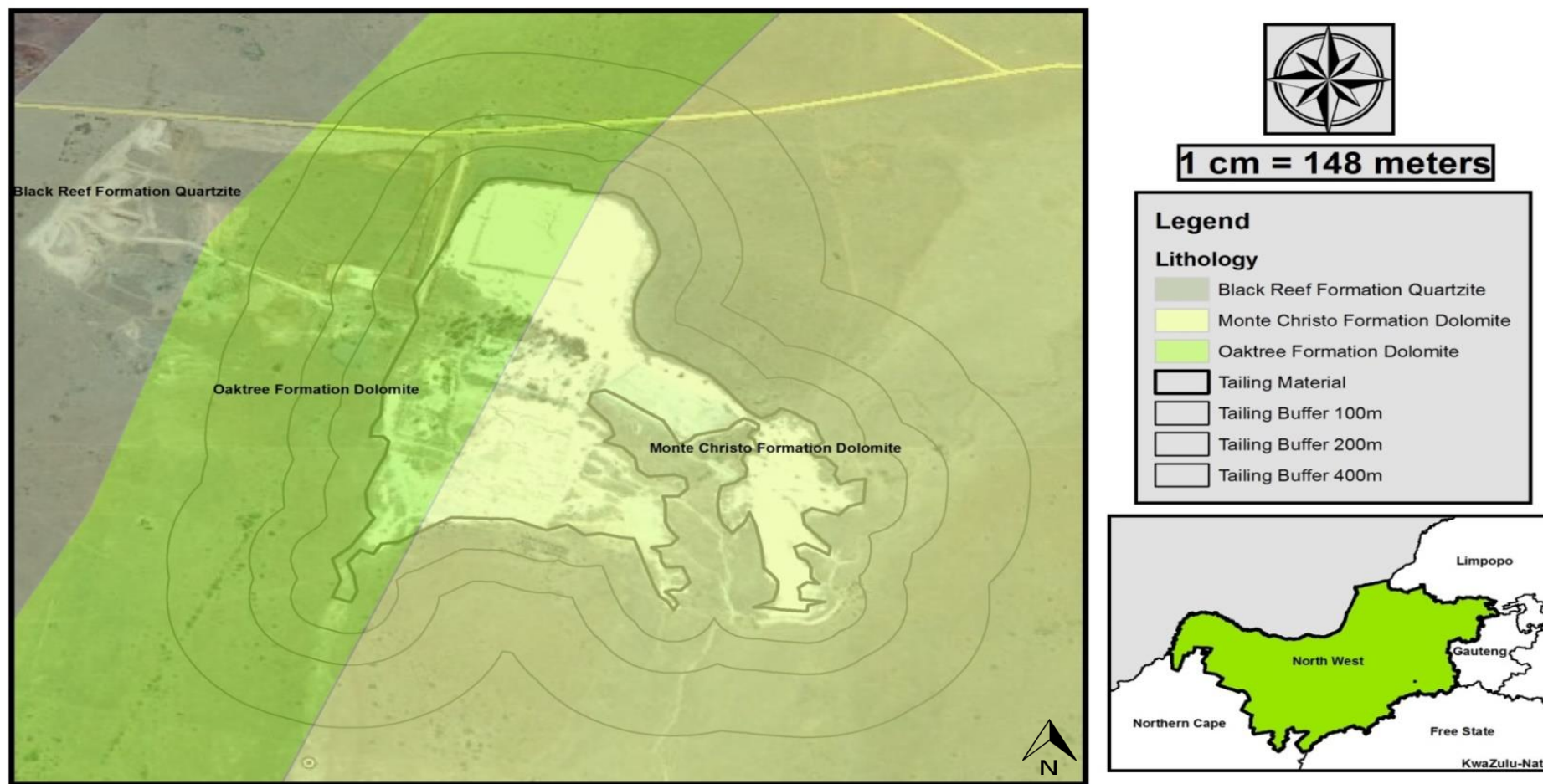


Figure 6: Surface geology of the New Machavie Tailings Storage Facility

3.4 Pedology

Back in the olden days, the common practice among tailings designers was to construct TSF's upon dolomitic landscapes, as the rapid drainage associated with the underlying geology, ensured quick and easy drainage away from the TSF (Koch, 2014). With the geotechnical stability of the tailings material increasing with a decrease in water content, the construction method not only ensured increased production, but also an overall increase in safety (Robertson, 2008 (cited by Koch, 2014)). Underlain by the Malmani Subgroup dolomites, the New Machavie TSF, was constructed upon very shallow dolomitic soils, identified as lime-poor Mispah and Glenrosa (Fa14a) soil forms to the east, while the western portion was dominated by dystrophic Hutton or Avalon (Ba42b) soil forms (SIR, 1987).

Based on the results derived from a series of soil profiles and literature (Botha, 2015; Koch, 2014 and Aucamp and van Schalkwyk, 2003), the pedology of the study area was divided into two main classes. Identified as land type Ba42b (SIR, 1987), also known as dystrophic red and/or yellow-brown apedal soils (Hutton and Avalon soil forms), these soil forms were found to cover the majority of the western portion of the New Machavie TSF (see Figure 7). Characterised by their low exchangeable cation content (Ca, K, Mg and Na), generally as a result of excessive leaching, these red apedal soils tend to transition from red to yellow apedal soils, as one moves downslope (Koch, 2014). The phenomenon according to literature could be ascribed to the soil type's dependents on the oxidation state of iron, while the same phenomenon also indicates the presence of plintic-catenas in the soil form (Koch, 2014). While the majority of the western portion's hillcrest areas were dominated by Hutton soil forms, the upper slopes tend to show signs of prevailing shallow Mispah soil forms (Aucamp, 2000). The lower slopes on the other hand were found to be dominated by Westleigh, Valsrivier and Glencoe soil forms, while Rensburg soil forms prevailed in the lower-lying valleys (Aucamp, 2000).

Underlain by both the Oaktree and Monte Christo dolomites (Aucamp, 2000), the eastern portion of the New Machavie TSF (see Figure 7), was found to be covered by what could be described as a pedologically young landscape, of mixed origin (SIR, 1987). With rock weathering being identified as the dominant soil forming process in the area, the majority of the eastern portion was found to be covered in shallow orthic A-horizons, underlain by a lithocutanic B-horizon, also known as the Glenrosa soil form. Identified as land type Fa14a, these Mispah and/or Glenrosa soil forms tend to be depleted of lime, as lime-nodules were rarely noted in the soil samples of the surrounding area of influence (SIR, 1987). Site investigations characterised the hillcrest areas in the eastern portion of the TSF, as being covered in rocky Mispah soil form, while the upper and lower side-slopes were covered in what was identified as shallow Glenrosa soil forms (Aucamp, 2000). The low lying floodplain of the Kromdraaispruit on the other hand,

was found to be covered by transported tailings material (Aucamp and van Schalkwyk, 2003), while underlying soils comprised of Hutton and/or Westleigh soil forms (Aucamp, 2000).

Ascribed to the presence of manganese in both the Oaktree, as well as the Monte Christo Formation, Koch (2014) stated that manganese-oxides, in the form of manganocrete, tend to form pedocretes within the A-horizon, as well as the B-horizon of the associated soils, found at the New Machavie TSF. The statement correlated well with that of Van Deventer and Slabbert (2011), who stated that manganese-cations tend to be the dominant ion-species present in dolomitic soils; therefore one could expect Mn, Ni and Zn to be present in high concentrations. Ascribing the enrichment to natural anomalies found in underlying dolomites, both Koch (2014), as well as Van Deventer and Slabbert (2011) agreed that these iron and manganese-oxide rich soils tend to adsorb radionuclides and therefore acts as a buffer to slow the migration of radionuclides to the surrounding area of influence.

New Machavie Pedology



Figure 7: Surface pedology of the New Machavie Tailings Storage Facility

CHAPTER 4: MATERIALS AND METHODS

4.1 Materials

One of the main disadvantages with regards to radiometric spectrometry is that radiometric measurements need to be calibrated for radioactive disequilibrium (IAEA, 2003). As a result the study was in need of an alternative analytical technique, one preferably recording total element concentrations, to not only account for uranium disequilibrium, but also to serve as a ground-truthing method. With the IAEA (2003) recommending measurements taken from augur holes, the decision was made to incorporate ground truthing measures in the form of PXRF spectroscopy. Geochemical surface sampling, running concurrent with a radiometric survey of the New Machavie TSF, therefore commenced in early January 2016. Table 7 provides an indication to the type of material that was sampled from the New Machavie TSF.

Table 7: A summary of the two types of material sampled from the New Machavie TSF

Material	Description
Gold Tailings Samples	Tailings material derived from the Black Reef Formation. Although dominated by quartz and phyllosilicates (Aucamp and van Schalkwyk, 2003), the composition many vary depending on which channel the ore was derived from.
Geochemical Soil Samples	Shallow dolomitic soils derived from the surrounding area of influence. Identified as either Ba42b or Fa14a soil forms (SIR, 1987), these soils were found to be extensively contaminated with transported tailings material (Aucamp and van Schalkwyk, 2003).

4.2 Analytical methods

Literature states that radiometric surveys provide the user with seven respective radiometric signals (Total count, eU, eTh, K%, eU/eTh, eU/K% and eTh/K%), each with the potential to identify uranium anomalies (IAEA, 1979). Analytical techniques were therefore chosen to capitalise on the data acquired from the radiometric survey, by incorporating analytical techniques that not only complement each other, but were also recommended by literature. Table 8 provides a summary of the analytical techniques used to process and interpret the data.

Table 8: A summary of the various analytical techniques and geochemical indices, used throughout the duration of the project

Analytical method	Description
Elevation survey	Derived from DSM images, courtesy of Stellenbosch University's Centre for Geographical Analysis, the data was used to create a DEM of the New Machavie TSF. The DEM was later used to visualise data in 3D.
Field Portable X-ray Fluorescence	Described as a fast, powerful and cost effective technology, used for site characterization (US EPA, 2007), the analytical technique was used as an alternative method to natural gamma-ray spectrometry.
Ground radiometric survey	Synonymous with mineral exploration and environmental monitoring practises (IAEA, 2003), a ground radiometric survey was used to estimate radionuclide concentrations (K%, eTh and eU), in situ and in the field.
Ordinary Prediction-based Kriging	A geostatistical interpolation technique, used to predict attribute values at unsampled location (Goovaerts, 1999). The results were later overlain over a DEM, in order to visualise the data in 3D.
Radiation Exposure Rate and Equivalent Radiation Dose Rate calculations	Derived from the ground radiometric survey data, RER and REDR were used respectively to calculate radioactivity. The results were later overlain over a DEM, in order to visualise the data in 3D.
Ratio maps	A geochemical index, generally used during uranium exploration to identifying and confirming uranium-enriched areas (Assran <i>et al.</i> , 2012). In this case used in conjunction with the radiometric survey and UMI.
Statistical analyses	Statistical analyses were used to evaluate the statistical soundness of each dataset (McKillup and Dyar, 2010), before it was geostatistically modelled

	in both 2D and 3D.
Uranium Migration Index calculations	A geochemical index, generally used during uranium exploration to identify uranium migration patterns from one region to another (Assran <i>et al.</i> , 2012). In this case, used in conjunction with the radiometric survey and Ratio maps.
X-ray Fluorescence	Described as a non-destructive analytical technique, used to determine the element composition of a sample (Thermo Fisher Scientific Inc., 2008), XRF analyses were used as a confirmatory analysis to the results derived from the PXRF (US EPA, 2007).

4.3 Project methodology

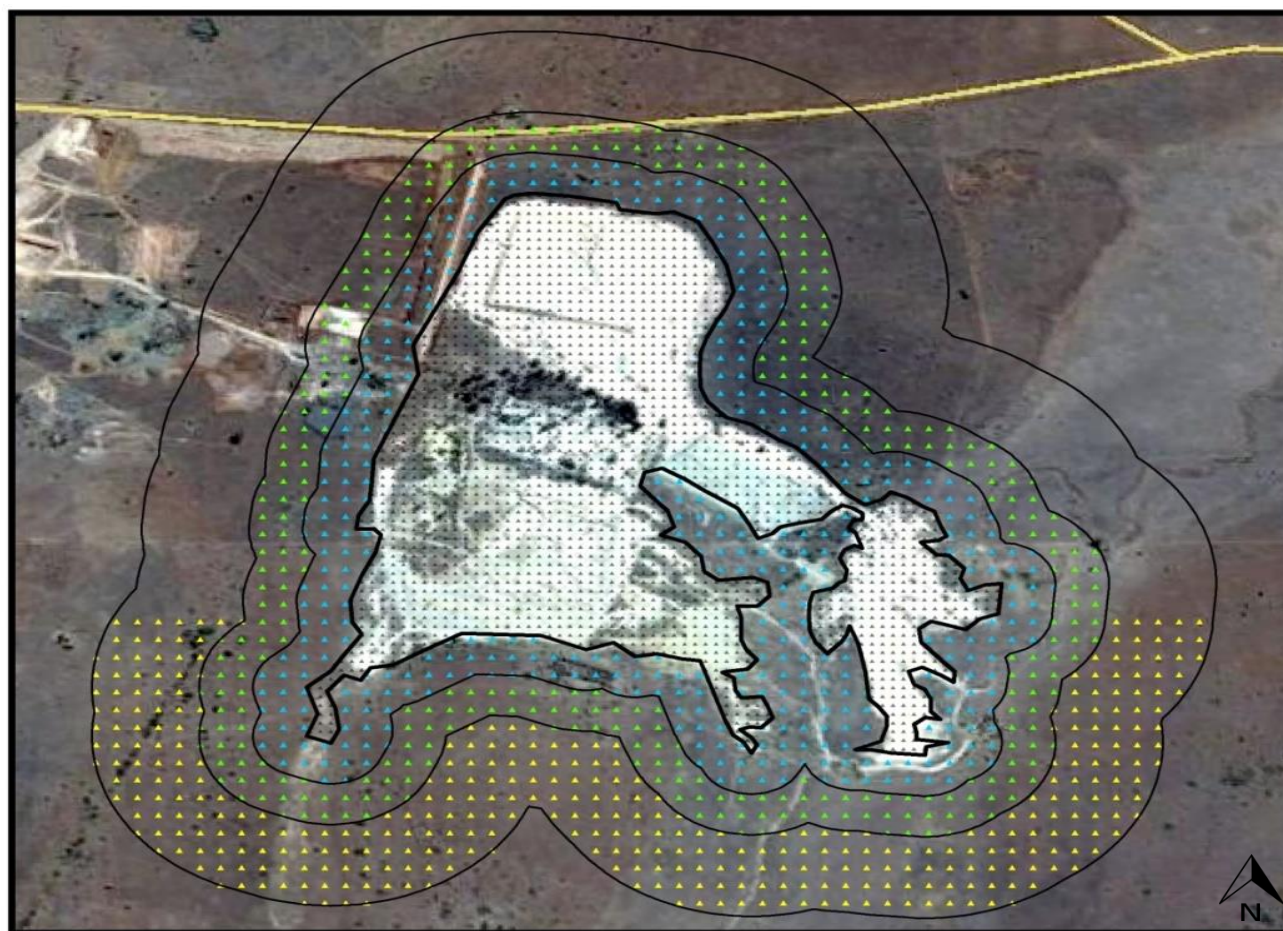
4.3.1 Site selection and sample grid establishment

As mentioned in literature, several factors should be taken into consideration when designing a sample grid for a radiometric field survey (Van Rensburg, 2011 and IAEA, 2003). These include, but are not limited to spatial resolution, required level of accuracy, ground truthing methods and equipment specifications (Van Rensburg, 2011 and IAEA, 2003). The latter is of special importance, as some radiometric spectrometers require static measurements on a fixed grid, while others have the ability to collect data while the operator is on the move (Van Rensburg, 2011 and IAEA, 2003). Despite the RS-230 Bismuth Germanium Oxide crystal (BGO) Spectrometer being one of the latter, literature further stated that grid spacing between transect lines had to be roughly 15 to 20 meters apart (Van Rensburg, 2011), while running perpendicular to the assumed strike of the anomaly or area of investigation (IAEA, 2003). With this information in mind, while incorporating design elements of sample grids, previously used in similar studies (Koch, 2014; Larkin, 2013 and Tutu *et al.*, 2009), a sample grid, covering an area of roughly 4.93 km² and housing 3038 individual sample locations was created.

With McKillup and Dyar (2010) stating that closer spacing delivered increased accuracy, resolution and interpolation, albeit at a higher cost to company, a fishnet sampling grid, with sample intervals specified at 20 meters apart, was created using ArcGIS 10.3 mapping software. Designed to cover not only the tailings impoundments, but also the toe paddocks and transported material (see Figure 8), the close proximity of the sample locations ensured a high resolution radiometric survey over the New Machavie TSF. In order to identify the radionuclide


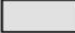


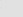
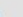
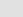
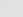
distribution patterns from the tailings material itself to the surrounding area of influence, a fishnet sampling grid, with sample intervals specified at 40 meters apart, was constructed around the initial 20 meter sampling grid (see Figure 8). Taking into consideration, factors such as topography, general wind direction, as well as surface water flow-paths, the 40 meter sampling grid, stretched to the boarder of the study area and covered a buffered area, divided into 100, 200 and 400 meter intervals respectively. By increasing the sample intervals to 40 meters over the surrounding area of influence, area coverage was increased, while still delivering high density radiometric survey data, at a much lower cost to company.

Surface Geochemical Sampling Grid



1 cm = 136 meters

Legend

-  Tailing Material
-  Tailing Buffer 100m
-  Tailing Buffer 200m
-  Tailing Buffer 400m
-  20m Sampling Grid
-  40m Grid Buffer 100m
-  40m Grid Buffer 200m
-  40m Grid Buffer 400m

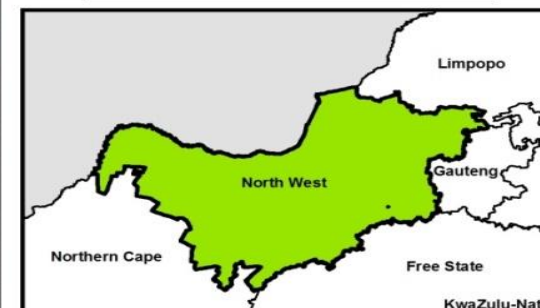


Figure 8: Surface geochemical sampling grid: Highlighting the extent and density of the sampling procedure

4.3.2 Geochemical sampling and sample preparation

As previously mentioned, due to the presence of radioactive disequilibrium, the study was in need of an alternative analytical technique, which would also serve as a ground truthing method to the radiometric survey. Having settled on PXRF spectroscopy, geochemical soil sampling commenced in early January 2016, comprising of 30 cm deep surface samples, taken by means of a hand auger. Individual sample locations were identified using a Garmin E-trax 20 field Global Positioning System (GPS), in conjunction with the pre-established sampling grid (see Figure 8). This was made possible by exporting the individual sample locations from ArcGIS 10.3 (as a csv. file), before importing it to Garmin's Basecamp software and later exporting it to the GPS itself (as gpx. file), for fieldwork purposes. Based on Method 5035, as stipulated by the US EPA (2014; 1997), the sampling method itself consisted of clearing the sample location of any organic material, in order to limit the possibility of contamination, taking the geochemical soil or tailings sample, where after it was bagged and tagged in plastic bags, for transportation and storing purposes.

Based on Method 5035, as well as that stipulated by literature (Koch, 2014; Tutu *et al.*, 2009; Aucamp and van Schalkwyk, 2003 and IAEA, 2003), samples were prepared to laboratory standards, following strict guidelines in order to limit contamination. Taking into consideration the amount of samples that had to be prepared, the samples were air-dried for the duration of one week, in order to decrease the moisture content of the samples (Aucamp and van Schalkwyk, 2003 and Tutu *et al.*, 2003). After removing any organic material left in the sample, the samples were crushed to a particle size smaller than two millimetres (<2 mm), by means of a mortar and pestle, in order to increase the reaction surface area of the particular sample (Aucamp and van Schalkwyk, 2003). Finally, the samples were sieved through a two millimetre sieve (<2 mm), before being distributed evenly (by means of a riffler) to ensure the samples homogeneity.

With regards to the XRF and PXRF spectroscopy, literature stated that in order for the prepared samples to reach radioactive disequilibrium, the samples needed to be stored for a duration of at least two months, prior to any analyses (Koch, 2014; IAEA, 2003 and Tutu *et al.*, 2003). After being stored for a duration of three months, the prepared samples were once again distributed evenly, to ensure sample homogeneity (as finer particles might have segregated from the coarser particles during the waiting period), where after it was pressed into one centimetre deep petri-dishes, used to conduct the PXRF spectroscopy. Using the same samples used for the PXRF analyses, 42 samples were selected for XRF analyses, based on their location relative to measurement taken by the radiometric survey (geochemical sample locations that intersected with that of the radiometric survey). The prepared samples were crushed further to a particle

size smaller than 75 micron ($<75\ \mu\text{m}$), before being turned into pressed pellets and fusion discs respectively.

4.3.3 Analytical methods

4.3.3.1 Radiometric survey

For the purpose of this study, a multi-channel (1024 channels) RS-230 BGO natural gamma-ray spectrometer was used to conduct a thorough ground radiometric survey of the New Machavie TSF. For the duration of the radiometric survey, four radiometric channels would record measurements, each with the ability to identify uranium anomalies, once interpolated. According to literature, spectrometers do not measure ^{238}U and ^{232}Th directly, instead it measures the radionuclide's concentration indirectly, using its respective progeny daughter isotopes ^{226}Ra , ^{214}Pb and ^{214}Bi for the ^{238}U series, and ^{228}Ac , ^{212}Pb and ^{208}Tl for the ^{232}Th series) (Tutu *et al.*, 2009 and Tutu *et al.*, 2003). To be more precise, ^{214}Bi and ^{228}Ac are used as proxies for the ^{238}U and ^{232}Th series respectively, as both isotopes have a strong ability to emit gamma radiation (Tutu *et al.*, 2009 and Tutu *et al.*, 2003). Potassium on the other hand is measured directly by the spectrometer, as measurements are generally recorded as weight percentages (wt.%), rather than parts per million (ppm) (Tutu *et al.*, 2009 and Tutu *et al.*, 2003).

Set to survey mode, while being kept at a constant height above the ground (one meter), the spectrometer was able to measure the K, Th, and U channels every 2 seconds as the operator maintained a constant speed (roughly $1.0\ \text{m}\cdot\text{s}^{-1}$) over the pre-established sampling grid (Van Rensburg, 2011 and IAEA, 2003). While set to survey mode, the spectrometer also concurrently conducted an assay every 30 seconds while the operator was walking the grid, thereby recording average measurements as the concentration of K (in wt.%), equivalent Th (in ppm) and equivalent U (in ppm) respectively (Van Rensburg, 2011 and IAEA, 2003). It was therefore essential that the operator contained a constant speed, to ensure that measurements were evenly spaced between the individual sample locations. It was also of great importance that care was taken to prevent the effect of vertical attenuation, especially over the slopes of the impoundment, as the phenomena tend to increase gamma readings, thereby influencing the measured concentrations (Koch, 2014). When done properly however, the spectrometer has the ability to record measurements, at any given point along the transect line, to a maximum radius of 15 meters horizontally and a maximum depth of 30 centimetres vertically (Van Rensburg, 2011).

Literature states that natural gamma-ray spectrometers, whether in ground or airborne guise, need to be calibrated over concrete calibration pads, prior to any radiometric survey (IAEA, 2003; 1996; 1979). With the RS-230 BGO natural gamma-ray spectrometer containing state-of-

the art auto-stabilising technology, no additional calibration sources were needed to calibrate the spectrometer prior to the survey itself. However, as varying environmental conditions have the ability to influence count measurements, a background measurement, recorded before and after every survey session, was taken at a specified location, on a daily basis. These background measurements, as well as the survey results itself, were downloaded and checked for detector drift on a daily basis, using the provided RS-analyst software.

4.3.3.2 Field Portable-XRF analysis

Described as a non-destructive analytical technique, used to determine the elemental composition of a sample, X-ray Fluorescence (XRF) spectroscopy determines the chemistry of a sample by measuring the fluorescent, “secondary” X-rays emitted from an excited atom (Thermo Fisher Scientific Inc., 2008). As each individual element present in the analysed sample, produces a unique set of characteristic fluorescent X-rays, when excited by a primary X-ray source, XRF spectroscopy provides the ideal foundation for qualitative, as well as quantitative analysis of material composition (Thermo Fisher Scientific Inc., 2008).

According to literature, the X-ray fluorescence process generally starts out with the irradiation of a solid or liquid sample by means of high energy X-rays, produced from a controlled X-ray tube (Thermo Fisher Scientific Inc., 2008). When an X-ray with energy greater than that of the atom’s K or L shell binding energy, hit an atom within the sample, an electron from the atoms inner orbital shell get dislodged. By filling the vacancy in the inner orbital with an electron from a higher energy orbital shell, the atom regains stability (Thermo Fisher Scientific Inc., 2008). As the electron drops from the higher to the lower energy state, energy, equal to the difference between the two quantum states, is released in the form of fluorescent X-rays. This forms the basis upon which XRF analyses are based (Thermo Fisher Scientific Inc., 2008). By measuring the energy produced by the secondary X-rays, XRF peaks of varying intensities are created as a function of the energy peaks and graphically represented by the XRF analyser. These spectral peaks are then interpreted as specific elements, while peak height or intensity provides indication of that specific elements measured concentration (Thermo Fisher Scientific Inc., 2008).

Field portable-XRF spectroscopy, based on Method 6200, as stipulated by the US EPA (2007), were conducted using a Thermo Scientific, Niton XL3t GOLDD+ series analyser, containing a 50kV X-ray tube, stated to be the most versatile X-ray tube ever used in a PXRF (Thermo Fisher Scientific Inc., 2008). Geochemical samples (3038 in total), taken in accordance with a pre-established sampling grid and prepared to laboratory standards, were individually analysed for a maximum duration of 120 seconds, using the “*Test-All-Geo*” mode. While in “*Test-All-Geo*” mode, the analyser analysed the full range of elements, ranging from magnesium (Mg) to

Uranium (U). To ensure the analyser provided accurate data to the user, standard XRF reference material, courtesy of African Mineral Standards (AMIS), were analysed and compared to analysis results on a daily basis. Taking into account the vast amount of samples analysed on a daily basis, a reference sample, with pre-established element concentrations, was re-scanned after every 20 samples analysed. Whenever drift in elemental concentrations were detected, the drift was accounted for by calculating the absolute standard deviation between the pre-established elemental concentrations and that of the scanned reference sample, thereby calculating the amount of drift, before fitting the “fix” to the final dataset.

4.3.4 Geostatistical data processing

4.3.4.1 Data normalisation

Literature states that the normality of a dataset not only determines the statistical soundness of the data itself, but also underlies all further statistical analyses that will be performed on the data (McKillup and Dyar, 2010; Bohling, 2007 and Webster and Oliver, 2007). As a result the statistical soundness of each dataset was investigated, by means of data normalisation, before any further analyses were conducted. The normality of each dataset was evaluated by creating histograms of each analysed element, using Microsoft Excel and plotting the data against a normal distribution curve, also known as the “bell curve”. Despite interpolation playing a vital role in the success of the project, literature recommended that statistical computations be applied to the original radiometric data, without employing any type of transformation (Abu Deif *et al.*, 2001). As a result, radiometric datasets were kept as original as possible. Once the normality of a specific dataset was confirmed, the statistical soundness of the dataset in question was further investigated, by comparing its relationship with that of other variables.

4.3.4.2 Correlation and regression comparisons

In order to evaluate the statistical soundness of a specific dataset even further, scatterplots of various combinations of data, were created using Microsoft Excel. These combinations included, but were not limited to comparisons between different radionuclides, as well as comparisons between elements analysed using different analytical methods. Once relationships between specific datasets were identified, the correlation coefficient (r), as well as the coefficient of determination “*regression*” (r^2) for that specific combination was calculated. This provided the user with an indication of not only the variables linear relationship with other variables, but also its degree of variability and predictability respectively.

In order to state the viability of using PXRF spectroscopy and natural gamma-ray spectrometry as alternatives to traditional laboratory based chemical analyses, it was important that both techniques record similar radionuclide concentration values, when compared to a more

traditional laboratory based analysis. For the purpose of this study, elemental concentrations derived from laboratory based X-ray Fluorescence was used to evaluate the accuracy of each analytical technique respectively. Using ArcGIS's "search by location" tool, 42 samples were selected for X-ray Fluorescence analyses (see Table 10 in Appendix A), based on the position of an individual radiometric measurement, relative to the position of the corresponding geochemical sample (same samples used for the PXRF spectroscopy). The linear relationship and degree of variability between each analytical technique were then evaluated, using both a correlation coefficient and coefficient of determination respectively.

4.3.4.3 Uranium Migration Index (UMI)

Based on the persistence of thorium to mobilise under oxidising conditions (Aswathanarayana, 1985), the Uranium Migration Index provides the ideal tool to quantify the migration of uranium from one region to another (Assran *et al.*, 2012). According to literature (Assran *et al.*, 2012; Talaat *et al.*, 2012; Asfahani *et al.*, 2007 and Abu-Deif *et al.*, 2001) the Uranium Migration Index could be calculated using three simple equations:

Equation 8: $U_o = eTh \times (unit\ eU / eTh)$

Equation 9: $U_m = U_p - U_o$

Equation 10: $U_{m\%} = (U_m / U_p) \times 100$

In order to calculate the rate of uranium migration ($U_{m\%}$), one must first calculate the original uranium concentration (U_o), using the eU/eTh ratio of the geological unit under investigation. As previously mentioned, the uranium and thorium present in the tailings material were derived from the Black Reef Formation. Since no uranium mining was conducted at the New Machavie TSF in the past, the assumption could be made that the eU/eTh ratio should be constant in the tailings material, as the tailings were derived from the same rock type as the originally enriched rock unit. With no access to data providing the original *unit eU/ eTh* ratio of the Black Reef Formation ore, the original *unit eU/eTh* ratio had to be calculated. This was done by first segregating the radiometric data into two classes, namely soil and tailings material respectively, using ArcGIS's selection tools. After computing the arithmetic mean of each class respectively, the unit eU/eTh ratio of each class was incorporated into Equation 8, where after the original uranium concentration was calculated.

With reference to Equation 8, by multiplying the average measured thorium concentrations (in ppm) of the sample (eTh), with the average (*unit eU/ eTh*) ratio of the original geological unit, one is left with the original uranium concentration (U_o) of that specific sample, before migration prevailed. After attaining the (U_o) using Equation 8, the migration value (U_m) could be attained, by subtracting the original uranium concentration (U_o) from the measured uranium

concentration (U_p), as illustrated by Equation 9. The final step consists of calculating the uranium migration rate ($U_{m\%}$), as illustrated by Equation 10. By dividing the uranium migration value (U_m), through the measured uranium concentration (U_p) and multiplying the answer by a 100, one is left with either a positive or negative percentage ($U_{m\%}$), representing the migration in or out of a specific region respectively. After all the calculations were performed to each individual sample location of each respective class, the respective datasets were once again merged into a single dataset, before being geostatistically interpolated, using Ordinary Prediction-based Kriging.

4.3.4.4 Radionuclide Ratio Maps

With literature stating that the most promising uranium prospects generally consist of high eU abundances, while coinciding with high eU/eTh and eU/K% ratios (Saunders and Potts, 1976), the project was once again in need of an alternative method of identifying uranium anomalies, hence the Radionuclide Ratio Maps. Synonymous with uranium exploration, Radionuclide Ratio Maps not only provided a better indication of preferential accumulation (IAEA, 2003), but also assisted in uranium exploration by identifying and confirming uranium-enriched areas (Assran *et al.*, 2012). The following equations were applied to each individual sample point of the radiometric survey's dataset, before being geostatistically interpolated by means of ordinary prediction-based Kriging, in order to produce Radionuclide Ratio Maps:

Equation 11: eU/eTh

Equation 12: eU/K%

Equation 13: eTh/K%

4.3.4.5 Radiation Exposure Rate and Equivalent Radiation Dose Rate

While a number of studies have been carried out with regards to uranium pollution and environmental contamination, only a few of them contained measurements of radioactivity (Larkin, 2013 and Tutu *et al.*, 2009). With literature stating that both the RER and ERDR could easily be calculated from the apparent K (%), eU (ppm) and eTh (ppm) concentrations (Assran *et al.*, 2012 and IAEA, 1991), courtesy of the radiometric survey, a decision was made to assess the environmental implications of radioactivity over the New Machavie TSF. The following equations were applied to each individual sample point of the radiometric survey's dataset, before being geostatistically interpolated by means of ordinary prediction-based Kriging, in order to produce RER and ERDR maps respectively:

Equation 14: $RER (\mu R/h) = 1.505 * K (\%) + 0.653 * eU (ppm) + 0.287 * eTh (ppm)$

Equation 15: $ERDR (mSv/y) = 0.0833 * RER (\mu R/h)$

4.3.5 3D Geostatistical surface modelling

4.3.5.1 Elevation survey

As previously mentioned, an elevation survey of the New Machavie TSF was conducted using DSM images. Courtesy of Stellenbosch University's Centre for Geographical Analysis and the SMC-Synergy group, DSM images of block 2626DB, with a spatial resolution of 30 centimetres, were used to create surface contours, by means of ArcGIS's 3D analyst. After creating two contour datasets, with contours specified at 30 cm and 1 m intervals respectively, the contour shapefiles were later triangulated to create a Triangulated Irregular Network (TIN) of the New Machavie TSF. The TIN was later exported to ArcScene 10.3 where it was used to create a DEM of the New Machavie TSF (see Figure 2 to Figure 4). Despite being used to conduct a thorough elevation survey of the New Machavie TSF, the DEM was also used as a base, over which radiometric data was visualised in 3D guise. The DEM therefore served a dual purpose, while providing the ideal platform to assess radionuclide distribution and migration patterns.

4.3.5.2 Ordinary Prediction-based Kriging

According to literature, spatial interpolation techniques can be divided into two main categories. The first, known as deterministic interpolation techniques, refers to techniques where surfaces are created from measured points, based on either the extent of similarity (inverse distance weighing) or degree of smoothing (ESRI, 2001). The second, known as geostatistical interpolation techniques, refers to techniques that utilise statistical properties to measure points, in order to quantify the spatial autocorrelation among these measured points, while taking into account the spatial configuration of sample points around the predicted location (ESRI, 2001). Where deterministic interpolation techniques utilise either global (uses the entire dataset to calculate predictions) or local (calculates predictions from measured points within smaller spatial areas of the larger study area) techniques for analysis, geostatistical interpolation techniques on the other hand utilise a combination of the two techniques (ESRI, 2001). As geostatistical interpolation techniques are based on statistics, it could be used to produce predicted surfaces, as well as error or uncertainty surfaces, therefore giving the user an indication of how good the predictions are (ESRI, 2001).

Although many methods are associated with geostatistical interpolation techniques, they all fall under the kriging family (ordinary, simple, universal, probability, indicator and disjunctive kriging). Stated by both Naoum and Tsanis (2004) and Isaaks and Srivastava (1989), kriging could be described as an interpolator that uses spatial relationships within known datasets to interpolate or predict unknown points in between known points. Kriging utilises variograms in order to calculate the spatial relationship between specific points, while assuming that the points

are statistically homogeneous, before fitting it to an output surface (Naoum and Tsanis, 2004 and Isaaks and Srivastava, 1989). Isaaks and Srivastava (1989) further describes kriging as being a linear (linear estimation of weights between points) and unbiased (produces results with errors as close to zero as possible) interpolator, that aims to minimize the variance of errors. Bohling (2005) on the other hand describes the advantages of using kriging, as having an interpolator that compensates for the effect of clusters, by ascribing less weight to the points within the cluster, compared to isolated points, as well as providing the user with an estimation of variance, which in turn leads to more statistically reliable data.

Described by the IAEA (2003), to be “*well suited*” for the interpolation of radiometric data, ordinary prediction-based Kriging was chosen as the geostatistical interpolator of choice and applied to both the radiometric survey data, as well as the data derived from PXRF spectroscopy. Interpolated using Geostatistical Wizard (from the ArcGIS 10.3 toolbox), the choice to use ordinary prediction-based Kriging, instead of other Kriging methods, was solely based on it having a more reliable statistical base (from which the data was interpolated), while showing greater versatility (Chakraborty *et al.*, 2017 and Koch, 2014). Despite datasets consisting of enough sample locations for any geostatistical interpolator to perform well, ordinary prediction-based Kriging was found to produce the most realistic distribution patterns. The variogram parameters, used to create the optimal Ordinary Prediction-based Kriging interpolation model for each respective dataset is summarised in Table 11 of Appendix A.

CHAPTER 5: GEOSTATISTICAL DATA PROCESSING

5.1 Introduction

Despite its use being limited to the creation of colourful probability maps in the past, natural scientists are showing a growing interest in the use of geostatistics, especially for the prediction of attribute values at unsampled locations (Goovaerts, 1999). According to Goovaerts (1999) the growing interest could be ascribed to scientists realising the importance of incorporating spatial correlation among observations, especially when quantifying spatial predictions. On the other hand, geostatistics offers an increasingly wide palette of techniques, each with the ability to cope with diverse datasets, in order to predict attribute values, using information related to one or more attributes (Goovaerts, 1999). Unfortunately, before geostatistics could be applied to a given dataset, it is important to first assess the statistical soundness of the dataset in question, as statistical soundness forms the foundation upon which all future statistical analyses would be based (McKillup and Dyar, 2010).

According to Bohling (2007), geostatistical methods are optimal when data is stationary and normally distributed, as significant deviations from normality and stationarity could cause problems later on. McKillup and Dyar (2010) on the other hand, stated that the normality of a dataset not only determines the statistical soundness of the data itself, but also underlies all future statistical analyses that may be performed on the data. In addition to the statements mentioned above, Webster and Oliver (2007) regards normality as the cornerstone of statistical theory. Even though the author's focal points may differ, they do agree on the importance of a normally distributed dataset, as well as the preferred method that should be used to investigate it. Bohling (2007), as well as Webster and Oliver (2007) stated that normality is represented by a vertical cross-section through the bell curve of a histogram. The result is data that is distributed in a continuous and symmetrical fashion, with its peak at the mean of the distribution (Webster and Oliver, 2007). Webster and Oliver (2007) further stated that in many instances, distribution is far from normal and that departures from normality tend to give rise to unstable estimate, which in turn decreases the accuracy of predicted attributes.

As previously mentioned, for the purpose of this project, two alternative methods of data acquisition were used to collect radiometric data, in order to create a 3D geostatistical surface model of the New Machavie TSF. Given that one of the project's objectives was to validate the viability of the approach, the importance of generating statistically sound data was of the highest priority, as these datasets would be used to compare the accuracy of the various analytical techniques to each other, despite their contrasting strengths and limitations. Based on methods recommended by literature (Bohling, 2007; Webster and Oliver, 2007; IAEA, 1992 and IAEA,

1979) and used in similar studies (Koch, 2014 and Abu Deif *et al.*, 2001), the normality of each dataset was assessed by creating histograms of each analysed radionuclide and plotting the acquired data against a normal distribution curve. Taking into consideration that similarity is of the same importance for two variables, as normal distribution is to one (Webster and Oliver, 2007), statistical relationships between variables were evaluated using correlation and regression analyses, once normality was confirmed.

5.2 Chapter objectives and motivations

The main objective for this particular section is to evaluate the statistical soundness of each acquired dataset, before being geostatistically-interpolated for the creation of the 3D surface model. Since the combination of PXRF spectroscopy, natural gamma-ray spectrometry and Ordinary Prediction-based Kriging has not been tested for uranium exploration or environmental assessment over tailings impoundments before, this particular section aims to validate the viability of the approach from a statistical perspective. Therefore, as a subordinate of the current objective, the best suited analytical technique, for quick and cost effective uranium prospecting or environmental assessment, over tailings impoundments, will be identified.

5.3 Results and discussion

5.3.1 Data normalisation

As previously mentioned, literature refers to normally distributed data as having a bell curve where its peak is positioned above the mean of the distribution (Bohling, 2007 and Webster and Oliver, 2007). In the case of both Figure 9 and Figure 10 however, which represents data derived from the PXRF, the computed arithmetic means were calculated as 17.16 and 9.23 respectively, while the peaks of both bell curves were positioned slightly to the left of the expected normal. The slight deviation in position could be ascribed to the positive skewness of both datasets, as both datasets were found to be significantly skewed, producing a skewness value of 3.53 and 1.46 respectively. Literature states that perfectly distributed data, represented by a bell curve with exact symmetry, should have a skewness value of nil (Webster and Oliver, 2007). Variability on the other hand, measured using absolute standard deviation, was calculated as 16.66 and 6.52 for Figure 9 and Figure 10 respectively.

With regards to the normality of the datasets derived from the radiometric survey, both datasets produced similar results when directly compared to the PXRF, as both bell curves once again deviated slightly from the expected normal, while the computed arithmetic means were calculated as 12.95 and 6.59 for Figure 11 and Figure 12 respectively. The slight deviation was once again ascribed to the positive skewness of both datasets, as both datasets were found to be significantly skewed, producing a skewness and variability value of 3.32 / 14.96 and 1.95 /

4.12 for Figure 11 and Figure 12 respectively. While the slight deviation from the expected normal was ascribed to the skewness of each respective dataset, the skewness itself could be ascribed to the distribution of both uranium and thorium over the New Machavie TSF, as well as the surface dimensions of the geochemical sampling grid, which clearly favours the surrounding area of influence. As low level concentrations were in most cases associated with the surrounding area of influence, the greater dimensions of the surrounding area of influence, compared to that of the tailings material, resulted in a greater quantity of low level measurements, thereby increasing the skewness and lowering the average mean concentration in the process.

Another factor that might have influenced the normality of the datasets is the presence of radioactive disequilibrium and how it influenced the mobility of each particular radionuclide, relative to its progeny isotopes (Tutu *et al.*, 2009). Given that the uranium datasets recorded significantly higher skewness and variability values, it could be assumed that the higher values are attributable to environmental factors, in particular uranium disequilibrium, rather than analytical errors. Despite the slight deviations from expected normal, the datasets derived from both analytical techniques were labelled accurate and normally distributed, and therefore used to conduct further geostatistical analyses. The decision was made not to alter the datasets in the pursuit of normality, as alterations to the raw data might affect the credibility of the model when used for either environmental or reclamation purposes. This is in accordance with the work of both Abu Deif *et al.* (2001) and Sarma and Cock, 1980 (cited by Abu Deif *et al.*, 2001), who both recommended that statistical computations be performed on the original data, without employing any type of transformation, when working with radiometric measurements. As a result, normality was confirmed.

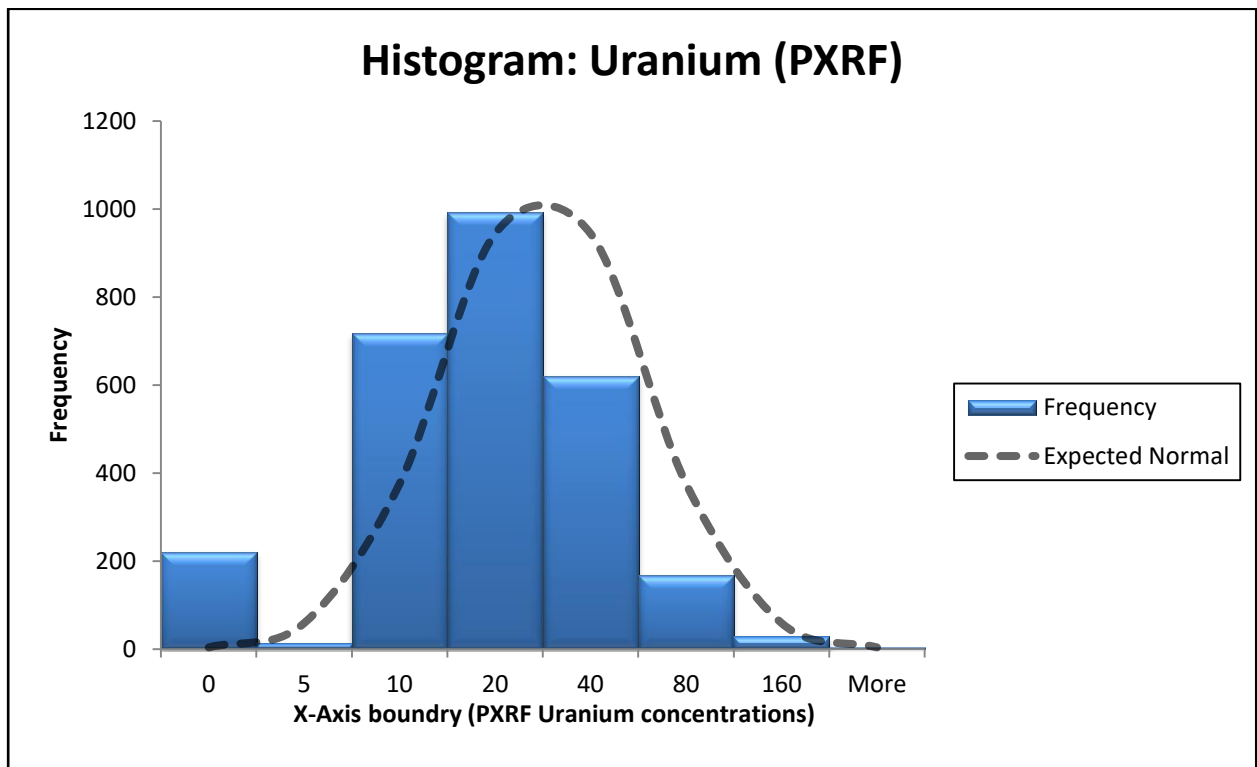


Figure 9: Data normalisation: PXRF derived uranium concentrations (ppm), plotted against the expected normal distribution of the dataset

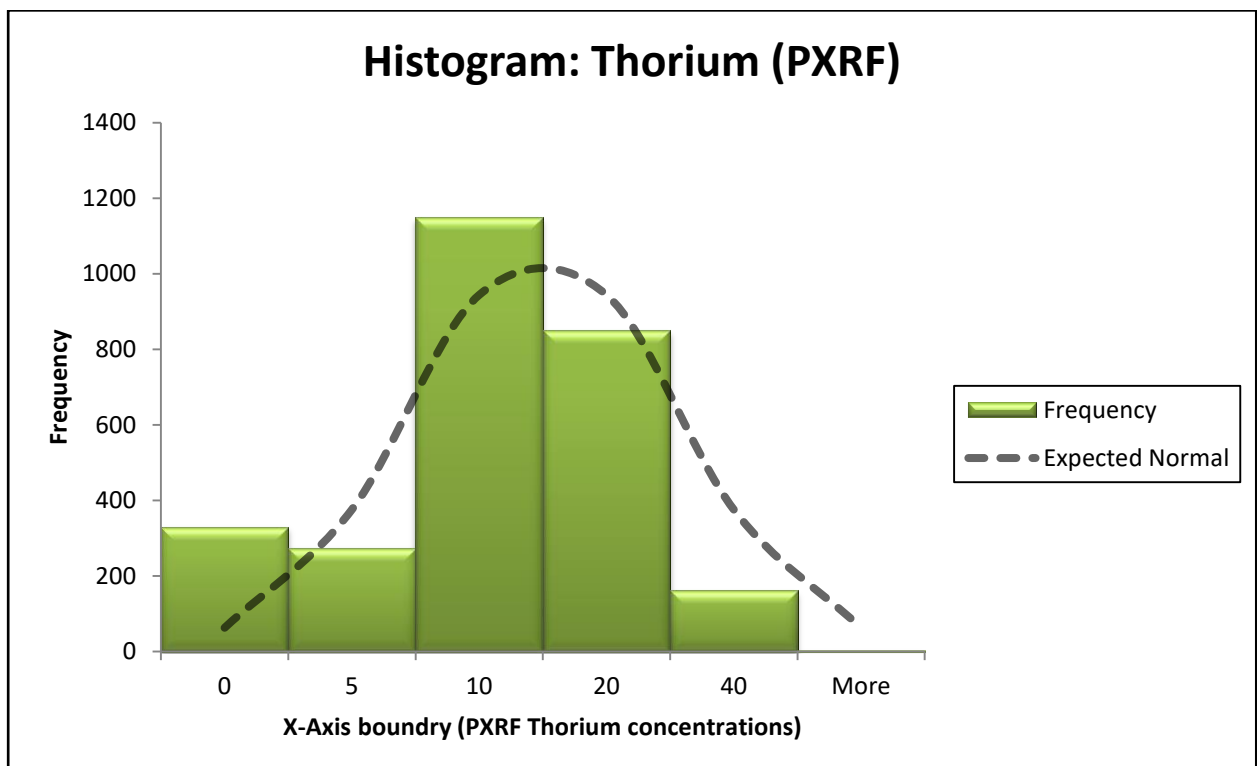


Figure 10: Data normalisation: PXRF derived thorium concentrations (ppm), plotted against the expected normal distribution of the dataset

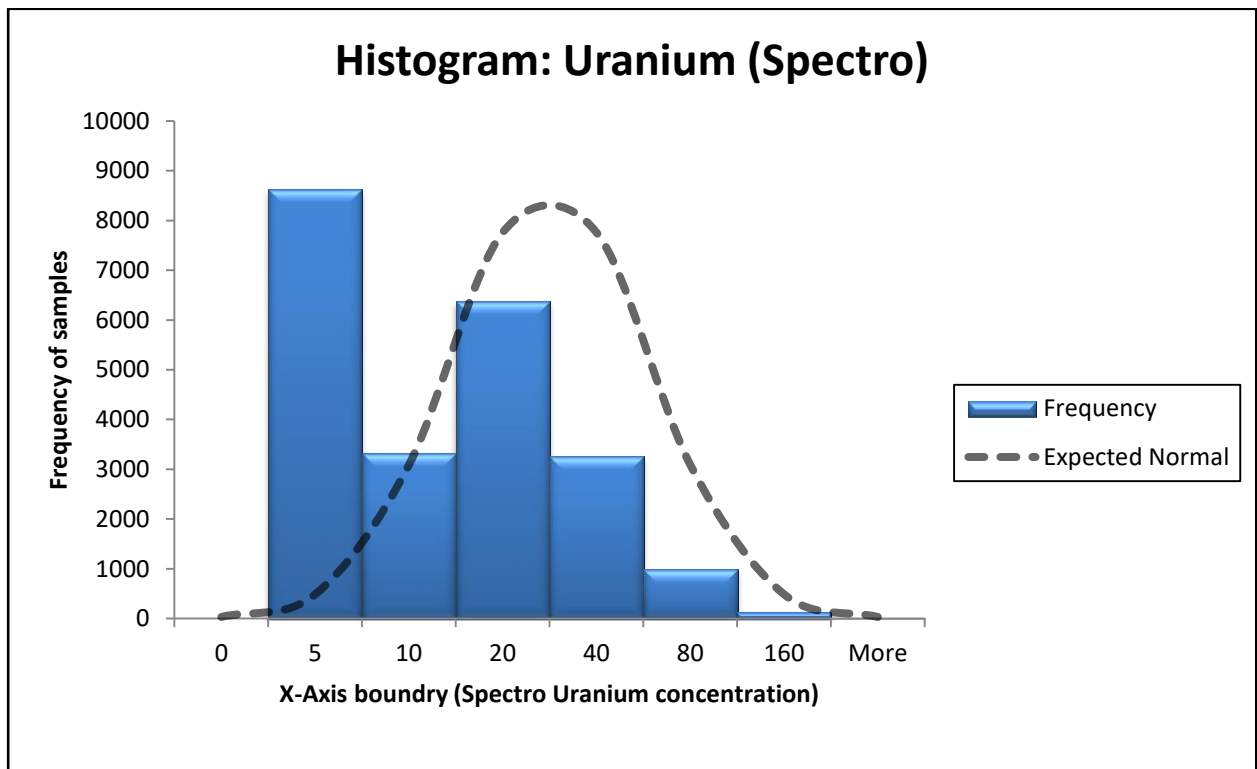


Figure 11: Data normalisation: Equivalent uranium concentrations (ppm), plotted against the expected normal distribution of the dataset

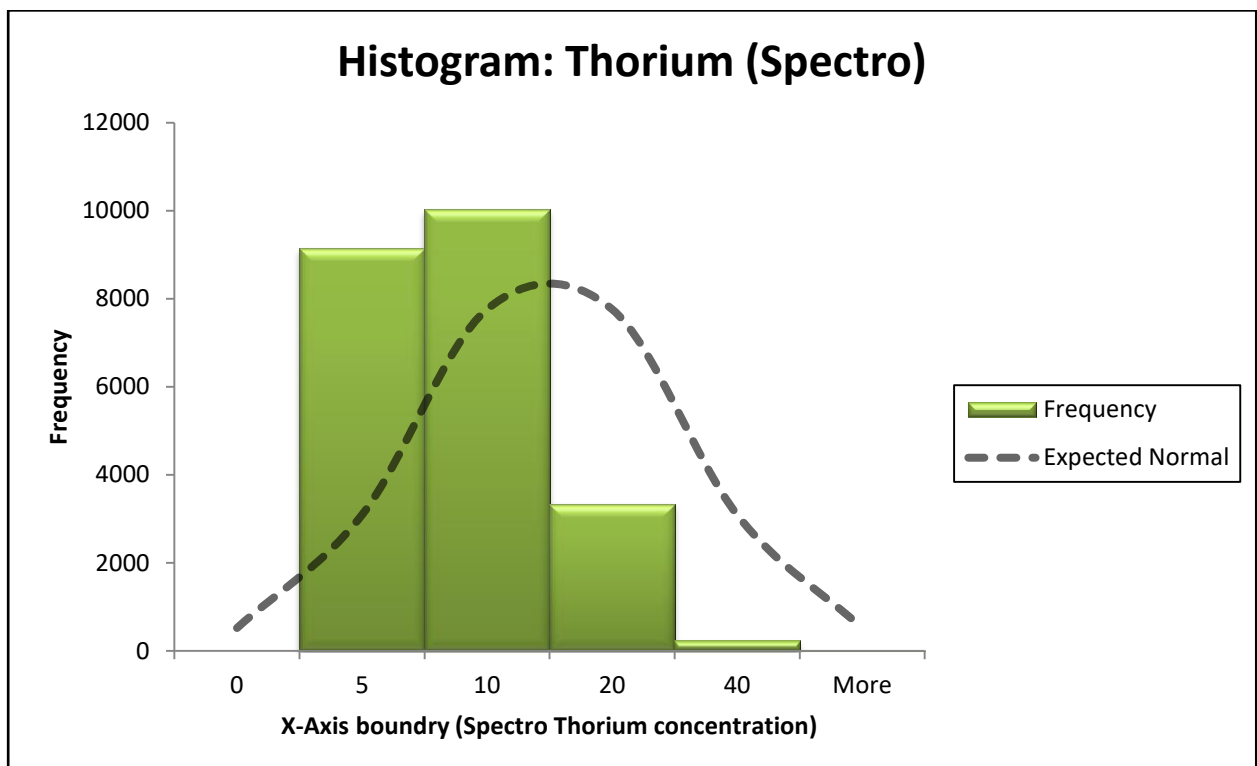


Figure 12: Data normalisation: Data normalisation: Equivalent thorium concentrations (ppm), plotted against the expected normal distribution of the dataset

5.3.2 Correlation and regression comparisons

With the confirmation of normality, attention was shifted to the statistical relationships found between the variables, as well as the evaluation of each analytical technique's ability to accurately measure radionuclide concentration levels, over the New Machavie TSF. According to Webster and Oliver (2007) similarity is of the same importance to two variables, as normal distribution is to one. When working with two variables, attention is focussed on the joint distribution, which is bivariate normal, rather than normally distributed (Webster and Oliver, 2007). For the purpose of this project, similarity was evaluated using a correlation coefficient (r), indicated in Table 9, which evaluated the linear relationship found between two variables, while a coefficient of determination "*regression*" (r^2) was used to quantify the degree of variability and predictability of the different variables.

In order for this particular section to state the viability of using PXRF spectroscopy and natural gamma-ray spectrometry as an alternative to traditional laboratory based chemical analyses, specifically focused on the assessment of radionuclides, it was important that both alternative techniques record similar radionuclide concentration values, when analysing the same sample. With regards to Figure 13, which compared both techniques' ability to accurately measure uranium concentrations, the comparison produced a correlation coefficient of 0.822 and a coefficient of determination of 0.669 between the two techniques (see Table 9). Mentioned by both Bohling (2007) and Webster and Oliver (2007), correlation coefficients range from -1.0 for a perfectly negative correlation to 1.0 for a perfectly positive correlation, while a correlation coefficient in the vicinity of nil represents uncorrelated variables. Webster and Oliver (2007) further states that a correlation coefficient will have a positive value, when both variables contain units with large values, while negative values will be attained if the large values of one variable are matched by small values of the other. A correlation coefficient of 0.822 therefore indicates a well-defined linear relationship, while a coefficient of determination of 0.669 indicates a relatively good degree of predictability.

Table 9: Pearson Correlation Matrix showing the linear elemental relationships found between the respective measured concentrations

Pearson Correlation Matrix						
	XRF (U)	PXRF (U)	Spectro (U)	XRF (Th)	PXRF (Th)	Spectro (Th)
XRF (U)	1.000					
PXRF (U)	0.928	1.000				
Spectro (U)	0.863	0.822	1.000			
XRF (Th)	-0.221	-0.065	-0.207	1.000		
PXRF (Th)	0.542	0.692	0.549	0.047	1.000	
Spectro (Th)	0.540	0.665	0.691	0.253	0.614	1.000

Figure 14 on the other hand, which compared both techniques' ability to accurately measure thorium concentrations, produced a correlation coefficient of 0.614 and a coefficient of determination of 0.377 respectively (see Table 9). Although significantly lower compared to the uranium measurements, a correlation coefficient of 0.614 still indicated an above average linear relationship, while a coefficient of determination of 0.377 indicated a poor degree of predictability. While the high variance in the case of normality was ascribed to environmental conditions rather than analytical errors (with regards to similarity), this was not necessarily the case, as detector limitations also played its part. In accordance to Koch (2014), in situations where very low concentrations are recorded, for example over the surrounding area of influence, count rates tend to decrease, while the error margin of the detector increases, as a direct result of the decrease in statistical representational counts. Koch's (2014) statement therefore provides an explanation to the increased variation between the measured values and the actual concentrations, evidenced by the high degree of variance between the two datasets, as highlighted in Figure 14. The high degree of variability could also be ascribed to the small portion of a sample that is analysed when using the PXRF, compared to the infinite sample size recorded by the radiometric survey, as evidenced by the quantity of nil ppm measurements (below detector limits), recorded by the PXRF.

In order to further state the viability of using PXRF spectroscopy and natural gamma-ray spectrometry as an alternative to traditional laboratory based chemical analyses, it was important that both techniques record similar radionuclide concentration values, when compared to a more traditional laboratory based analysis, in this case X-ray Fluorescence. Using exactly the same samples as used in previous comparisons, Figure 15, which compared the radiometric measurements with the uranium measuring ability of X-ray Fluorescence, produced a correlation coefficient of 0.863 and a coefficient of determination of 0.745 respectively (see Table 9). Figure 17 on the other hand, which compared the PXRF uranium measurements with that of the X-ray Fluorescence, produced a correlation coefficient of 0.928 and a coefficient of determination of 0.856 respectively (see Table 9). Taking into consideration that all three uranium comparisons produced well-defined linear relationships (>80%) between the respective datasets, the results therefore state the viability of the approach as an alternative to traditional laboratory based chemical analyses. In the case of the uranium, variability between datasets could be ascribed to radioactive disequilibrium not being accounted for. As the project never intended to quantify the uranium resources contained within the impoundments, project resources were instead allocated to ensuring the accuracy of the 3D surface model, rather than accounting for radioactive disequilibrium.

With regards to the comparison of thorium concentrations, both Figure 16 and Figure 18, which compared both the radiometric and PXRF measurements, to the thorium measuring ability of X-

ray Fluorescence respectively, indicated a poor linear relationship between the respective datasets. Both comparisons produced correlation coefficients below 30% (0.253 and 0.047 respectively), while indicating high variability and low predictability between the respective datasets (see Table 9). Despite literature emphasis on the rarity of radioactive disequilibrium with regards to thorium and its progeny isotopes, the results seem to indicate the influence of an alternative source, other than detector limitations and sample size. While the influence of low count rates should not be ignored, it could be assumed that the extreme conditions associated with the oxidised impoundments have contributed to the mobilisation of both radionuclides (Vandenhove *et al.*, 2009), allowing them to decouple from their respective progeny isotopes (Tutu *et al.*, 2009), which in turn contributed to the high variability found between the datasets.

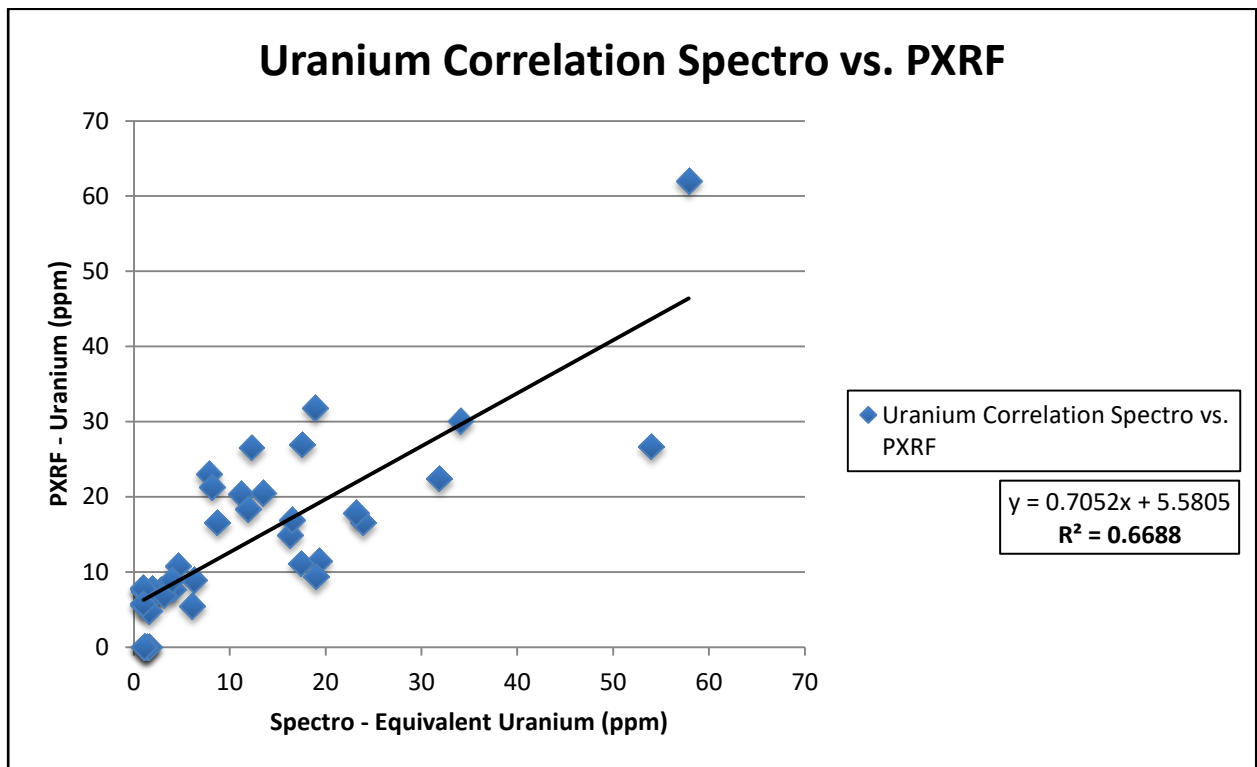


Figure 13: Statistical comparison of recorded uranium concentrations, as measured by the portable-XRF and natural gamma-ray spectrometry respectively

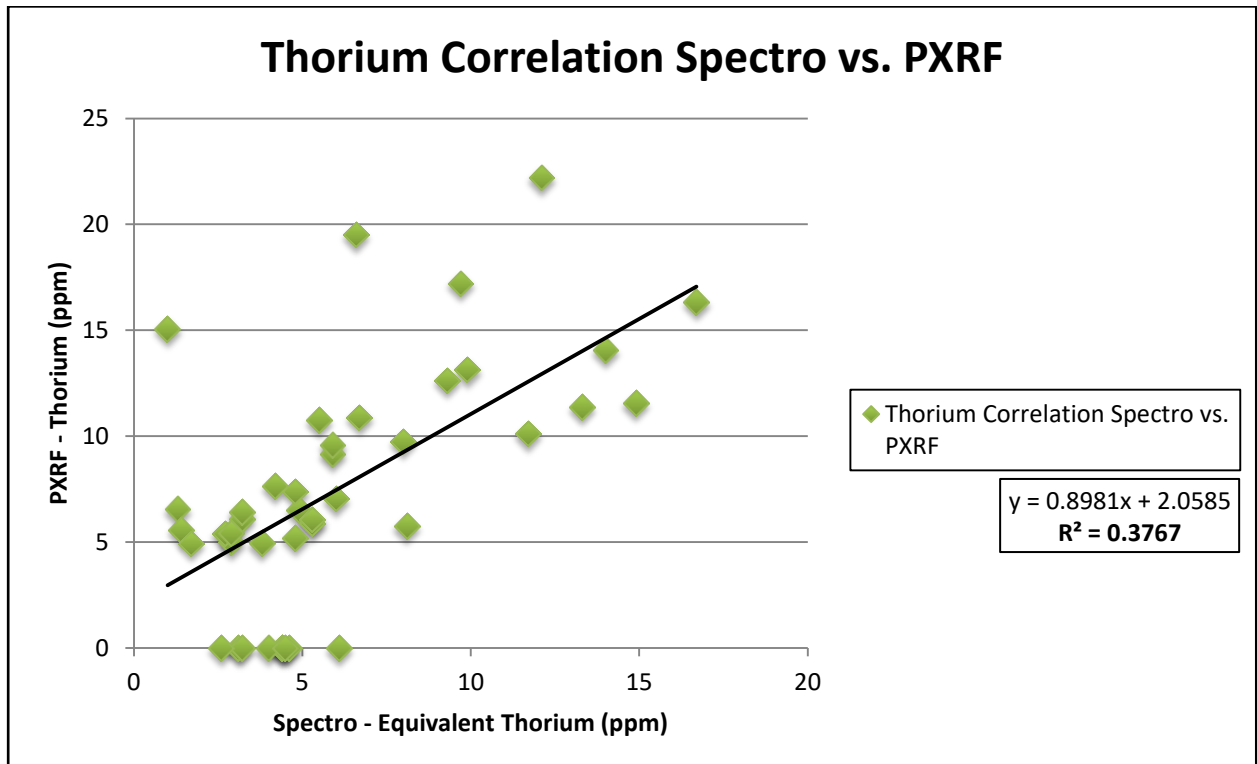


Figure 14: Statistical comparison of recorded thorium concentrations, as measured by the portable-XRF and natural gamma-ray spectrometry respectively

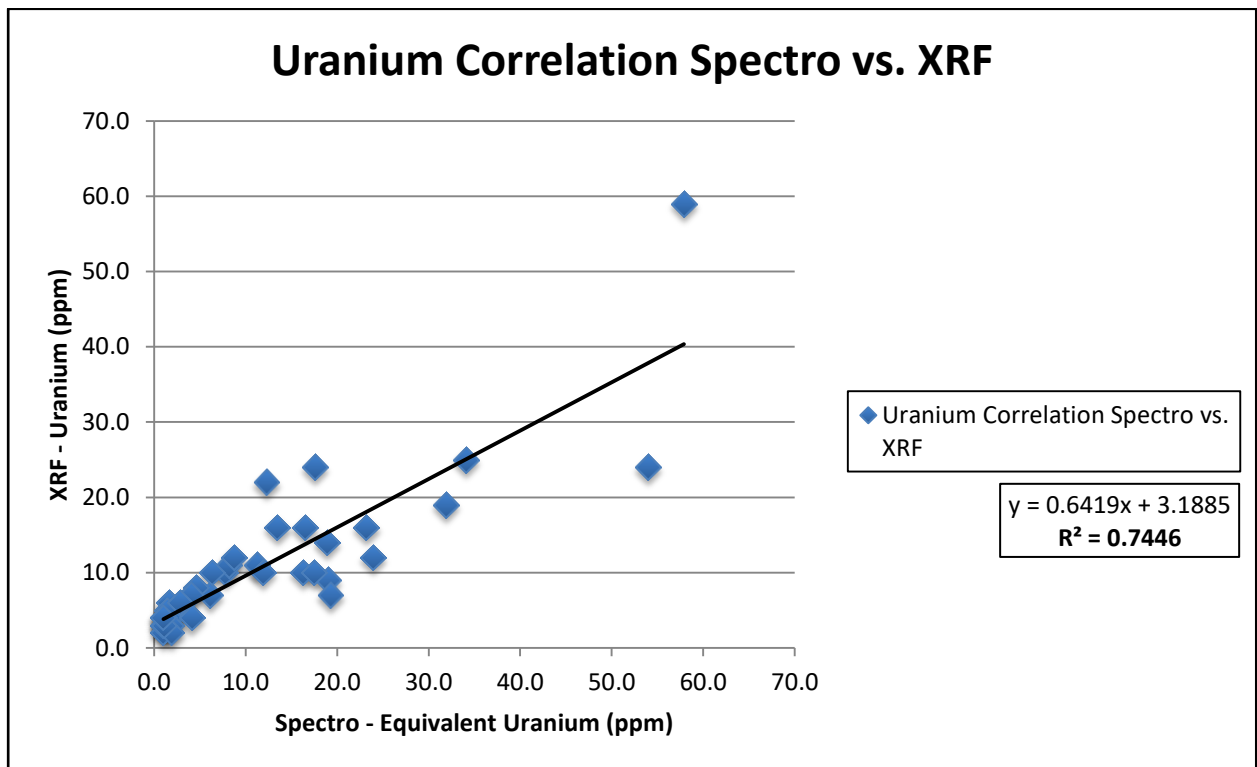


Figure 15: Statistical comparison of recorded uranium concentrations, as measured by laboratory based XRF and natural gamma-ray spectrometry respectively

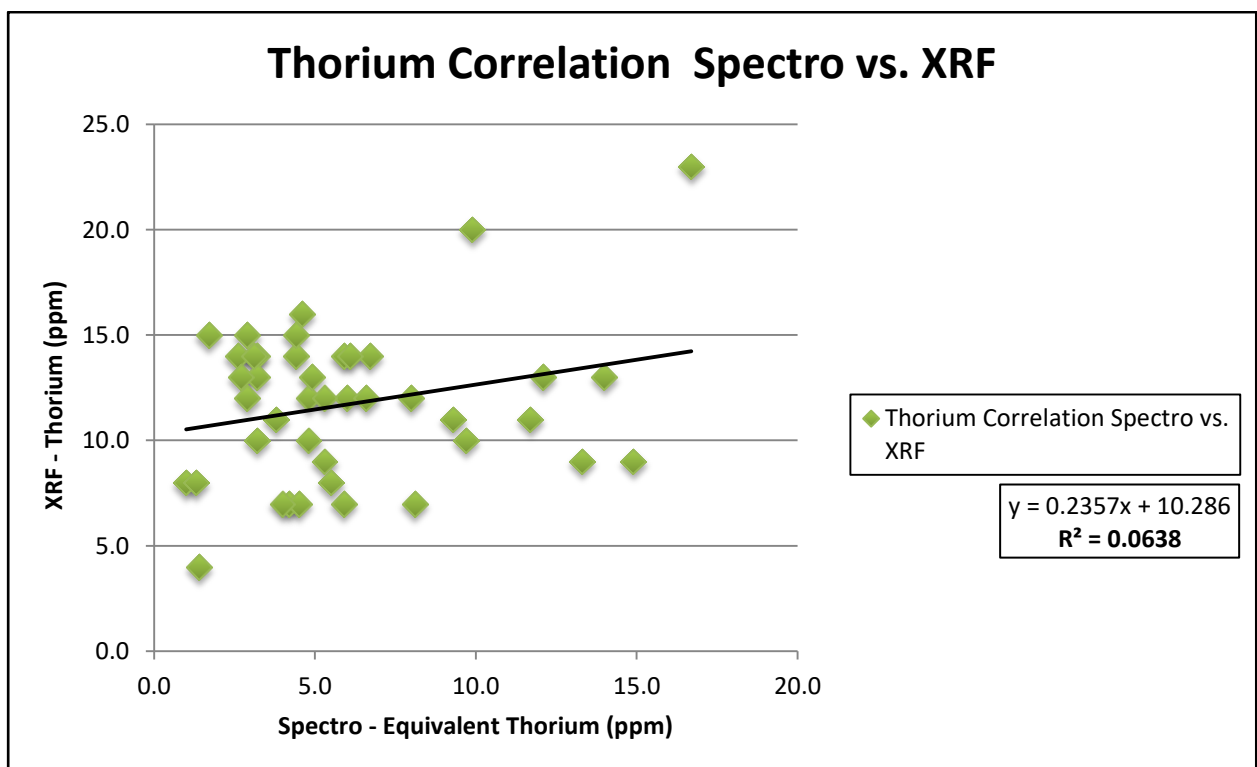


Figure 16: Statistical comparison of recorded thorium concentrations, as measured by laboratory based XRF and natural gamma-ray spectrometry respectively

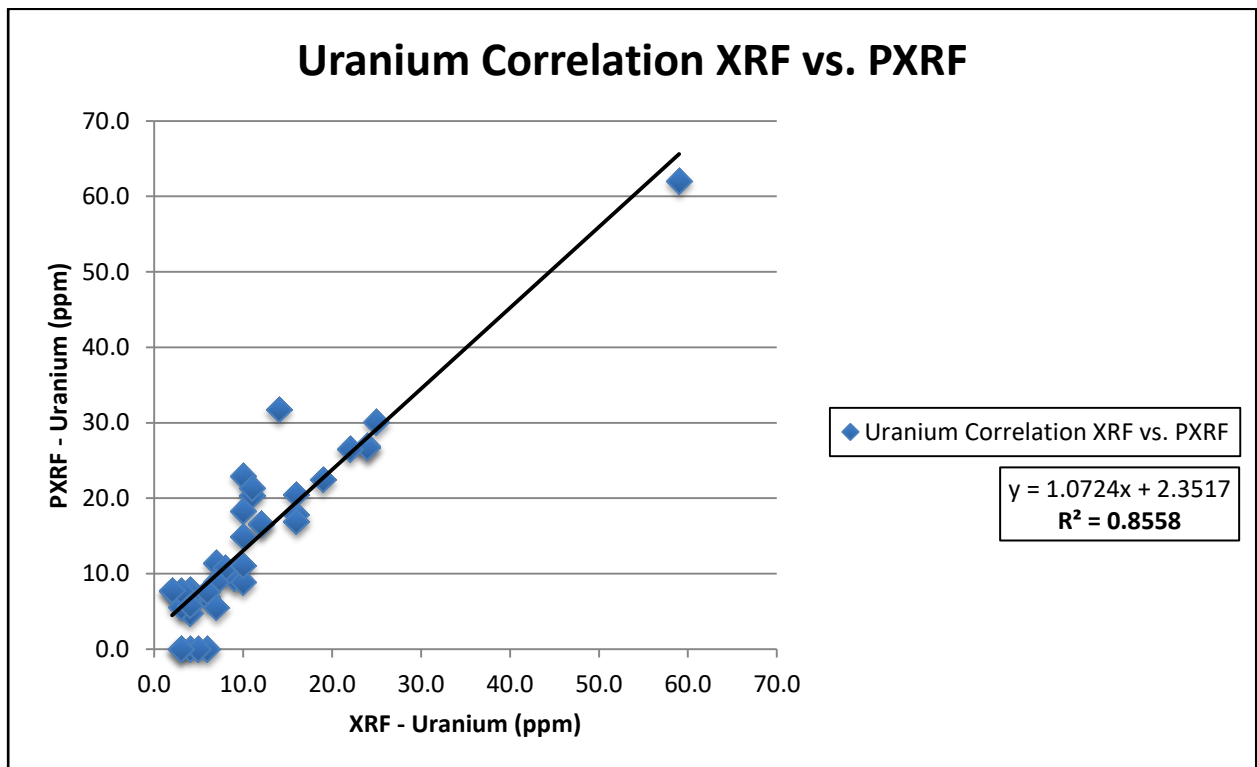


Figure 17: Statistical comparison of recorded uranium concentrations, as measured by laboratory based XRF and the portable-XRF respectively

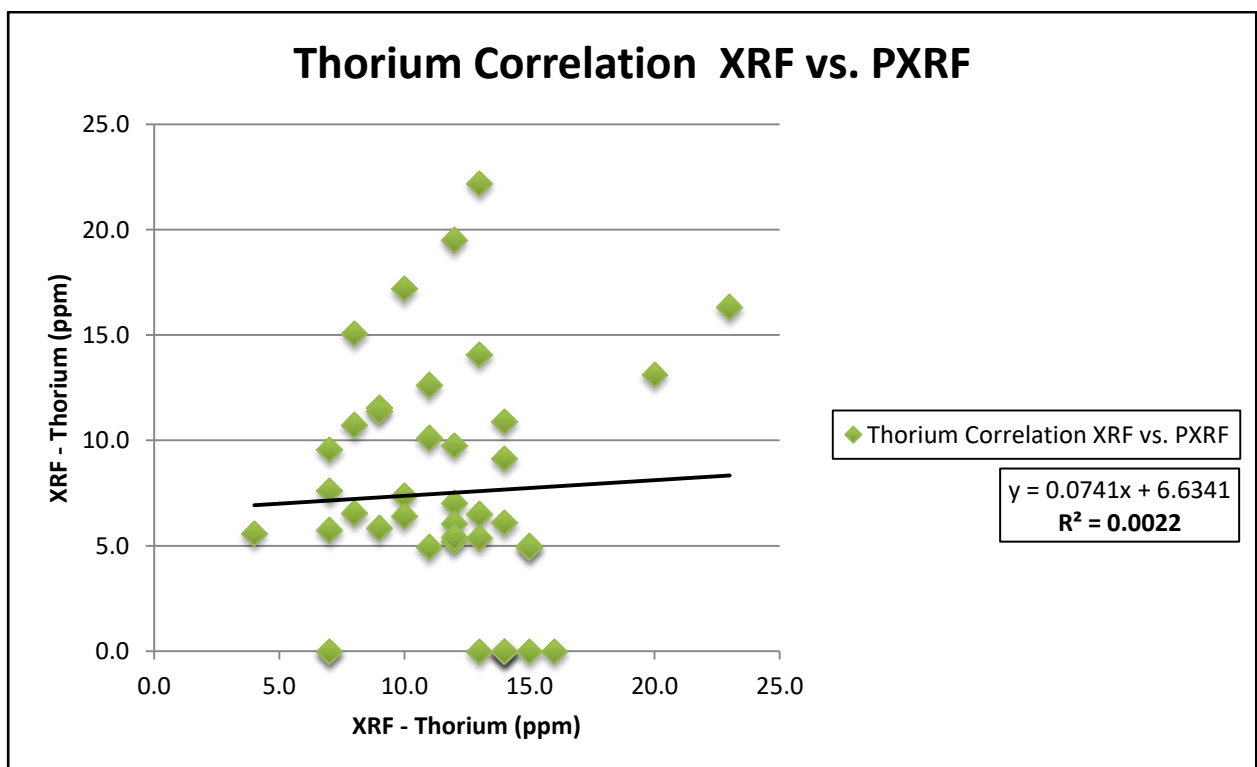


Figure 18: Statistical comparison of recorded thorium concentrations, as measured by laboratory based XRF and the portable-XRF respectively

5.4 Chapter conclusion

Chapter 5 set out to evaluate the statistical soundness of each acquired dataset, before being geostatistically-interpolated for the creation of the 3D surface model. Since the combination of PXRF spectroscopy, natural gamma-ray spectrometry and Ordinary Prediction-based Kriging has not been tested for uranium exploration or environmental assessment over tailings impoundments before, this particular section aimed to validate the viability of the approach from a statistical perspective. Despite the disadvantages associated with each analytical technique respectively, the alternative approach proved to be quite sufficient in the accurate identification of radionuclide content, as the approach not only produced results that complemented each other to some extent, but also validated the viability of the approach as an alternative to traditional laboratory based chemical analyses.

With literature emphasising the importance of performing statistical analyses on the original data, when working with radiometric measurements, datasets derived from both analytical techniques were confirmed normally distributed, despite their slight deviation from normality. Based solely on each respective technique's statistical performance (using the XRF results as the baseline) to accurately identify uranium concentration levels *in situ* and in the field, PXRF spectroscopy was found to perform slightly better than the natural gamma spectrometry. Evidenced by both the comparative correlation coefficients (0.928 and 0.863 respectively), as well as their respective degrees of variability, the "*not expected*" result could be ascribed to radioactive disequilibrium not being accounted for in the case of the radiometric survey. With regards to thorium, natural gamma-ray spectrometry outperformed the PXRF, despite both techniques producing poor correlation coefficients when compared to that of the X-ray Fluorescence. High variability between datasets was ascribed to either detector limitations in conjunction with low count rates, as was the case with the radiometric survey or the size of the sample being analysed, as was the case with both the XRF and PXRF. However, as thorium is not actively pursued as a resource in South African gold tailings (Koch, 2014), the accuracy of the data would not be important for resource estimation purposes.

Viewed from an economical perspective, both techniques exceeded expectations, delivering reliable and accurate results, at a much lower cost to company, compared to the equivalent laboratory based chemical analysis. Compared to traditional laboratory based chemical analyses; both "*alternatives*" outperformed the prior, since initial costs only include the capital expenditure of the instrument, while the actual measurements are fairly simple, time efficient and does not necessarily need a professional technician to perform, unlike the traditional methods. Since both "*alternative techniques*" accurately estimated the uranium content, despite the oxidative nature of the TSF in question, this section validated the viability of the approach.

CHAPTER 6: SPATIAL DISTRIBUTION PATTERNS OF RADIONUCLIDES

6.1 Introduction

Since its development in the early 1960's, gamma-ray spectrometry, whether in airborne, ground or laboratory guise, has become synonymous with mineral exploration and environmental monitoring practises (IAEA, 2003). Its application in geological mapping, soil surveying, mineral exploration and regolith studies, all traces back to its ability to estimate radionuclide concentrations (K%, eTh and eU), *in situ* and in the field (IAEA, 2003). According to the IAEA (2003; 1979), when used as a mapping tool, it is important that the user possess over the necessary knowledge, with regards to the geochemistry of radionuclides in rocks, as well as soils, as mineralogical and geochemical studies play a fundamental role in the interpretation of radionuclide distribution, mobility and their petro- or pedogenetic associations. Because most of the gamma-rays, emanating from the surface of the earth, originates in the top 30 centimetres, a good understanding of surface processes, for example weathering and the relationship between surficial materials and bedrock geology, is required to successfully interpret radiometric data (IAEA, 2003).

In accordance with the IAEA (2003), the spatial distribution of radionuclides in surficial material is governed by a combination of factors, including geomorphological, erosional and weathering processes. Although viewed from a geochemical perspective, the statement correlated well with that of other authors, who stated that the weathering of underlying geology is regarded as the primary factor controlling the distribution of uranium in overlaying soils (Kabata-Pendias, 2011), while Pulford (2010) and Vandenhove *et al.* (2007) both stated that the adsorption and precipitation of radionuclides are considered secondary factors controlling distribution. The IAEA (2003) further stated that radionuclide concentrations are influenced by a trade-off between weathering and deposition, depending on the erosional activity at a specific site. In addition the IAEA (2003) reported that in the case of active depositional regimes, radionuclide concentrations in surficial material would most likely resemble that of the source rock.

In the case of the New Machavie tailings material, although derived from Black Reef Formation quartzite, it could be assumed that radionuclide content within the material would be governed by factors similar to those governing radionuclides in surficial material, rather than those governing radionuclides within a geological unit. In other words, radionuclide concentrations within the tailings material itself should resemble concentrations similar to that of the source rock it was derived from, while radionuclide concentrations within the soils surrounding the tailings impoundment would be governed by the weathering and erosional processes associated with the tailings material. The assumption correlated well with the statement of Dickson and

Scott (1997), who stated that among other factors, the colluvial and aeolian transport of material enriched with radionuclides, tend to increase radionuclide concentrations in surrounding soils. Wilford *et al.* (1997) on the other hand, stated that the effect of topographic relief on radionuclide distribution patterns should not be underestimated. With Koch (2014), as well as Aucamp and van Schalkwyk (2003) indicating an accumulation of mobilised radionuclides along the natural flow paths of the New Machavie TSF, the statements mentioned above might hold some merit after all.

6.2 Chapter objectives and motivation

The main objective of this particular section is to identify the spatial distribution patterns of selected radionuclides (eU, eTh), using the created geostatistical 3D surface model of the New Machavie TSF. With literature stating the need for future research to focus on the evaluation of not only radioactive trends (Tutu *et al.*, 2009), but also the distribution of radionuclides in tailings impoundments (Koch, 2014 and Tutu *et al.*, 2003), this particular section aims to address the mentioned knowledge deficiencies, using alternative methods of data acquisition, in conjunction with a capable geostatistical-interpolator. Since the combination of PXRF spectroscopy, natural gamma-ray spectrometry and Ordinary Prediction-based Kriging has not been tested for uranium exploration or environmental assessment over tailings impoundments before, this particular section aims to validate the viability of the approach from a modelling perspective.

6.3 Results and discussion

6.3.1 Spatial distribution patterns of radionuclides

According to the IAEA (2003:113), *“any element of an interpretation that is considered important, but whose source is questionable, should be checked on the ground”*. Ground truthing therefore plays a significant role in any geophysical interpretation, but even more so in the case of radionuclide mapping, where anomalies are generally exposed or weathered (IAEA, 2003). With reference to radiometric surveys performed on tailings material, Tutu *et al.* (2003) stated that uranium tend to separate from its decay products, due to uranium being oxidised to the U^{6+} state, which results in locally enriched areas. In addition Tutu *et al.* (2003) stated that conventional gamma-ray spectrometers may not be able to detect these anomalies, as uranium concentrations are measured indirectly off its progeny daughter isotopes. With the IAEA (2003) recommending that ground truth studies should include measurements taken from augur holes, when working in highly weathered terrain, the decision was made to incorporate ground truthing measures in the form of PXRF spectroscopy, as it also provided an alternative approach to identifying uranium anomalies, *in situ* and in the field.

With reference to Figure 19 and Figure 20, which represents the spatial distribution patterns of uranium concentrations over the New Machavie TSF, both analytical techniques provided evidence of uranium migration and environmental contamination, upon first observation. Evidenced by a correlation coefficient of 0.822 between the two analytical techniques (see Table 9), both techniques highlighted uranium anomalies in similar locations, while delivering similar measured concentrations. In both cases the equivalent uranium (eU) concentrations could be divided into three main classes, namely Low-, Intermediate- and High eU concentrations (Assran *et al.*, 2012). With reference to the radiometric data (see Figure 19), the Low eU class, represented by shades of the colour green, indicated concentrations varying from 1.0 ppm to 10.0 ppm and occupied most of the surrounding area of influence. The Intermediate eU class on the other hand, represented by shades of the colour yellow and orange, indicated concentrations varying from 10.0 ppm to 60.0 ppm and occupied most of the tailings material, toe paddocks, as well as the transported material found in the surrounding area of influence. Lastly the High eU class, represented by shades of the colour red, indicated concentrations varying from 60.0 ppm to a maximum recorded value of 211.0 ppm, which was recorded in the vicinity of an erosion trench found on top of Tailings dam No.2. The High eU class was mostly associated with uranium anomalies distributed over the tailings impoundments itself, as well as areas where uranium accumulated as a result of wind and water transportation mechanisms.

In the case of the PXRF derived data (see Figure 20), the Low eU class, represented by shades of the colour green, indicated concentrations varying from 0.0 ppm to 13.0 ppm and once again occupied most of the surrounding area of influence. The Intermediate eU class on the other hand, represented by shades of the colour yellow and orange, indicated concentrations varying from 13.0 ppm to 64.0 ppm and occupied most of the tailings material, as well as the toe paddocks, while indicating a larger presence in the surrounding area of influence, compared to the corresponding radiometric data. Lastly the High eU class, represented by shades of the colour red, indicated concentrations varying from 64.0 ppm to a maximum recorded value of 197.0 ppm, recorded from the sample taken within the erosion trench found on top of Tailings dam No.2. The High eU class was mostly associated with the same uranium anomalies identified by the radiometric survey, but included new anomalies along the natural flow path of the surface water, in the direction of the Kromdraaispruit.

With reference to Figure 21 and Figure 22, which represents the spatial distribution patterns of thorium concentrations over the New Machavie TSF, both analytical techniques produced results similar to those of Tutu *et al.* (2009), who stated that thorium tend to show signs of immobility. Although smaller discrepancies were noted among the measured concentrations, compared to that of the uranium, lower counting statistics still contributed to variations between the measured and actual concentrations (Koch, 2014; Tutu *et al.*, 2009), as indicated by the

0.614 correlation coefficient (see Table 9). Similar to that of the uranium, equivalent thorium (eTh) concentrations were divided into three main classes, namely Low-, Intermediate- and High eTh concentrations (Assran *et al.*, 2012). With reference to the radiometric data (see Figure 21), the Low eTh class, represented by shades of the colour green, indicated concentrations varying from 1.0 ppm to 6.0 ppm and occupied most of the surrounding area of influence. The Intermediate eTh class on the other hand, represented by shades of the colour yellow and orange, indicated concentrations varying from 6.0 ppm to 30.0 ppm and occupied most of the tailings material, toe paddocks, as well as the transported material found in the surrounding area of influence. Lastly the High eTh class, represented by shades of the colour red, indicated concentrations varying from 30.0 ppm to a maximum recorded value of 53.6 ppm, which was recorded in the vicinity of an erosion trench found on top of Tailings dam No.2. The High eTh class was mostly associated with thorium anomalies distributed over the tailings impoundments itself, as well as areas where thorium accumulated as a result of mobilisation.

In the case of the PXRF derived data (see Figure 22), the Low eTh class, represented by shades of the colour green, indicated concentrations varying from 0.0 ppm to 7.0 ppm, which once again occupied most of the surrounding area of influence. The Intermediate eTh class on the other hand, represented by shades of the colour yellow and orange, indicated concentrations varying from 7.0 ppm to 40.0 ppm, while being confined to the tailings- and transported material. Attributable to its immobility, the High eTh class, represented by shades of the colour red, indicated concentrations varying from 40.0 ppm to a maximum recorded value of 74.4 ppm, while occupying most of the tailings, toe paddock and transported material. Evidenced, not only by literature (Tutu *et al.*, 2009), but also by the absence of thorium in the surrounding area of influence, unless mobilised under extreme conditions (Koch, 2014), thorium tended to accumulate in the tailings material, as a result of its resistance to weathering (Vandenhove *et al.* 2009).

6.3.2 Spatial distribution patterns of uranium over the tailings impoundments

According to literature, uranium anomalies in tailings dams are expected to be found to the centre of the tailings impoundment, where particle size fractions are considered to be the smallest (Koch, 2014 and Pulford, 2010). The statement correlated well with that of Pulford (2010) and Vandenhove *et al.* (2009), who both stated that the finer-grained material within a tailings dam has a greater adsorption charge and therefore acts as an adsorption site, where the mobility of uranium is decreased. Hillen (2004) on the other hand stated that the finer-grained fractions tend to retain moisture for longer, due to the stronger adsorption forces found between the water and the finer-grained particles. This according to Koch (2014) reduces the oxidative properties of the tailings material, which in turn decreases the mobilisation of uranium.

Spatial Distribution of Equivalent Uranium

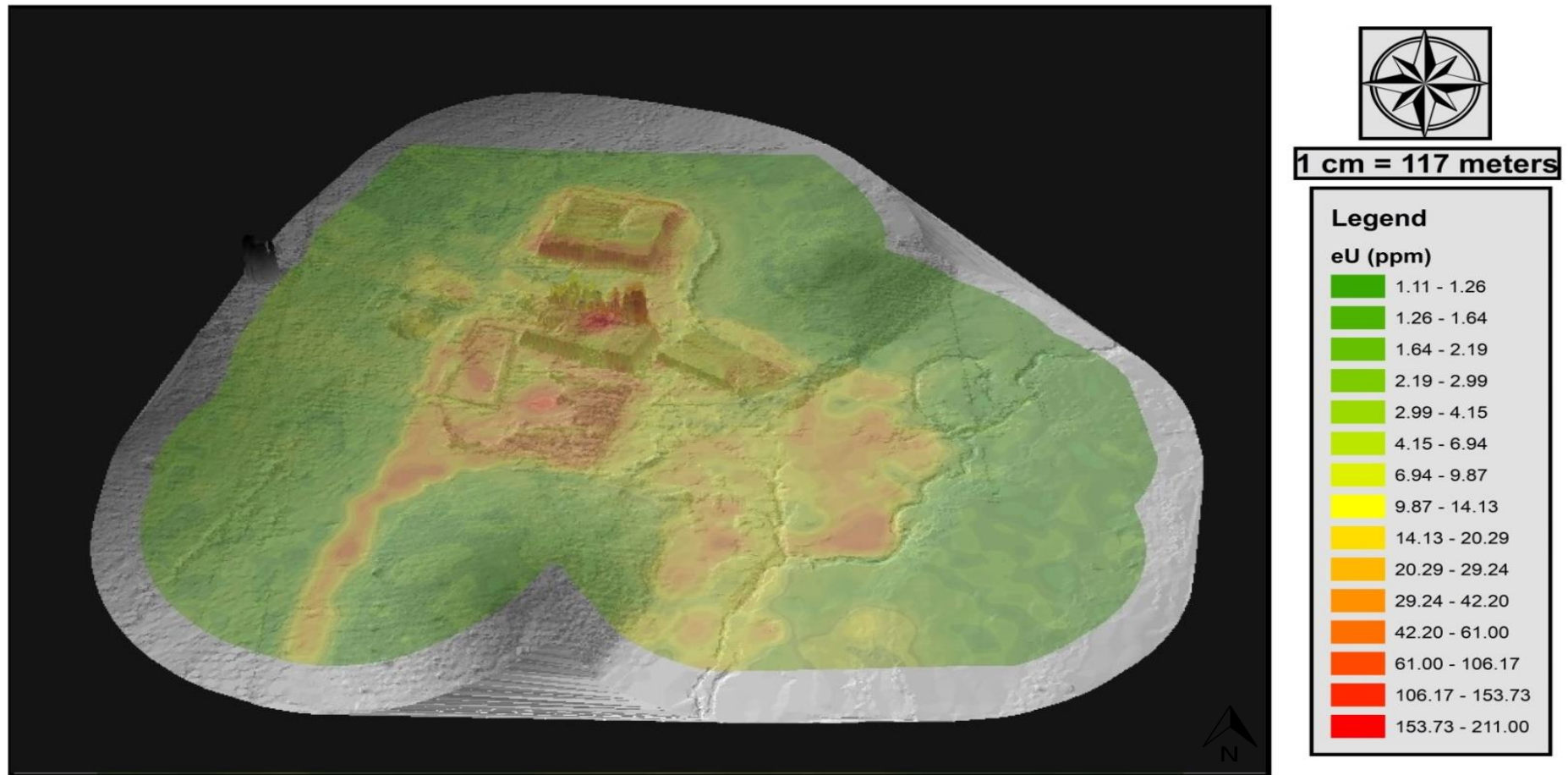


Figure 19: 3D surface model illustrating the spatial distribution of equivalent uranium concentrations, as measured by the natural gamma-ray spectrometer

Spatial Distribution of Measured Uranium

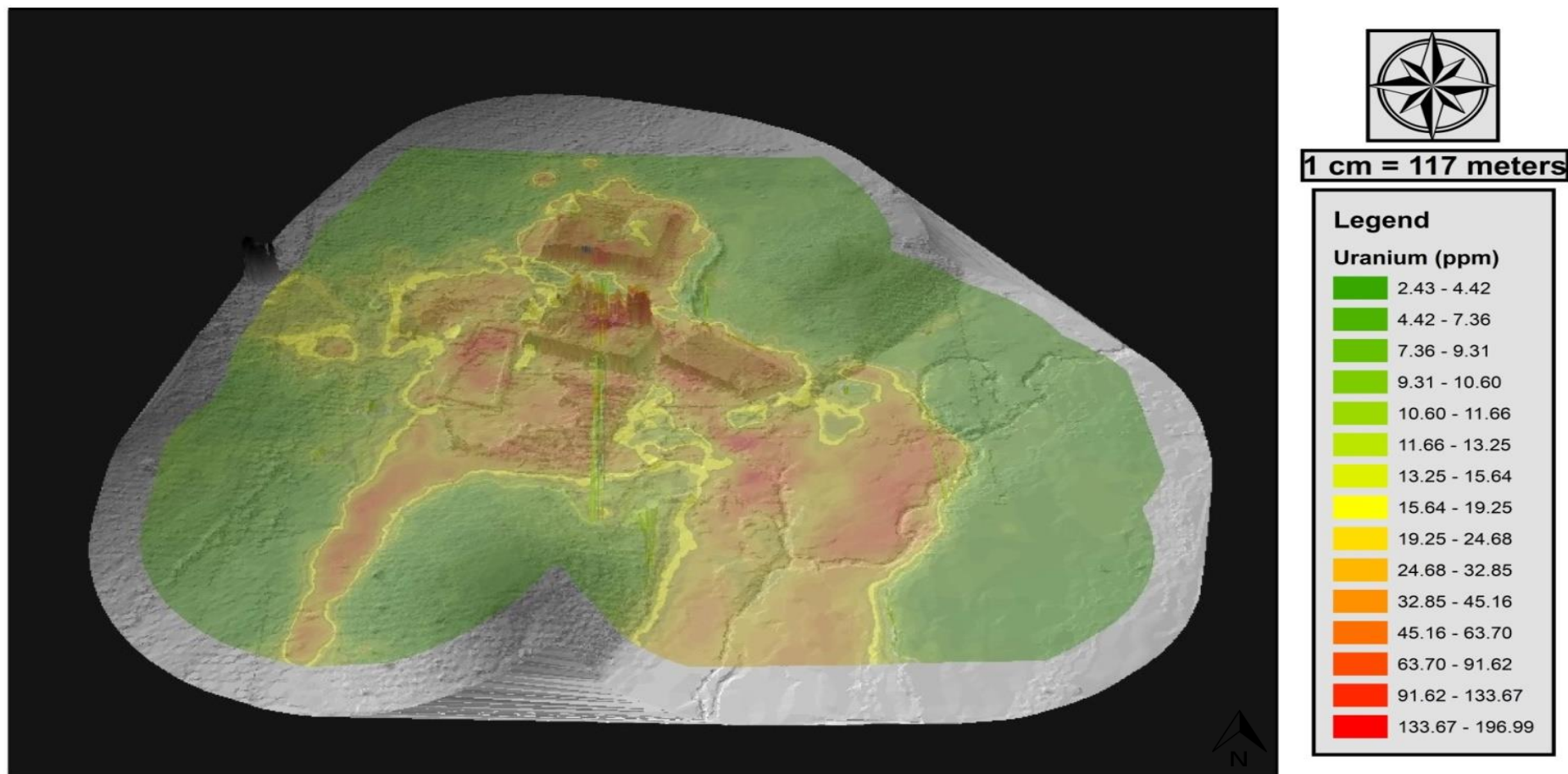


Figure 20: 3D surface model illustrating the spatial distribution of measured uranium concentrations, as derived from the portable-XRF

With reference to both Figure 19 and Figure 20 (also Figure 36 and Figure 37 in Appendix B) however, this was not the case, as most of uranium anomalies were associated with the heavily eroded sections of each respective tailings impoundment. Although an increase in uranium concentrations were noted to the centre of each respective tailings impoundment, the anomalies itself were ascribed to the accumulation of mobilised uranium in the low lying areas of each tailings impoundment, rather than to a decrease in particle size. However, based on site investigations, the low lying areas were found to contain increased amounts of fine-grained particles. Because the study did not include particle size distribution analyses, the theory of the effect particle size has on uranium migration, could not be ruled out. The results however correlated well with that of Koch (2014), who stated that radionuclides, while in the process of being leached, tend to accumulate in the lower and in some cases wetter areas of a tailings impoundment. In addition Koch (2014) also stated that transportation tend to occur along preferential flow paths, which in the case of the New Machavie tailings, is along the natural flow direction.

Under close inspection of the New Machavie 3D surface model (see Figure 19 and Figure 20), a general trend was noted where uranium accumulated on the lower side slopes, or to be more precise, the southern slopes of each respective tailings impoundment, while the largest part of the top of the tailings showed signs of depletion. Taking into consideration that the New Machavie TSF has been derelict for more than 60 years, while the topography of the study area decreases to its lowest point in a south-easterly direction, one could assume that the hydraulic properties of the TSF has conformed to that of the surrounding environment, over the years. The assumption was later confirmed by Koch (2014), who whilst drilling noticed that the saturated zone was the closest to the surface in the south-eastern corner of New Machavie's Tailings dam No.1 and later ascribed the phenomenon to the natural flow direction being mimicked within the tailings impoundment. The assumption also correlated well with that of Wilford *et al.* (1997) who stated that topographic relief tend to influence the distribution of radionuclides to some extent.

The phenomenon of uranium accumulating specifically on the southern slopes of the tailings impoundments could also be described from a geochemical perspective. Koch (2014) stated that the oxidation zone of a typical gold tailings impoundment extends from the top of the tailings impoundment, along the side slopes, right down to its base. The oxidation of sulphide minerals in the oxidation zone, as discussed in Chapter 2, therefore produces the ideal environment in which uranium is first oxidised and later mobilised, generally in the form of a uranium-sulphate species (UO_2SO_4 and $\text{UO}_2(\text{SO}_4)^{2-}$), as these sulphate-complexes tend to be mobile and leachable (Alloway, 2012; Vandenhove *et al.*, 2009 and Tutu *et al.*, 2003). According to Yibas *et al.* (2010), the mature oxidation zone is typically characterised by the depletion of

metals, relative to that of the oxidation front and ascribed the depletion to pore water carrying soluble secondary minerals to the lower levels during migration. The statement of Yibas *et al.* (2010), in conjunction with alterations in elevation, provided an explanation to the depletion of uranium seen on top of the tailings impoundments, relative to the accumulation on the side slopes, as well as in the low lying areas. The results also correlated well with that of Koch (2014), who indicated a decrease in uranium concentrations at the top of Tailings dam No.1, while increased concentrations were noted on the side slopes, as well as within the oxidation front.

With reference to the distribution patterns seen over Tailings dam No.1, recorded eU concentrations were found to be the highest on the southern slope, with a maximum recorded value of 138.0 ppm (see Figure 19). The highly oxidised environment found on the side slopes tends to favour the mobilisation and leaching of uranium away from the tailings impoundment, while accumulation prevailed at the base of the side slopes, as well as in the toe paddocks. Aucamp and van Schalkwyk (2003) reported that the climate at New Machavie allows for evaporation to exceed precipitation, which in turn allows for the uranium-enriched leachate to move towards the surface of the side slopes. The precipitation of these salt- and metal-enriched leachates, in conjunction with the formation of uranium-adsorbing iron oxides on the lower slopes, therefore results in the immobilisation and accumulation of uranium. Not only does the statement provide an explanation to the uranium-enriched side slopes, but also to the yellowish salts precipitates and iron oxides, observed during site investigations.

In the case of Tailings dam No.2, recorded eU concentrations assumed the shape of concentric circles, with eU concentrations increasing as one move closer to the erosion trench, found on the northern side of the tailings impoundment (see Figure 19). Although small uranium anomalies were noted on the southern slope, the majority of the leached uranium accumulated within the erosion trench, as well as at the base of the northern slope. The accumulation could be ascribed to a combination of two factors. In the first, uranium accumulation is ascribed to variations in elevation, as the 3D surface model indicated that the elevation of Tailings dam No.2 decreased to the north, while the northern toe paddock was situated at a slightly lower elevation compared to the surrounding environment (see Figure 2 and Figure 4). With the paddock being situated within the natural flow path of Tailings dam No.1, it could be assumed that uranium-enriched leachate from both Tailings dam No.1 and No.2 would accumulated in the low lying northern toe paddock.

The second explanation ascribes the accumulation to both precipitation, as well as a decrease in particle size. Both Kabata-Pendias (2011) and Pulford (2010) stated that the mobility of uranium is controlled by the adsorption of uranium to clay minerals and metal-oxides, as well as precipitation in the form of organic complexes. With an increase in vegetation (presence of

eucalyptus trees) to the north of the impoundment, it could be assumed that the uranium either precipitated as discussed earlier, or formed bonds with the soil organic material, in which case the uranium precipitated as organic complexes (Vandenhove *et al.*, 2007). With regards to the decrease in particle size, it could be assumed that finer-grained particles would accumulate on the northern side of Tailings dam No.2, given its location. With a general wind direction of north to north-east (Botha, 2015), Tailings dam No.2 was positioned directly downwind, as well as downstream (south-east) of Tailings dam No.1, meaning fine-grained material could have been transported as either waterborne or aeolian material and later deposited in the low lying paddock.

Characterised by its greyish-black colour, Tailings dam No.3 produced the lowest eU concentration of the five tailings impoundments, with a maximum recorded value of 43 ppm (see Figure 19). Koch (2014) reported that the low eU concentrations are attributable to the inorganic carbon content of the material, which tends to retain and immobilise the uranium, by forming carbon complexes. De Bever (1997) on the other hand, stated that New Machavie's poor gold recoveries, were also attributed to the presence of inorganic carbon, as it tend to reabsorb the gold during processing, while the pyrrhotite and marcasite, which are also present in the material, oxidised rapidly to produce cyanicides. The 3D surface model revealed a decrease in elevation, with an increase in uranium concentration along the spine of Tailings dam No.3 (see Figure 19 and Figure 36 in Appendix B). Uranium accumulation was mostly associated with the erosion trenches, which covered most of the eastern corner of the tailings impoundment, while running parallel with the natural surface flow direction.

Tailings dam No.4 on the other hand, which showed signs of being reclaimed (Aucamp and van Schalkwyk, 2003), produced a maximum recorded eU value of 118.0 ppm (see Figure 19 and Figure 20). Uranium accumulation showed signs of being associated with the material itself, as most of the uranium accumulated in the south-eastern corner of the unclaimed material. The uranium anomaly on the other hand, was found to the north-west of the unclaimed material, situated within a low lying area. The anomaly could be ascribed to leachate accumulating in the low lying area, while the source was identified as both Tailings dam No.5, as well as the unclaimed material. Characterised by its pinkish colour, Tailings dam No.5, identified as a calcine tailings, is situated to the north-west of Tailings dam No.4 and produced a maximum recorded eU value of 125.0 ppm (see Figure 19 and Figure 20). Uranium was found to accumulate upon the lower step of the tailings impoundment, while preferential flow paths were noted in both the direction of Tailings dam No.4, as well as the surrounding area of influence. Given the shape and position of Tailings dam No.4, it could be assumed that uranium-enriched aeolian material would accumulate in the low lying area, thereby producing the uranium

anomaly, in conjunction with the leachate originating from both Tailings dam No.5, as well as the unclaimed material.

With regards to the toe paddocks of the tailings impoundments, uranium accumulation tends to favour the low lying areas, while following the natural flow direction of the TSF. Uranium anomalies on the other hand, with an average recorded eU value of 66 ppm between them, were in most cases situated to the south-east of the tailings impoundment (see Figure 19 and Figure 20). Koch (2014) reported that samples derived from the New Machavie toe paddocks, showed a decrease in radionuclides, with an increase in anion content, as the anions tend to decrease the mobilisation of the uranium. In addition Koch (2014) stated that, while uranium mobilisation was dominated by uranyl sulphate complexes in the tailings material, the toe paddock samples tend to be dominated by uranyl ions forming complexes with oxides and hydroxides. The statement of Koch (2014) correlated well with that of Gorman-Lewis *et al.* (2008), who stated that uranium mobility, especially under oxidising conditions, where the pH value is greater than five, tends to be dominated by the complexation of uranyl ions to oxides and hydroxides. The decrease in uranium concentrations could therefore be ascribed to an increase in uranium-mobile chemical species, while the distribution patterns are ascribed to either adsorption or precipitation along the natural flow direction.

6.3.3 Spatial distribution patterns of uranium over the surrounding area of influence

Literature states that the transportation of dissolved uranium from tailings impoundments to the surrounding area of influence is considered to be a major pathway for the contamination of stream water, groundwater and floodplain sediments (Winde *et al.*, 2004). Kabata-Pendias (2011) stated that the distribution of uranium in soils is regulated by the presence of soil organic material and changing pH conditions, as it leads to an increase in uranium adsorption at higher pH values. The statement correlated well with that of Tutu *et al.* (2003) who stated that the chemical speciation of uranium, under weak acidic conditions, may become dominated by the formation of stable complexes, in the presence of organic substances such as humic acids. This, in accordance to Tutu *et al.* (2003) commonly results in the retention and accumulation of uranium in peat deposits. Tutu *et al.* (2003) further stated that in addition to the dissolved phase, the re-mobilisation of labile uranium from soil and floodplain sediments, during physical erosion processes, should also be taken under consideration when addressing environmental contamination.

Winde *et al.* (2004) reported that the mechanisms responsible for the immobilisation of uranium in natural systems included the precipitation of low solubility uranium speciation's in water, the precipitation of salt crusts (as a result of evaporation), co-precipitation with calcium carbonates, as well as within the matrix of Fe and Mn oxihydroxides and lastly pH-dependent adsorption

onto negatively charged surfaces (for example organic matter, clays and iron hydroxides). In addition Winde *et al.* (2004) stated that the extent of diffuse contamination could be ascribed to uranium precipitation processes, rather than adsorption onto floodplain sediments from groundwater, as immobilisation preferably occurs where chemical conditions changes significantly.

With reference to the surrounding area of influence at the New Machavie TSF, the extent of the environmental contamination is not only mentioned in literature (Botha, 2015; Larkin, 2013; Winde and Sandham, 2004 and Aucamp and van Schalkwyk, 2003), but also visually illustrated by means of 3D surface modelling (see Figure 19 and Figure 20). According to Coetzee (1995) airborne gamma-ray spectroscopy analyses of mining areas in the Witwatersrand Basin, identified streams as the preferred pathway for radionuclide transportation, as dissolved uranium, associated with the enriched-leachate from the tailings material, diffusely enters adjacent streams by means of overland flow and other aqueous pathways (Winde and Sandham, 2004). However, in the case of the New Machavie TSF, radionuclide accumulation was in most cases associated with the transported material, scattered over the floodplains of the Kromdraaispruit, rather than the Kromdraaispruit itself. Three distinct spatial distribution patterns were identified over the surrounding area of influence and will now be discussed in more detail.

Identified as the dominant transport mechanism of radionuclide-enriched material over the western portion of the TSF, wind transportation contributed significantly to the distribution of various low level (1.0 – 10.0 ppm) contamination plumes, within the surrounding area of influence (see Figure 19 and Figure 20). Evidenced by the accumulation of fine-grained tailings material on the northern slope of the southern hill, as well as the deposition of fine-grained material in the low lying areas of the 100 meter tailings buffer, distribution patterns could be ascribed to both alternating wind directions, as well as the mass of the uranium-enriched tailings particles. With literature (Pulford, 2010 and Vandenhove *et al.*, 2009) stating that finer-grained particles contain greater adsorption charges, it could be assumed that the uranium associated with the wind-transported particles, would be adsorbed to the negatively charged surface of the particle, while its mass in conjunction with the wind speed, would govern the extent of its transportation. The statement therefore provided an explanation to the deposition of fine-grained material in close proximity to the tailings impoundments, while a dominant wind direction of north to north-east provides an answer to the contamination plumes found in the western portion of the TSF.

Situated in the south-western portion of the TSF, the second distribution pattern was identified as a storm-drainage system, which is governed by preferential flow paths, that follows the naturally descending topography (see Figure 2 and Figure 19). During the wet season, enriched acidic leachate, originating from both Tailings dam No.4 and No.5 migrates diffusely across the

valley floor, where after it precipitates as highly water-soluble sulphate salts, as the result of evaporation (Winde and Sandham, 2004 and Aucamp and van Schalkwyk, 2003). One could also assume that the uranium would tend to co-precipitate within the matrix of Fe and Mn oxihydroxides, which according to literature, not only accumulates in the unsaturated zones of floodplain sediment (Winde and Van der Walt, 2004), but also freely occurs in both the underlying geology (Fe and Mn-rich dolomites of the Oaktree and Monte Christo Formations, Eriksson *et al.*, 2006), as well as the overlying soil formations (as Mn-pedocretes (Koch, 2014)). In addition to the precipitation, it could also be assumed that the uranium might be adsorbed to the negatively charged surfaces of either the organic matter or finer-grained particles, as both mechanisms contributes to the immobilisation of the uranium (Winde *et al.*, 2004). This in turn provides an explanation to the high eU values recorded over the storm-drainage system, as the uranium tend to be immobilised for prolong periods of time, compared to the floodplain sediments of the Kromdraaispruit.

Covering an area of more than 1.2 km², the redistribution of enriched tailings material by means of wind and water erosion (see Figure 36 and Figure 37 in Appendix B), in the direction of the Kromdraaispruit, was identified as the dominant transport mechanism at the New Machavie TSF (Aucamp and van Schalkwyk, 2003). Aided by fluctuations in the groundwater table, as well as changes to the redox-potential of the floodplain sediments, dissolved uranium is frequently removed from the groundwater and immobilised within the floodplain sediments, by means of redox-initiated co-precipitation with insoluble Fe-hydroxides and Mn-oxides (Winde and Van der Walt, 2004). Stated by literature (Winde *et al.*, 2004 and Winde, 2002) and evidenced by lower recorded eU values over the floodplain sediments, the absence of uranium retention, by means of adsorption to the highly adsorptive sediments, were noted. In the case of the floodplain sediments, the absence of uranium retention could be ascribed to the presence of dissolved carbonates within the groundwater, which originated from the underlying dolomites and contributes to the formation of uranyl carbonate complexes (Winde *et al.*, 2004). In addition Winde *et al.* (2004) stated that these uranyl carbonate complexes would prevent the adsorption of uranium to the negatively charged surfaces of the floodplain sediments, as they themselves are either neutrally or negatively charged.

However, evidence of uranium accumulation within the floodplain sediments, were also noted (Winde, 2002). Generally associated with either the formation of sulphate salt crusts on the higher and drier sections of the floodplain, or the accumulation of fine-grained material in the wetter and lower lying areas, these anomalies produced higher eU values, compared to the rest of the floodplain sediments. In the case of the sulphate salt crusts, the higher recorded eU values could be ascribed to the formation of uranyl sulphate complexes, which prevents the uranium cation from binding to the floodplain sediments (Winde, 2002). Unfortunately, their high

solubility also contributes to the re-mobilisation of uranium, as surface-runoff tend to flush the dissolved uranium into adjacent streams (Winde, 2002). In the case of the wetter material, the higher recorded eU values could be ascribed to the precipitation of low solubility uranium speciation's (precipitation by reduction to U^{4+}), depending on the pH-conditions of the water (Winde *et al.*, 2004 and Tutu *et al.*, 2003). The overall decrease in recorded eU values over the floodplain sediments, compared to that of the uranium-enriched toe paddocks, could therefore be ascribed to both dilution by less contaminated groundwater (Tutu *et al.*, 2003), as well as the transformation of dissolved uranium to less mobile solid forms, by means of immobilisation mechanisms.

6.3.4 Spatial distribution patterns of thorium over the New Machavie TSF

According to literature, uranium and thorium tend to behave isochemically during the formation of a geological unit, as both are characterised by similarities in their ionic radii (Koch, 2014 and Abu Deif *et al.*, 2001). However, during crustal processes, for example weathering, U^{4+} is easily oxidised to U^{6+} (Talaat *et al.*, 2012), which is known to be soluble in groundwater, whereas thorium maintain stability under oxidising conditions (Koch, 2014). Despite thorium not being actively pursued as an ore in South African gold tailings (Koch, 2014), it could however be used as a proxy to calculate the original uranium concentration of a rock unit (Aswathanarayana, 1985). With regards to the spatial distribution patterns of thorium, Tutu *et al.* (2009) stated that thorium tend to associate with the tailings material itself, ascribing the distribution to thorium's low solubility and high sorption tendencies. Tutu *et al.* (2009) further stated that in the case of radioactive disequilibria, thorium tend to either precipitate or be adsorbed by Fe and Mn co-precipitates, as both mechanisms contributes to its immobility.

The statement correlated well with that of Vandenhove *et al.* (2009), who stated that organic matter, in addition to the Fe and Mn oxides mentioned earlier, tend to be the main adsorption particulates of thorium, in the natural environment. Although the solubility of thorium is considered to be significantly lower than that of uranium, Alloway (2012) stated that thorium would still be soluble under a wide range of pH conditions, as a direct result of its Th^{4+} valence state. Despite thorium's persistence to resist weathering, both Vandenhove *et al.* (2009), as well as Aswathanarayana (1985) stated that thorium could be mobilised under the extreme conditions, associated with the oxidation zone of gold tailings.

With regards to the spatial distribution of thorium over the New Machavie TSF, evidence of both mobilisation, as well as immobilisation was observed (see Figure 21 and Figure 22). Where the uranium showed signs of being leached from the tailings impoundments, the thorium tend to show signs of stability under oxidising conditions (Koch, 2014). Evidenced by both smaller discrepancies between the measured concentrations, as well as lower peak concentrations, the

stability of thorium as well as its progeny isotope (^{228}Ac) is attributable to its relative immobility, compared to uranium. Tutu *et al.* (2009) reported that in the absence of measurement discrepancies, it could be assumed that the thorium is in radioactive equilibrium with the actinium (^{228}Ac), as thorium is indirectly measured via the ^{228}Ac isotope. However, as in the case of the uranium, thorium might also be decoupled from its progeny isotopes (Tutu *et al.*, 2009), as a direct result of AMD, thereby explaining the signs of mobilisation seen over the 3D surface model (see Figure 21 and Figure 22).

Both the radiometric survey (see Figure 21 and Figure 38 in Appendix B), as well as the data derived from PXRF spectroscopy (see Figure 22 and Figure 39 in Appendix B), indicated a general trend of thorium migrating in a south-easterly direction, following the natural flow path of the TSF. Evidenced by the accumulation of thorium on the southern slopes of the tailings impoundments, while the majority of the top of the tailings showed signs of depletion, it could be assumed that mobilisation of thorium did occur. However, the extent of the migration tends to be limited (Tutu *et al.*, 2009), as thorium concentrations decreased significantly, with an increase in distance from the tailings or transported material. Ascribing the mobilisation of thorium to the extreme conditions encountered over the New Machavie TSF, Koch (2014) stated that the toe paddocks showed the greatest thorium mobility, followed by the coarser-grained Tailings dam No.2. As most of the thorium anomalies were associated with either erosion trenches, or the accumulation of fine-grained material in low lying areas, it could be assumed that thorium favours adsorption to finer-grained particles, while precipitation is reserved to the toe paddocks and transported material. Although low in concentration, signs of thorium accumulation were noted over the southern toe paddocks, while northern toe paddocks showed signs of depletion.

With regards to the surrounding area of influence, thorium once again showed signs of stability, as recorded eTh values only increased with an increase in transported tailings material (Tutu *et al.*, 2009). Despite spatial distribution pattern showing similarities with that of the uranium, a less significant thorium presence was noted in the surrounding area of influence (see Figure 21 and Figure 22). The absence of low level wind-transported contamination plumes in the surrounding area of influence could be ascribed to a decrease in count rates, recorded over the very low concentrations, as it not only increases the error margin of the detector, but also increases variations between the measured and actual concentration (Koch, 2014 and Larkin, 2013). In the case of both the storm drainage system, as well as the Kromdraaispruit floodplain, thorium accumulation could be ascribed to either the deposition of thorium-enriched fine-grained particles along the flow path, or the precipitation of thorium complexes from the enriched acidic-leachate, originating from the tailings impoundments (Vandenhove *et al.*, 2009). Evidenced by the accumulation of thorium over the heavily vegetated southern toe paddock of Tailings dam No.3 (see Figure 38 and Figure 39 in Appendix B), as well as several low lying areas in the

surrounding area of influence, it could be assumed that these low lying areas act as sinks for the deposition of enriched fine-grained material, while organic matter and Fe and Mn oxides adsorption particulates aid in the immobilisation of the thorium (Vandenhove *et al.*, 2009).

Spatial Distribution of Equivalent Thorium

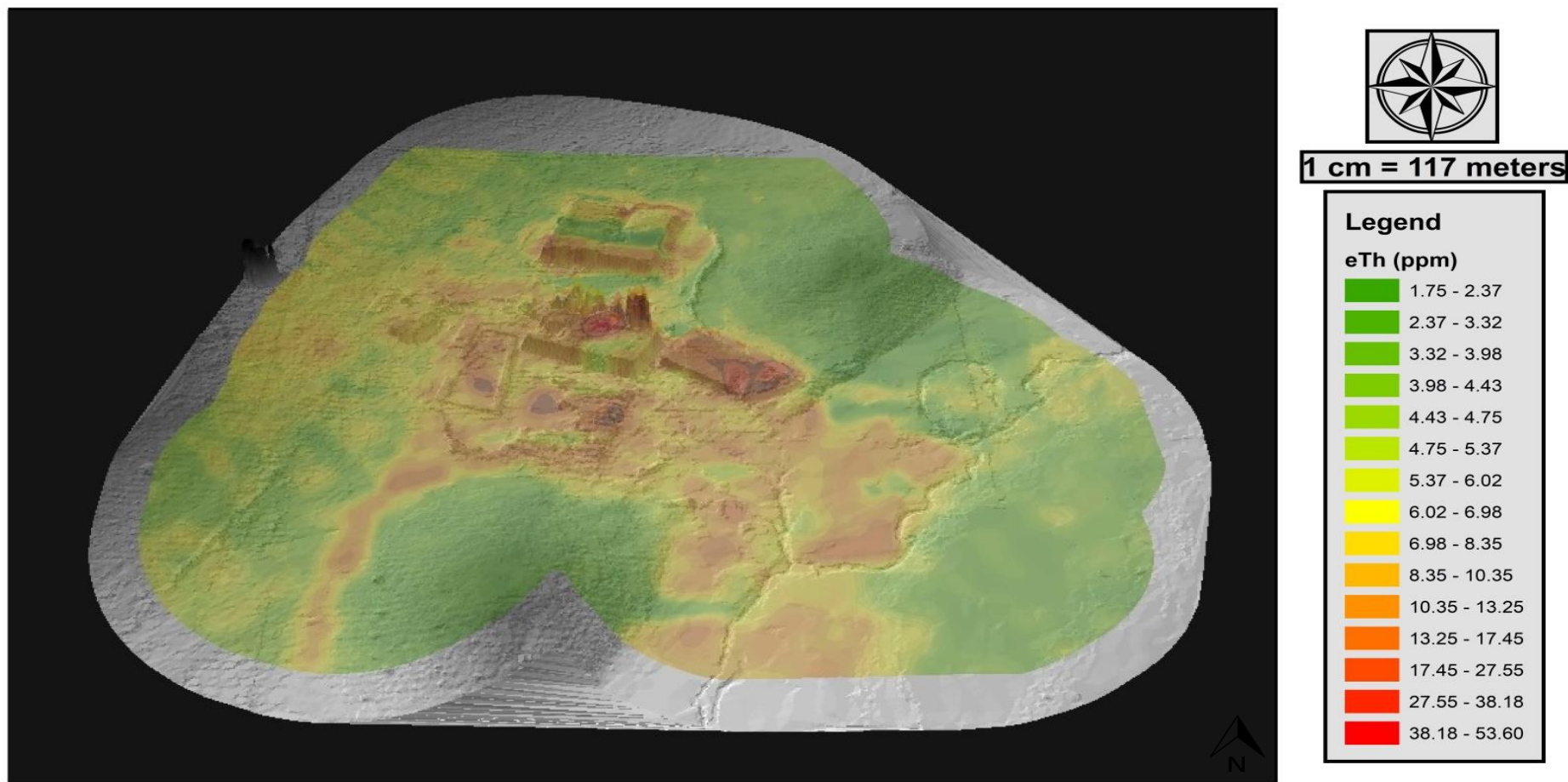


Figure 21: 3D surface model illustrating the spatial distribution of equivalent thorium concentrations, as measured by the natural gamma-ray spectrometer

Spatial Distribution of Measured Thorium

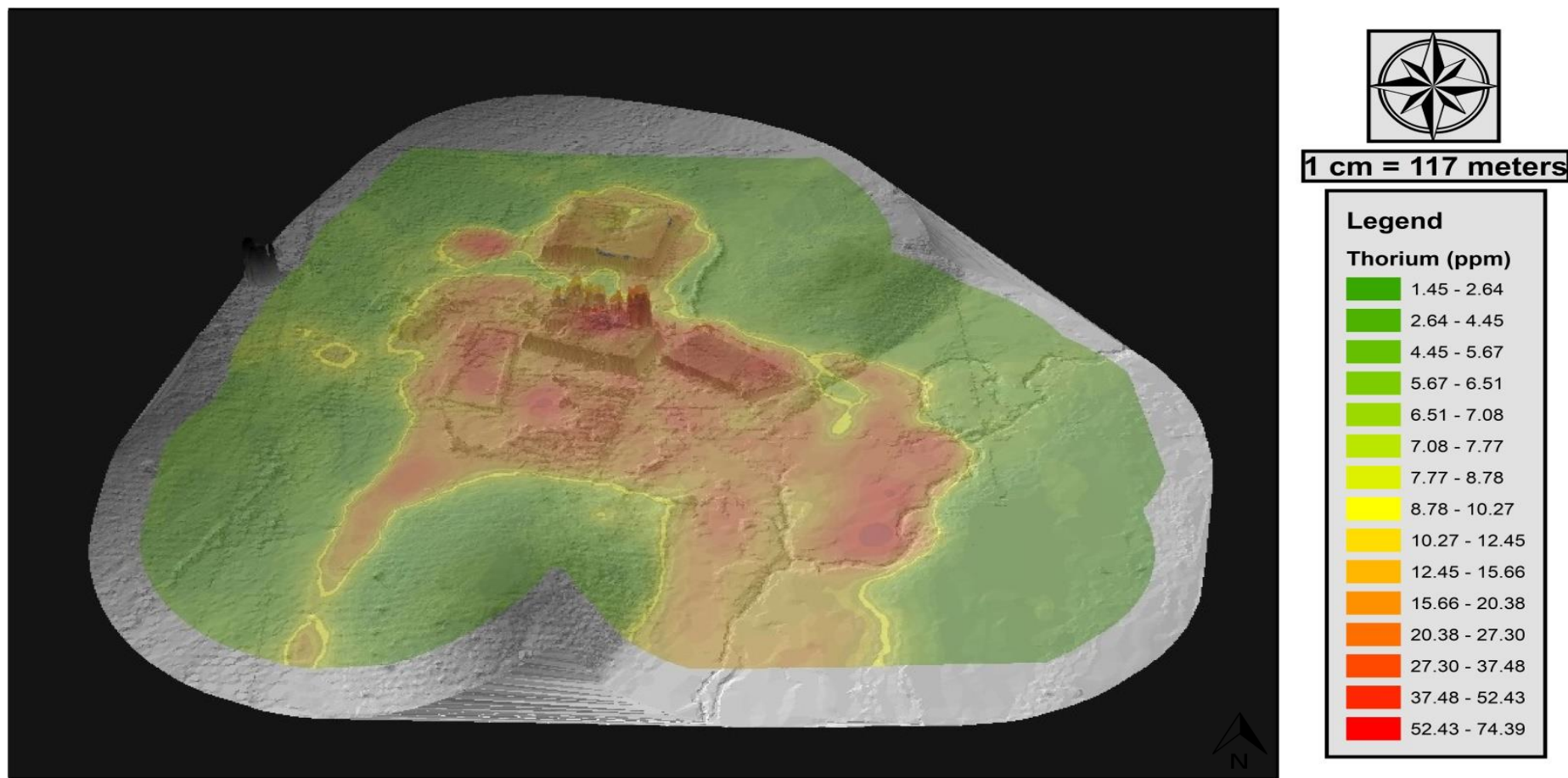


Figure 22: 3D surface model illustrating the spatial distribution of measured thorium concentrations, as derived from the portable-XRF

6.4 Chapter conclusion

Chapter 6 set out to identify the spatial distribution of both uranium and thorium over a typical gold TSF, using alternative methods of data acquisition, in conjunction with a capable geostatistical-interpolator. Despite the disadvantages associated with each technique respectively, the combination of techniques proved to be quite sufficient in the identification of radionuclide distribution patterns, as the approach not only produced results that complemented each other to some extent, but also validated the viability of the approach as an alternative to traditional laboratory based chemical analyses.

With regards to the identification of uranium distribution patterns, both analytical techniques provided evidence of uranium migration and environmental contamination, all while highlighting uranium anomalies in similar locations and recording similar concentrations. Given the anionic and oxidative nature of the tailings impoundments in question, the extent of uranium migration came as no surprise, as the oxidation of pyrite not only decreased the pH, but also produced abundant sulphate anions to complex with uranyl, which in turn increased the transportability of the uranium. Evidence by the general accumulation of uranium along the natural flow path of the TSF, both analytical techniques identified variations in elevation as the dominant mechanism, controlling the distribution of dissolved uranium over the TSF. While the formation of uranyl-sulphate complexes were identified as the dominant mechanism controlling mobilisation and chemical speciation of uranium over the impoundments itself, the toe paddocks and transported material seemed to be dominated by the complexation of uranyl with the oxides and hydroxides present in these particular sections. Ascribed to an increase in uranium-mobile chemical species, both analytical techniques recorded lower uranium concentrations over the toe paddocks and transported material, as distribution seemed to be dominated by the adsorption, precipitation and re-mobilisation of uranium along the various drainage systems present in the surrounding area of influence.

Despite literature emphasising the rarity of radioactive disequilibrium with regards to thorium and its progeny isotopes, results provided evidence of both mobilisation and immobilisation, as thorium tended to decouple from its progeny isotopes, under the extreme conditions associated with the oxidised impoundments. Ascribed to its relative immobility, compared to uranium, thorium in general tended to show signs of stability under oxidising conditions, as recorded thorium concentrations seemed to decrease significantly with an increase in distance from either the tailings impoundments itself, or the transported material. Despite measurements producing smaller discrepancies between the two techniques, decreased count rates, especially over the surrounding area of influence, tended to increase the error margin of the detector, which in turn increased the variation between the equivalent values and the actual concentrations. Overall,

thorium produced similar distribution patterns, when directly compared to uranium, while occupying a less significant presence in the surrounding area of influence. The absence of low level wind-transported contamination plumes could be ascribed to either thorium's persistence to resist weathering or the decreased count rates mentioned earlier. However, results did indicate that low lying areas acted as sinks for the deposition of enriched fine-grained material, while organic matter and Fe and Mn oxide adsorption particulates aided in the immobilisation of the thorium, along the various natural drainage systems present in the surrounding area of influence.

As previously mentioned, one of the subordinates of this chapter's objective, was to identify the best suited analytical technique for quick and cost effective uranium prospecting and environmental assessment purposes. Since neither PXRF spectroscopy nor natural gamma-ray spectrometry have been used in conjunction with Ordinary Prediction-based Kriging, for either uranium prospecting or environmental assessment purposes, over tailings impoundments, the project aimed to validate the viability of the approach, as an alternative to traditional geochemical sampling and laboratory analyses. Based solely on each respective technique's ability to identify radionuclide anomalies *in situ* and in the field, for uranium prospecting purposes, natural gamma-ray spectrometry was identified as the best suited analytical technique for the job at hand.

Despite PXRF spectroscopy punching well above its weight, the spatial resolution of the acquired data, especially after being geostatistically-interpolated, could not compete with what was generated using natural gamma-ray spectrometry. With literature stating that uranium migration has the potential to greatly affect resource estimations (Koch, 2014), it is of the utmost importance that the modelled uranium concentrations are accurate and derived from the highest resolution possible, as the data could be used to assist in the design of a grid-based drilling scheme, for re-mining purposes. Unfortunately, the quantification of natural gamma radiation, especially in the presence of radioactive disequilibrium, is only accurate when performed in conjunction with an alternative method, capable of measuring uranium directly (Koch, 2014). This data could then be used to account for radioactive disequilibrium, thereby ensuring the accuracy of the radiometric derived data, albeit by increasing the total cost to company in the process.

For environmental assessment purposes on the other hand, PXRF spectroscopy makes more sense, as it provides the user with a versatile, accurate and rapid assessment tool, capable of assessing a much wider range of parameters, *in situ* and in the field. Despite the spatial resolution trailing behind that of natural gamma-ray spectrometry, the combination of PXRF spectroscopy, working in conjunction with Ordinary Prediction-based Kriging, provided a suitable alternative for the identification of radionuclide anomalies, as well as its distribution

patterns. As an alternative approach, although it did not form part of this particular project, by combining PXRF spectroscopy analyses with both Ordinary Prediction-based Kriging (used to determine element concentration levels at unsampled locations), as well as non-parametric Indicator Kriging (used to estimate the probability of data exceeding a certain threshold level), the user is provided with an approach capable of rapid soil pollution hotspot mapping (Chakraborty *et al.*, 2017).

CHAPTER 7: URANIUM MIGRATION AND ANOMALY VERIFICATION

7.1 Introduction

Based on the persistence of thorium to mobilise under oxidising conditions (Aswathanarayana, 1985), the Uranium Migration Index provides the ideal tool to quantify the migration of uranium from one region to another (Assran *et al.*, 2012). With regards to the Uranium Migration Index, thorium is used as a reference concentration, in order to calculate the original uranium concentration, prior to the formation of an oxidising environment (Koch, 2014). As a result the Uranium Migration Index not only assists in modelling the migration of uranium, but could also be used for resource planning purposes, during exploration, or in this case the re-mining of a TSF (Koch, 2014).

Since no uranium mining was conducted at the New Machavie TSF in the past, the assumption could be made that the eU/eTh ratio should be constant in the tailings material, as the tailings were derived from the same rock type as the originally enriched rock unit. This assumption is supported by both Asfahani *et al.* (2007), as well as Aswathanarayana (1985), as both authors stated that the eU/eTh ratio is considered to be constant in rocks of the same type. Although the assumption seems to be valid, similar studies have mentioned that mobilisation of thorium does however occur and that by using the eU/eTh ratio, thorium mobilisation will tend to increase the error margin of the modelled uranium mobilisation within the oxidation zone (Koch, 2014). In contradiction to the statement made by Koch (2014), both Asfahani *et al.* (2007), as well as Abu-Deif *et al.* (2001) stated that due to the long half-lives of both uranium and thorium, it could be assumed that the current eU/eTh ratio represents a similar ratio to that of the original eU/eTh ratio, as long as the oxidation of uranium has not occurred. In the case of the New Machavie TSF however, the statement made by Koch (2014) might hold some merit, as the highly oxidised environment not only oxidised the uranium, but also mobilised both the uranium, as well as the thorium present within the tailings material. Despite the presence of radioactive disequilibrium, the Uranium Migration Index should still prove useful in identifying the migration potential of uranium, irrespective of the cause of mobilisation.

According to literature (Assran *et al.*, 2012; Talaat *et al.*, 2012; Asfahani *et al.*, 2007 and Abu-Deif *et al.*, 2001), the Uranium Migration Index is calculated using three simple equations (see Equation 8, Equation 9 and Equation 10). In order to calculate the rate of uranium migration, one must first calculate the original uranium concentration (U_o), using the eU/eTh ratio of the geological unit under investigation. With reference to Equation 8, U_o represents the original uranium concentration of the rock unit, while eTh represents the average thorium content (in ppm) of a certain geological unit. *Unit (eU/eTh)* on the other hand represents the average

eU/eTh ratio of the geological unit under investigation. As mentioned in Chapter 4, the average *Unit (eU/eTh)* ratio had to be calculated in the absence of the original *Unit (eU/eTh)* ratio of the Black Reef Formation. Calculated as 2.284:1 and 0.899:1 for the tailings material and surrounding soils respectively, the original *Unit (eU/eTh)* ratio of the Black Reef Formation was first calculated, before it was incorporated into Equation 8.

Using Equation 9, the uranium migration value (U_m) of both the samples derived from the tailings material, as well as the soils from the surrounding area of influence, was calculated. The final step consisted of calculating the uranium migration rate ($U_{m\%}$) of each sample, by incorporating the uranium migration value, attained from Equation 9, into that of Equation 10. The end result is a single dataset containing positive and negative uranium migration percentages, indicating either a migration into or out of a specific region. According to literature (Assran *et al.*, 2012; Talaat *et al.*, 2012; Asfahani *et al.*, 2007 and Abu-Deif *et al.*, 2001), positive $U_{m\%}$ values tend to indicate the movement of uranium into a region, while negative $U_{m\%}$ values on the other hand tend to show the movement of uranium away from a specific region. Abu-Deif *et al.* (2001) further stated that an U_m value larger than two ($U_m \text{ value} > 2$), represented a loss in uranium, during the later evolution of a geological body, while an U_m value smaller than minus two ($U_m \text{ value} < -2$) indicated that a considerable amount of uranium has migrated into a specific rock unit. Values falling in-between two and minus two ($-2 < U_m \text{ value} < 2$) on the other hand, points to a high probability that the migration is equivalent in and out of a specific rock unit (Abu-Deif *et al.*, 2001).

Aiding in the identification of uranium anomalies, both Assran *et al.* (2012), as well as the IAEA (1996) stated that the ratios of the observed radio-elements, serve as a much better indicator of preferential accumulation, compared to that of absolute concentrations. This according to Boyle (1982), could be ascribed to absolute concentrations being highly variable and dependent on a number of factors (outcrops, topography, distance between exposures and survey lines), while ratios of the observed radio-elements seems to be much less affected by the above mentioned factors. Because uranium and thorium usually accompanies each other during the formation of a geological unit, the eU/eTh ratio is considered an important geochemical index, not only for the migration of uranium, but also for the economic potential of the unit in question (Assran *et al.*, 2012). Correlating well with the statement of Saunders and Potts (1976), both authors stated that the most promising uranium anomalies have high eU abundances, while coinciding with high eU/eTh and eU/K_% ratios.

7.2 Chapter objectives and motivation

The main objective of this particular section is to quantify the extent of the uranium migration, while also verifying the uranium anomalies, using geochemical indices, generally reserved for uranium exploration within a geological unit. With only a few tailings related projects mentioning use of these geochemical indices, the chapter aims to validate the viability of the approach. As a subordinate of the current objective, the radioactivity of the New Machavie TSF will be assessed, using both RER and ERDR equations, as the lack of radioactivity measurements have been identified as a deficiency in literature by Tutu *et al.* (2009).

7.3 Results and discussion

7.3.1 Uranium Migration Index

Despite the discrepancy with regards to how radioactive disequilibrium would influence the results derived from the Uranium Migration Index, the geochemical index proved to be quite sufficient in the identification of not only accumulation hotspots, but also preferential flow paths leading to the anomalies. Evidenced by a correlation coefficient of 0.739 between the equivalent uranium (eU) and uranium migration value (U_m), a good correlation was found to exist between the uranium anomalies identified by means of the Uranium Migration Index and that identified using natural gamma-ray spectrometry (see Figure 19 and Table 12). By combining these datasets to create geostatistically-interpolated images (Assran *et al.*, 2012), various points of interest, initially not noticeable, were later not only revealed, but also provided explanations to some of the identified spatial distribution patterns, previously mentioned in Chapter 6.

Under first observation of Figure 23 (also Figure 41 in Appendix C), which represents the calculated original uranium concentration (in ppm) of the tailings material, uranium distribution seemed to be confined to the impoundments itself, while indicating limited migration to the surrounding area of influence. That phenomenon became even more apparent when directly compared to the radiometric survey data (see Figure 19), as most impoundments, except Tailings dam No.1, showed signs of moderately-severe enrichment over the top portions of the impoundments, while Figure 19 indicated accumulation over the side slopes and toe paddocks. Figure 23 also differs from Figure 19 in terms of uranium migration, as Figure 23 indicated the accumulation of uranium in close proximity to the impoundments, while the radiometric survey identified the severe enrichment of the Kromdraaispruit floodplain and soils surrounding the TSF. It should be noted that the contradiction between the two datasets was to be expected, as the U_0 dataset represents uranium concentrations prior to the formation of the oxidising environment seen today, while the radiometric data represents the uranium content and distribution patterns of the present.

As previously mentioned, a good correlation was found to exist between the uranium migration value (U_m) and the equivalent uranium concentrations, courtesy of the radiometric survey. Evidenced by near identical distribution patterns (when compared to Chapter 6), the Uranium Migration Index performed exactly as expected, by not only identifying uranium anomalies, but also the preferential flow paths leading towards the anomalies itself (see Figure 24 and Figure 42 in Appendix C). Where Figure 23 indicated a moderately-severe enrichment over the top portions of most impoundments, Figure 24 indicated the migration away from the top portions, in a similar manner to what was indicated in both literature (Koch, 2014) and Chapter 6, as uranium was found to accumulate on both the side slopes, as well as the southern toe paddocks.

Interestingly, Figure 24 indicated migration patterns away from both Tailings dam No.2 and No.3, as well as the eastern slope of Tailings dam No.5. In the case of both Tailings dam No.2 and No.5; Figure 24 indicated the migration away from the slopes, in the direction of Tailings dam No.4, before accumulating in their respective southern toe paddocks, leaving the slopes relatively depleted of uranium. Tailings dam No.3 on the other hand indicated the migration of uranium, away from the impoundment, before accumulating in the northern margin of the Kromdraaispruit floodplain. Finally, where Figure 23 indicated uranium accumulation in close proximity to the impoundments (with regards to the surrounding area of influence), Figure 24 revealed the remobilisation of uranium in both the storm drainage system and Kromdraaispruit floodplain, before accumulating further down each respective system.

With reference to Figure 25 (also Figure 43 in Appendix C), which represents uranium migration patterns over the New Machavie TSF, $U_{m\%}$ values were divided into two main classes, namely the Migration In- and Migration Out class respectively (Assran *et al.*, 2012; Talaat *et al.*, 2012 and Abu-Deif *et al.*, 2001). Represented by shades of the colour orange and red, the Migration In class consisted of positive $U_{m\%}$ values, ranging from 0 to 100% and was in most cases associated with either the tailings material or transported material, distributed over the surrounding area of influence. The Migration Out class on the other hand, represented by shades of the colour yellow and green, consisted of negative $U_{m\%}$ values, ranging from -1 to -500% and was found to occupy the majority of the surrounding area of influence, top sections of the tailings impoundments and elevated sections of the toe paddocks.

Without being formally recognised as a class, but rather as a subdivision of both classes mentioned above, the “No Migration” class, represented by $U_{m\%}$ values ranging between -25 and 20%, resembles areas where neither mobilisation nor accumulation has yet occurred (Abu-Deif *et al.*, 2001). Although in the minority, these values according to Koch (2014) represent signatures similar to that of the original eU/eTh ratio, before an oxidizing environment was established. In the case of the New Machavie TSF however, it could be assumed that these

values indicate areas less susceptible to mobilisation, rather than identifying no mobilisation, as most of the surface material has already been extensively oxidised.

In Chapter 6, uranium anomalies were in most cases found to be associated with either erosion trenches, low lying areas or the accumulation of dissolved uranium on the southern side slopes of the tailings impoundments (see Figure 19 and Figure 20). Literature on the other hand stated that uranium anomalies in tailings dams, were expected to be found to the centre of the tailings impoundment, as finer-grained particles, carrying greater adsorption charges tend to accumulate to the centre of the impoundment (Pulford, 2010 and Vandenhove *et al.*, 2009). Evidenced by a correlation coefficient of 0.739 (see Table 12), migration patterns, derived from the Uranium Migration Index tend to agree with the spatial distribution patterns identified in Chapter 6, as uranium was once again found to accumulate on the southern side slopes, while transportation followed the natural flow direction of the TSF. As a result a general trend was noted where dissolved uranium migrated away from the top of the tailings impoundments, leaving elevated sections depleted, before accumulating elsewhere, depending on the geochemical conditions. These results correlated well with that of Koch (2014) who stated that while in the process of being leached, uranium was found to be mobilised away from the oxidised top area of the impoundment, while accumulation occurred in the saturated zone, under a reducing environment (Koch, 2014).

With reference to the migration patterns seen over the tailings material, the Uranium Migration Index emphasized the migration out of the tailings impoundments, before migrating into lower lying areas, for example the toe paddocks, following the natural flow direction of that particular section. Evidenced by the migration patterns seen over Tailings dam No.1 and No.2, the uranium migration rate ($U_{m\%}$) showed an overall increase with a decrease in elevation, as higher $U_{m\%}$ values were recorded over the toe paddocks, instead of the eU anomalies identified in Chapter 6. Tailings dam No.3 on the other hand once again retained the uranium, as the majority of the impoundment recorded negative $U_{m\%}$ values. Figure 25 did however indicate that Tailings dam No.3 contributed significantly to the contamination of the northern margin of the floodplain, as high $U_{m\%}$ values were recorded over the south-eastern section of the impoundment and adjacent floodplain sediments.

Although migration patterns into the north-western toe paddock were noted, identified pathways, leading to the toe paddock revealed Tailings dam No.1 and No.2 to be the source of the migrating uranium, rather than Tailings dam No.3 (see Figure 25). Ascribed to either the formation of enriched-crusts or the precipitation of uranium-complexes, along the natural flow path, the sporadic nature of the migration into the north-eastern toe paddock, supported the assumption that the “No Migration” class represents areas less susceptible to mobilisation, rather than identifying no mobilisation. Migration to this particular toe paddock only occurs

during heavy rains, when the north-western toe paddock overflows and enriched-leachate is funnelled along the north-eastern toe paddock. As a result, the salt-crusts and precipitated uranium-complexes are only mobilised during the raining season, thereby making them less susceptible to migration throughout the year.

Having no toe paddocks of its own, uranium migration over Tailings dam No.4 was found to migrate either along the storm-drainage system, previously identified in Chapter 6, or by following the natural flow path, in the direction of the Kromdraaispruit floodplain. Evidenced by negative $U_{m\%}$ values recorded over elevated sections of the floodplain, uranium was found to migrate into low-lying areas of both the storm-drainage system and Kromdraaispruit floodplain, generally accumulating in close proximity to its source (see Figure 25). Similar to what was seen over Tailings dam No.4; migration patterns over Tailings dam No.5 were also found to divide.

Being ascribed to variations in elevation, in both cases, enriched-leachate was found to be funnelled away from the impoundment, before accumulating elsewhere along the flow path. In both cases, the migration patterns seem to support the assumption that precipitation is considered to be the dominant immobilisation mechanism of uranium (Winde and Van der Walt, 2004), as uranium is easily re-mobilised (Tutu *et al.*, 2003), despite being immobilised for prolonged periods of time. In addition, migration patterns seemed to be fairly localised, as recorded $U_{m\%}$ values were found to form concentric shapes around migration anomalies, clearly indicating the inward migration of uranium, generally in the direction of the lowest-lying sections (see Figure 25).

In Chapter 6, low level (1.0 – 10.0 ppm) contamination plumes, distributed over the New Machavie TSF, were ascribed to aeolian material being deposited in close proximity to the various tailings impoundments. Although uranium migration was ascribed to uranium being adsorbed to the finely-grained aeolian material, an assumption was made that the mass of these enriched-particles, in conjunction with fluctuating wind-directions, governed the distribution of these aeolian particles. The Uranium Migration Index however, revealed various migration anomalies in similar locations to that of the low level contamination plumes, mentioned in Chapter 6 (see Figure 19 and Figure 25).

Since no migration pathways were identified contributing to the migration, the accumulation of enriched-particles behind the vegetated-berm surrounding most of Tailings dam No.1, were ascribed to the deposition of aeolian material. Further evidence of aeolian deposition was identified to the east of the previously mentioned anomalies, as well as on the northern slope of the southern hill. Previously solely ascribed to enriched leachate originating from one of the erosion trenches, the Uranium Migration Index revealed the accumulation of fine-grained aeolian material behind Tailings dam No.3. Under closer inspection, recorded $U_{m\%}$ values

tended to support the aeolian material theory, as the spatial signature resembled that of the other low level contamination plumes identified in Chapter 6. Based on the results, as well as site investigations, it could be assumed that the anomalies identified behind Tailings dam No.3, were created by a combination of accumulating leachate, in conjunction with the deposition of fine-grained material at the foot of the impoundment itself. Since Figure 25 provided evidence of uranium migrating along a preferential pathway, which originates from the erosion trench, the proposed explanation seemed to be the most logical.

Spatial Distribution of Uranium Migration (Uo)

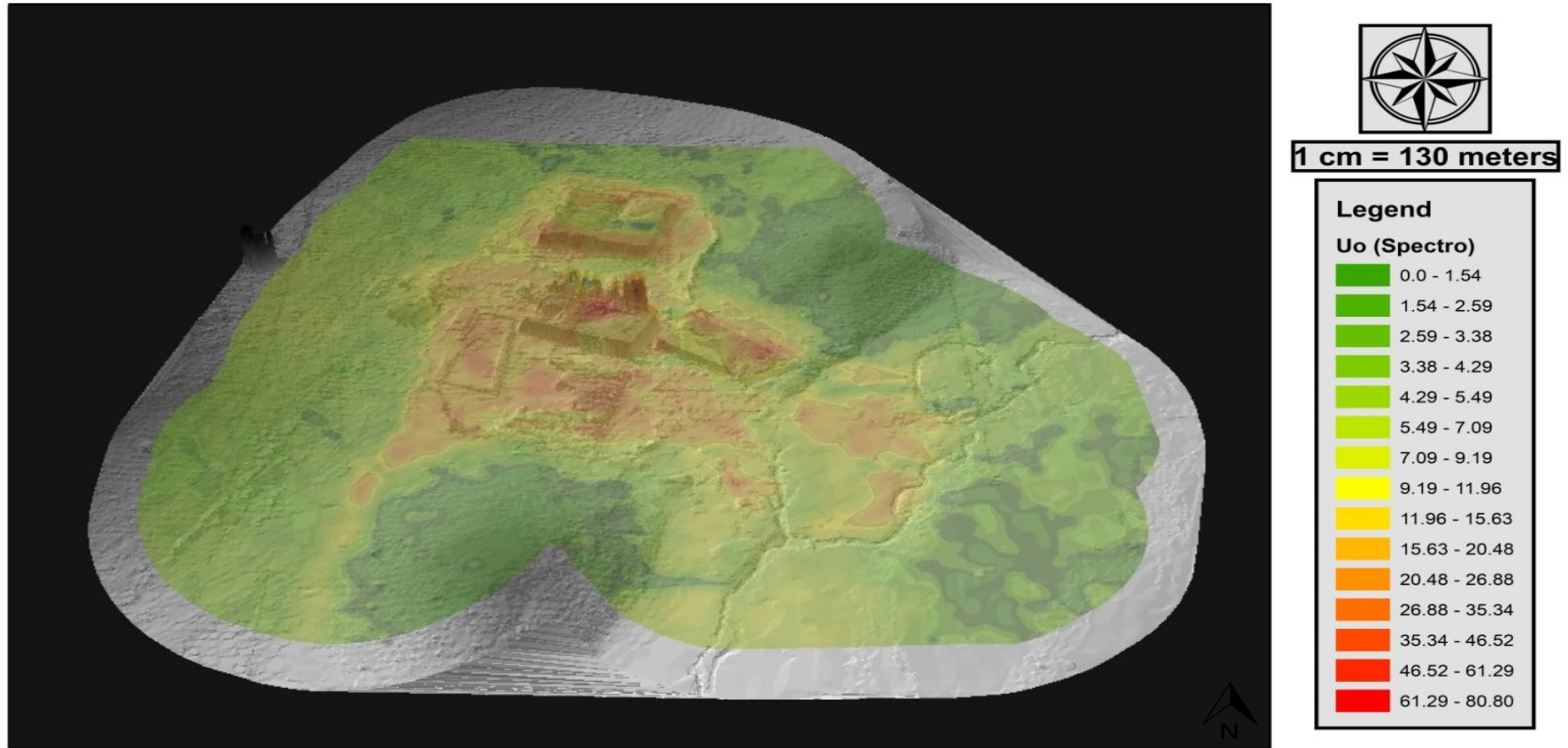


Figure 23: 3D surface model illustrating the spatial distribution of calculated “original” uranium concentrations, prior to the formation of the oxidising environment seen today

Spatial Distribution of Uranium Migration (Um)

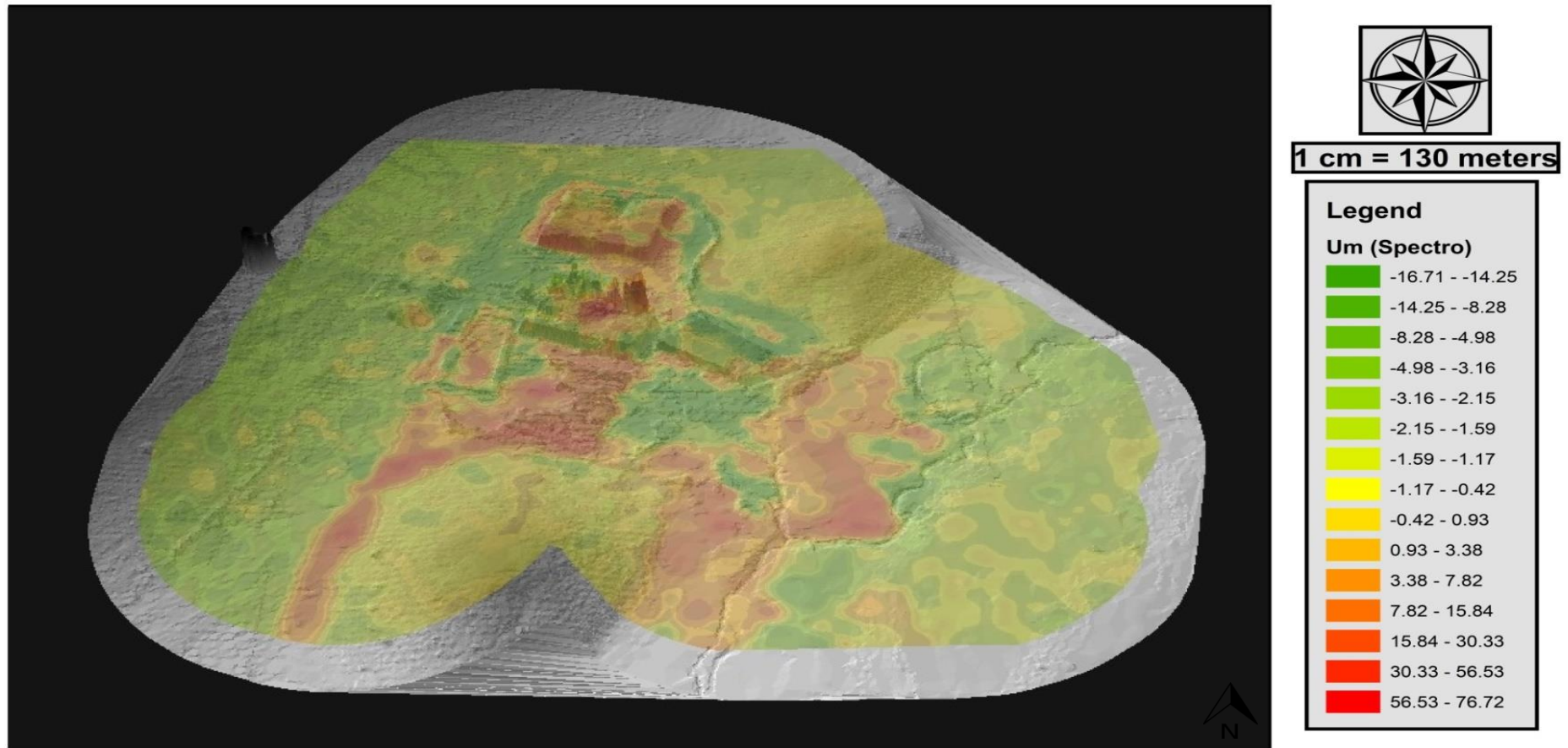


Figure 24: 3D surface model of quantified uranium migration values, illustrating the migration of uranium away from the impoundments, following the natural flow direction of the TSF

Spatial Distribution of Uranium Migration (Um%)

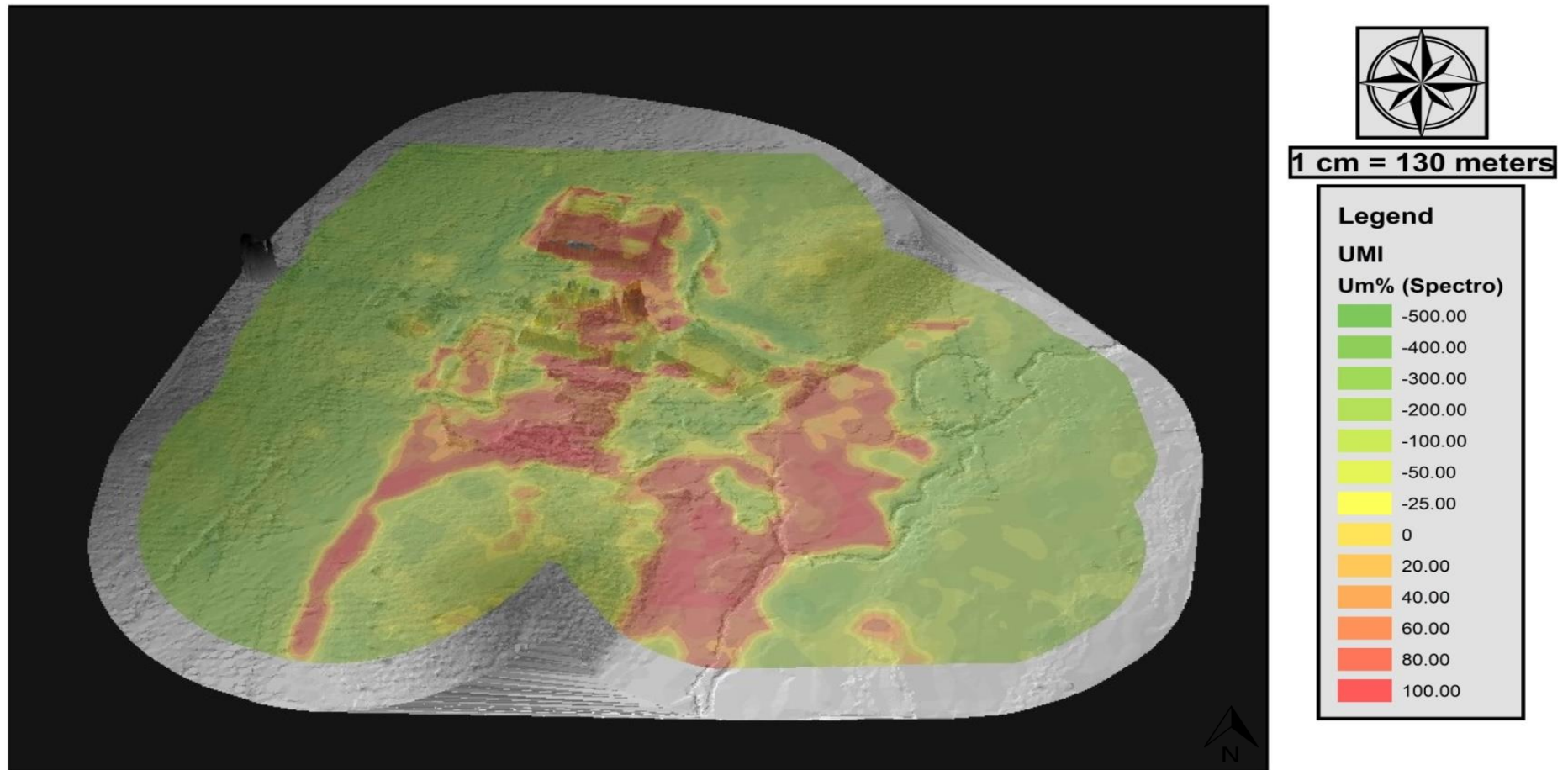


Figure 25: 3D surface model illustrating the rate of uranium migration, either into (+ values) or away from (- values) a specific location

7.3.2 Radionuclide Ratio Maps

Considered to be a powerful geological mapping tool, natural gamma-ray spectrometry allows for the determination of individual concentrations of the three natural occurring radio-elements, present within the surface of the earth (Abu Deif *et al.*, 2001). At the surface, the distribution of these radio-elements are controlled by the composition of the bedrock itself, while geological processes (the most dominant being weathering, erosion and transportation), contributes to the modification of these distribution patterns (Abu Deif *et al.*, 2001). With absolute concentrations being highly variable and dependent on a number of factors, several authors recommend the use of radio-element ratios, as they reduce the effect of terrain geometry on the estimated concentrations (Assran *et al.*, 2012; Abu Deif *et al.*, 2001; IAEA, 1996 and IAEA, 1979).

Although anomalies can be identified using any of the seven radiometric survey signals (Total count, eU, eTh, K%, eU/eTh, eU/K% and eTh/K%), the inspection of eU/eTh, eU/K% profiles are considered to be the most effective in detecting preferential uranium-enrichment (IAEA, 1979). According to Abu Deif *et al.* (2001), an eTh/K% ratio larger or equal to two ($eTh/K\% > 2$), indicates an enrichment in thorium, while an eTh/K% ratio smaller or equal to one ($eTh/K\% < 1$), indicates an enrichment in potassium. With regards to uranium, both an eU/eTh ratio, as well as an eU/K% ratio larger or equal to one ($eU/eTh > 1$ and $eU/K\% > 1$), indicates an enrichment in uranium (IAEA, 2003 and Abu Deif *et al.*, 2001). These uranium-enriched anomalies as stated by the IAEA (1988), offer good prospects for uranium exploration, as they contain relatively high concentrations of uranium, with respect to both thorium and potassium, which are important diagnostic factors, in the recognition of possible uranium deposits.

With reference to Figure 26 and Figure 27 (also Figure 44 and Figure 45 in Appendix C), which represents uranium anomalies, identified by means of Equation 11 and Equation 12 respectively, both ratios provided evidence of uranium-enrichment and migration, upon first observation. Although the enrichment of the tailings material came as no surprise, the manner in which the data correlated with both the radiometric survey, as well as the Uranium Migration Index, however did (see Table 12). Despite uranium generally being accompanied by its progeny isotopes, distribution patterns previously indicated that the mobilisation and transportation of uranium resulted in the decoupling of uranium from its progeny isotopes. Evidenced by both literature (Tutu *et al.*, 2009 and IAEA, 1979) and high eU/eTh values, results once again indicated the accumulation of uranium in both the southern toe paddocks, as well as the floodplain sediments, in some cases without being accompanied by thorium.

In the case of Figure 26, eU/eTh values were divided into two main classes, namely the Thorium-enriched and Uranium-enriched class respectively. Represented by shades of the colour green, the Thorium-enriched class consisted of eU/eTh values, ranging from 0 to 0.99

and was in most cases associated with the surrounding area of influence. Figure 26 did however identify Tailings dam No. 3 as being enriched with Thorium. The enrichment could be ascribed to thorium being retained in a similar manner to uranium, as both elements tend to behave isochemically and are characterised by similarities in their ionic radii (Koch, 2014 and Abu Deif *et al.*, 2001). Another possible explanation for the enrichment came in the form of uranium migration, as Figure 26 also indicated enrichment in uranium over the south-eastern portion of the impoundment. The migration of the uranium also seemed to state the decoupling assumption, as uranium is known to be the more mobile species, compared to its progeny isotopes.

The uranium-enriched class on the other hand, represented by shades of yellow, orange and red respectively (depending on the amount of enrichment), consisted of eU/eTh values, ranging from 1.0 to 20.0, while occupying most of the tailings- and transported material. Although literature stated that eU/eTh values > 1 identified uranium-enriched areas (IAEA, 2003 and Abu Deif *et al.*, 2001), results indicated that uranium was accompanied by thorium in areas represented by shades of the colour yellow ($2 > \text{eU/eTh} > 1$), as thorium was previously found to occupy a significant presence over the transported material (see Figure 21). Evidenced by both an average eU/eTh value of 1.96, as well as the spatial distribution patterns of thorium over the New Machavie TSF, an assumption was made that lower eU/eTh values indicated areas where uranium co-occurred with thorium, while an increase in eU/eTh values indicated an increase in both segregation and mobilisation of uranium. Providing further evidence, an above average correlation of 0.570 (see Table 12), was found to exist between the anomalies identified by means of the eU/eTh Ratio Map and that of the Uranium Migration Index. Both geochemical indices identified their respective anomalies in similar locations, thereby stating the assumption mentioned above.

With regards to Figure 27, the eU/K_% Ratio Map was found to have a remarkable resemblance to that of Figure 19. Evidenced by a correlation coefficient of 0.715 between the recorded eU content and eU/K_% values (see Table 12), both survey signals indicated enrichment in uranium (average eU/K_% value of 14.24), with respect to potassium. Equivalent eU/K_% values, were once again divided into two main classes, namely the Potassium-enriched and Uranium-enriched class respectively. Although in the minority, the Potassium-enriched class, represented by eU/K_% values < 1.0 , were in most cases associated with the vegetated surrounding area of influence. Figure 27 did however identify several zones over Tailings dam No.4, where both uranium and potassium were found to accumulate in a linear fashion, while recording intermediate eU/K_% values. These zones of linear accumulation were also noted over both Figure 26 and Figure 40 respectively. A possible explanation to the phenomenon came from Figure 4, which highlighted erosion trenches in similar positions to the zones of linear

accumulation. The phenomenon was therefore ascribed to the accumulation of radionuclides within these trenches, but would require further investigation for a detailed explanation. The uranium-enriched class on the other hand, represented by eU/K_% values between 1 and 60, was found to occupy most of the tailings- and transported material, while confirming most of the uranium anomalies, identified by the other survey signals.

Spatial Distribution of eU/eTh Ratio's

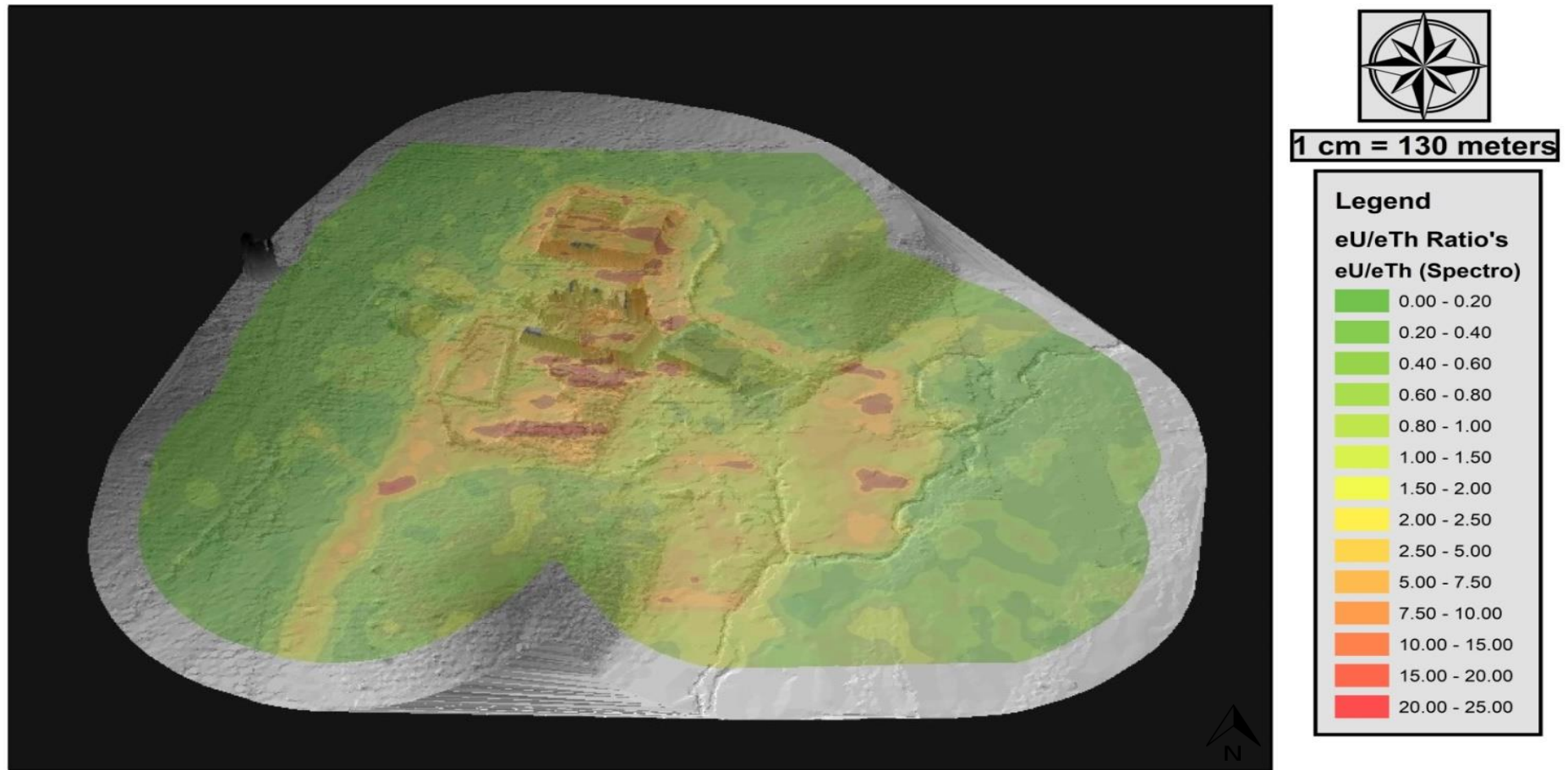


Figure 26: 3D surface model illustrating eU/eTh ratios: Verifying uranium anomalies relative to thorium concentrations

Spatial Distribution of eU/K% Ratio's

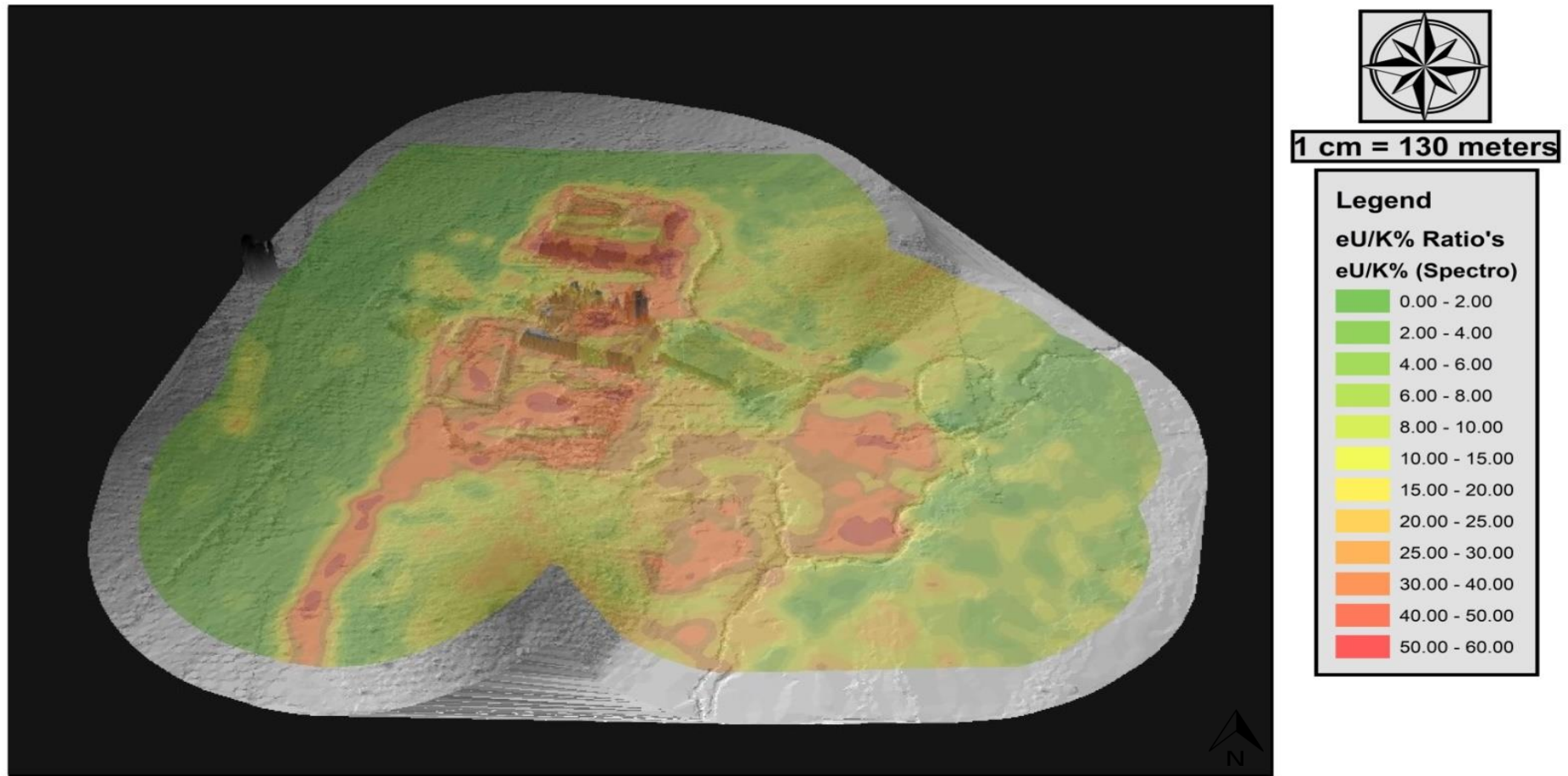


Figure 27: 3D surface model illustrating eU/K% ratios: Verifying uranium anomalies relative to potassium concentrations

7.3.3 Radiation Exposure Rate (RER) and Equivalent Radiation Dose Rate (ERDR)

While a number of studies have been carried out, with regards to uranium pollution and environmental contamination, only a few of them contained measurements of radioactivity (Larkin, 2013 and Tutu *et al.*, 2009). Knowledge regarding the environmental background levels of naturally occurring radiation, its nature and variability, is of paramount importance, as its not only essential to the evaluation of human exposure, but also in the detection of possible changes in radioactivity, brought about by human activity (Larkin, 2013 and IAEA, 2003). These “*human activities*” generally implies the accumulation or relocation of naturally occurring radioactive material, which according to the IAEA (2003), could easily be accessed by means of ground or airborne radiometric surveys.

In South Africa the management of radiation and radionuclides, are strictly enforced by the National Nuclear Regulator and backed up by a number of legislations, including, but not limited to the Mine Health and Safety Act, no 29 of 1996 and the National Health Amendment Act, no. 12 of 2013 (Koch, 2014). In accordance with the IAEA (1979), the average natural background radiation humans are exposed to on a daily basis (through the air we breathe and the food we consume), is considered to be 1 milli Sievert per annum (mSv/a). Literature further states that it has been recommended that no human should receive more than 50 mSv/a, from all natural and artificial sources of radiation (Assran *et al.*, 2012 and IAEA, 1979). A dose limit of 50 mSv/a is also regarded as the maximum dose limit for radiation exposure to the skin of the general public, as well as radiation workers (IAEA, 2007), although a recommendation has been made, to lower the maximum dose rate, to a value not exceeding 1.0 mSv/a (IAEA, 2000 (cited by Assran *et al.*, 2012)).

Literature states that both the RER and ERDR could easily be calculated from the apparent K (%), eU (ppm) and eTh (ppm) concentrations (see Equation 14 and Equation 15), in this case derived from the ground radiometric survey concentrations (Assran *et al.*, 2012 and IAEA, 1991). With reference to both Figure 28 and Figure 29 (also Figure 47 and Figure 48 in Appendix C), which represents the Radiation Exposure Rate and Equivalent Radiation Dose Rate respectively, most parts of the study area remained on the safe side (average ERDR of 0.967 mSv/a), recording ERDR values well below the maximum permissible radiation dose rate of 50 mSv/a.

The results correlated well with that of Koch (2014), who stated that exposure to gamma radiation over Tailings dam No.1, was only slightly higher than the natural daily exposure limit, despite having an average surface eU concentration of 55 ppm or 1.8 mSv/a. Although well below the recommended exposure limit, the majority of the tailings material, especially the transported material, recorded ERDR values ranging from as low as 1.0 mSv/a to a maximum of

9.13 mSv/a. These anomalies correlated well with those identified by the ground radiometric survey and Uranium Migration Index respectively (correlation coefficient of 0.995 and 0.694 respectively, see Table 12), as ERDR values tend to increase with a decrease in elevation, once again following the natural south-easterly flow direction of the New Machavie TSF.

Radiation Exposure Rate

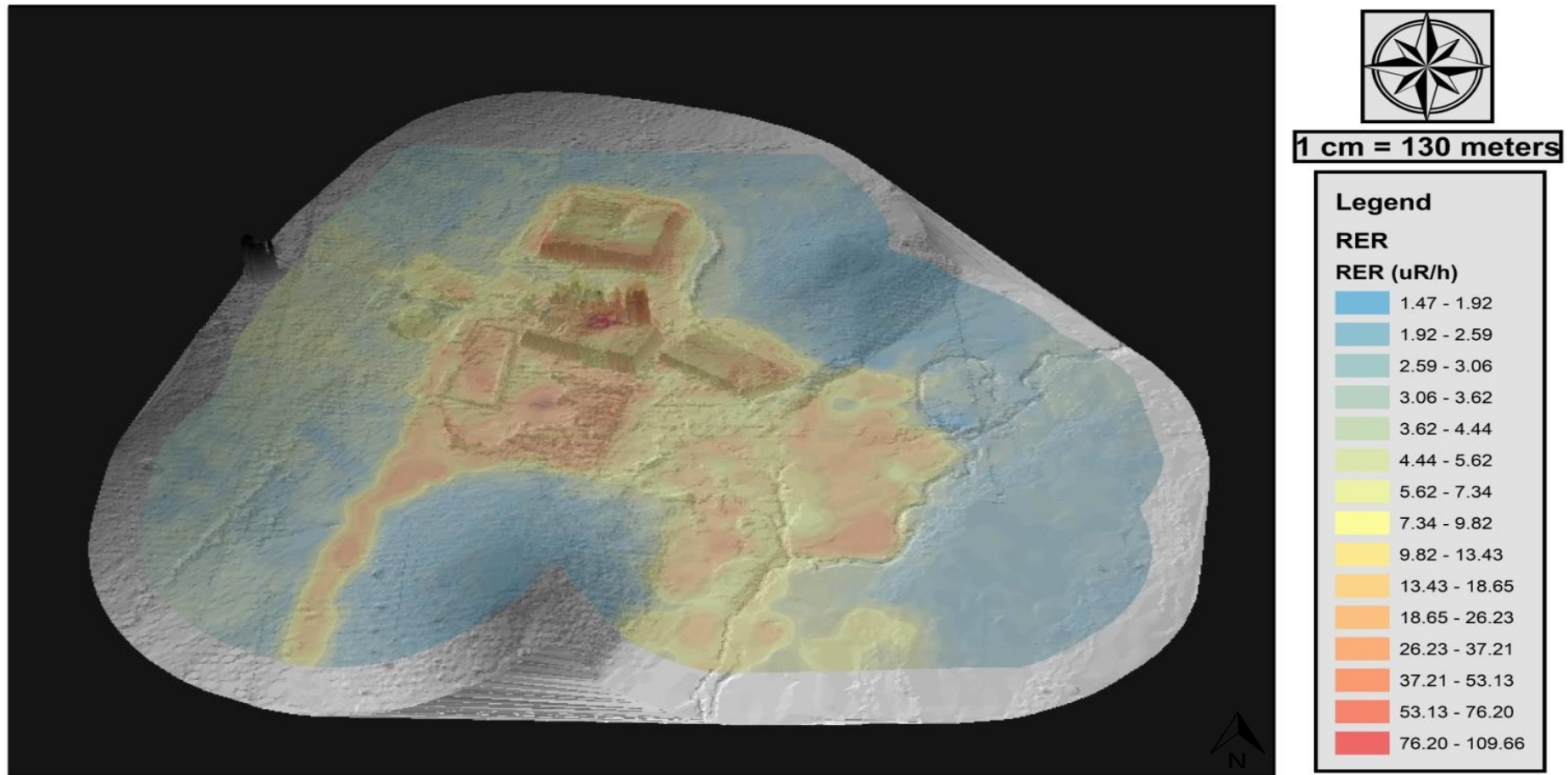


Figure 28: 3D surface model illustrating the rate of uranium exposure over the New Machavie TSE

Equivalent Radiation Dose Rate

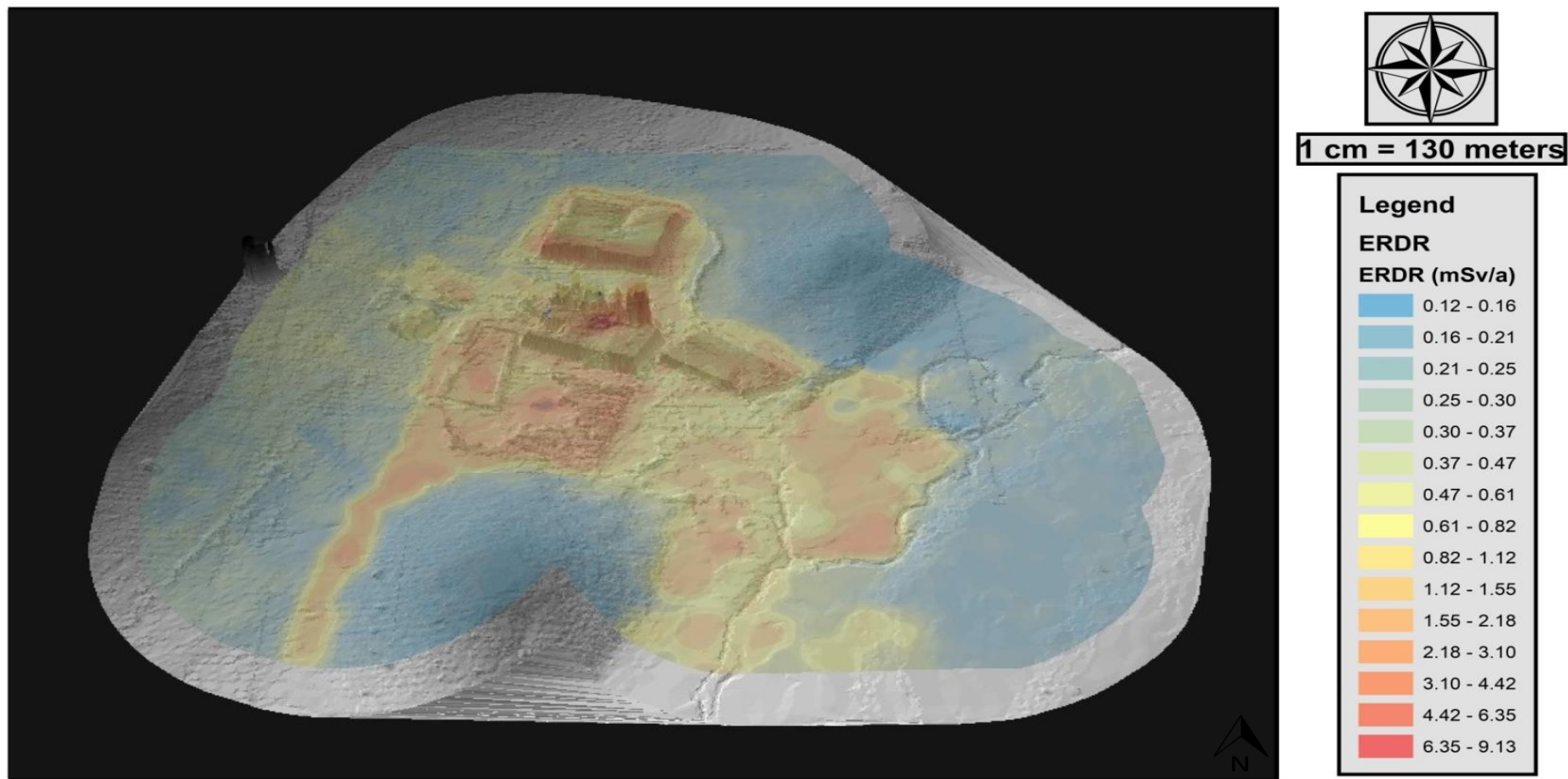


Figure 29: 3D surface model illustrating the equivalent dose of radiation a person would be exposed to over the New Machavie TSF

7.4 Chapter conclusion

Chapter 7 set out to quantify the extent of the uranium migration, while also verifying the uranium anomalies, previously identified in Chapter 6. Using geochemical indices generally reserved for uranium exploration within a geological unit, rather than oxidised tailings impoundments, Chapter 7 aimed to validate the viability of the approach. Despite literatures doubtfulness with regards to how radioactive disequilibrium would influence the results derived from either geochemical index, both indices proved to be quite sufficient in the identification of accumulation hotspots, as well as their respective preferential flow paths, as the results were found to complement those discussed in Chapter 6.

With regards to the use of the Uranium Migration Index, a good correlation was found to exist between the uranium anomalies identified by means of natural gamma-ray spectrometry and those verified using the geochemical index. Used to replicate an environment prior to the formation of the oxidised environment seen today, the U_o model performed admirably, although evidence of uranium mobilisation was still noted. The presence of mobilisation, prior to the formation of an oxidising environment, in this case however, could be ascribed to the absence of the real *unit eU/eTh ratio* of the Black Reef Formation, as it could not be sourced and had to be calculated. Despite the minor discrepancy, the model still performed as expected, indicating uranium to be confined to the impoundments itself, while providing evidence of limited migration to the surrounding area of influence.

In contrast to the results derived from the U_o model, the U_m model was found to produce near identical distribution patterns to that identified in Chapter 6, as uranium migration was once again greatly influenced by changes in elevation, along the natural flow path of the TSF. Where the U_o model indicated the accumulation of uranium in close proximity to the impoundments, both the radiometric survey and U_m model indicated the severe enrichment of both the Kromdraaispruit floodplain and soils surrounding the TSF. Both models verified the migration of uranium away from the top of the impoundments, before accumulating in either the side slopes or southern toe paddocks respectively. This not only confirmed the distribution patterns identified in Chapter 6, but also supported the migration trends illustrated in literature.

The $U_{m\%}$ model on the other hand, which indicated the rate of uranium migration, either in or out of a specific region, confirmed the assumption that the toe paddocks and transported tailings material comprised of more mobile uranium-species, as higher $U_{m\%}$ values were recorded over these two sections, compared to the impoundments itself. The statement was later confirmed by literature, as Koch (2014) came to the same conclusion using coulomb leaching tests. Finally, the $U_{m\%}$ model verified the presence of low level contamination plumes, previously ascribed to the deposition of enriched aeolian particles, as the $U_{m\%}$ model recorded high $U_{m\%}$ values, in

similar locations to that identified in Chapter 6. The assumption was confirmed based on the model not providing any evidence of preferential pathways leading to the anomalies itself, which in turn supported the assumption that the anomalies were formed by deposition, rather than accumulating leachate.

While the Uranium Migration Index provided evidence of uranium migrating along the various drainage systems scattered over the TSF, the Ratio Maps not only assisted in the identification of preferential accumulation hotspots, but also provided evidence of both uranium and thorium decoupling from their respective progeny isotopes. Although the enrichment of the tailings material came as no surprise, the manner in which the various techniques complemented each other however did. Both the eU/eTh and $eU/K\%$ Ratio Map confirmed that the uranium anomalies, identified using natural gamma-ray spectrometry, offered good uranium prospects, as they contain relatively high concentrations of uranium, with respect to both thorium and potassium. The Ratio Maps did however indicate the enrichment of Tailings dam No.3 with thorium, which was ascribed to either thorium being retained by the inorganic carbon found within the tailings impoundment, or the migration of uranium along the natural flow path, in the direction of the northern margin of the Kromdraaispruit. The latter did provide a more realistic explanation to the enrichment, as both geochemical indices identified Tailings dam No.3 as being the source of contamination to the northern margin of the Kromdraaispruit floodplain.

In conclusion, one of the subordinates of this chapter's objectives was to quantify the radioactivity of the New Machavie TSF, as the lack of radioactivity measurements were identified as a deficiency in literature by Tutu *et al.* (2009). Although the majority of the study area remained on the safe side, recording ERDR values well below the maximum permissible radiation dose rate of 50 mSv/a, ERDR values of up to 9.13 mSv/a, were recorded in close proximity to the uranium anomalies, identified in Chapter 6. Based on the success achieved using these geochemical indices, despite the extent to which radioactive disequilibrium might have influenced the results, the chapter validated the viability of the approach, for future use in the assessment of uranium migration over tailings impoundments.

CHAPTER 8: FINAL CONCLUSION AND RECOMMENDATIONS

8.1 Conclusion

Motivated by an identified need for research specifically focused on providing industry with a better understanding of tailings impoundments, the project aimed to deliver a geostatistical 3D surface model of a typical tailings storage facility, which upon completion, would be capable of identifying radionuclide distribution pattern, for either prospecting or environmental assessment purposes. Further motivated by literatures resistance to change, the project set out to validate the viability of using alternative methods of data acquisition, in conjunction with a capable geostatistical-interpolator, as an alternative to the more traditional geochemical sampling and laboratory analysis approach. Evidenced by the successful identification of both radionuclide anomalies and their respective migration pathways over the New Machavie TSF, results were found to confirm the proposed hypothesis, as the approach provided the user with a respectable alternative to conventional methods.

With regards to the approach's ability to identify the spatial distribution of radionuclides, both analytical techniques provided evidence of radionuclide migration and environmental contamination, upon first observation. Given the anionic and oxidative nature of the TSF in question, both analytical techniques identified changes in elevation, as being the dominant mechanism governing the distribution of mobilised radionuclides over the New Machavie TSF. While literature proposed the accumulation of radionuclides to the centre of the impoundments, results seemed to indicate the exact opposite, as radionuclides were found to migrate away from the top of the impoundments, before accumulating on the lower side slopes, following the natural flow direction of the TSF. Despite the discrepancies with literature, results did however agree that uranyl-sulphate complexes tend to be the dominant mechanism controlling the chemical speciation of uranium over tailings impoundments, while the toe paddocks and transported material provided evidence of increased remobilisation.

With both analytical techniques pointing out the extent of the migration, geochemical indices, in the form of the Uranium Migration Index and Ratio Maps, were incorporated into the project. Despite literatures doubtfulness with regards to how radioactive disequilibrium would influence the results derived from either geochemical index, both indices proved to be quite sufficient in the verification of the previously identified accumulation hotspots. While results were found to complement that of the above mentioned analytical techniques, both geochemical indices emphasised the migration of radionuclides along the natural flow direction of the TSF, as higher migration values were recorded over the toe paddocks and transported material. Despite literatures emphasis on the rarity of radioactive disequilibrium influencing the mobility of thorium

and its progeny isotopes, results seemed to indicate both uranium and thorium's tendency to decouple from its progeny isotopes, before accumulating in low lying areas, along the various drainage systems present in the surrounding area of influence.

8.2 Recommendations

8.2.1 Resource evaluation purposes

While resource evaluation was never the main objective of this particular project, the successful identification of uranium anomalies over the various tailings impoundments, did however highlight the possibility of using the approach as a cost effective alternative to more conventional methods, when conducting project feasibility studies. Unfortunately, the accurate quantification of natural gamma radiation, over an oxidised tailings impoundment such as the New Machavie TSF, would only be possible if radioactive disequilibrium is accounted for. Only then, would it be possible to accurately estimate the resources hidden within these legacy tailings, using natural gamma spectrometry (Koch, 2014). Another consideration that should be taken into account is the effect of uranium migration on resource estimations, as the project clearly indicated the extent of the migration and how it affected the accumulation of uranium, both within the tailings impoundments itself, as well as over the surrounding area of influence.

Taking into consideration the success achieved using the approach to create a 3D surface model of the New Machavie TSF, the next logical step would be to assess the spatial distribution of the resources (gold and uranium) contained within a legacy tailings, using a full 3D model, derived from borehole data, rather than surface measurements. Despite a similar study already existing (see Koch, 2014), where down-hole natural gamma probing was used to assess both the uranium distribution and its migration within an impoundment, the research did not include the distribution of gold and how the oxidative nature of the tailings material would affect its distribution. The author therefore recommends the use of PXRF spectroscopy as a method of data acquisition for future projects, as it not only provides the user with a more cost effective alternative to conventional methods, but also allows for the evaluation of both resources simultaneously (gold and uranium), as well as the distribution of other metal trace elements, relative to present radionuclides.

8.2.2 Environmental assessment purposes

As previously mentioned, when viewed from an environmental perspective, the potential usefulness of both the *“alternative approach”*, as well as the derived 3D surface model, exceeds that of its exploratory purpose, as it provides a cost effective platform to investigate the mechanics at work within a tailings impoundment. Although this particular project focused specifically on the spatial distribution of selected radionuclides over a typical TSF, a need within

literature was identified for research focused on the distribution of metal trace elements, both relative to radionuclides, as well as the various oxidation zones present within a typical impoundment (Koch, 2014). Taking into consideration that the “*Test-All-Geo*” mode analysed the full range of elemental concentrations, the 3D surface model already consisted over the necessary data needed to assess the distribution patterns of selected metal trace elements, in a similar manner to that of the radionuclides. While a number of publications have mentioned the use of PXRF spectroscopy for rapid environmental assessment purposes, it is the approach of Chakraborty *et al.* (2017) that really shows potential for environmental assessment over tailings storage facilities.

Using a similar approach to what was used for the assessment of radionuclides in this project, Chakraborty *et al.* (2017) proposed the use of PXRF spectroscopy in conjunction with both Ordinary Prediction-based Kriging (to determine element concentration levels at unsampled locations), as well as non-parametric Indicator Kriging (to estimate the probability of data exceeding a certain threshold level). By applying the proposed methodology to the data derived from both the radiometric survey and PXRF analyses, the 3D surface model gained the ability to predict the probability of a selected element (MTE or PTE), exceeding a specific threshold level (see Figure 30 to Figure 33 as examples of the proposed methodology). The author therefore recommends the approach to be used for future environmental assessment purposes, as it provides the user with a rapid mapping tool, capable of assessing and interpolating a much wider range of parameters, at a lower cost to company, compared to more traditional approaches.

While the effect of particle size on the mobility of radionuclides has been recommended for future research in the past (Koch, 2014 and Bezuidenhout and Rousseau, 2005), the project emphasised the importance of the proposed research, as results indicated a strong correlation between the accumulation of radionuclides and the deposition of fine-grained material. This statement correlated well with that of the other authors, who emphasised how particle size affected both the hydraulic flow and deposition of radionuclides within a tailings impoundment respectively (Koch, 2014 and Bezuidenhout and Rousseau, 2005). Contributing to the creation of low level contamination plumes, the project also highlighted the extent of environmental contamination by means of aeolian transportation and how particle size governed the deposition of these radionuclide-enriched particles. These statements therefore underscore the importance of particle size distribution and why it should be considered for future research purposes.

Spatial Distribution of Measured Copper

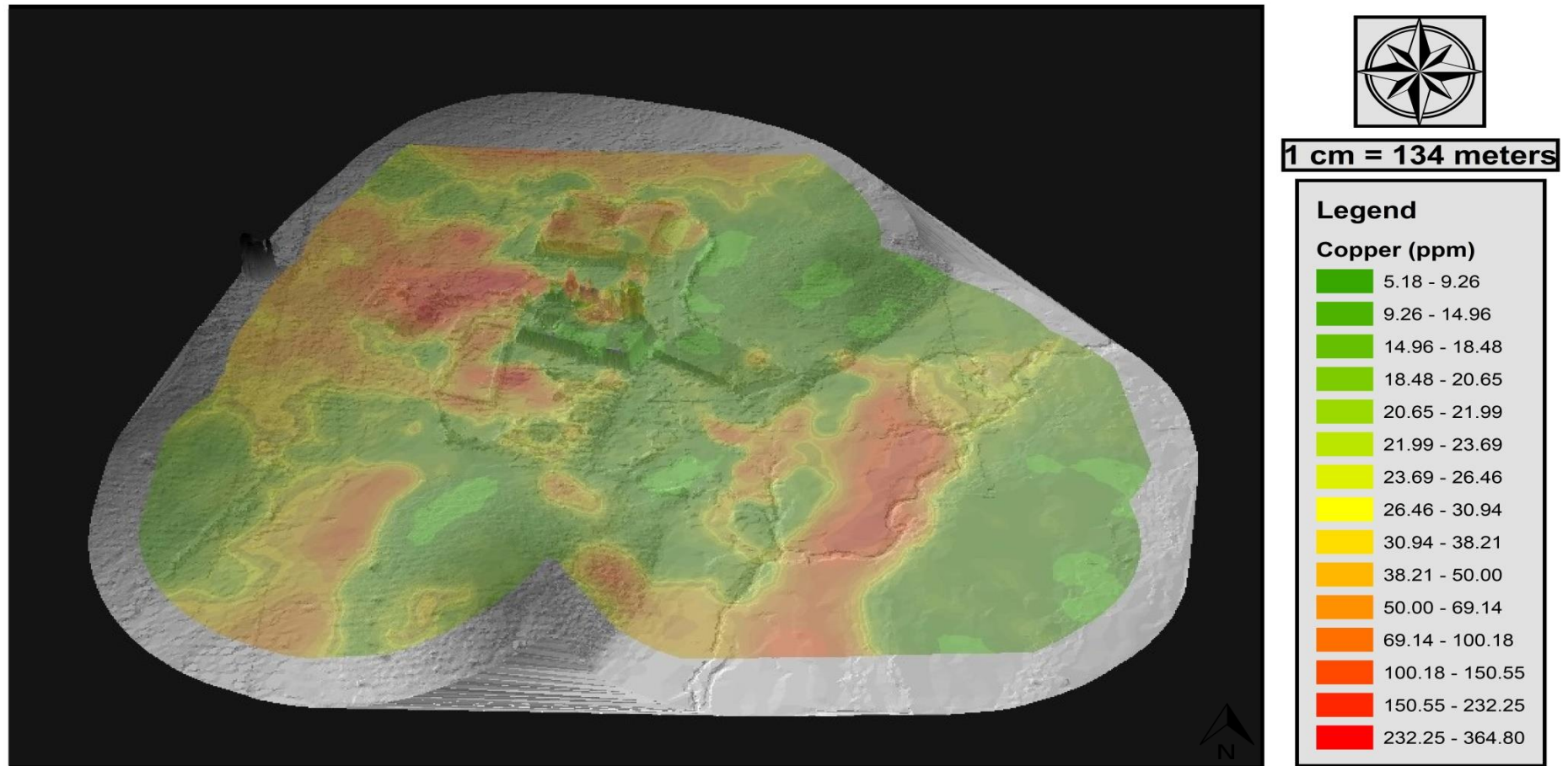


Figure 30: 3D surface model illustrating the methodology of Chakraborty *et al.* (2017), using measured copper concentration as an example

Probability Distribution of Copper Exceeding NEMWA Standard

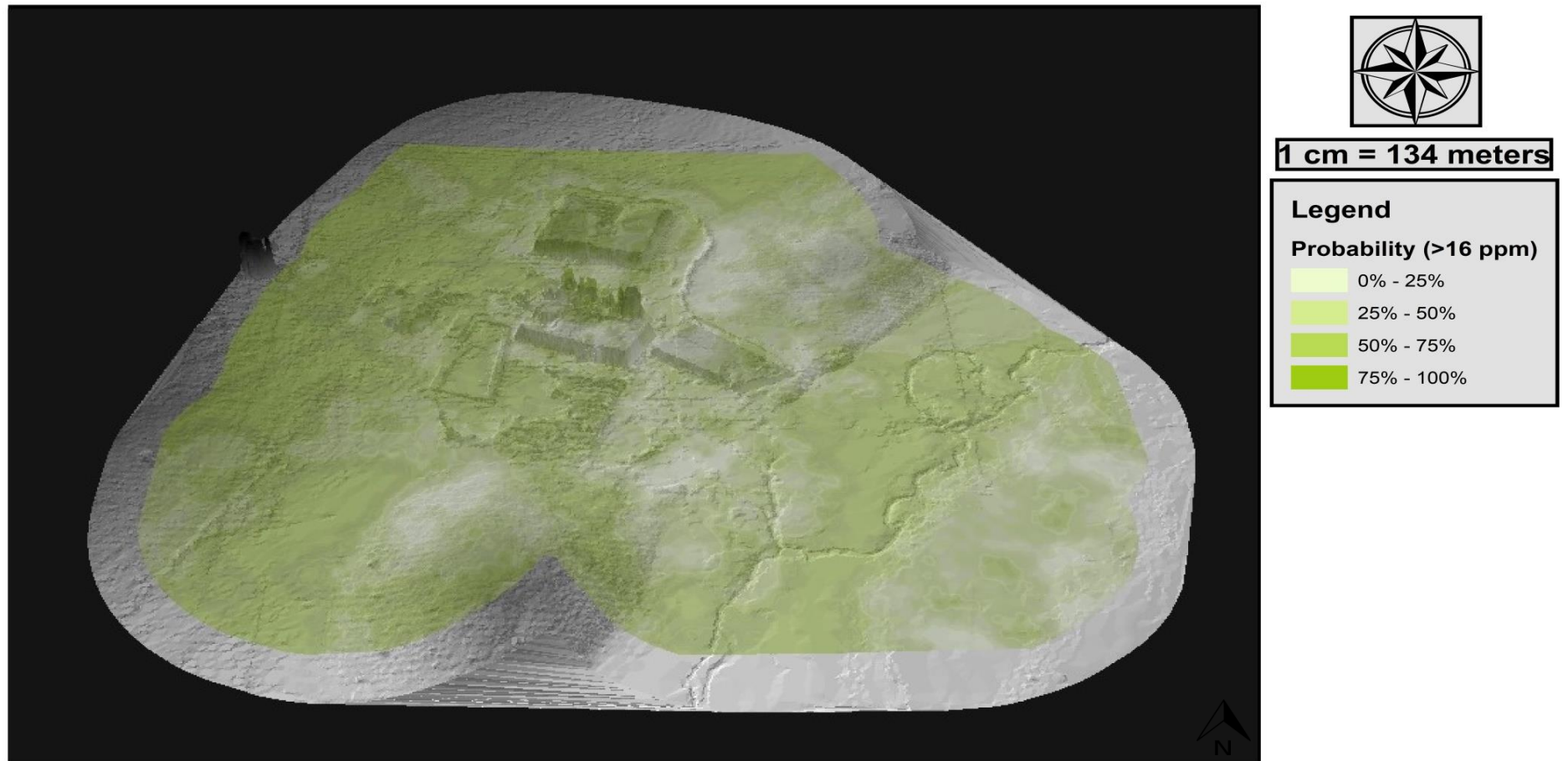


Figure 31: 3D surface model illustrating the probability distribution of measured copper concentrations, exceeding the NEMWA threshold level of 16ppm

Spatial Distribution of Measured Arsenic

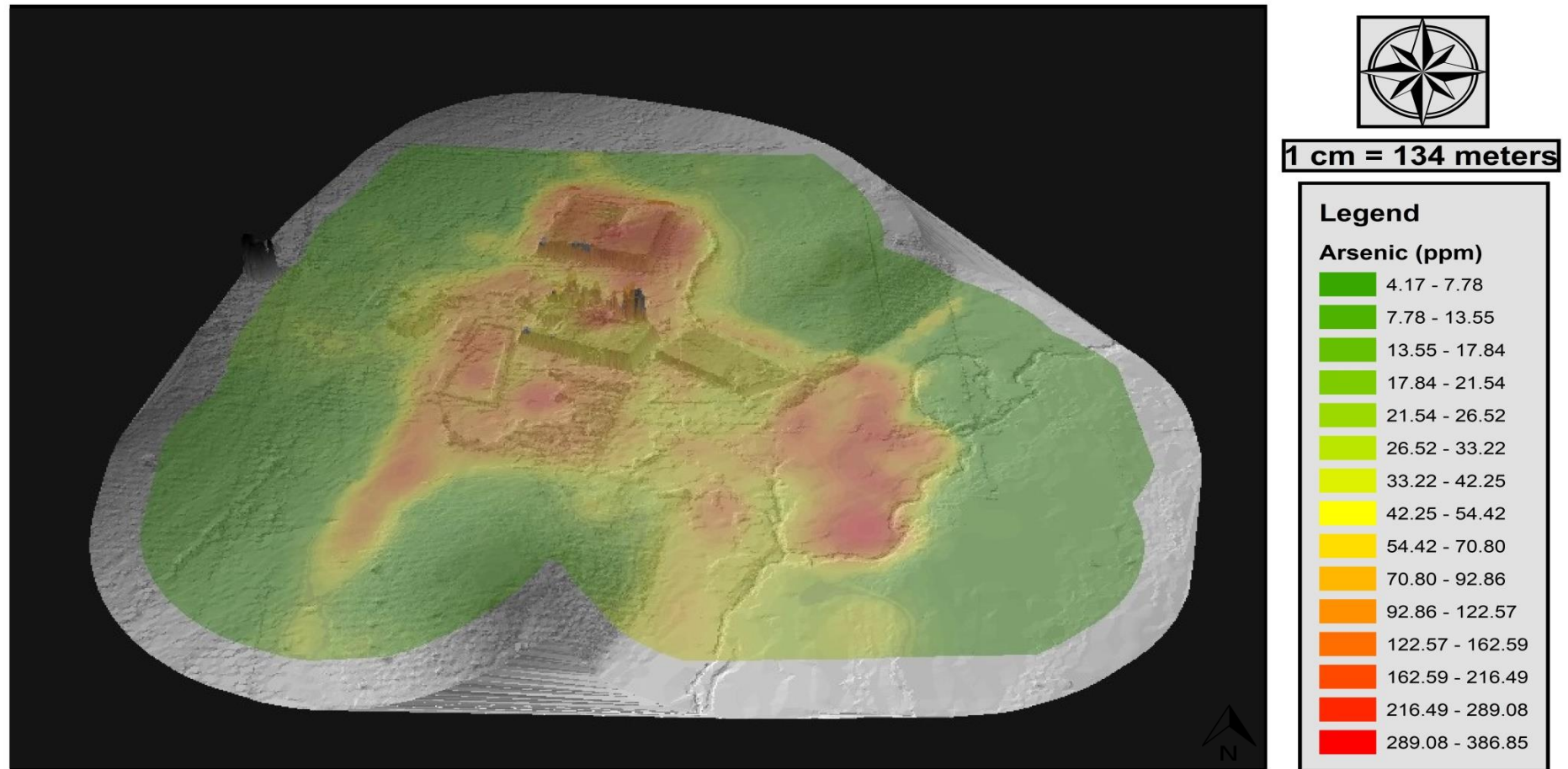


Figure 32: 3D surface model illustrating the methodology of Chakraborty *et al.* (2017), using measured arsenic concentration as an example

Probability Distribution of Arsenic Exceeding NEMWA Standard

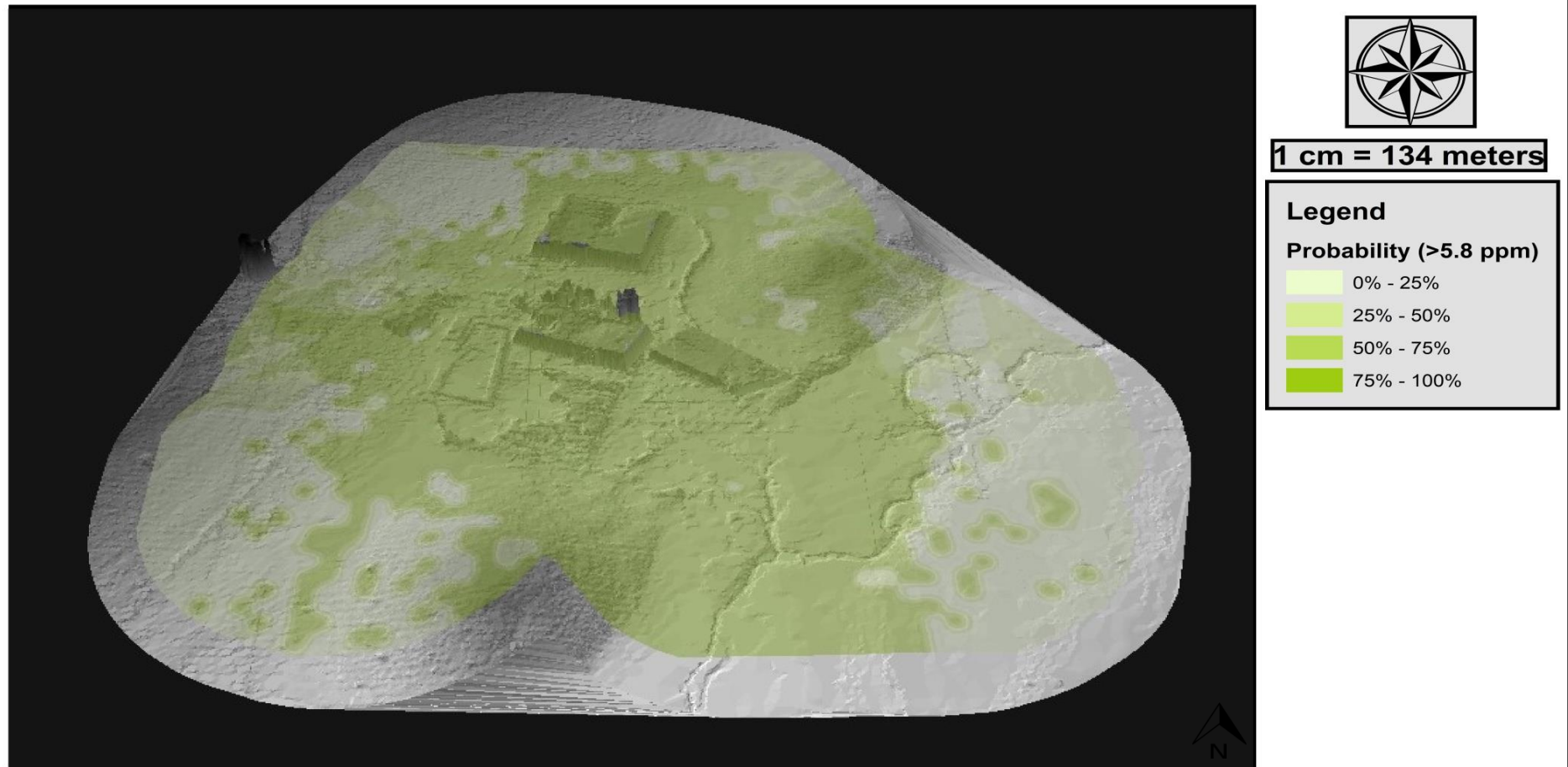


Figure 33: 3D surface model illustrating the probability distribution of measured copper concentrations, exceeding the NEMWA threshold level of 16ppm

REFERENCES

- Abu-Deif, A., Abouelnaga, H.S. and Hassanein, H.I. 2001. Distribution of radioelements and its relation to uranium migration, El Erediya exploratory tunnels, central Eastern Desert, Egypt. *J King Abdulaziz Univ (Earth Sci)*, 13:19-40.
- Adler, R. A., Claassen, M., Godfrey, L. and Turton A. R. 2007. Water, mining, and waste: an historical and economic perspective on conflict management in South Africa. *The Economics of Peace and Security Journal*, 2(2):33-41. <http://www.ehrn.co.za/publications/download/119.pdf> Date of access: 20 May 2016.
- Akcil, A. and Koldas, S. 2006. Acid Mine Drainage (AMD): Causes, treatment and case studies. *Journal of Cleaner Production*, 14:1139-1145. [http://www.researchgate.net/profile/Ata_Akcil2/publication/236108760_Acid_Mine_Drainage_\(AMD\)_causes_treatment_and_case_studies/links/5485f0ce0cf2ef34478a614d.pdf](http://www.researchgate.net/profile/Ata_Akcil2/publication/236108760_Acid_Mine_Drainage_(AMD)_causes_treatment_and_case_studies/links/5485f0ce0cf2ef34478a614d.pdf) Date of access: 20 May 2016.
- Alloway, B.J. 2012. Uranium (*In* Alloway, B.J., ed. Heavy Metals in Soils. 3rd ed. Springer Science. London. p. 565-578).
- Anhaeusser, C.R., Johnson, M.R. and Thomas, R.J. 2006. The Geology of South Africa. The Geological Society of South Africa. Pretoria. ISBN 1-919908-77-3. p. 691.
- Antrobus, E.S.A., Brink, W.J.C., Brink, M.C. Caulkin, J., Hutchinson, R.I., Thomas, D.E., Van Graan, J.A. and Viljoen, J.J. 1986. The Klerksdorp Goldfield. (*In* Anhaeusser, C.R. and Maske, S., eds. Mineral deposits of Southern Africa, Vol. I. Geological Society of South Africa, Johannesburg. p. 549-598).
- Asfahani, J., Aissa, M. and Al-Hent, R. 2007. Uranium migration in a sedimentological phosphatic environment in northern Palmyrides, Al-Awabed area, Syria. *Applied Radiation and Isotopes*, 65(9):1078-1086.
- Assran, A.S., Abdelhadi, H.M., El Shayeb, H.M., Ashami, A.S. and Zaeimah, M.A. 2012. Ground Gamma-Ray Spectrometric Study and Environmental Impact for Moreid-Elsahu Area, Southwestern Sinai, Egypt. *Arab Journal of Nuclear Sciences and Applications*, 45(2):240-253.
- Aswathanarayana, U. 1986. Principles of nuclear geology. Rotterdam, The Netherlands: AA Balkema.
- Aucamp, P.J. 2000. Trace element pollution of soils by abandoned gold mine tailings near Potchefstroom, South Africa. Pretoria: UP. (Dissertation - MSc).

- Aucamp, P. and Van Schalkwyk, A. 2003. Trace element pollution of soils by abandoned gold mine tailings, near Potchefstroom, South Africa. *Bulletin of Engineering Geology and the Environment*, 62(2):123-134.
- Barton, E.S. and Hallbauer, D.K. 1996. Trace-element and U-Pb isotope compositions of pyrite types in the Proterozoic Black Reef, Transvaal Sequence, South Africa: Implications on genesis and age. *Chemical Geology*, 133(1-4):173-199.
- Benzaazoua, M., Bussière, B., Demers, I., Aubertin, M., Fried, É. and Blier, A. 2008. Integrated mine tailings management by combining environmental desulphurization and cemented paste backfill: Application to mine Doyon, Quebec, Canada. *Minerals Engineering*, 21(4):330-340.
- Bezuidenhout, N. and Rousseau, P.D.S. 2005. An Investigation into the Depth and Rate of Weathering on Gold Tailings Dam Surfaces as Key Information for Long-Term AMD Risk Assessments. Water Research Commission. WRC Report No. 1347/1/05.
- Blowes, D.W., Reardon, E.J., Jambor, J.L. and Cherry, J.A. 1991. The formation and potential importance of cemented layers in inactive sulfide mine tailings. *Geochimica et Cosmochimica Acta*, 55:965-978.
- Body, J.L. 1988. The Black Reef on the Witwatersrand and Adjacent areas: Its mining history, geology and economic potential. (Unpublished).
- Bohling, G.C. 2007. Introduction to Geostatistics. *Kansas Geological Survey Open File Report no*, 26(2007):50.
- Bois, D., Poirier, P., Benzaazoua, M., Bussière, B. and Kongolo, M. 2005. A feasibility study on the use of desulphurized tailings to control acid mine drainage. *Cim Bulletin*, 98(1087):361-380.
- Booyens, S. 2016. Water quality assessment of the Koekemoerspruit: Integrating water physico-chemistry and phytoplankton assemblages. Potchefstroom: NWU. (Dissertation - MSc).
- Bosch, D.W. 1987. Retreatment of residues and waste rock. *Extr. Metallurgy Gold South Africa*, 2:707-743.
- Botha, A.J. 2015. Surface impacts of gold mining activities on the Kromdraai/Koekemoerspruit: a situation analysis. Potchefstroom: NWU. (Dissertation - MSc).
- Boyle, R.W. 2013. Geochemical prospecting for thorium and uranium deposits. 16th ed. Amsterdam: Elsevier.

- Bussière, B., Benzaazoua, M., Kongolo, M. and Aubertin, M. 2002. Intégration de la désulfuration dans la restauration des sites miniers générateurs de DMA. (*In Proceedings of the Symposium sur l'Environnement et les Mines, Rouyn-Noranda, The Canadian Institute of Mining, Metallurgy and Petroleum*).
- Chakraborty, S., Man, T., Paulette, L., Deb, S., Li, B., Weindorf, D.C. and Frazier, M. 2017. Rapid assessment of smelter/mining soil contamination via portable X-ray fluorescence spectrometry and indicator kriging. *Geoderma*, 306:108-119.
- Chandra, A.P. and Gerson, A.R. 2010. The mechanisms of pyrite oxidation and leaching: a fundamental perspective. *Surface Science Reports*, 65(9):293-315.
- Chapman, P.M. 2007. Determining when contamination is pollution-weight of evidence determinations for sediments and effluents. *Environment International*, 33(4):492-501.
- Coetzee, H. 1995. Radioactivity and the leakage of radioactive waste associated with Witwatersrand gold and uranium mining. (*In Merkel B., Hurst S., Löhnert E.P. and Struckmeier W., eds. Uranium-Mining and Hydrology. Proceedings of the International GeoCongress Conference and Workshop in Freiberg, Germany, October 1995. p.134–139*).
- Coetzee, H.P.A. 1996. The stratigraphy and sedimentology of the Black Reef Quartzite Formation, Transvaal Sequence, in the area of Carletonville and West Rand Goldfields. Potchefstroom: PU for CHE. (Thesis – B.Sc. Honours).
- De Bever, J. 1997. An overview of the early-proterozoic, auriferous Black Reef placer in the Transvaal Basin. Johannesburg: Rhodes. (Dissertation - MSc).
- Demers, I., Bussière, B., Benzaazoua, M., Mbonimpa, M. and Blier, A. 2008. Column test investigation on the performance of monolayer covers made of desulphurized tailings to prevent acid mine drainage. *Minerals Engineering*, 21(4):317-329.
- DeSisto, S. 2008. Dynamic arsenic cycling in scorodite-bearing hardpan cements, Montague Gold Mines, Nova Scotia. Kingston, Ontario: Queen's University. (Dissertation - MSc).
- Dickson, B.L. and Scott, K.M. 1997. Interpretation of aerial gamma-ray surveys-adding the geochemical factors. *AGSO Journal of Australian Geology and Geophysics*, 17(2):187-200.
- Dold, B. and Fontboté, L. 2001. Element cycling and secondary mineralogy in porphyry copper tailings as a function of climate, primary mineralogy, and mineral processing. *Journal of Geochemical Exploration*, 74(1): 3-55.

- Dold, B. and Fontboté, L. 2002. A mineralogical and geochemical study of element mobility in sulfide mine tailings of Fe oxide Cu–Au deposits from the Punta del Cobre belt, northern Chile. *Chemical Geology*, 189(3):135-163.
- Els, B.G., Van den Berg, W.A. and Mayer, J.J. 1995. The Black Reef Quartzite Formation in the western Transvaal: sedimentological and economic aspects, and significance for basin evolution. *Mineralium Deposita*, 30(2):112-123.
- Eriksson, P.G., Altermann, W. and Hartzler, F.J. 2006. The Transvaal Supergroup and its precursors. (In Johnson, M.R., Anhaeusser, C.R. and Thomas, R.J., eds. The geology of South Africa. Geological Society of South Africa, Johannesburg and Council for Geoscience, Pretoria. p. 237-260).
- Frankel, J.J. 1940. Notes on some of the minerals in the Black Reef series. *South African Journal of Geology*, 43(1):1-8.
- Fuchs, S., Williams-Jones, A.E. and Przybylowicz, W.J. 2016. The origin of the gold and uranium ores of the Black Reef Formation, Transvaal Supergroup, South Africa. *Ore Geology Reviews*, 72(1):149-164.
- Gavrilescu, M., Pavel, L.V. and Cretescu, I. 2009. Characterization and remediation of soils contaminated with uranium. *Journal of Hazardous Materials*, 163(2):475-510.
- Goovaerts, P. 1999. Geostatistics in soil science: State-of-the-art and perspectives. *Geoderma*, 89(1):1-45.
- Graupner, T., Kassahun, A., Rammlmair, D., Meima, J.A., Kock, D., Furche, M., Fiege, A., Schippers, A. and Melcher, F. 2007. Formation and sequences of cemented layers and hardpans within sulfide-bearing mine tailings (mine district Freiberg, Germany). *Applied Geochemistry*, 22:2486-2508.
- Hansen, R.N. 2014. Numeric geochemical reaction modelling, incorporating systems theory and implications for sustainable development – Study on East Rand Basin acid mine drainage, Witwatersrand, South Africa. Stellenbosch: Stellenbosch University. (Dissertation-Ph.D).
- Hansen, R.N. 2015. Contaminant leaching from gold mining tailings dams in the Witwatersrand Basin, South Africa: A new geochemical modelling approach. *Applied Geochemistry*, 61:217-223.

Herselman, J.E., Wade, P.W., Steyn, C.E. and Snyman, H.G. 2005. An evaluation of dedicated land disposal practices for sewage sludge. Water Research Commission, WRC Report No. 1209/1/05.

Hooda, P.S. 2010a. Introduction. (*In Hooda, P.S., ed. Trace elements in soils. West Sussex: Blackwell Publishing Ltd. p. 3-8).*

Hooda, P.S. 2010b. Assessing bioavailability of soil trace elements. (*In Hooda, P.S., ed. Trace elements in soils. West Sussex: Blackwell Publishing Ltd. p. 229-265).*

IAEA (International Atomic Energy Agency). 1979. Gamma-Ray Surveys in Uranium Exploration.

http://www.iaea.org/inis/collection/NCLCollectionStore/_Public/10/454/10454955.pdf Date of access: 23 Feb. 2017.

IAEA (International Atomic Energy Agency). 1991. Airborne Gamma-Ray spectrometer surveying. http://www.iaea.org/inis/collection/NCLCollectionStore/_Public/22/072/22072114.pdf Date of access: 23 Feb. 2017.

IAEA (International Atomic Energy Agency). 1996. Uranium exploration data and techniques applied to the preparation of radioelement maps. http://www-pub.iaea.org/MTCD/Publications/PDF/te_980_prn.pdf Date of access: 23 Feb. 2017.

IAEA (International Atomic Energy Agency). 2003. Guidelines for Radioelement Mapping Using Gamma Ray Spectrometry Data. http://www-pub.iaea.org/mtcd/publications/pdf/te_1363_web.pdf Date of access: 23 Feb. 2017.

IAEA (International Atomic Energy Agency). 2007. Terminology Used in Nuclear Safety and Radiation Protection. http://www-pub.iaea.org/MTCD/publications/PDF/Pub1290_web.pdf Date of access: 23 Feb. 2017.

Isaaks, E.H. and Srivastava, R.M. 1989. An Introduction to Applied Geostatistics. New York: Oxford University Press.

Johnston, K., Ver Hoef, J.M., Krivoruchko, K. and Lucas, N. 2001. Using ArcGIS geostatistical analyst. Redlands: Esri.

Jurjovec, J., Ptacek, C.J. and Blowes, D.W. 2002. Acid neutralization mechanisms and metal release in mine tailings: a laboratory column experiment. *Geochimica et Cosmochimica Acta*, 66(9):1511-1523.

- Kabata-Pendias, A. and Mukherjee, A.B. 2007. *Trace elements from soil to human*. Berlin: Springer, Science and Business Media.
- Kabata-Pendias, A. 2011. *Trace elements in soils and plants*. 4th ed. United States of America: CRC press.
- King, H.L., Pringle, I.C., Oosterhuis, W.R. and Ehlers, D.L. 2007. *The metallogeny of the West Rand*. Pretoria: Council for Geoscience.
- Koch, J. 2014. *Migration and gamma ray assessment of uranium on a gold tailings disposal facility*. Potchefstroom: NWU. (Dissertation - MSc).
- Kruger, A. C. 2004. *Climate of South Africa. Climate Regions. WS45*. South African Weather Service. Pretoria. South Africa.
- Larkin, J.F.S. 2014. *Comparative investigation of airborne and ground-based radiometric survey techniques*. Johannesburg: WITS. (Dissertation - MSc).
- Lottermoser, B.G. and Ashley, P.M. 2006. Mobility and retention of trace elements in hardpan-cemented cassiterite tailings, north Queensland, Australia. *Environmental Geology*, 50(6):835-846.
- Mahed, G. 2009. *Development of a local sampling and monitoring Protocol for radioactive elements in fractured rock Aquifers in South Africa using a case study in Beaufort West*. Cape Town: University of the Western Cape. (Dissertation - MSc).
- McCarthy, T. S. 2011. The impact of acid mine drainage in South Africa. *South African Journal of Science*, 107(5):1-7.
http://www.scielo.org.za/scielo.php?pid=S003823532011000300002&script=sci_arttext Date of access: 24 Aug. 2016.
- McGregor, R.G. and Blowes, D.W. 2002. The physical, chemical and mineralogical properties of three cemented layers within sulfide-bearing mine tailings. *Journal of Geochemical Exploration*, 76:195-207.
- McKillup, S. and Dyar, M.D. 2010. *Geostatistics explained: An introductory guide for earth scientists*. United Kingdom: Cambridge University Press.
- Mintails. 2012. *Turning mine dumps into gold*. <http://www.mintails.co.za/mintails-in-the-news-mintails-in-articles/57-turning-mine-dumps-into-gold>. Date of access: 26 May 2016.

- Mucina, L. and Rutherford, M.C. 2006. The vegetation of South Africa, Lesotho and Swaziland: *Memoirs of the Botanical Survey of South Africa*. Pretoria: Strelitzia 19 and South African National Biodiversity Institute.
- Muir, A., Mitchell, J., Flatman, S.R. and Sabbagha, C. 2005. A practical guide to re-treatment of gold processing residues. *Minerals engineering*, 18(8):811-824.
- Naoum, S. and Tsanis, I.K. 2004. Ranking spatial interpolation techniques using a GIS-based DSS. *Global Nest*, 6(1):1-20.
- Nengovhela, A.C., Yibas, B. and Ogola, J.S. 2007. An investigation into the availability and role of oxygen gas in gold tailings dams of the Witwatersrand basin with reference to their acid mine drainage potential. *Water SA*, 33(2):271-274.
- Obbes, A.M. 2000. The structure, stratigraphy and sedimentology of the Black Reef-Malmani-Rooihooft succession of the Transvaal Supergroup southwest of Pretoria. *Bulletin of the council for geoscience*, 127:1-89.
- Pulford, I.D. 2010. Gold and uranium. (In Hooda, P.S., ed. Trace elements in soils. West Sussex: Blackwell Publishing Ltd. p. 551-565).
- Richards, D.J. 1981. Geophysical Field Manual for Technicians: Technical Manual on Radiometrics. Johannesburg: South African Geophysical Association.
- Robb, L.J. and Meyer, F.M. 1995. The Witwatersrand Basin, South Africa: Geological framework and mineralization processes. *Ore Geology Reviews*, 10(2):67-94.
- Rösner, T. and Van Schalkwyk, A. 2000. The environmental impact of gold mine tailings footprints in the Johannesburg region, South Africa. *Bulletin of Engineering Geology and the Environment*, 59(2):137-148.
- Rösner, T., Boer, R., Reyneke, R., Aucamp, P. and Vermaak, J. 2001. A preliminary assessment of pollution contained in the unsaturated and saturated zone beneath reclaimed gold mine residue deposits. WRC Report No. 797/1/01, Pretoria.
- Saunders, D.F. and Potts, M.J. 1976. Interpretation and application of high sensitivity airborne gamma-ray spectrometric data. (In International Atomic Energy Agency, ed. Exploration for Uranium Ore Deposits, Vienna, p. 107-125).
- Soil and Irrigation Research Institute (SIR). 1987. Land Types of the Maps 2626 Wes-Rand, 2726 Kroonstad. Memoirs on the Agricultural Natural Resources of South Africa, No 4. Department of Agriculture and Water Supply.

Talaat, S.M., Ragab, F. and Abd El Maksoud, T.M. 2012. Uranium migration in Paleozoic lateritic Paleosol Samples, Southwestern Sinai, Egypt. *Australian Journal of Basic and Applied Sciences*, 6(10):681-688.

Thermo Fisher Scientific Inc. 2008. Mining exploration and geochemical analysis of mining samples. <https://tools.thermofisher.com/content/sfs/brochures/Mining-Exploration-Geochemical-Analysis-of-Mining-Samples-with-NitonXL3tGOLDD.pdf> Date of access: 16 Mar. 2017.

Tucker, R.F., Viljoen, R.P. and Viljoen, M.J. 2016. A Review of the Witwatersrand Basin: The World's Greatest Goldfield. *Episodes*, 39(2): 105-133.

Tutu, H., Cukrowska, E.M., McCarthy, T.S., Mphephu, N.F. and Hart, R. 2003. Determination and modelling of geochemical speciation of uranium in gold mine polluted land in South Africa. (*In Proceedings of the International Congress on Mine Water and the Environment*. p. 137-155).

Tutu, H., McCarthy, T.S. and Cukrowska, E. 2008. The chemical characteristics of acid mine drainage with particular reference to sources, distribution and remediation: The Witwatersrand Basin, South Africa as a case study. *Applied Geochemistry*, 23(12):3666-3684.

Tutu, H., Cukrowska, E.M., McCarthy, T.S., Hart, R. and Chimuka, L. 2009. Radioactive disequilibrium and geochemical modelling as evidence of uranium leaching from gold tailings dumps in the Witwatersrand Basin. *International Journal of Environmental and Analytical Chemistry*, 89(8-12):687-703.

U.S. EPA (Environmental Protection Agency). 1997. Standard Operating Procedure: Soil Sampling. <https://archive.epa.gov/region9/toxic/web/pdf/ee-soilsampling-sop-env-3-13.pdf> Date of access: 05 Jan. 2016.

U.S. EPA (Environmental Protection Agency). 1999. Understanding Variation in Partition Coefficient, K_d, Values. Volume II: Review of Geochemistry and Available K_d Values for Cadmium, Cesium, Chromium, Lead, Plutonium, Radon, Strontium, Thorium, Tritium (3H), and Uranium. EPA 402-R-99-004B.

U.S. EPA (Environmental Protection Agency). 2007. Field Portable X-ray Fluorescence Spectrometry for the determination of element concentrations in soils and sediments. <https://www.epa.gov/sites/production/files/2015-12/documents/6200.pdf> Date of access: 23 Feb. 2017.

- U.S. EPA (Environmental Protection Agency). 2014. SEDS Operating Procedure: Soil Sampling. https://www.epa.gov/sites/production/files/2014-03/documents/appendix_n_soil_sampling.pdf Date of access: 05 Jan. 2016.
- Van den Berg, W.A. 1994. The stratigraphy and sedimentology of the Black Reef Quartzite Formation, Transvaal Sequence, in the Potchefstroom, Klerksdorp and Ventersdorp districts. Potchefstroom: PU for CHE. (Dissertation-MSc).
- Van der Westhuizen, W.A. and De Bruijn, H. 2006. The Ventersdorp Supergroup. (In Johnson, M.R., Anhaeusser, C.R. and Thomas, R.J., eds. The geology of South Africa. Geological Society of South Africa, Johannesburg and Council for Geoscience, Pretoria. p. 187-208).
- Van Deventer, P.W. and Slabbert, A.J. 2011. Study programme 3: Hydrological impacts of gold mining activities on a drainage system. Potchefstroom: NWU. (NRF/THRIP-Mine Waste Solutions research proposal, Ref: TP2011071700002, Pretoria).
- Van Rensburg, R.J. 2011. Short Course on Gamma Surveying. Geotron Systems (Pty) Ltd.
- Vandenhove, H., Van Hees, M., Wannijn, J., Wouters, K. and Wang, L. 2007. Can we predict uranium bioavailability based on soil parameters? Part 2: Soil solution uranium concentration is not a good bioavailability index. *Environmental Pollution*, 145(2):577-586.
- Vandenhove, H., Gil-García, C., Rigol, A. and Vidal, M. 2009. New best estimates for radionuclide solid-liquid distribution coefficients in soils. Part 2: Naturally occurring radionuclides. *Journal of Environmental Radioactivity*, 100(9):697-703.
- Webster, R. and Oliver, M.A. 2001. Geostatistics for environmental scientists (Statistics in Practice). 2nd ed. West Sussex, England: John Wiley and Sons Ltd.
- Whiteside, H.C.M. 1970. Uranium reserves, future demand and the extent of the exploration problem. (In International Atomic Energy Agency, eds. Uranium Exploration Geology: 1970 Uranium Exploration Geology Conference organized by The International Atomic Energy Agency, Vienna. p. 19).
- Wilford, J.R., Bierwirth, P.E. and Craig, M.A. 1997. Application of airborne gamma-ray spectrometry in soil/regolith mapping and applied geomorphology. *AGSO Journal of Australian Geology and Geophysics*, 17(2):201-216.

- Wilkins, B. 2013. The changing face of tailings retreatment. *Modern Mining*, 9(8):62-67.
<http://www.crown.co.za/reader/modernmining/2013/August/files/assets/common/downloads/publication.pdf> Date of access: 22 Mar. 2016.
- Winde, F. 2002. Uranium contamination of fluvial systems. Mechanisms and processes. Part I: Geochemical mobility of uranium along the water path, the Koekemoerspruit (South Africa) as a case study. *Cuadernos de investigación geográfica*, 28(2):49-57.
- Winde, F. 2006. Challenges for sustainable water use in dolomitic mining regions of South Africa - A case study of uranium pollution part I: Sources and pathways. *Physical Geography*, 27(4):333-347.
- Winde, F. and Sandham, L.A. 2004. Uranium pollution of South African streams: An overview of the situation in gold mining areas of the Witwatersrand. *GeoJournal*, 61(2):131-149.
- Winde, F., Wade, P. and Van der Walt, I.J. 2004. Gold tailings as a source of water-borne uranium contamination of streams-The Koekemoerspruit (Klerksdorp goldfield, South Africa) as a case study-part I of III: Uranium migration along the aqueous pathway. *Water SA*, 30(2):219-225.
- Winde, F. and Van der Walt, I.J. 2004. Gold tailings as a source of water-borne uranium contamination of streams-The Koekemoerspruit (Klerksdorp goldfield, South Africa) as a case study-part II of III: Dynamics of groundwater-stream interactions. *Water SA*, 30(2):227-232.
- Yibas, B., Pulles, W. and Nengovhela, C. 2010. Kenetic Development of Oxidation Zones in Tailings Dams With Specific Reference to The Witwatersrand Gold Mine Tailings Dams. Water Research Commission. WRC Report No. 1554/1/10.

Appendix A:

Geostatistical Data Processing



DEPARTMENT

GEOLOGY

UNIVERSITY OF THE FREE STATE

1918-2018

CELEBRATING 100 YEARS



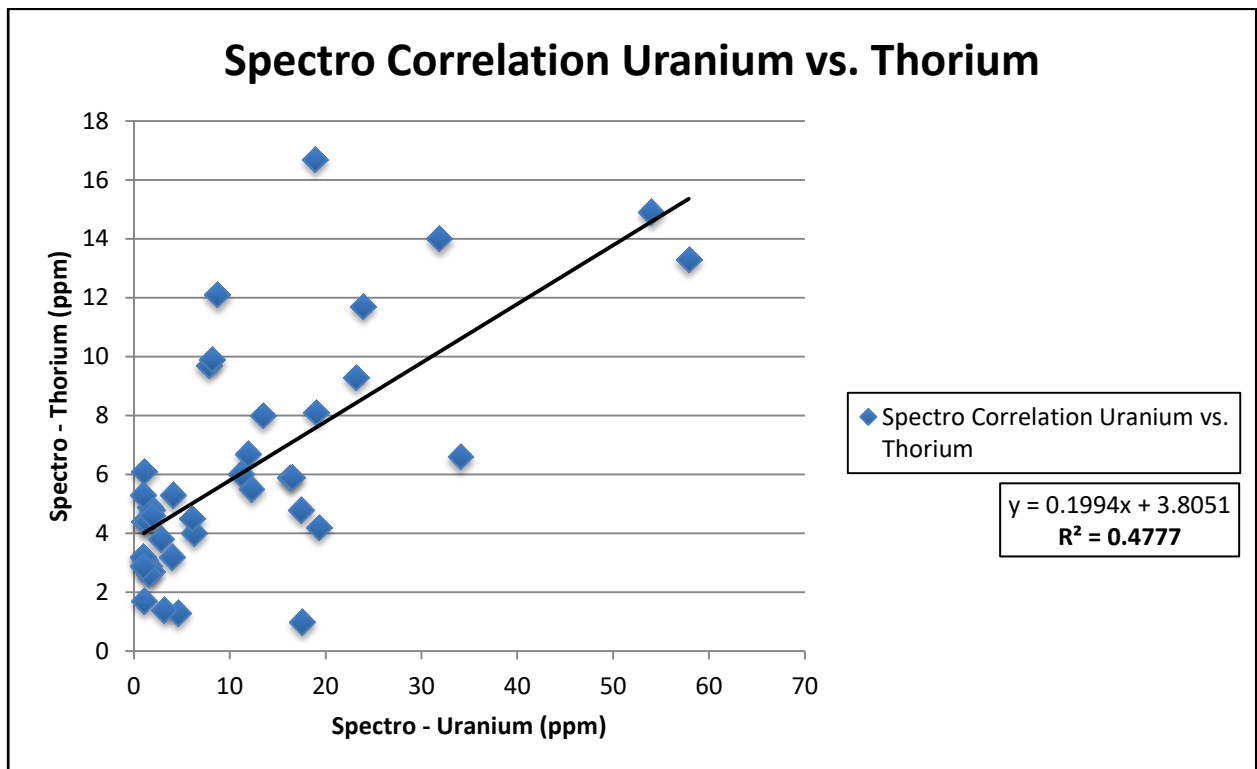


Figure 34: Statistical comparison between recorded uranium and thorium concentrations, as measured by natural gamma-ray spectrometry

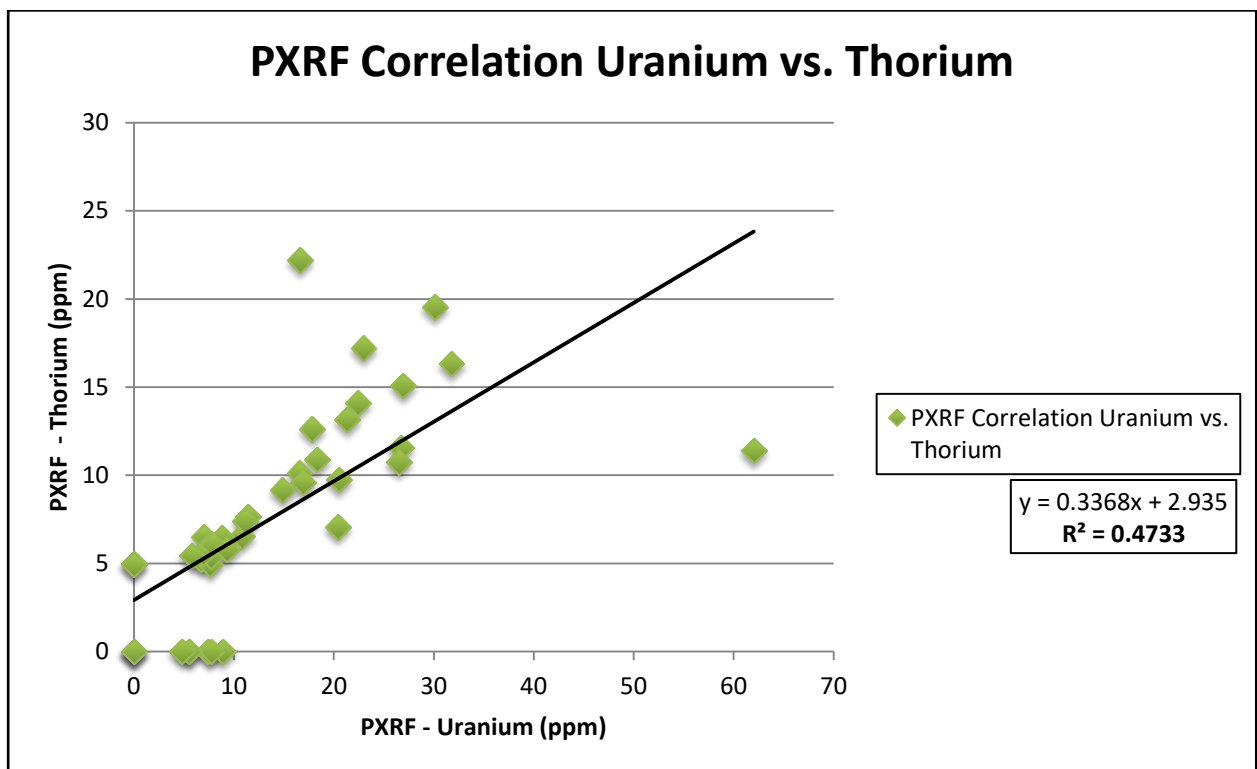


Figure 35: Statistical comparison between recorded uranium and thorium concentrations, as measured by portable-XRF spectroscopy

Table 10: Table illustrating the raw radionuclide concentrations of the selected samples, used to evaluate the statistical relationship between the measured concentrations of each analytical techniques respectively.

Sample No.	Uranium (ppm)			Thorium (ppm)		
	XRF	PXRF	Spectro	XRF	PXRF	Spectro
81	11.0	20.4	11.2	12.0	7.0	6.0
412	9.0	9.4	19.0	7.0	5.8	8.1
755	19.0	22.5	31.9	13.0	14.1	14.0
811	14.0	31.8	18.9	23.0	16.3	16.7
959	10.0	23.0	7.8	10.0	17.2	9.7
978	16.0	17.8	23.2	11.0	12.6	9.3
988	10.0	18.4	11.9	14.0	10.9	6.7
997	12.0	16.6	23.9	11.0	10.1	11.7
1027	11.0	21.3	8.2	20.0	13.1	9.9
1059	25.0	30.1	34.1	12.0	19.5	6.6
1173	10.0	14.9	16.3	14.0	9.2	5.9
1193	6.0	6.9	3.2	4.0	5.6	1.4
1262	7.0	11.4	19.3	7.0	7.6	4.2
1355	16.0	20.5	13.5	12.0	9.8	8.0
1414	7.0	5.5	6.1	7.0	0.0	4.5
1471	3.0	7.4	1.1	14.0	0.0	6.1
1519	24.0	27.0	17.6	8.0	15.1	1.0
1533	12.0	16.6	8.7	13.0	22.2	12.1
1557	10.0	8.9	6.3	7.0	0.0	4.0
1563	24.0	26.7	54.0	9.0	11.6	14.9
1642	59.0	62.0	57.9	9.0	11.4	13.3
1764	22.0	26.5	12.3	8.0	10.8	5.5
1852	8.0	10.8	4.6	8.0	6.6	1.3
1896	16.0	16.9	16.5	7.0	9.6	5.9
1913	4.0	6.7	1.9	12.0	5.2	4.8
2102	6.0	0.0	1.6	15.0	5.0	2.9
2184	10.0	11.1	17.5	10.0	7.4	4.8
2502	7.0	8.9	4.0	10.0	6.4	3.2
2505	4.0	4.8	1.6	14.0	0.0	2.6
2530	4.0	7.1	1.7	13.0	6.5	4.9
2550	4.0	0.0	1.1	14.0	0.0	4.4
2592	4.0	7.9	1.0	12.0	6.1	5.3
2595	5.0	0.0	1.4	15.0	0.0	4.4
2601	4.0	7.7	4.1	9.0	5.9	5.3
2603	6.0	7.7	2.8	11.0	5.0	3.8
2612	2.0	7.8	1.0	14.0	6.1	3.2
2623	3.0	5.6	1.0	13.0	0.0	3.2
2641	3.0	0.0	1.2	14.0	0.0	3.1
2642	3.0	7.7	1.9	13.0	5.4	2.7
2671	2.0	7.8	1.9	16.0	0.0	4.6
2840	3.0	0.0	1.1	15.0	4.9	1.7
2888	4.0	5.8	1.0	12.0	5.4	2.9

Table 11: Variogram parameters used to create the optimal Ordinary Prediction-based Kriging interpolation model for each individual dataset

Model Information				Neighbour Search					Variogram							
Dataset	Type of Kriging	Output Type	Transformation	Search Type	Neighbours	Sector Type	Major Semiaxis	Minor Semiaxis	Type	No. Lags	Lag Size	Nugget	Range	Partial Sill	Anisotropy	RMSE
Field Portable X-ray Fluorescenes Spectroscopy																
Th	Ordinary	Prediction	No	Standard	5	4 @ 45°	0.00770	0.00770	Semivariogram	12	0.000975	23.95	0.00770	23.02	No	0.918
U	Ordinary	Prediction	No	Standard	5	4 @ 45°	0.00294	0.00294	Semivariogram	12	0.000349	0.00	0.00294	318.16	No	0.885
Natural Gamma-ray Spectrometry																
K%	Ordinary	Prediction	No	Standard	5	4 @ 45°	0.00545	0.00545	Semivariogram	12	0.000687	0.00	0.00545	0.38	No	0.947
eTh	Ordinary	Prediction	No	Standard	5	4 @ 45°	0.00127	0.00127	Semivariogram	12	0.000154	8.19	0.00127	13.58	No	0.703
eU	Ordinary	Prediction	No	Standard	5	4 @ 45°	0.00135	0.00135	Semivariogram	12	0.000157	47.94	0.00135	246.85	No	0.579
Uranium Migration Index																
Uo	Ordinary	Prediction	No	Standard	5	4 @ 45°	0.00489	0.00489	Semivariogram	12	0.000629	0.00	0.00489	130.76	No	0.802
Um	Ordinary	Prediction	No	Standard	5	4 @ 45°	0.00143	0.00143	Semivariogram	12	0.000173	25.20	0.00143	89.34	No	0.706
Um%	Ordinary	Prediction	No	Standard	5	4 @ 45°	0.00428	0.00428	Semivariogram	12	0.000545	8374.59	0.00428	13947.95	No	0.741
Ratio Maps																
eU/eTh	Ordinary	Prediction	No	Standard	5	4 @ 45°	0.00065	0.00065	Semivariogram	12	0.000074	0.00	0.00065	2.96	No	0.939
eu/K%	Ordinary	Prediction	No	Standard	5	4 @ 45°	0.00336	0.00336	Semivariogram	12	0.000433	41.50	0.00336	92.96	No	0.853
eTh/K%	Ordinary	Prediction	No	Standard	5	4 @ 45°	0.00191	0.00191	Semivariogram	12	0.000238	11.94	0.00191	10.34	No	1.082
Dose & Radioactivity																
RER	Ordinary	Prediction	No	Standard	5	4 @ 45°	0.00133	0.00133	Semivariogram	12	0.000157	26.45	0.00133	137.95	No	0.570
ERDR	Ordinary	Prediction	No	Standard	5	4 @ 45°	0.00133	0.00133	Semivariogram	12	0.000157	0.18	0.00133	0.96	No	0.570

Appendix B:

Spatial Distribution Patterns of Radionuclides



DEPARTMENT

GEOLOGY

UNIVERSITY OF THE FREE STATE
1918–2018
CELEBRATING 100 YEARS



Spatial Distribution of Equivalent Uranium

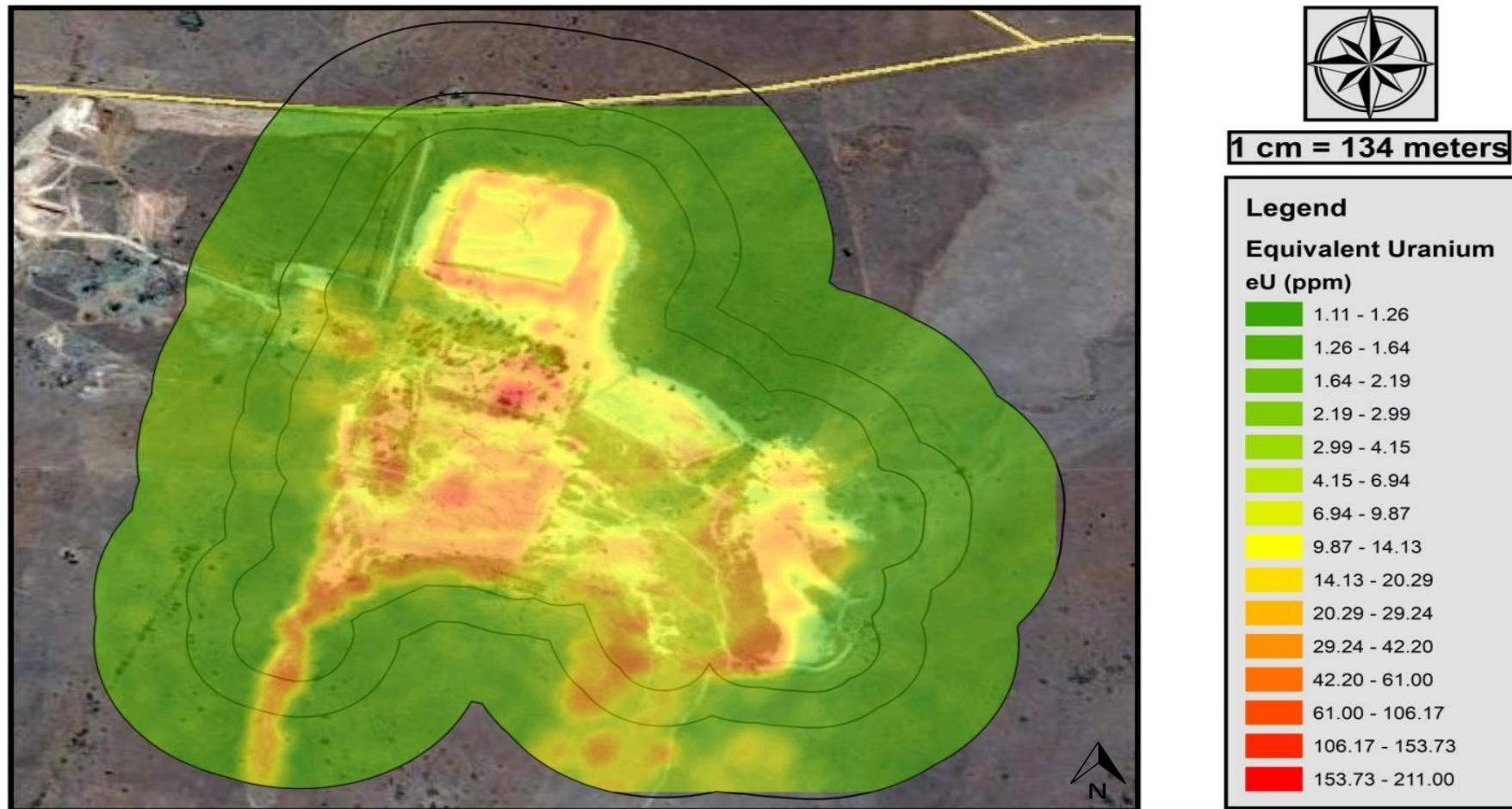


Figure 36: Ordinary prediction-based Kriging interpolation of equivalent uranium concentrations, projected over contemporary high resolution imagery

Spatial Distribution of Measured Uranium

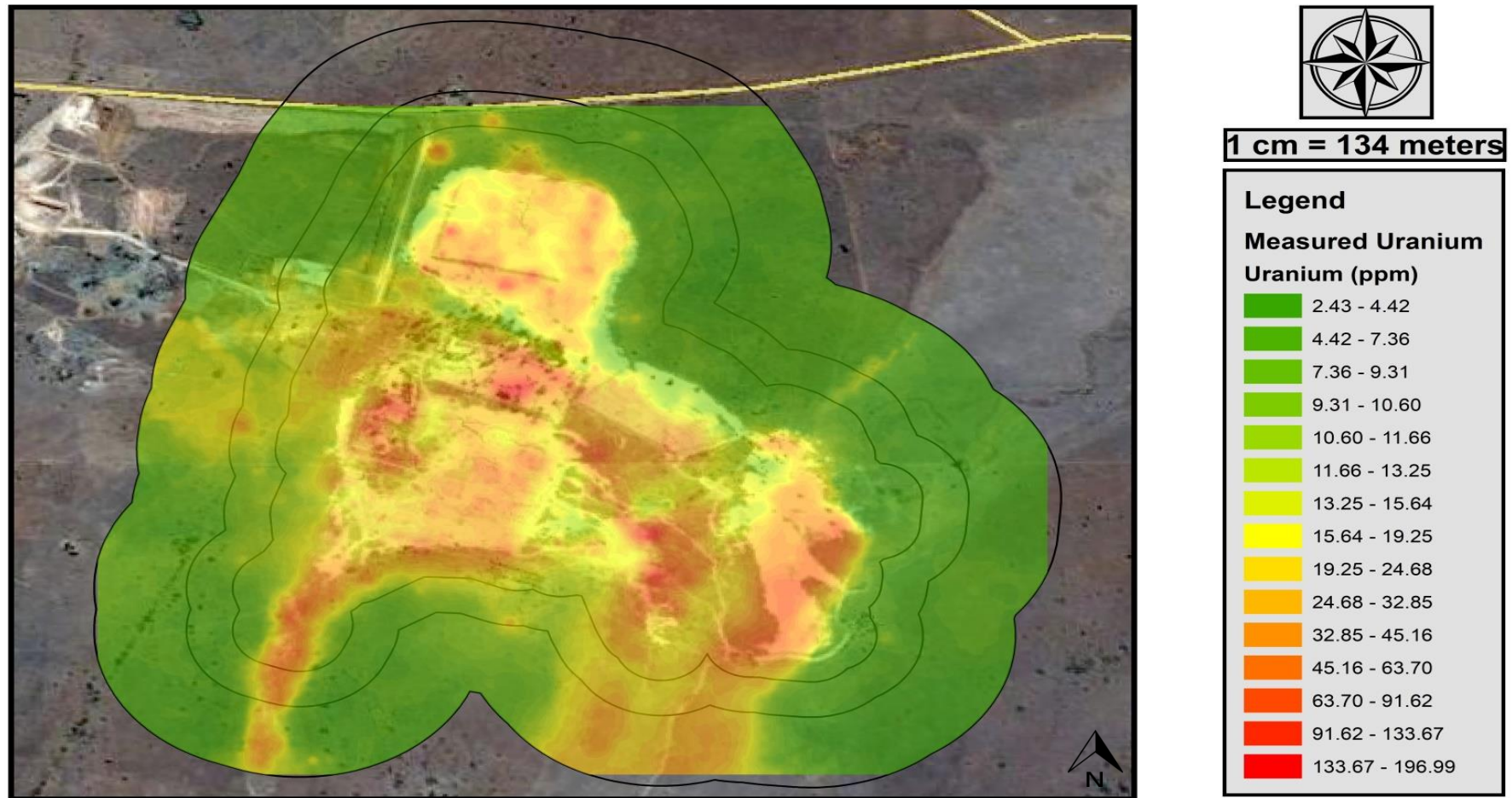


Figure 37: Ordinary prediction-based Kriging interpolation of measured uranium concentrations, projected over contemporary high resolution imagery

Spatial Distribution of Equivalent Thorium

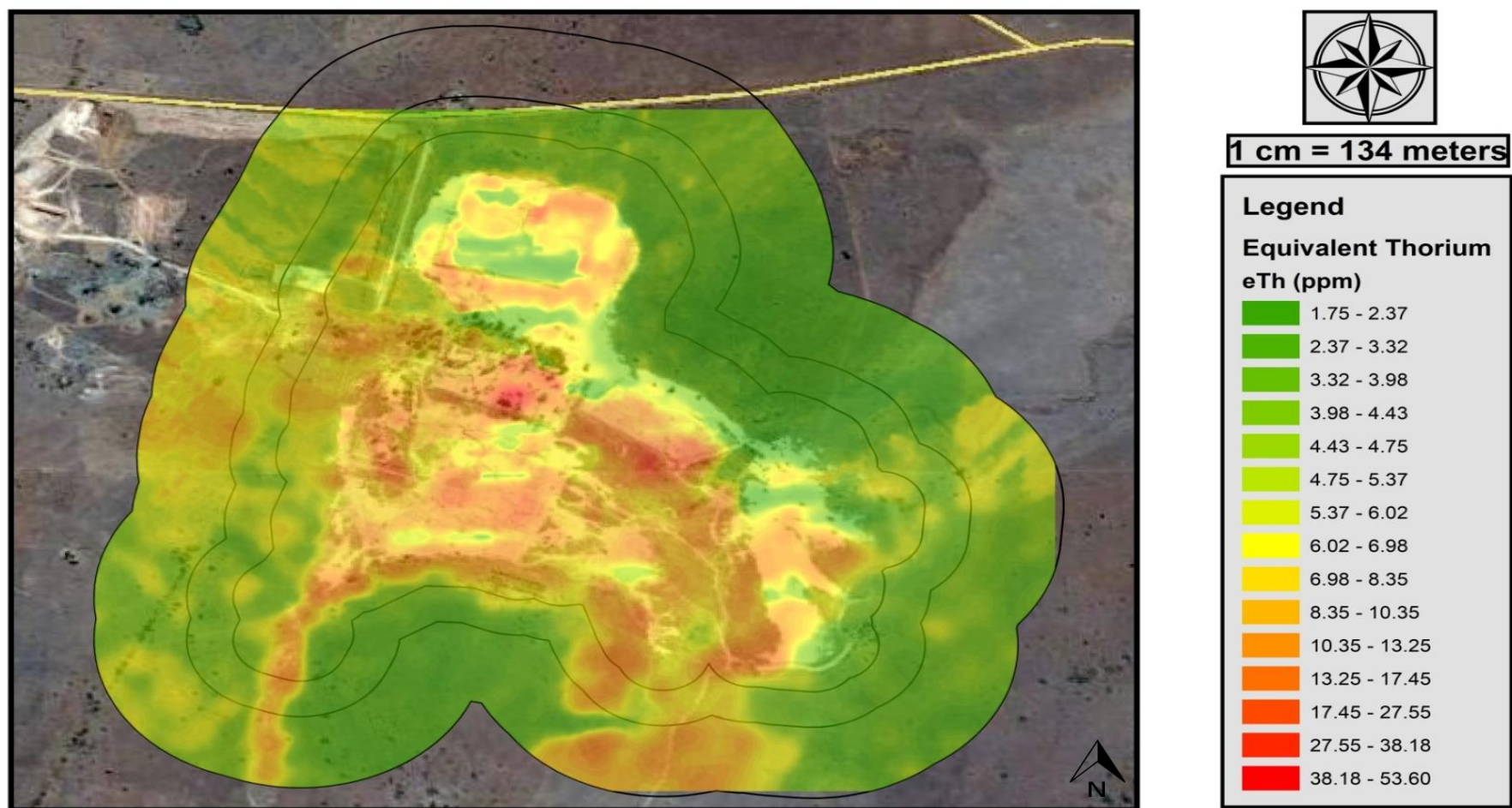


Figure 38: Ordinary prediction-based Kriging interpolation of equivalent thorium concentrations, projected over contemporary high resolution imagery

Spatial Distribution of Measured Thorium

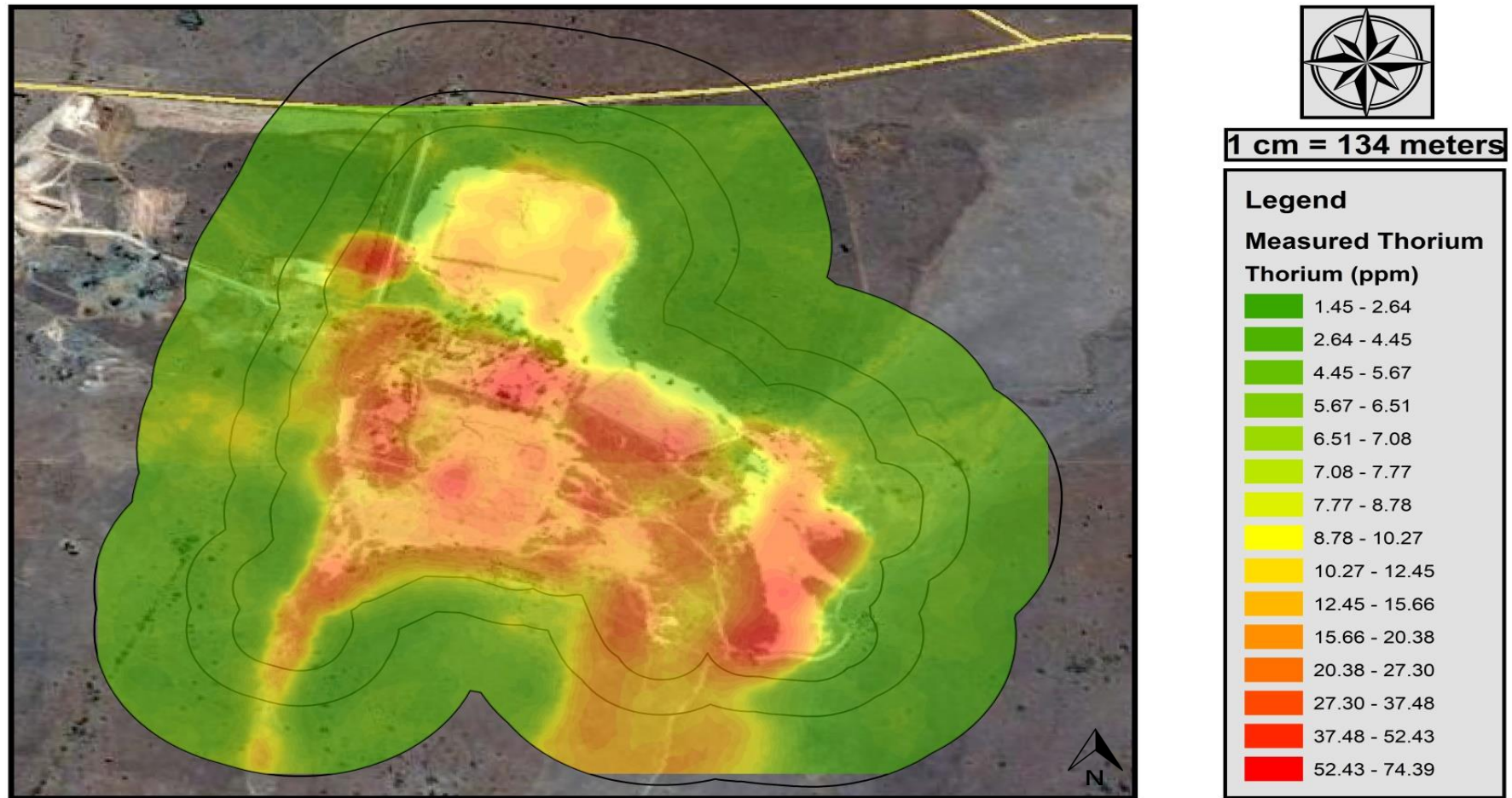


Figure 39: Ordinary prediction-based Kriging interpolation of measured thorium concentrations, projected over contemporary high resolution imagery

Spatial Distribution of Measured Potassium

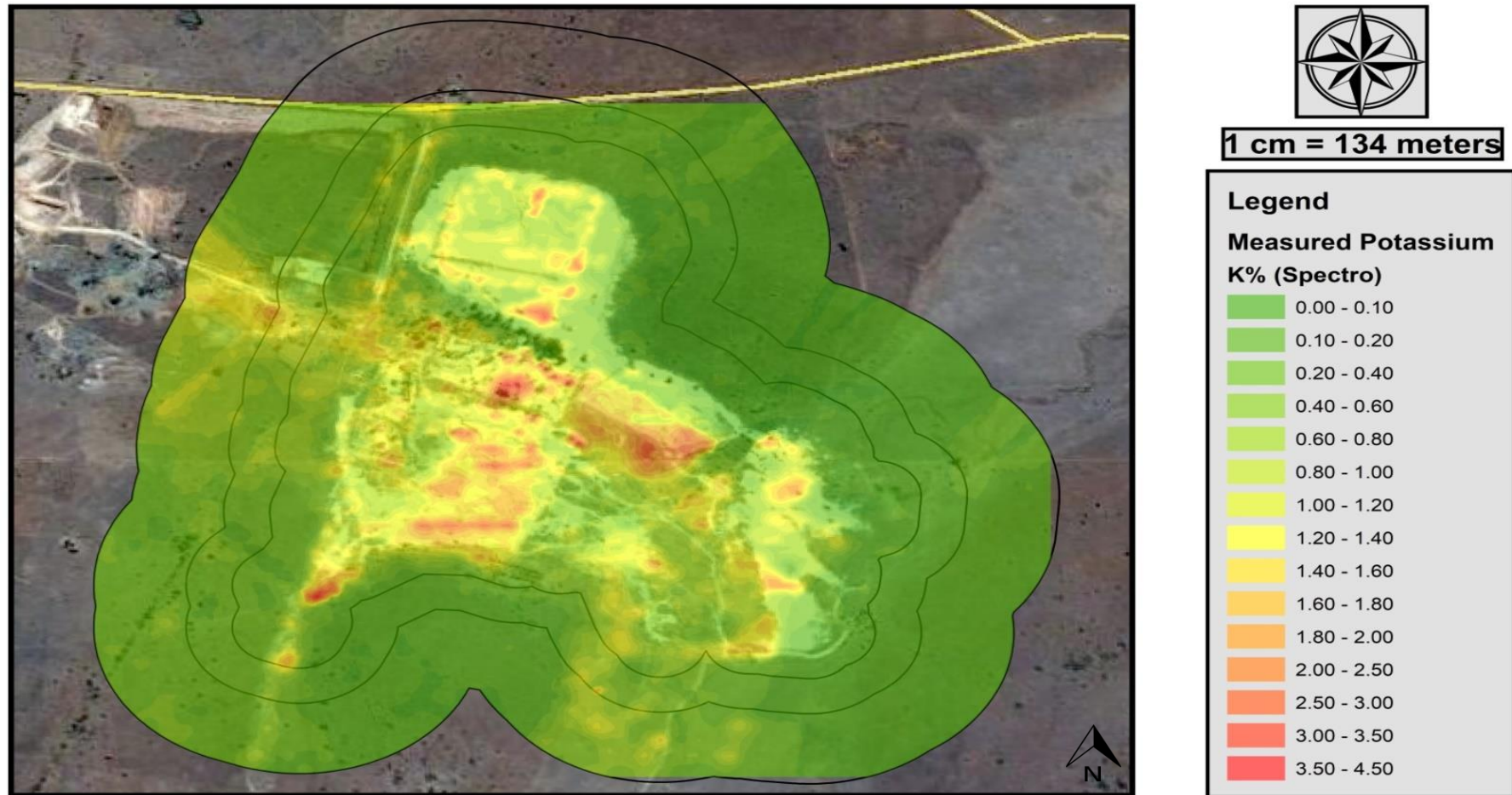


Figure 40: Ordinary prediction-based Kriging interpolation of measured potassium concentrations (%), projected over contemporary high resolution imagery

Table 12: Pearson Correlation Matrix, showing the linear relationship found between respective datasets.

		Pearson Correlation Matrix									
		K %	eU _(ppm)	eTh _(ppm)	U _o	U _m	U _m %	eU/eTh	eU/K %	eTh/K %	ERDR _(mSv/y)
Pearson Correlation Matrix	K %	1.000									
	eU _(ppm)	0.627	1.000								
	eTh _(ppm)	0.555	0.768	1.000							
	U _o	0.565	0.789	0.929	1.000						
	U _m	0.388	0.740	0.216	0.170	1.000					
	U _m %	0.264	0.406	0.064	0.079	0.565	1.000				
	eU/eTh	0.611	0.437	0.008	0.119	0.570	0.518	1.000			
	eU/K %	0.152	0.715	0.490	0.545	0.550	0.455	0.353	1.000		
	eTh/K %	-0.424	-0.062	0.181	0.094	-0.201	-0.286	-0.385	0.267	1.000	
	ERDR _(mSv/y)	0.678	0.995	0.813	0.824	0.694	0.379	0.426	0.683	-0.066	1.000

Appendix C:

Uranium Migration and Anomaly Verification



DEPARTMENT

GEOLOGY

UNIVERSITY OF THE FREE STATE
1918-2018
CELEBRATING 100 YEARS



Spatial Distribution of Uranium Migration (Uo)

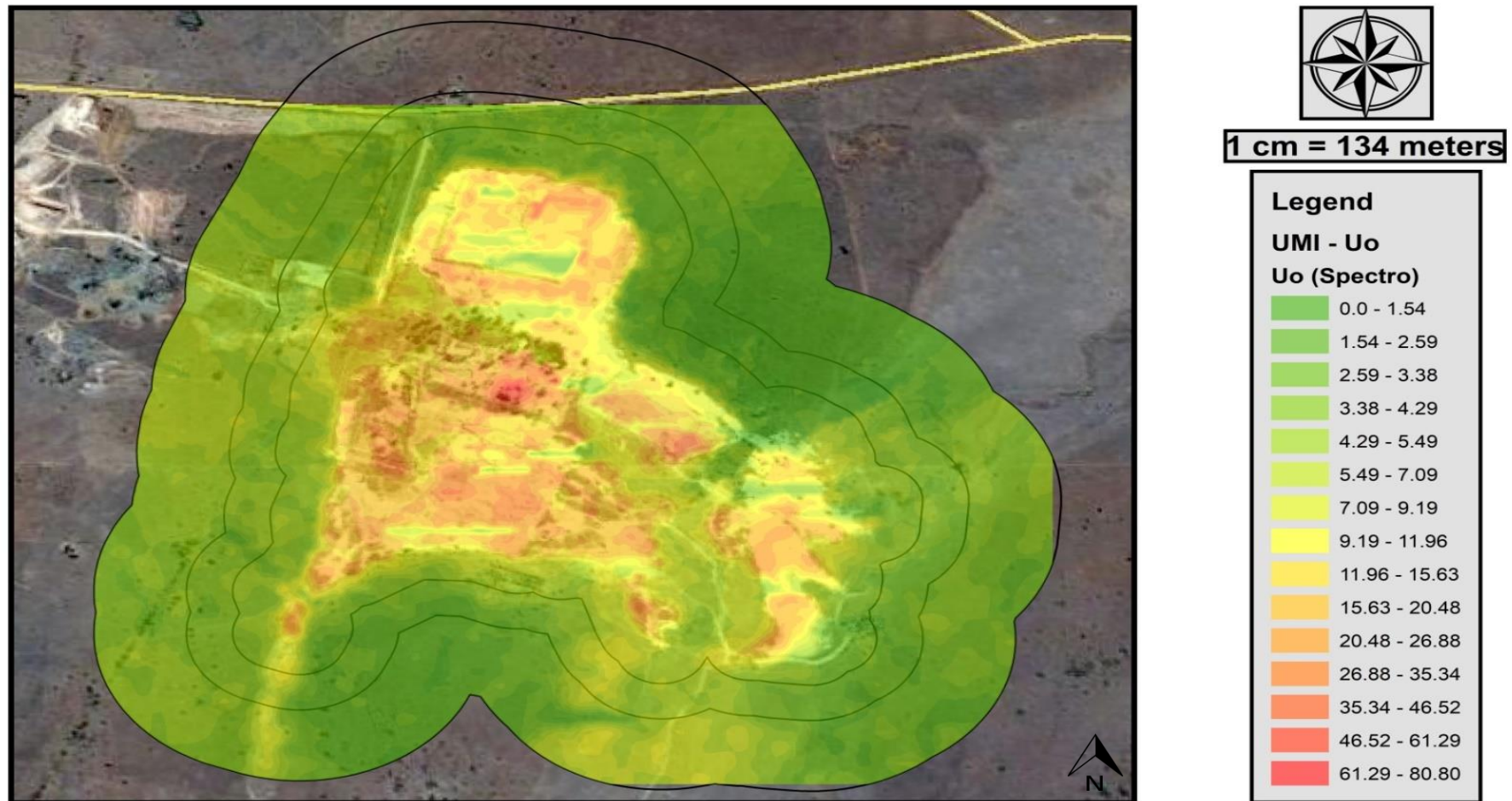


Figure 41: Ordinary prediction-based Kriging interpolation of calculated “original” uranium concentrations, projected over contemporary high resolution imagery

Spatial Distribution of Uranium Migration (Um)

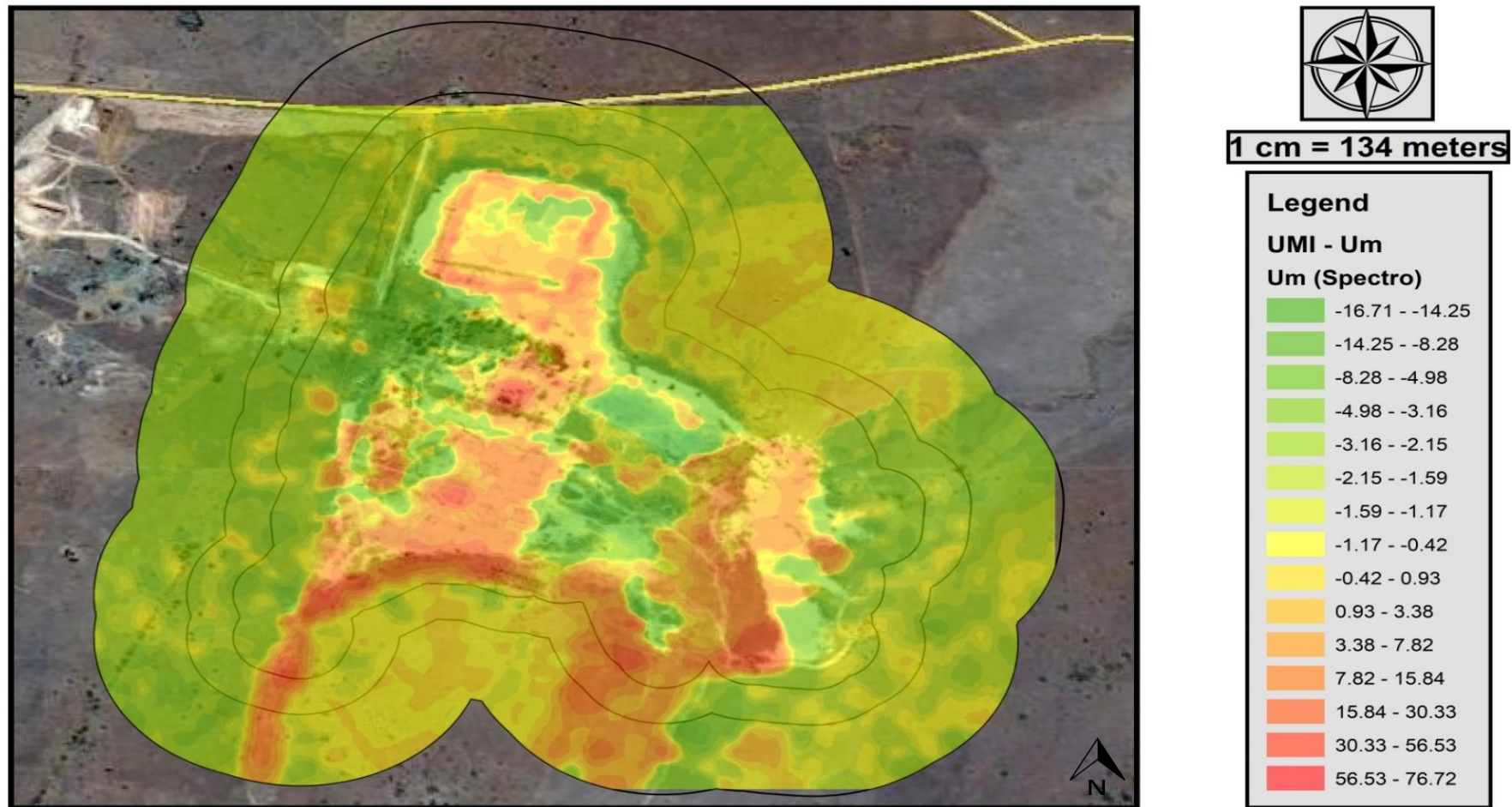


Figure 42: Ordinary prediction-based Kriging interpolation of quantified uranium migration values, projected over contemporary high resolution imagery

Spatial Distribution of Uranium Migration (Um%)

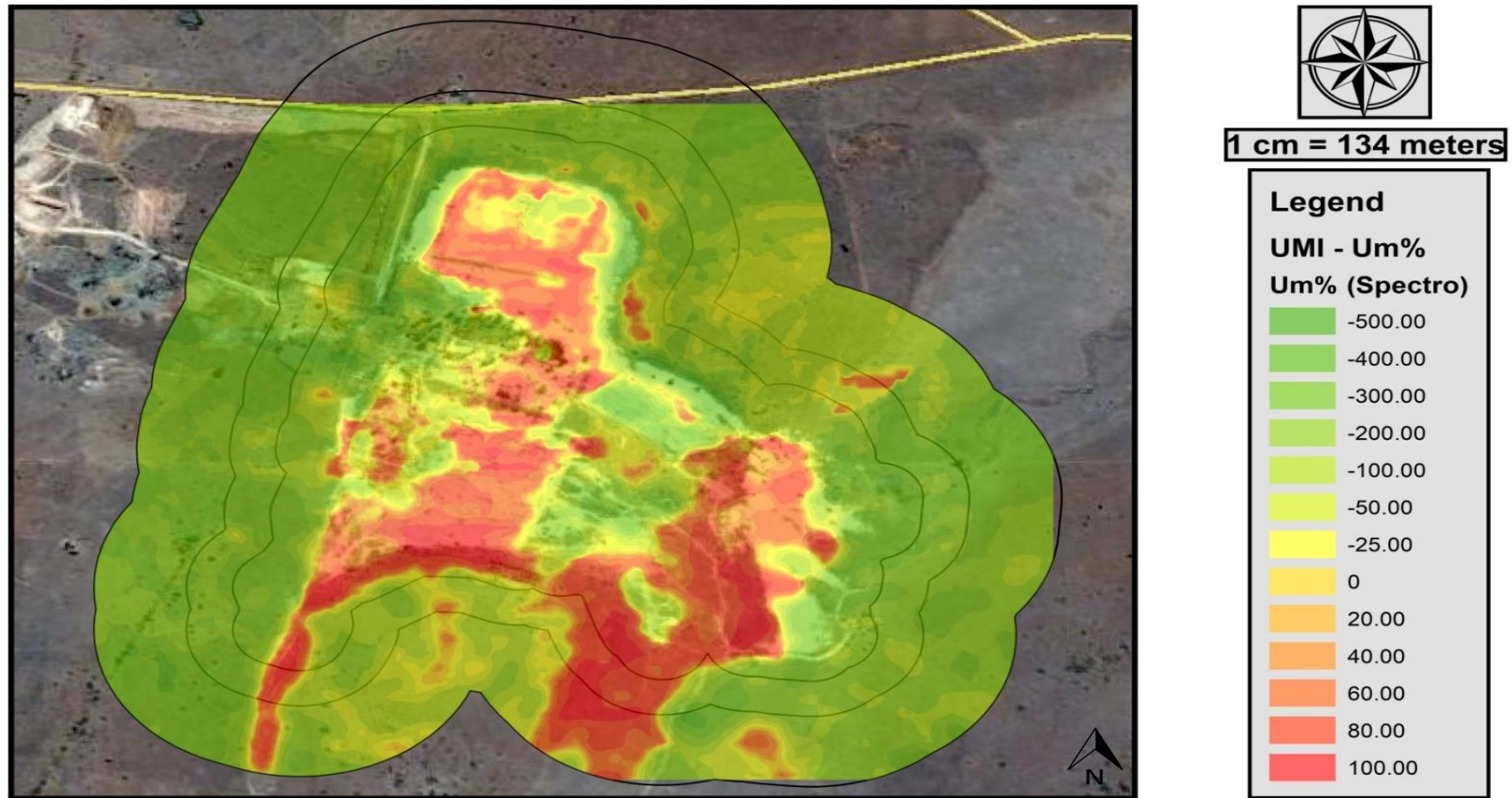


Figure 43: Ordinary prediction-based Kriging interpolation of uranium migration rate values, projected over contemporary high resolution imagery

Spatial Distribution of eU/eTh Ratio

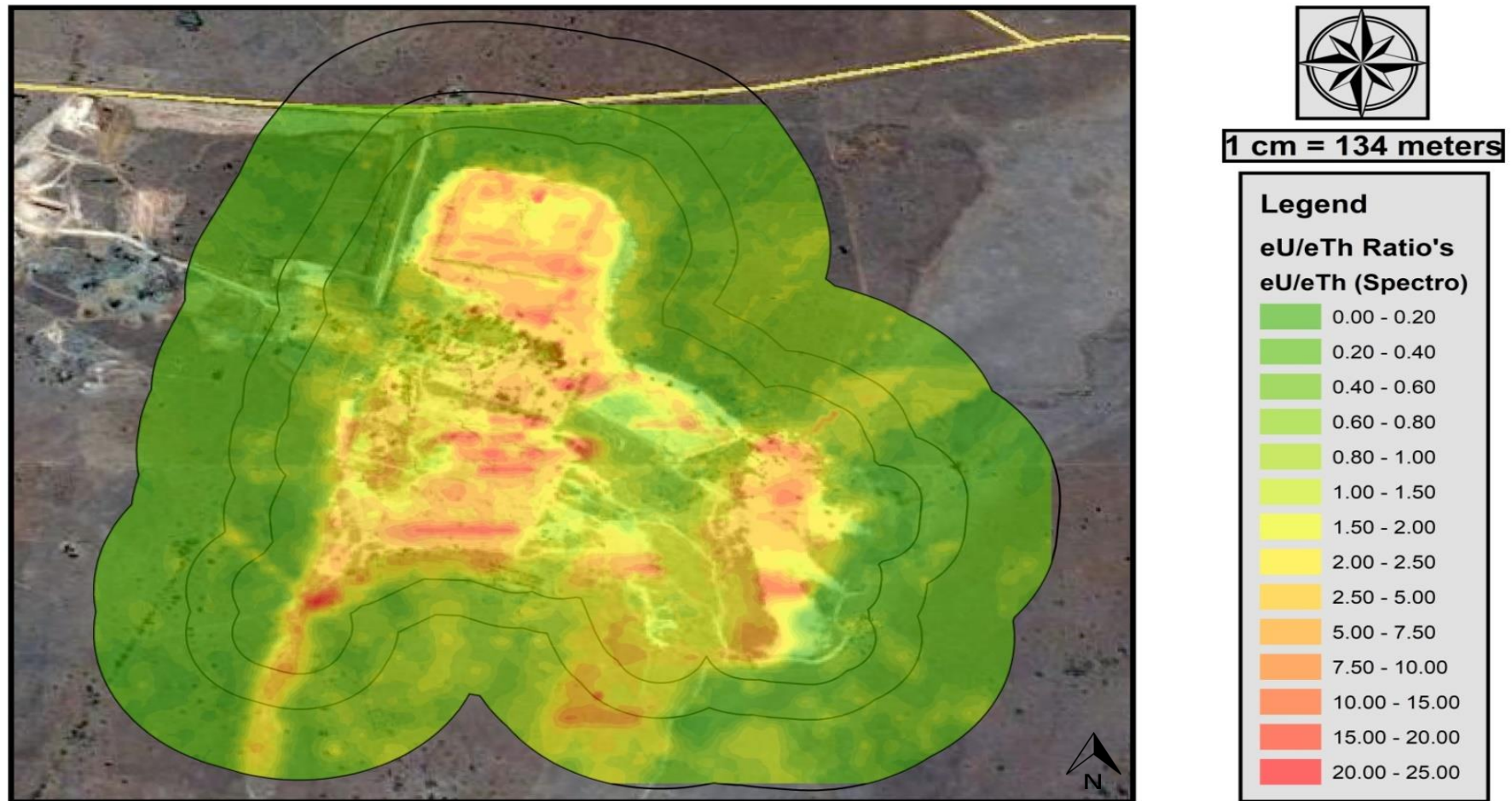


Figure 44: Ordinary prediction-based Kriging interpolation of eU/eTh ratios, projected over contemporary high resolution imagery

Spatial Distribution of eU/K% Ratio

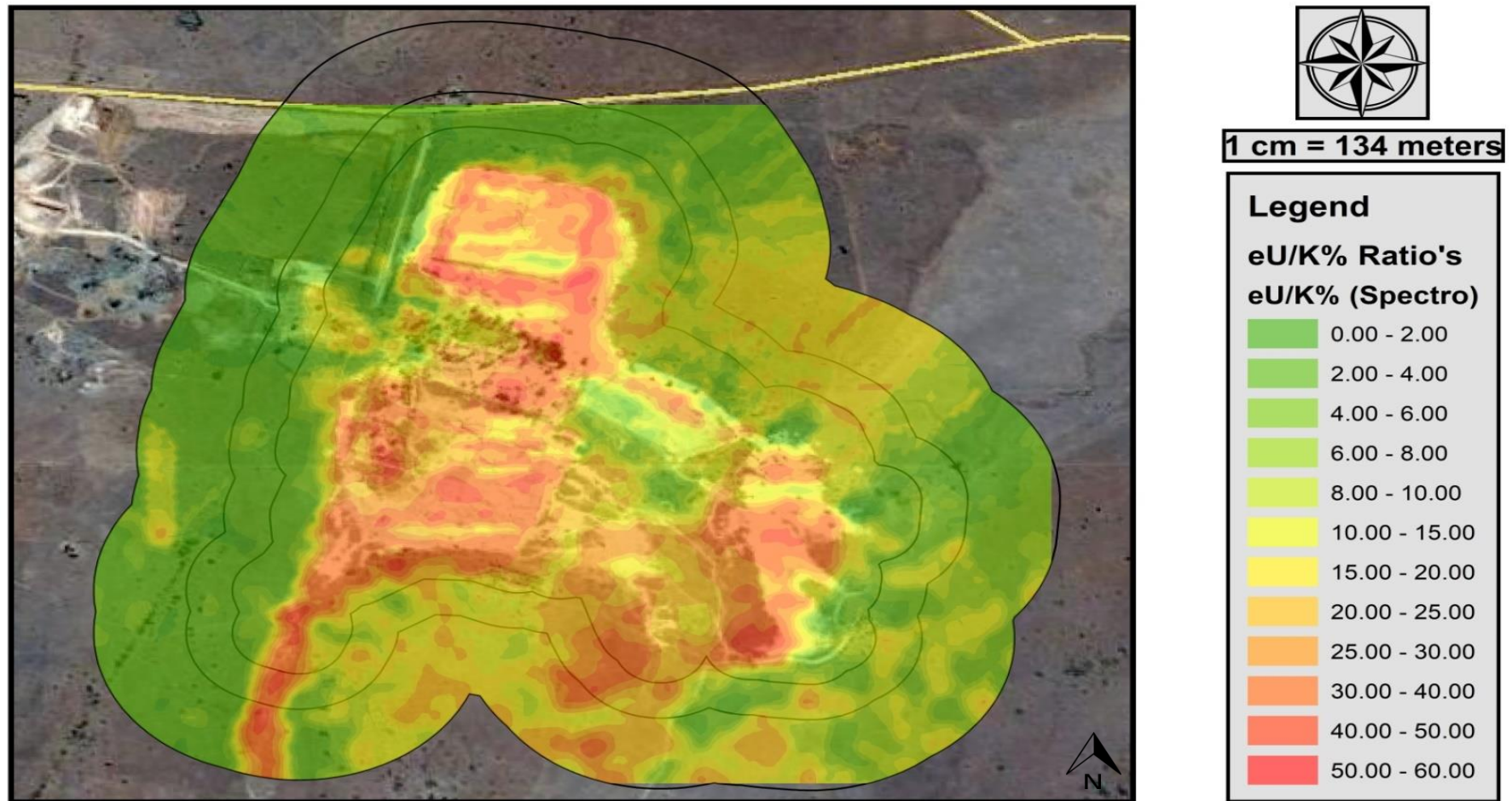


Figure 45: Ordinary prediction-based Kriging interpolation of eU/K% ratios, projected over contemporary high resolution imagery

Spatial Distribution of eTh/K% Ratio

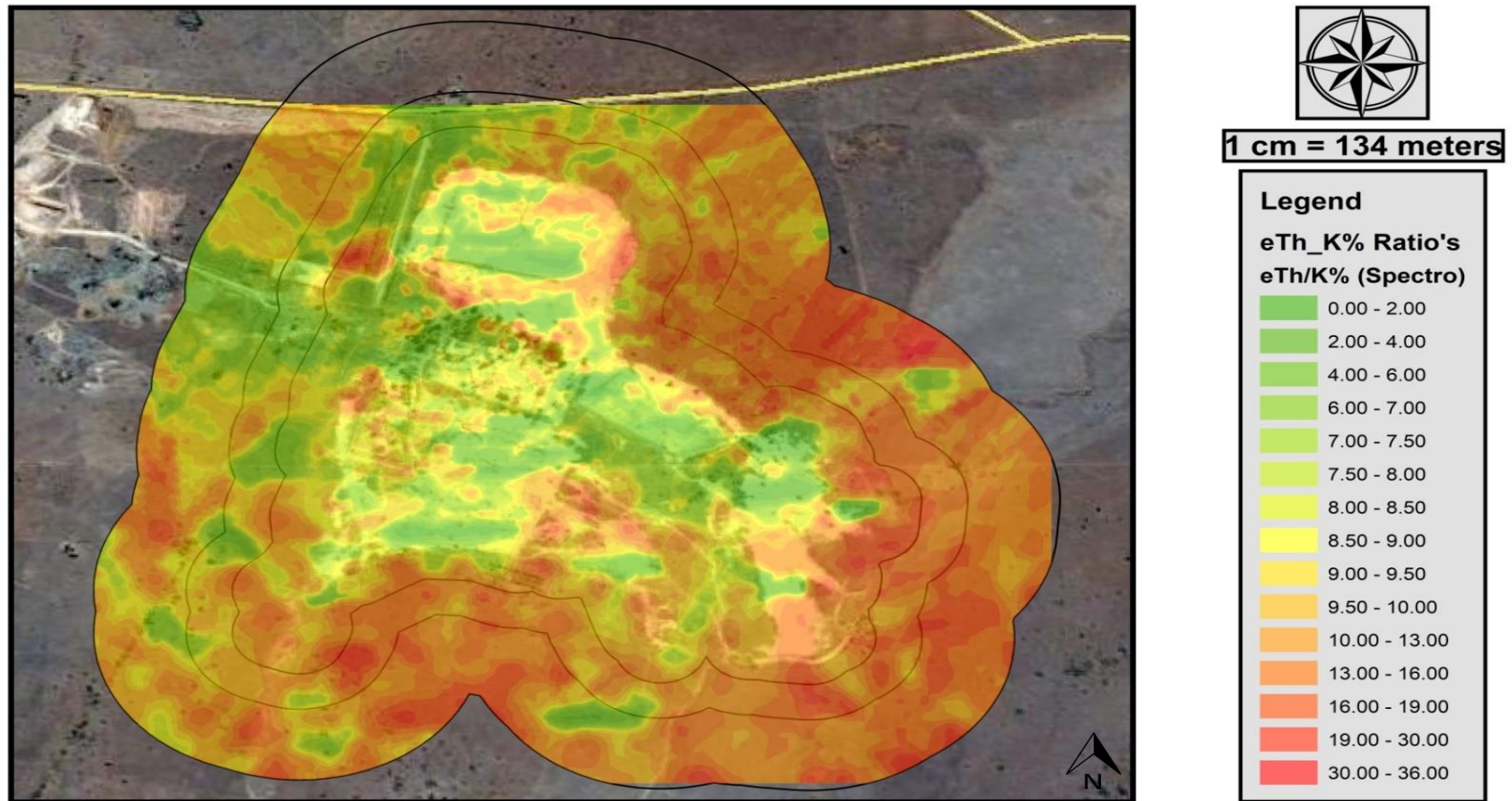


Figure 46: Ordinary prediction-based Kriging interpolation of eTh/K% ratios, projected over contemporary high resolution imagery

Radiation Exposure Rate

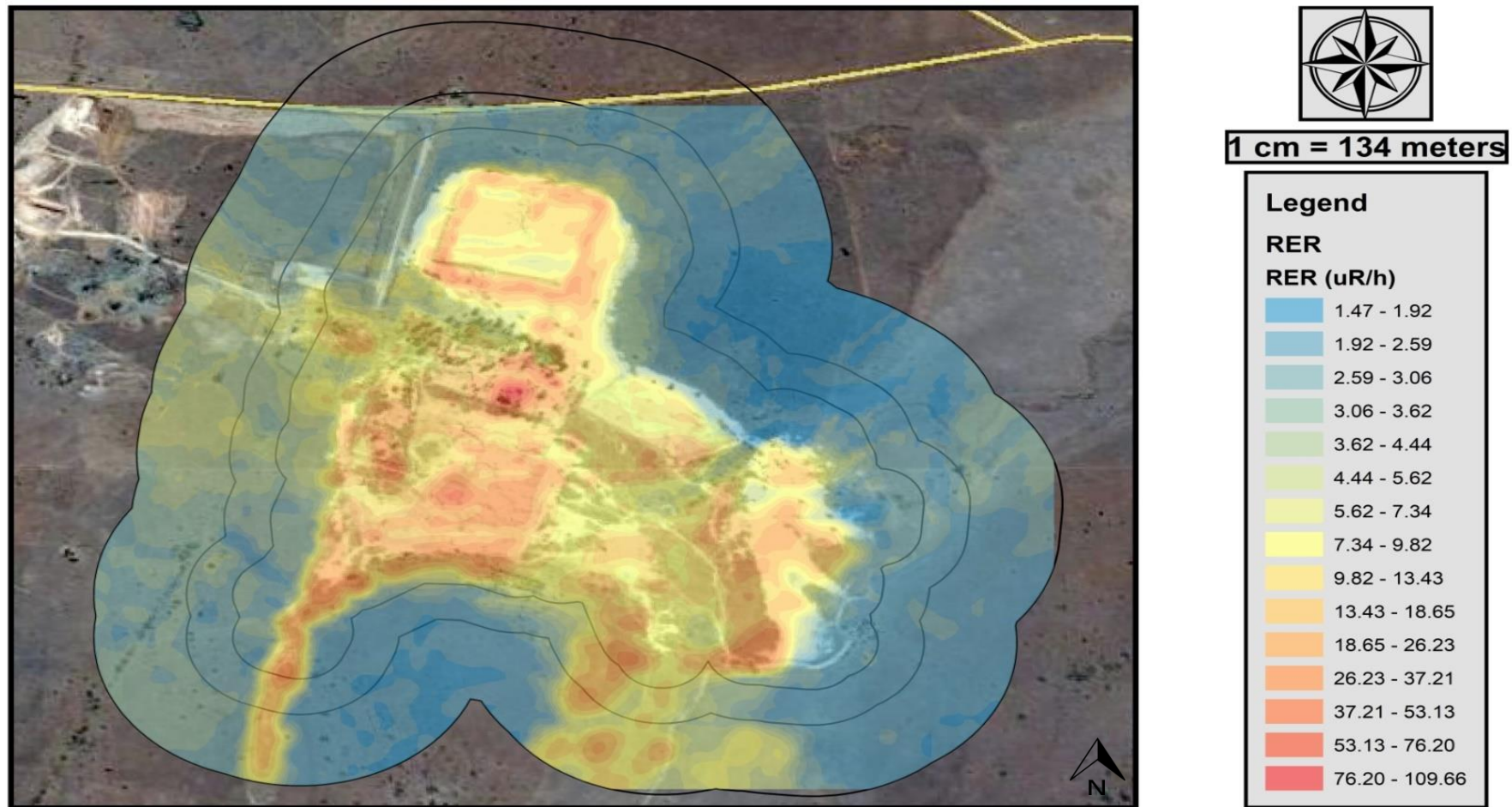


Figure 47: Ordinary prediction-based Kriging interpolation of Radiation Exposure Rate values, projected over contemporary high resolution imagery

Equivalent Radiation Dose Rate

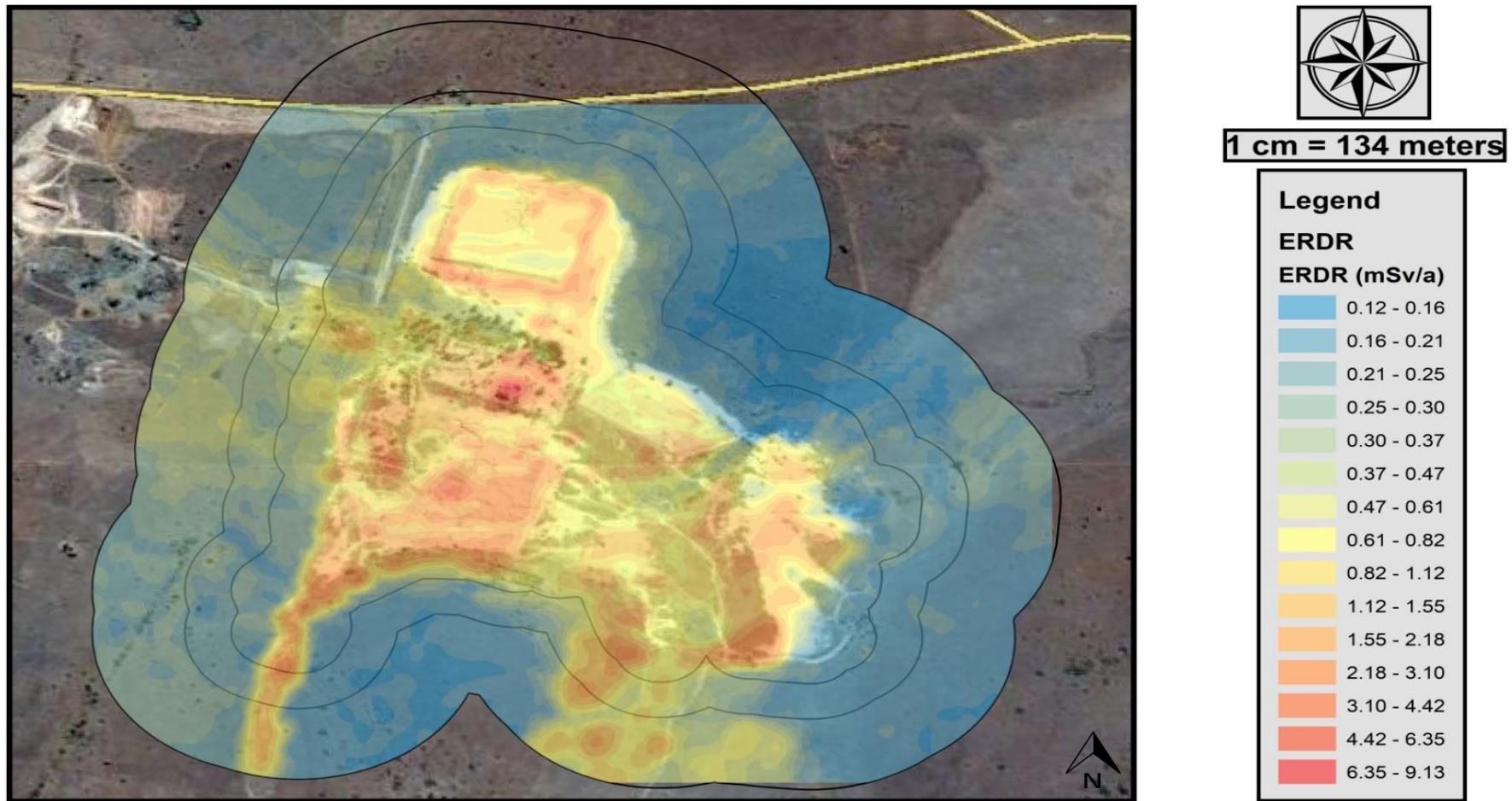


Figure 48: Ordinary prediction-based Kriging interpolation of Equivalent Radiation Dose Rate values, projected over contemporary high resolution imagery